Gold nanoparticle functionalization and thin-film deposition of layered group VI transition metal dichalcogenides

Sebastian Grieger

Inaugural dissertation submitted for the degree of

Doctor Rerum Naturalium

Department of Chemistry
University of Heidelberg

Gold nanoparticle functionalization and thin-film deposition of layered group VI transition metal dichalcogenides

Inaugural dissertation submitted for the degree of
Doctor Rerum Naturalium (Dr. rer. nat.)

Thesis submitted to the
Combined Faculty of Mathematics, Engineering and Natural Sciences
Ruprecht-Karls-Universität
Heidelberg, Germany

Submitted by
M. Sc. Sebastian Grieger
born in Weinheim an der Bergstraße

Date of Submission: 20.01.2022
1. Examiner: Prof. Dr. Claudia Backes
2. Examiner: Prof. Dr. Petra Tegeder

Date of oral exam:
25.02.2022

„Ein Chemiker, der kein Physiker ist, ist überhaupt gar nichts.“

- Robert Wilhelm Bunsen

Acknowledgements

This thesis is the product of several years of work and concludes a significant stage of my life. As no scientist is an island, this stage of life is associated with many individuals whose contribution to my personal and scientific development cannot be overestimated. This chapter is dedicated to them.

First of all, I would like to thank *Prof. Dr. Claudia Backes* for providing not only funding and the opportunity for doing scientific research in a dynamic and diverse field, but also for her frequent advice, lively discussions, sheer endless creativity, and for finding the ideal balance between close supervision and leaving space for individual ideas. No part of this work would have been possible without your support.

Furthermore, I want to thank all my colleagues from the PC2D and NMOE group at the Institute for Applied Physical Chemistry for maintaining high standards in the lab as well as a welcoming and friendly atmosphere to work in. Especially, I would like to express my gratitude towards *Dr. Kevin Synnatschke*, who introduced me to the group and to the basic workflow during my master thesis and helped me in the entirety of my works either by providing professional help in form of discussions and literature knowledge or by patiently listening to the occasional rant. You were always the first to ask if help was due and the last to leave if things went wrong. Your level of professionalism, organization and diligence are a constant inspiration. Also, I would like to thank my office mates *Dr. Farnia Rashvand*, *Max Krings*, *Tim Nowack,* and *Sebastian Lindenthal* for their patience with my constant urge for discussions and debatable taste in music. I like to thank *Dr. Vaishnavi Rao* and *Dr. Beata Szydłowska* and all other contributors for scientific support ultimately leading to valuable insights in form of a publication. I want to express my gratitude towards *Klaus Schmitt* and the precision mechanics workshop at the Institute of Physical Chemistry for their valuable advice in planning and flawless execution in building of various custom made setups employed for the work discussed in this thesis. I want to thank the Electron Microscopy Core Facility at the European Molecular Biology Laboratory in Heidelberg and especially *Martin Schorb* for access and support of their transmission electron microscopy equipment. Furthermore, I like to thank my research interns *Marcus Dodds*, *Eva Steinmann,* and *David Schmitt* for being brave enough to choose me as their supervisor. Especially, I would like to thank *Sophia Terres*, as she significantly contributed to the development and investigation of the modified Langmuir-Blodgett deposition method with tireless dedication during her internship and following master thesis under my supervision. Last but not least, I would like to thank *Prof. Dr. Jana Zaumseil* for sharing her profound

knowledge and excellent facility with the PC2D group, but also for entrusting me with the development of a student lab class which I greatly enjoyed.

Finally, I want to thank many people outside of the laboratory for their enduring support. First and foremost *Lena*, who not only accompanied me with constant patience and compassion during this challenging and at times exhausting stage of my life but also frequently provided a different view on scientific and non-scientific matters. Your support and care are irreplaceable and I want to apologize that you had to proof-read all of this. Furthermore, I would like to thank *Andrea, Volker, Irma, Christiane,* and *Sven* for their constant, unconditional support from the very first day of studying chemistry until now and guidance in life as a whole, *Annalena* for frequent proof-reading and together with *Nicole* for dog-related comfort, and *Doris* and *Hans-Peter* for providing shelter and much-needed cake more than once. You all provided me with the stability and energy necessary for successful completion of such a challenging task and I am deeply grateful for that.

Abstract

Transition metal dichalcogenides (TMDs) are an intensively investigated class of layered materials and are regarded as promising candidates for various applications based on their exotic, layer-dependent optical and electronic properties. When applications are envisioned for a new material, control over the properties of the material is indispensable for efficient integration. Hence, the functionalization of layered nanomaterials is an ever-growing field with countless possibilities for tailoring these properties. However, literature focuses mostly on novel functionalization approaches and proof-of-principle applications, with fundamental questions of heterogeneous reactions at the nanosheet-solution interface rarely being tackled. In the first part of this thesis, insights into the influence of the surface chemistry on heterogeneous functionalization reactions at surfactant stabilized transition metal dichalcogenide nanosheets will be presented. A significant dependence of the heterogeneous gold nanoparticle functionalization of group VI TMDs, namely WS_2 and MoS_2, will be presented and a simple model is developed to explain observed regioselectivities based on the choice of surfactant and material. Preferential adsorption of representatives of commonly employed surfactants to distinguishable sites on the nanosheets is demonstrated and linked to the chemical structure of the respective surfactant.

Based on this demonstration, precise surfactant-mediated control of heterogeneous functionalization reactions can be envisioned and a generalization of the model for other material-surfactant systems is plausible.

The layer dependence and sensitivity of optical properties of transition metal dichalocgenides towards their environment is one particularly fascinating characteristic of this class of materials. However, a major drawback of the same characteristic is, that reproducibility and comparability of experimental results cannot be guaranteed where perfect control over the environment is not maintained. Especially for film deposition, where individual nanosheets come in close proximity, film morphology has a severe impact on optical properties and can lead to uncertainties in data interpretation. In the second part of this thesis, a promising method for thin-film production from liquid dispersions of nanosheets is presented, capable of largely alleviating these problems, at least on the laboratory scale. A custom deposition setup was developed to enable reproducible formation and transfer of films after preassembly of the layered materials at the interface between two immiscible solvents. These films are extremely thin and smooth, both on the order of 10^0 to 10^1 nm, and nanosheets are aligned over a sizeable area. A proof-of-principle experiment is presented that demonstrates non-covalent solid-state

functionalization of WS_2 thin-films with organic dyes and indications for electronic interactions between films and dyes are discussed based on changes in photoluminescence of both dyes and films. This well-defined deposition method is further compared to a complementary deposition approach producing porous films with randomized nanosheet orientation and the influence of morphology on the electrocatalytic activity of WS_2 thin-film electrodes towards the hydrogen evolution reaction is discussed.

This deposition method should enable experimental designs previously inaccessible to layered nanomaterials produced from liquid phase exfoliation and improve reliability of both film production and data interpretation.

Zusammenfassung

Übergangsmetalldichalkogenide sind Vertreter der Klasse der Schichtmaterialien und stehen im Fokus vielfältiger Forschung und der Entwicklung verschiedenster Anwendungen, motiviert durch ihre exotischen, lagenzahlabhängigen optischen und elektronischen Eigenschaften. Um eine effiziente Implementierung dieser Materialien in Bauteilen zu ermöglichen, ist Kontrolle über die Materialeigenschaften unerlässlich. Aufgrund der unerschöpflichen Möglichkeiten, die die Funktionalisierung von schichtartig aufgebauten Nanomaterialien bietet, ist der wissenschaftliche Aufwand in diesem Forschungszweig stetig gestiegen. Oftmals liegt der Fokus wissenschaftlicher Arbeiten in diesem Bereich auf neuartigen Ansätzen oder der Demonstration neuer Anwendungen. Fundamentale Fragen über die Natur heterogener Reaktionen an der Grenzfläche zwischen Nanomaterial und Lösungsmittel werden jedoch selten in den Fokus eben solcher Arbeiten gerückt. Im ersten Teil der hier vorgestellten Arbeit werden neue Erkenntnisse über den Einfluss der Oberflächenchemie tensidstabilisierter Nanomaterialdispersionen auf heterogene Funktionalisierungsreaktionen am Beispiel der Gruppe VI Übergangsmetalldichalkogenide WS_2 und MoS_2 beschrieben. Ein einfaches Modell zur Erklärung beobachteter Regioselektivitäten, in Abhängigkeit des gewählten Tensids und Materials, wird diskutiert und auf die bevorzugte Adsorption von Vertretern üblicher Tensidklassen an unterscheidbaren Adsorptionsplätzen und schließlich auf deren chemische Struktur zurückgeführt.

Eine gezielte, tensidvermittelte Kontrolle über heterogene Funktionalisierungsreaktionen könnte zukünftig neuartige Materialeigenschaften zugänglich machen, während eine Ausdehnung der hier entwickelten Konzepte auch in Bezug auf andere Material-Tensid-Systeme plausibel erscheint.

Die empfindliche Abhängigkeit optischer Eigenschaften der Übergangsmetalldichalkogenide von deren Umgebung ist einerseits ein faszinierendes Merkmal dieser Materialklasse, andererseits jedoch auch ein möglicher Fallstrick bei der Interpretation und beim Vergleich von experimentellen Ergebnissen. Dies ist darauf zurückzuführen, dass eine perfekte Kontrolle über die direkte Umgebung der Materialien selten möglich ist. Diese Problematik manifestiert sich im Besonderen in den optischen Materialeigenschaften nach der Filmabscheidung, da die räumliche Nähe der Nanomaterialien im Film, und daher die Filmmorphologie starken Einfluss auf die elektronische Struktur der dünnschichtigen Nanomaterialien nimmt. Im zweiten Teil dieser Arbeit wird eine vielversprechende Methode zur Dünnfilmherstellung aus Nanomaterialdispersionen vorgestellt, die einige dieser Probleme in der akademischen Forschung ausräumen und

die Interpretation von Messdaten erleichtern kann. Zu diesem Zweck wurde eine speziell angefertigte Abscheidevorrichtung entwickelt, bei der Filmausbildung und -transfer an der Phasengrenze zwischen zwei nicht mischbaren Flüssigkeiten stattfindet. Die erhaltenen Filme sind sehr dünn und glatt, in der Größenordnung von 10^0 bis 10^1 nm, und die einzelnen Nanoschichten sind über eine große Fläche parallel zum Substrat ausgerichtet. Zwecks Demonstration der Vorteile dieser Abscheidungsmethode wurden organische Chromophore auf dem Film abgeschieden und Hinweise auf elektronische Wechselwirkungen zwischen Chromophor und Film werden, basierend auf Änderung der Photolumineszenz von Filmen als auch Chromophoren, diskutiert. Im letzten Teil der Arbeit wird der Einfluss der Filmmorphologie auf die elektrokatalytischen Eigenschaften von WS_2-Dünnfilmelektroden in Bezug auf die elektrochemische Wasserstoffentwicklung untersucht. Die Methode wird dabei mit einer komplementären Abscheidungsmethode, die poröse Filme mit zufälliger Ausrichtung der Nanoschichten produziert, verglichen.

Die Entwicklung dieser Methode zur verlässlichen Abscheidung dünner Filme aus der flüssigen Phase birgt das Potential, flüssigphasenexfoliierte Nanomaterialien einer ganzen Reihe neuer experimenteller Konzepte zuzuführen und dabei die Interpretierbarkeit der Resultate zu verbessern.

Table of contents

Table of abbreviations

AB	Airbrush spray
AFM	Atomic force microscopy
APTES	3-(Aminopropyl)triethoxysilane
APTMS	3-(Aminopropyl)trimethoxysilane
a.u.	Arbitrary units
CHP	*N*-cyclohexyl-2-pyrrolidone
CMC	Critical micelle concentration
CTAB	Cetyltrimethylammonium bromide
CVD	Chemical vapor deposition
DGU	Density gradient ultracentrifugation
DI	Deionized (water)
DLVO	Derjaguin-Landau-Verwey-Overbeek
ECSA	Electrochemical (active) surface area
e.g.	for example (lat. *exempli gratia*)
F_4-TCNQ	2,3,5,6-Tetrafluoro-7,7,8,8-tetracyano-quinodimethane
FOTS	*1H,1H,2H,2H*-perfluorooctyltrichlorosilane
HER	Hydrogen evolution reaction (from electrochemistry)
HOMO	Highest occupied molecular orbital
IPA	Isopropanol
i.e.	that is (lat. *id est*)
LA	Longitudinal acoustic mode
LB	(modified) Langmuir-Blodgett
LDS	Lithium dodecyl sulfate
LPE	Liquid phase exfoliation
LS	(modified) Langmuir-Schaefer
LUMO	Lowest unoccupied molecular orbital
NADH	Reduced nicotinamide adenine dinucleotide
NMP	*N*-methyl-pyrrolidone
OTS	Trichlorooctylsilane
PBI	*N*,*N'*-Bis(1-pentylhexylperylene-3,4,9,10-bis(dicarboximide)
pH	$-\log_{10}\left(a\left(H_3O^+\right)\right)$
PL	Photoluminescence
PMMA	Poly(methyl methacrylate)
PS	Polystyrene
PTFE	Poly(tetrafluoroethylene)
RCF	Relative centrifugal force

RHE	Reversible hydrogen electrode
SC	Sodium cholate
SDBS	Sodium dodecyl benzene sulfonate
SDC	Sodium deoxycholate
SDS	Sodium dodecyl sulfate
SDTC	Sodium taurodeoxycholate
SEM	Scanning electron microscopy
SOS	Sodium octyl sulfate
STS	Sodium tetradecyl sulfate
SWNT	Single-walled (carbon) nanotubes
TAPP-4Br	2,9-Bis(heptafluoropropyl)-4,7,11,14-tetrabromo-1,3,8,10-tetraazaperopyrene
TAPP-4H	2,9-Bis(heptafluoropropyl)-1,3,8,10-tetraazaperopyrene
TEM	Transmission electron microscopy
TMDs	Transition metal dichalcogenides
TTAB	Tetradecyltrimethylammonium bromide
UV	Ultraviolet (electromagnetic spectrum)
vs.	Versus
XPS	X-ray photoelectron spectroscopy
XRD	X-ray diffraction

Formula directory

A	Area (general)
A_H	Hamaker constant
Abs	Absorption
b	Tafel slope
c	Concentration (general)
C_{DL}	Double layer capacitance
d	Distance (general)
$<d>$	Mean diameter
D	Diffusion coefficient
D_{ML}	Characteristic monolayer length
e	Elementary charge
eq	Molar equivalents, n_1/n_2
eq_{Ext}	Extinction equivalents, c_1/OD_2
E	Energy (general)
E_B	(Exciton) binding energy
E_g	Free particle bandgap
Ext	Extinction
f	Frictional coefficient
f_d	Dilution coefficient
$f(\kappa r)$	Henry function
F	Faraday constant
F_i	Force of origin i
ΔG_{mix}	Gibbs free energy of mixing
h	Nanosheet thickness
h_0	Crystallographic monolayer thickness
$h_{0'}$	Effective monolayer height
ΔH_{mix}	Mixing enthalpy
$<i>$	Arithmetic mean of parameter *i*
I	Current
$Im(Z)$	Imaginary part of impedance
J	Current density
J_0	Exchange current density
$<k>$	Mean lateral aspect ratio, $<L/W>$
$<k_\perp>$	Area/thickness aspect ratio, $<A/h>$
k_B	Boltzmann constant
k^r	Rate constant

L	Longest lateral dimension of a nanosheet
m	Mass (general)
N	Layer number of a nanosheet
N_A	Avogadro constant
$<N>_{Vf}$	Volume fraction weighted mean layer number
OD	Optical density
P	Portion of reacted
Q	Charge (general)
r	Radius (general)
R	Universal gas constant
$Re(Z)$	Real part of impedance
R_f	Roughness factor
R_S	Electrolyte resistance
R_Ω	Uncompensated Resistance (iR compensation)
s	Sedimentation coefficient
Sca	Scattering
ΔS_{mix}	Mixing Entropy
t	Time
T	Temperature
U_E	Electric field strength
v	Velocity (general)
V	Volume (general)
W	Lateral dimension orthogonal to L
x	Space coordinate along the x-axis
Y	Young's modulus
z	Number of transferred electrons for a redox reaction
Z	Impedance
α	Charge transfer coefficient
β	Number of nanosheets
γ	Surface energy
δ	Solubility parameter
ε	Extinction coefficient
ϵ_0	Vacuum permittivity
ϵ_r	Relative permittivity
ζ	ζ (Zeta) potential
η	Overpotential
η_S	Solvent viscosity
θ	Glancing angles

κ	Reciprocal Debye length
λ	Wavelength (of light)
λ_{exc}	Excitation wavelength
Λ	Ionic strength
μ_E	Electrophoretic mobility
ν	Scan rate
ρ	Density (general)
σ	Ionic charge
τ	Transmittance (of light)
φ	Potential
ϕ	Solute volume fraction
ω	Angular velocity

Index of figures, tables, and equations

2 State of research

4 Gold nanoparticle functionalization

8 Appendix

1 Introduction

Two-dimensional materials are a class of nanomaterials, characterized by the fact that only one dimension of the material is small enough to achieve quantization effects as a result of spatial confinement. Although this definition does not necessarily exclude any material as long as one dimension can be reduced in size significantly compared to the other material dimensions, it is commonly used to refer to layered materials. In these materials, the crystal structure comprises individual layers with covalent bonds within two dimensions, forming a two-dimensional lattice and the lack of such bonds between adjacent layers. This enables a reduction in material thickness down to a few-atom thick single layer without excessive production of dangling bonds. High hopes are put into these materials for integration in electronic and optoelectronic devices,[1-2] energy storage,[3] electrocatalysts,[4] or polaritonics.[5] However, in order to pave the way for such applications, a comprehensive understanding of the fundamental principles is necessary. Especially means to control and tailor material properties are a mandatory requirement prior to any considerations of scalable device fabrication. As electronical and optical properties of layered materials are highly susceptible to changes in their direct environment, tailoring of material properties can be readily achieved by chemical manipulation of the material. Environmental influences are multifold and can entail choice of substrates, film morphology, and surface modification in the solid phase or choice of solvent, surfactant, and wet-chemical surface reactions in the liquid phase.

In the following, new insights into the influence of the choice of surfactants on heterogeneous functionalization reactions will be presented, exemplary shown using the spontaneous reaction of the sulfur-based transition metal dichalcogenides WS_2 and MoS_2 with chloroauric acid in aqueous surfactant solution. This model reaction was chosen based on both the characteristic absorption of the reactant and facile identification combined with localization of produced gold nanoparticles by electron microscopy techniques. Furthermore, the impact of film morphology on optical and electrocatalytic properties of WS_2 in the solid phase is demonstrated and possible caveats of data interpretation based on the deposition approach are identified and discussed. A deposition setup for film production from WS_2 and other materials in dispersion at a liquid-liquid interface is developed and its morphology characterized. Optical and electrocatalytic properties are compared to a complementary deposition approach and liquid-liquid interface film formation is proposed as superior method for reliable film formation in academic research due to its defined morphology and ease of data interpretation.

Initially, a brief summary of the current state of research regarding the production, stabilization, size-dependent optical properties and both covalent and non-covalent functionalization of transition metal dichalcogenides is presented in chapter 2.

The motivation for the experimental work in this thesis as well as central research questions are presented in chapter 3.

In chapter 4, experimental data on the spontaneous reaction of WS_2 and MoS_2 and chloroauric acid is presented. A detailed analysis of the reaction products by transmission electron microscopy is conducted and a significant influence of the surfactants employed for stabilization of the material in dispersion is demonstrated for WS_2. A simple model is developed that links the observed reaction products to preferential adsorption of surfactant molecules on different sites on the material based on the chemical structure of the surfactants. Furthermore, an impact of chemical identity of the nanomaterial is shown by functionalization of MoS_2. At last, the influence of the nanomaterial structure is explored by decoration of tubular WS_2 nanostructures and production of edge-functionalized nanosheets is observed.

The impact of film morphology on optical and electrocatalytic properties of WS_2 thin-films is discussed in chapter 5. Airbrush spray deposition and film formation at a liquid-liquid interface between *n*-hexane and water are directly compared by deposition of liquid dispersions of WS_2 on glass substrates. The complementary methods produce porous films with random nanomaterial orientation in the case of spray deposition and smooth films with high nanomaterial alignment for film formation at the interface. The utility of the interface method is further demonstrated by non-covalent surface functionalization of as-produced WS_2 thin-films using organic chromophores and experimental indications for electronic interactions between dyes and thin-film material are described. Finally, the electrocatalytic activity of produced WS_2 thin-films of both methods is discussed and related to their film morphology and the presence of conductive filler materials.

Concluding, a summary of the findings detailed in this thesis is given in chapter 6 and the significance of the conclusions is put in the greater context for future research.

A detailed description of experimental methods and employed equipment is presented in chapter 7, while additional data not shown in the main text can be found in the appendix in chapter 8.

The complete list of scientific publications referenced throughout this theses is given in chapter 9.

2 State of research

In this chapter, a concise overview of relevant research and concepts is given, on which the results of this thesis are built. As topics are diverse and the field is expanding quickly, no comprehensive discussion of all details is possible. The interested reader is referred to the literature referenced in the respective sections.

2.1 Layered materials

Layered materials can be defined as materials featuring a planar binding strength anisotropy in their crystal structure leading to layers of relatively strong binding strength in one plane of the lattice and relatively weak binding strength orthogonal to this plane. The classic example of such layered materials are van-der-Waals crystals. The crystal structure of these compounds features covalent bonds in one plane, while individual planes adhere to each other by van-der-Waals forces, thus forming the bulk crystal. As van-der-Waals forces are usually weak in comparison to covalent bonds, a splitting of the crystal structure along these covalent planes can be achieved, which leads to a layer separation, often referred to as exfoliation. The most prominent representative of van-der-Waals crystals is graphite. The carbon allotrope features individual layers of sp^2-hybridized atoms forming a hexagonal carbon lattice with a layer thickness of a single carbon atom diameter (figure 1, A).[6] Individual layers are then stacked on top of each other with a vertical offset, forming a typical AB lattice structure as indicated in figure 1, B.[6]

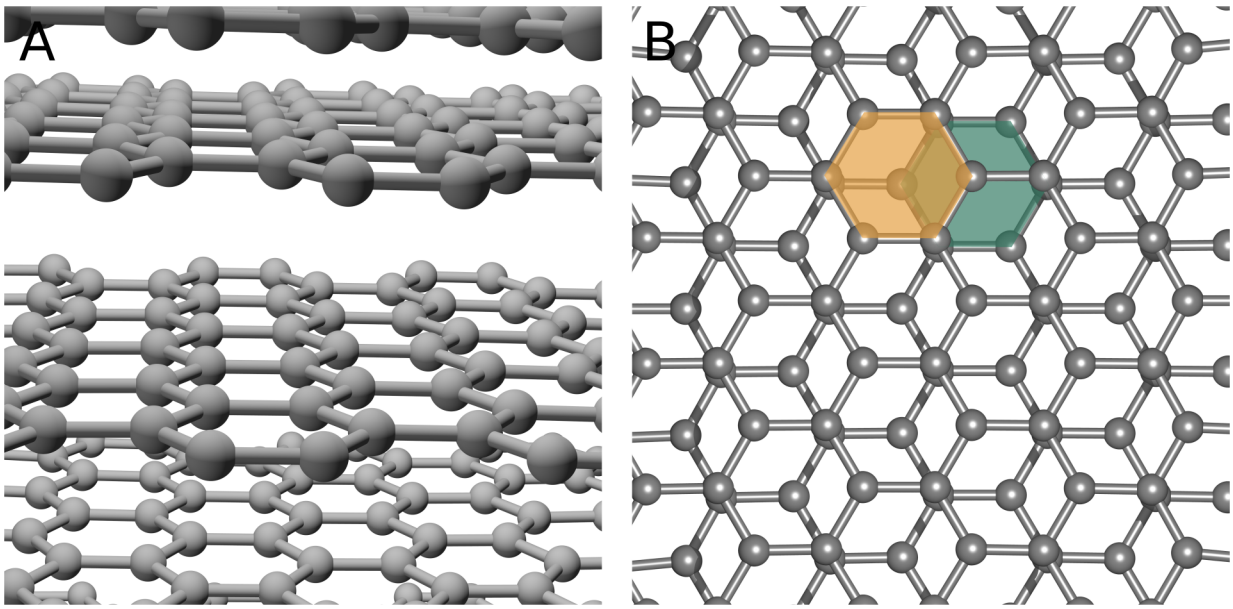

Figure 1: A) Schematic view on a small segment of the graphene crystal structure with carbon atoms depicted as spheres and intralayer covalent bonds shown as lines. Interlayer interactions are non-covalent. B) Top view of two layers of the graphite lattice showing the slipped AB structure of alternating layers. The upper layer is indicated using an orange and the underlying slipped layer is indicated using a teal hexagon.

This spatial bonding anisotropy leads to relatively large interlayer distances of 3.35 Å (taken as half the C-C distance from first to third layer) compared to the intralayer C-C distance of 1.42 Å.[6] Although graphite with its simple crystal structure being the most popular representative, a whole host of layered materials exists and different material classes are subject of current global research. Some of these compounds occur naturally in e.g. sulfide minerals, such as MoS_2[7] (molybdenite), WS_2[8] (tungstenite) or As_2S_3[9] (orpiment/anorpiment), oxide minerals, such as Sb_2O_3[10] (Valentinite), silicate minerals as talc[11] ($Mg_3Si_4O_{10}(OH)_2$) as well as native element minerals like bismuth[12] or antimony.[13-14] On top of that, plenty of synthetic compounds are accessible and have successfully been exfoliated and investigated, e.g. layered compounds of transition metal dichalcogenides (MX_2, such as $MoSe_2$[15] or PtS_2[16]), III-V (such as *h*-BN[17]), III-VI (such as GaS[18]) or IV-VI (such as GeS[19]) compounds, hydroxides ($M(OH)_2$, such as $Ni(OH)_2$[20]), transition metal hexathiohypo diphosphates (MPS_3 such as $Ni_2P_2S_6$[21]), transition metal carbides ($M_{n+1}X_n$, such as Ti_2C[22]) as well as elemental allotropes (e.g. black phosphorus[23]). In addition, organic compounds can show a layered crystal structure and organic polymers[24] or covalent organic frameworks[25] have been investigated recently. Such compounds bear great potential as their properties can easily be varied by adjusting the molecular structure of the building blocks during synthesis. Furthermore, it was shown previously that the binding strength anisotropy necessary for exfoliation is not restricted to the presence of van-der-Waals crystallinity, as successful exfoliation of materials, such as Se,[26] Te,[27] FeS_2,[28] WO_3[29] or even organic crystals held together mainly by π-π interactions like rubrene was achieved,[30] driven by the inherent spatial bonding strength anisotropy present in their respective crystal structures. This incomplete and still growing list underlines the broadness of the field of layered materials and the amount of scientific attention directed to it.

Research interest in layered materials is predominantly fueled by material properties arising or changing based on the dimensionality of the material. Upon delamination, as layer number is approaching the monolayer limit, one dimensional quantum confinement effects, high structural anisotropy, and significant increases in the surface to volume ratio result in exotic physical properties often impossible to achieve with other material classes. The first demonstration of fundamental changes in material properties can be found in the works of Geim and Novoselov on the exfoliation of graphite, awarded with the Nobel prize in physics 2010.[31] A single layer of graphite (i.e. graphene) is the first crystalline two-dimensional material and shows a pronounced ambipolar electric field effect with charge carriers approaching ballistic transport at 300 K on the submicrometre scale, room temperature quantum anomalous Hall effects, and the existence of massless Dirac fermions, rendering graphene a subject of research of high interest for fundamental physics.[32-33] Although graphene shows interesting properties, some of its characteristics

limit its applicability: it is considered chemically inert, which makes functionalization approaches difficult, and its electronic properties, being a zero bandgap semiconductor, complicate the usage of graphene in certain electronic devices.[34-35] Although progress has been made with chemical modification of graphene to achieve e.g. semiconducting properties[36-38] or introduction of functional groups,[39-40] research interest shifted to intrinsic layered semiconductors. In this thesis, group VI transition metal dichalocogenides (TMDs) are the subject of research. Rapid progress has been made in the field of TMDs, accelerated by the transfer of knowledge about processing and characterization of graphene and many other interesting materials have been identified.[41] Therefore, TMDs, and especially layered group VI TMDs, are often referred to as *post graphene* materials or two-dimensional materials *beyond graphene* to illustrate the significance of advances enabled by this material class.[34-35, 41-42]

2.2 Transition metal dichalcogenides

Transition metal dichalcogenides (TMDs) are materials featuring the general stoichiometry of MX_2, where M is a transition metal in the oxidation state +IV and X denotes a chalcogen element in the oxidation state -II. Many of these compounds form layered structures e.g. for group IV-VII and IX-X transition metals with chalcogens being S, Se and Te, with only few exceptions.[34] The individual layers can be described by a layer of transition metals sandwiched between two layers of chalcogen atoms. The chalcogen atoms terminate the layer and lone-pair electrons are facing the environment.[34] The coordination scheme in these layered compounds generally assumes a trigonal prismatic (D_{3h}) or octahedral coordination (D_{3d}), with no M-M bonds and M-X bonds of mostly covalent character.[34] The preferred coordination scheme mainly depends on the d-electron count of the transition metal: group IV and X TMDs adopt an octahedral structure, while group VI TMDs adopt a trigonal prismatic structure, which is due to progressive filling of states for increasing electron counts.[34, 43] The non-bonding d-band system is illustrated in figure 2 for the example of a group VI TMD.[44] With its d^2-configuration (occupied states are indicated by black arrows), the low spin trigonal prismatic configuration is favorable in comparison to the high-spin octahedral configuration, as the d_{z^2} orbital in trigonal prismatic configuration is of lower energy compared to the degenerate d_{xy}, d_{xz} and d_{yz} orbitals.[43] As all orbitals are either filled or empty for this configuration, the material is semiconducting (e.g. *2H*-WS_2 or *2H*-MoS_2).[34] On removal or introduction of additional electrons (d^1 or d^3), both coordination geometries have partially filled orbitals and therefore compounds exhibit metallic conductivity (e.g. *2H*-$NbSe_2$ and *1T*-ReS_2).[34]

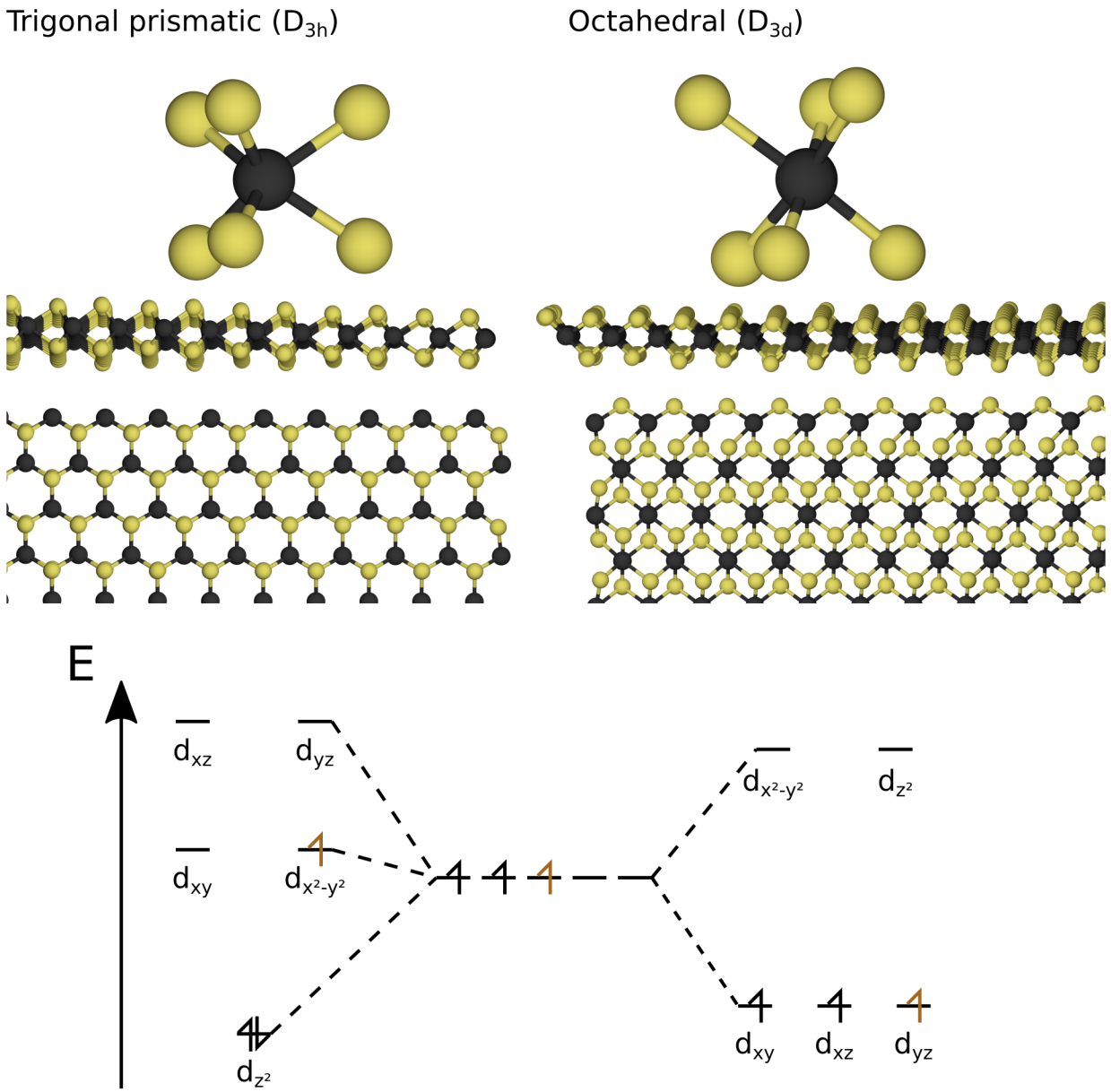

Figure 2: Trigonal prismatic (left) and octahedral (right) coordination of a MX_2 unit (upper row) and resulting layered strucutres (middle row). A simplified diagram illustrating the differences in ligand field splitting for trigonal prismatic (left) and octahedral (right) coordination environment for group VI TMDs is depicted below.

The case for introduction of an additional d-electron is illustrated by a brown arrow in figure 2. The additional electron populates the $d_{xy}/d_{x^2-y^2}$ level in trigonal prismatic configuration and the octahedral coordination becomes favorable. This is reflected in the octahedral structure of *1T*-ReS_2 or *1T*-MoS_2, while the latter can be produced by reductive intercalation of *2H*-MoS_2 with organolithium reagents.[34, 45] The terms *1T*, *2H* or *3R* indicate the structure of the unit cell: trigonal (T), hexagonal (H), or rhombohedral (R) are most commonly encountered for TMDs and the digit indicates the number of MX_2 units in the unit cell.[34]

Group VI TMDs are likely the most understood class of TMDs. In this group, only Mo and W form layered compounds with S, Se, and Te as chalcogens.[34] All compounds are semiconductors with bandgaps ranging from 1.3 to 1.0 eV in bulk.[44] Interestingly, the bandgap changes considerably for low numbers of layers in the crystal, as illustrated in figure 3 for MoS_2.

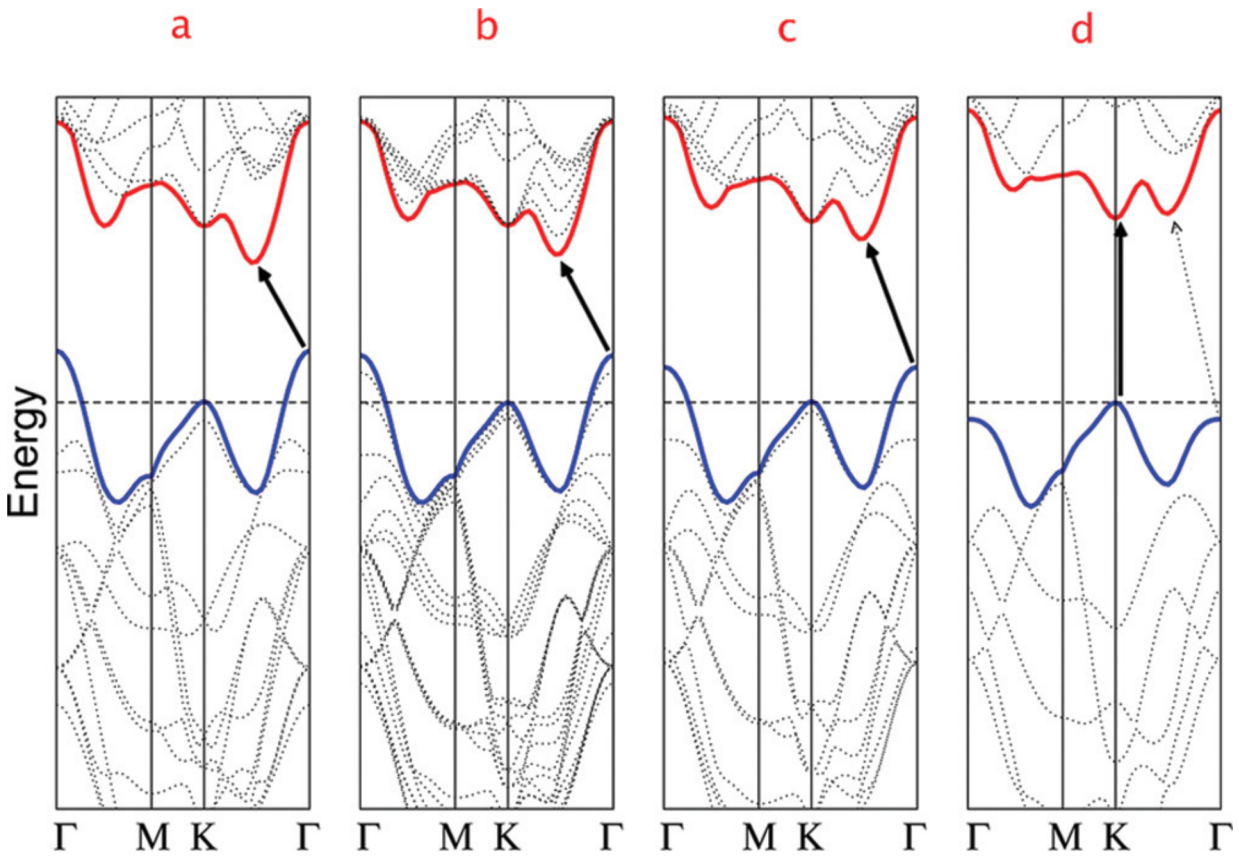

Figure 3: Calculated band structures of MoS_2 for bulk solid (a), four layers (b), two layers (c), and a monolayer (d). The solid arrow shows the lowest transition energy pathway from valence (blue edge) to conduction band (red edge). Reprinted with permission from Nano Letters, 10, 4, 1271-1275. Copyright © 2010 American Chemical Society.[46]

The indirect bandgap present in bulk (1.29 eV) is significantly smaller than the direct transition at the *K* point of the Brillouin zone (figure 3, a). The electronic states at the *Γ* point contain contributions from the chalcogen p_z and transition metal d_{z^2} orbitals. These states overlap largely for adjacent layers in the bulk crystal and, as layer number decreases, the transition energy of the indirect transition increases (figure 3, b-c).[47] At the *K* point however, states are strongly localized in the plane of the metal atoms (mixture of $d_{x^2-y^2}$, d_{xy} and d_{z^2} orbitals) and transition energies at this point are barely affected by the layer number.[47] In the monolayer limit, the indirect bandgap therefore becomes larger than the direct transition at the *K* point and the material becomes a direct bandgap semiconductor (1.9 eV, figure 3, d).[48] This leads to the emergence of photoluminescence for monolayered MoS_2 nanosheets due to the quantum confinement effects discussed

above.[46] The optical properties of TMDs are dominated by the resonance of bound electron-hole pairs.[47] Upon absorption of a photon of sufficient energy, an electron is promoted to the conduction band and a hole is left behind in the valence band. Due to coulombic interactions, the electron-hole-pair forms a bound state called exciton. This is schematically illustrated in figure 4, A.

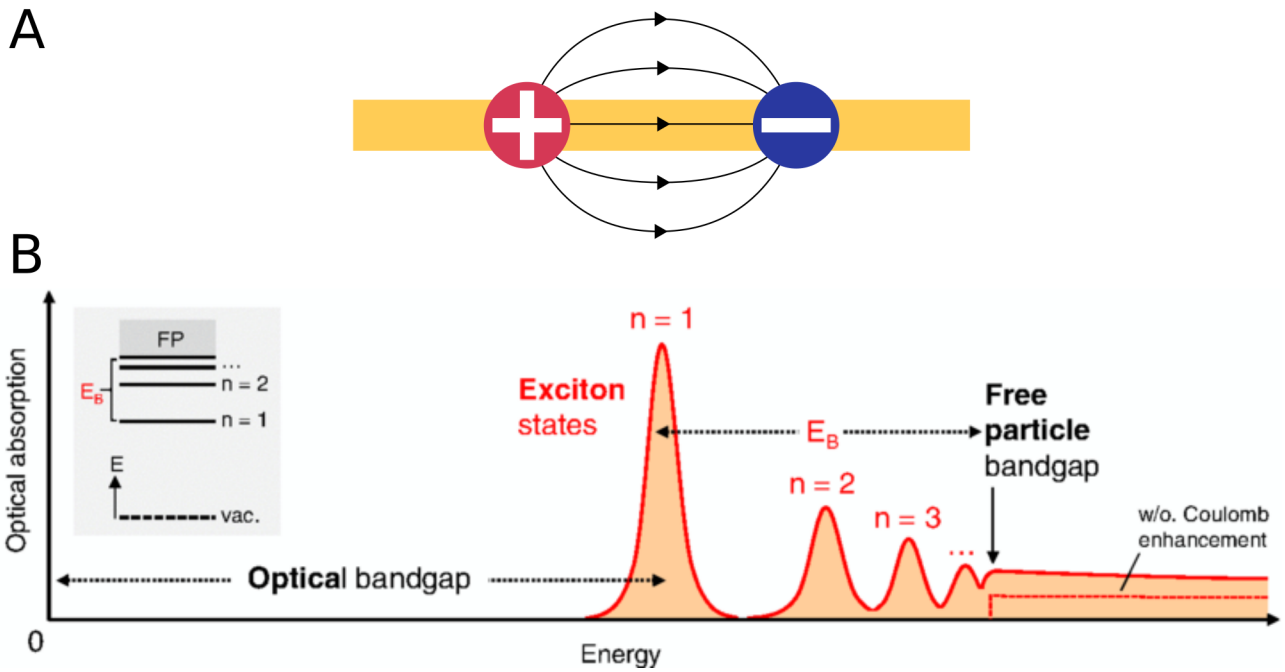

Figure 4: A) Simplified illustration of coulombic interactions in excitons formed in a TMD monolayer (yellow). B) Schematic illustration of the optical absorption of an ideal two-dimensional semiconductor including a series of excitonic transitions below the free particle bandgap E_g. The exciton binding energy and experimentally observable optical bandgap are labeled. The inset shows a simplified energy level diagram of the exciton states. Panel B is reproduced with permission from Review of Modern Physics, 90, 021001. Copyright © 2018 American Physical Society.

In comparison to conventional semiconductors like Si,[49] excitons are especially tightly bound together, which results in optical properties dominated by excitonic resonances, as already mentioned further above.[47] This leads to the situation that free-particle bandgaps are often masked in conventional absorption spectroscopy of TMDs and the optical bandgap relates to the exciton ground state. The binding energy of the exciton E_B is basically the difference of the energy of the excitonic ground state resonance and the free-particle bandgap E_g, with the latter being the energy required to create an unbound electron-hole pair, as illustrated in figure 4, B.[47] Exciton binding energies and free-particle bandgaps in TMDs are listed in table 1.[47]

Table 1: Averaged values for exciton binding energies E_B and free particle bandgaps E_g in monolayer TMDs from experiments summarized in literature.[47]

	E_B [eV]	E_g [eV]	E_B/E_g [%]
WSe_2	0.50 ± 0.22	2.20 ± 0.26	23
WS_2	0.53 ± 0.25	2.57 ± 0.25	21
$MoSe_2$	0.53 ± 0.04	2.17 ± 0.07	24
MoS_2	0.39 ± 0.12	2.29 ± 0.18	17

As illustrated in figure 4, A, the electric field between holes and electrons significantly permeates the environment of the nanosheet layer. Consequently, the binding energies of excitons and optical properties of TMDs are sensitive to changes in the (dielectric) environment, which includes a decrease in layer number. This behavior vastly complicates comparative discussions of results achieved for nanosheets produced by different methods or on different substrates or in different media.[47] Excitons in TMDs are of large radii with electron-hole interactions extending over many lattice periods (Wannier-Mott type excitons). In contrast to the correlation of electron and hole position, the exciton center-of-mass can propagate freely in the material.[47] Furthermore, strong spin-orbit coupling in TMDs lifts spin degeneracy and gives rise to two valence subbands at the *K* point, producing so-called valley degrees of freedom with optical selection rules based on light polarization.[47, 50] All of the properties described above render TMDs highly interesting for research in fundamental physics and promising for various applications like light-harvesting devices,[51] photodetectors,[52] or for spin-based information storage (Valleytronics).[50]

Experiments with liquid dispersions of both WS_2 and, to a lesser extent, MoS_2 will be discussed throughout this thesis. Details on the size-dependent optical properties of these materials visible in extinction and Raman spectroscopy are given in chapter 2.5.

2.3 Production of layered nanomaterials

Production of layered TMD nanomaterials is feasible along multiple pathways, categorized into either *bottom-up* approaches for synthesis of layered materials from molecular precursors or *top-down* approaches through delamination of layers from bulk crystals. Common *bottom-up* approaches are either based on gaseous reaction conditions or the liquid phase.

Growth of layered nanomaterials from the gas phase is usually conducted via chemical vapor deposition (CVD). For that, molecular precursors, in the simplest case powders of the constituting elements, are evaporated at elevated temperatures in an inert atmosphere.[53] This vapor is then transported with a carrier gas to a substrate or

preprocessed film[54] on which the targeted nanomaterials form through chemical reactions. The substrate plays an important role as epitaxial growth governs the quality of the produced samples with materials like mica,[55] sapphire,[56] SiO_2,[57] or quartz[58] commonly being used. Evaporation of solid phase powders of chalcogens (e.g. sulfur or selenium) and metal oxides (MoO_3 or WO_3) is employed. However, growth uniformity suffers from elongated sublimation times and hard to control precursor doses.[59] Therefore, gaseous precursors like organic sulfides or metal hexacarbonyls can be employed to alleviate such problems.[58] The advantage of using CVD grown TMDs is the production of highly crystalline samples with large nanosheet sizes on the micrometer scale and continuous monolayer coverage on the millimeter scale,[56] benefiting especially single nanosheet experiments. Downsides on the other hand are scalability of production, as the substrate size needs to be increased for an increased yield. Furthermore, high costs and the necessity of substrates in itself hampers applicability of wet chemical processing steps and ensemble measurements while production of grain boundary free films on the wafer scale for electronics remains challenging.[43, 59]

A different, niche approach for the *bottom-up* production of TMD nanomaterials is solution-based synthesis with established methods being solvothermal and hot-injection synthesis. *Solvothermal* describes material synthesis under high pressure and temperatures in solution. Note that if water is used as a solvent, the term hydrothermal may also be used. Early approaches employed MoO_3, elemental sulfur and hydrazine in pyridine or Na_2MoO_4, $Na_2S_2O_3$ and hydrazine in water for synthesis of MoS_2 with hydrazine needed as reducing agent.[60-61] Although morphology of products retrieved from these early experiments showed a certain crystallinity, cloud-like aggregates are produced in contrast to isolated nanosheets. For such nanosheets, the usage of surface active agents is vital to negate restacking of individual layers.

Hot-injection methods are characterized by rapid injection of reactant at elevated temperatures. Generation of individual nanosheet layers with this method is feasible by the use of oleylamine as solvent simultaneously acting as capping agent for the thermolytic decomposition of a single-source precursor [$Mo_2O_2S_2(S_2COEt)_2$] producing monolayered MoS_2 embedded in an oleylamine matrix.[62] Similarily, $MoSe_2$/WSe_2 monolayers were produced from W/$Mo(CO)_6$ and hot injection of diphenyl diselenide in oleic acid, with indications of a control over the average nanosheet layer number and lateral length based on the solvent and reaction conditions.[63] Although individual transitions of the latter reaction products in absorption spectra are less defined compared to WSe_2 produced from other established methods in liquid environment (e.g. liquid phase exfoliation, LPE),[15] progress made in the field is nevertheless promising. This is especially due to the high

potential for scalability and the additional control on dimensionality, that can be exerted on the molecular level.[43]

In contrast to *bottom-up* methods, *top-down* approaches start from bulk crystals and layer separation, in the following called exfoliation, can be accomplished by various means. Due to anisotropy present in nanosheets, forces acting on the layers can be divided into normal and shear forces, schematically depicted in figure 5.[64] Both types of forces can be exploited for efficient exfoliation. The first demonstrations of micro-mechanical exfoliation employing normal forces were presented by Geim and Novoselov in 2004 by repeated peeling of adhesive tape from pyrolytic graphite, therefore often referred to as *scotch-tape* method.[65] This extremely laborious method, as yield of layered materials is very low, produces high-quality nanosheets with lengths on the micrometer scale and low layer numbers including single-layered graphene with excellent electric properties.[33] However, micromechanical exfoliation can also be achieved using shear forces, e.g. by rubbing layered crystal against surfaces.[66] Demand for exfoliated layered materials increased significantly after these initial experiments and, therefore, exfoliation methods with increased yields have become necessary, especially if applications are envisioned. Although methods for mechanical exfoliation in the solid phase with increased yield were explored, e.g. through ball-milling,[67-68] liquid phase exfoliation quickly became popular for preparation of nanosheets in large scales as a cost-efficient exfoliation method. The first demonstration of sonication assisted liquid phase exfoliation by sonication of powdered graphite in *N*-methyl-pyrrolidone (NMP) aroused significant scientific interest in 2008. However, the first demonstration of sonication assisted exfoliation dates back to 1989.[69-70]

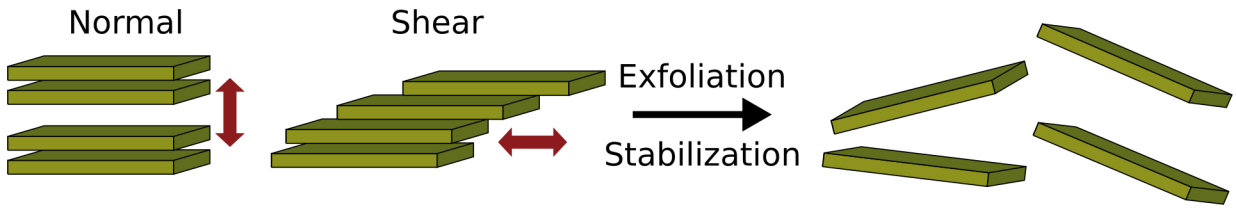

Figure 5: Schematic representation of normal and shear forces acting on layered nanomaterials resulting in delamination of the layered crystal. Exfoliated nanosheets are then stabilized in liquid dispersion to prevent reaggregation.

Ultrasound generators commonly employed for LPE are either sonication baths filled with a liquid medium (figure 6, A) or tip sonicators directly immersed in the target dispersion (figure 6, B). However, both methods produce acoustic waves propagating through the liquid medium. This causes displacement of solvent molecules from their equilibrium position and temporarily forms spots of increased and decreased density in the solvent.[71-72] The acoustic pressure produced from this is maximized at the center of increased density (peak positive pressure, compressions) and minimized at the centers of

decreased density (peak negative pressure, rarefaction) as the wave is passing through the medium (figure 6, C).[71-72] As this pressure wave propagates through the medium, interactions with gas bubbles take place and the bubble wall is set in pulsating motion, referred to as acoustic cavitation.[71] The bubbles are then acting as damped oscillators actuated by the pressure wave and grow in size during rarefaction due to pressure drops inside bubbles and subsequent evaporation of surrounding solvent and are compressed during compression.[72] If this pulsation is maintained over many wave cycles and the bubble stays physically intact, then relatively mild, short range vortices, called microstreams, are produced from this motion and the process is called non-inertial cavitation (b in figure 6, C).[71-72] For inertial cavitation on the other hand, the bubble undergoes significant expansion on interaction with the incident wave, leading to a rapid collapse (a in figure 6, C).[71] Hence, lifetimes of these bubbles are typically low. Rapid explosive expansion followed by rapid compression of gases in the bubble leads to high local temperatures and pressures.[72] The subsequent rebound after collapse therefore produces a high-pressure pulse able to mechanically damage structures in close proximity.[71] Note that the larger the collapsing bubble, the larger the amount of energy released.[72] The collapse can be either isotropic or asymmetric depending on obstacles in the direct environment limiting liquid flow.[71-73] Isotropic collapse can produce radial shock waves in the surrounding liquid propagating with velocities of almost 4000 m/s,[74] while an asymmetric collapse results in high speed microjets faster than 120 m/s.[73] It was shown in the past, that graphene exfoliation is mainly driven by inertial cavitation and increasing the dose of the latter can increase both yield and exfoliation rate.[75] Inertial cavitation can only occur if the bubble size, amplitude (the peak negative pressure) and the frequency of the incident wave cross a certain threshold.[71] The probability of inertial cavitation depends on the critical size range of bubbles which increases together with the acoustic pressure amplitude and decreases with the frequency (figure 6, D).[71, 76] For this reason, ultrasonic generators usually employ low frequency sonication around 20 kHz in order to maximize the share of bubbles contributing to inertial cavitation.[71] The probability for inertial cavitation also depends on container geometry and properties of the employed solvent, e.g. viscostiy, density and surface tension, further complicating control over the inertial cavtiation dose.[64] Additionally, at high pressure amplitudes, intense cavitation can lead to grouping of bubbles, acting as an acoustic shield that prevents extended penetration of the acoustic waves into the medium. Hence, the proportionality of increased cavitation on the nanomaterial yield is limited.[71, 75] All of the above demonstrates that control over exfoliation conditions with commercially available ultrasonic generators depends on many different parameters, making a direct comparison of exfoliation products from different researchers impractical.

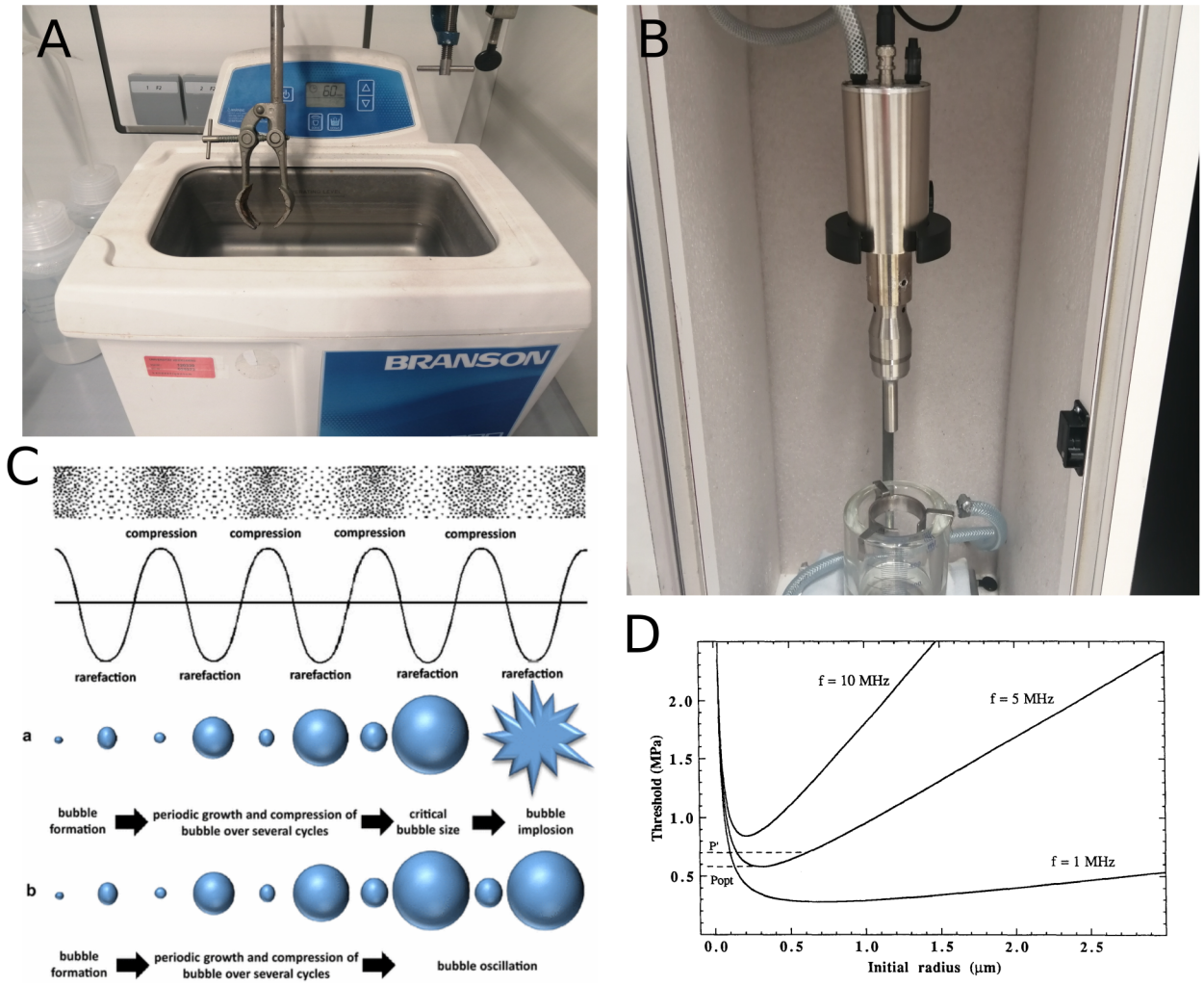

Figure 6: A) Commercially available bath sonicator as employed in this thesis. The dispersion container is fixed with a clamp in position in the water bath. B) Commercially available tip sonicator as employed in this thesis. The dispersion container is fixed on the bottom in a cooling water bath. C) Schematic illustration of bubble interactions with acoustic waves. The top row shows density fluctuations as a result of the acoustic wave propagating in solution. The sinusoidal graph beneath shows compression and rarefaction as maxima and minima in the acoustic pressure along the wave trajectory. a) Schematic illustration of inertial cavitation. b) Schematic illustration of non-inertial cavitation. Reprinted by permission from Journal of Medical and Biological Engineering, 39, 259-276, Copyright © 2018 Springer Nature.[72] *D) Threshold conditions for inertial cavitation depending on the bubble size for different acoustic frequencies. Inertial cavitation occurs at parameters above the respective threshold curves, e.g. higher peak negative pressures at a given bubble size. Reprinted from Ultrasound in Medicine & Biology, 17, 2, 179-185, Copyright © 1991, with permission from Elsevier.*[76]

If van-der-Waals crystals are in close proximity to the collapse event, forces exerted on the crystal may result in mechanical delamination. On microscopic scales, the exfoliation mechanism was demonstrated to be more complicated on the example of graphite crystals and can be divided into three different stages (schematically shown in figure 7).[77] In the first stage, kink band striation on large bulk crystals occurs due to in-plane compression.

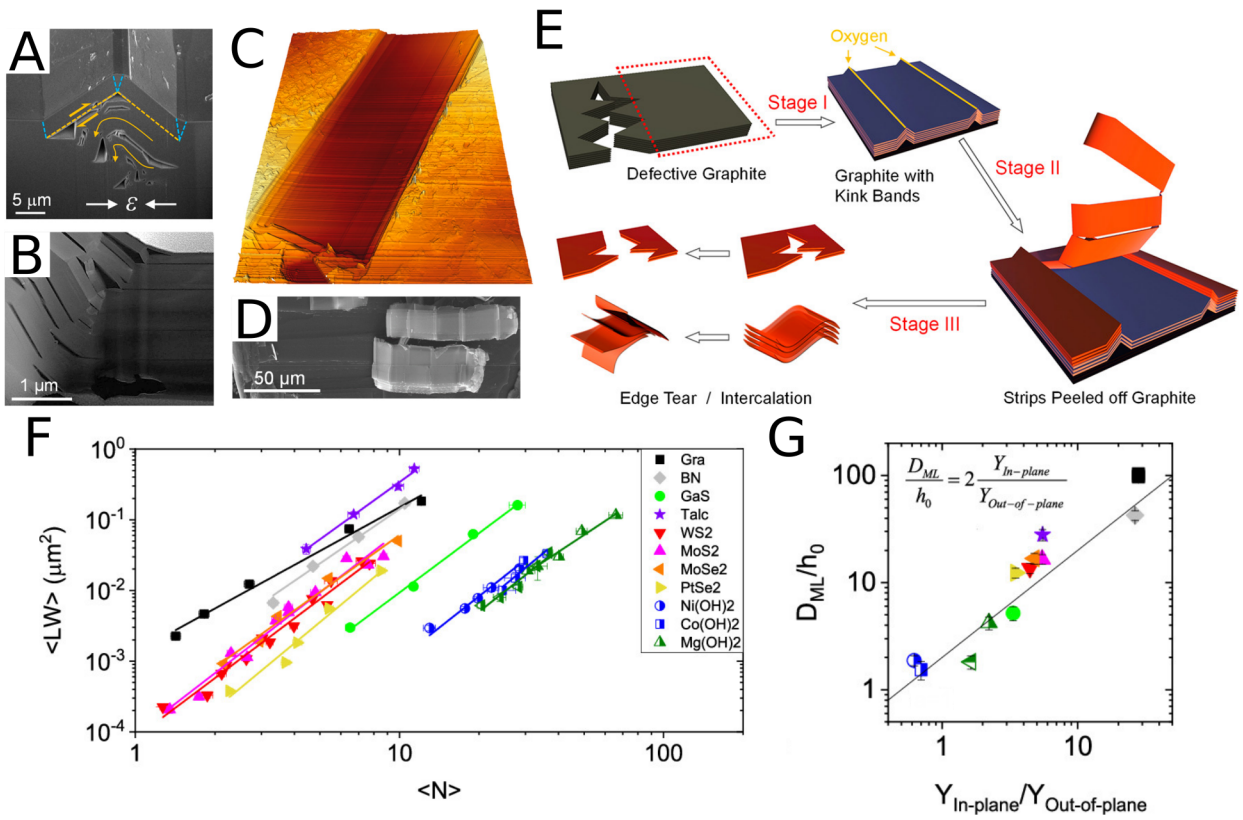

Figure 7: A) Scanning electron microscopy (SEM) cross section of a kink band striation. Twin boundaries are highlighted as blue dashed lines and shear direction and flow of subsurface layers are indicated using orange arrows. White arrows indicate the direction of in-plane compression. B) Annular dark field scanning electron transmission microscopy (ADF-STEM) image of a kink band shows subsurface delamination of layers in the kink band and emergence of voids. C) Three dimensional illustration of an atomic force microscopy (AFM) image along a trench remaining after peeling off a strip of graphite. The trench is roughly 400 nm deep and shows stepped edges. D) SEM image of graphite strips with visible stepped edges peeled off the parent crystal. E) Schematic illustration of the three stage mechanism leading to exfoliation of graphene. Panels A-E are reprinted with permission from ACS Nano 14, 9, 10976-10985. Copyright © 2020 American Chemical Society.[77] *F) Plot of approximated mean nanosheet area* $\langle LW \rangle$ *versus mean layer number* $\langle N \rangle$ *for various materials after successful liquid phase exfoliation. A power law scaling of area with thickness is evident. Extrapolation of the power law scaling to* $\langle N \rangle = 1$ *yields the square of the characteristic monolayer length* D_{ML}*, quantitatively describing the exfoliation efficiency of a material. G) Ratio of characteristic monolayer length* D_{ML} *and crystallographic monolayer thickness* h_0 *plotted versus the calculated ratio of in-plane and out-of-plane Young's moduli of the respective materials. The solid line represents the equation in the inset and shows a slope of 2. This implies equipartition of energy between delamination and fragmentation.*[64] *Panels F-G are reprinted with permission from ACS Nano 13, 6, 7050-7061. Copyright © 2019 American Chemical Society.*[78]

Pressure waves originating from acoustic cavitation are converted into surface acoustic waves propagating in the graphite lattice, which then form wedge-shaped kink bands at points of high stress, i.e. already existing defect sites or at points of wave collision (figure 7, A-B).[77] The depth of the kink band defect can entail several layers below the crystal surface and depends on the penetration depth of the surface acoustic

wave, increased with decreasing ultrasound frequencies, and whether the wave possesses sufficient energy to achieve bending of a thicker layer of graphite.[77] This kink band formation is only dominant for graphite crystals thicker than approximately 30 layers, as bending and sliding movements of the sheet stacks becomes more favorable at lower layer numbers.[77] The formation of kink bands produces local strain and hence significantly increases reactivity of the carbon lattice at kink band sites. In the second stage, these vulnerable structures are then attacked oxidatively by chemical species produced during sonication, presumably under involvement of ambient oxygen.[77] This kink band oxidation leads to fractures in the lattice along kink bands and small graphite strips are peeled off the crystal leaving trenches in the parent crystal in size equivalent to the length and thickness of the dispersed strips (figure 7, C-D). Size and thickness distribution of these strips therefore depends on density and depth of the kink band defects.[77] Further exfoliation of graphite strips to thin nanosheets occurs in the third stage. The kink band mechanism is largely suppressed for graphite thinner than approximately 30 layers and further exfoliation of graphite using sonication becomes increasingly difficult.[77] In-plane fragmentation and exfoliation of nanosheets become competing processes limiting the achievable size to thickness ratio from LPE.[77]

This competition can be understood macroscopically by statistical analysis of the nanosheet size and thickness distribution after completed exfoliation.[78] Note that large parent crystals may remain after sonication and have to be removed through centrifugation prior to such an analysis. A power law dependence, i.e. a linear dependence in a double logarithmic plot, is found for average nanosheet area $<LW>$ and average layer number $<N>$ (figure 7, F). Strikingly, a similar trend is observed irrespective of the type of exfoliated material, however, offset horizontally, whereas materials of the same material classes (e.g. group VI TMDs or metal hydroxides) appear grouped. This shows that the achievable lateral size/thickness ratios are predetermined by the in-plane to out-of-plane binding strength ratio, which is known to be similar for most representatives of a certain material class. In turn, this means that exfoliation conditions and quality of the starting material give no control over the resulting nanosheet aspect ratio, while still having a significant impact on the nanosheet yield.[75, 78-79] Furthermore, it was shown that this constant size/thickness ratio is not the product of e.g. size selection procedures after exfoliation but an intrinsic property of the exfoliation process.[78] Extrapolation of the trends in figure 7, F to an average layer number of $<N> = 1$ enables determination of a measure for the exfoliation efficiency of a certain material, termed characteristic monolayer length D_{ML}.[78] The authors were able to link this characteristic nanosheet dimension to the ratio of in-plane and out-of-plane binding energies of the respective material, as in-plane fragmentation and exfoliation occur simultaneously (figure 7, G).[78] A model was developed and fitting of data revealed equipartition of energy between the two processes as an

intrinsic limit of liquid-phase exfoliation: production of large and thin nanosheets in high quantities is not possible. However, as the degree of binding anisotropy in the material ultimately defines the achievable lateral size/thickness ratios, sonication assisted liquid-phase exfoliation should be applicable to any material and is not restricted to van-der-Waals crystals, as already mentioned in chapter 2.1.[64]

In addition to sonication assisted exfoliation in the liquid phase, also shear force exfoliation methods with rotating blade mixers[80] and high-pressure flow approaches[81-82] are subject of current research. A detailed comparison of these liquid phase exfoliation methods is available in literature.[64] Further exfoliation methods in the liquid phase mainly using normal forces acting on the layered crystals exist, e.g. in form of chemical[83] or electrochemical exfoliation.[84] These methods exploit intercalation of chemical species and subsequent formation of gaseous species in the interlayer space leading to delamination of layers.

2.4 Stabilization of layered nanomaterials in the liquid phase

Irrespective of the applied exfoliation method, exfoliated nanomaterials require some form of stabilization in the liquid phase to suppress the otherwise favorable reagglomeration. Stabilization is feasible using either suitable solvents or through additives. Suitable solvents for stabilization can be identified via solution thermodynamics: spontaneous mixing of solvent and solute is only possible if the Gibbs free energy of mixing ΔG_{mix} is negative. The latter consists of contributions of mixing enthalpy ΔH_{mix} and entropy ΔS_{mix} based on equation 1.[85]

$$\Delta G_{mix} = \Delta H_{mix} - T \Delta S_{mix} \tag{1}$$

For large and rigid objects such as nanosheets, the entropy of mixing is expected to be negligible. Hence, discussion of solvent applicability is mostly restricted to the enthalpy of mixing ΔH_{mix} and the latter is ideally minimized. The enthalpy of mixing can be approximated by the Hildebrand-Scatchard equation (equation 2).[69]

$$\frac{\Delta H_{mix}}{V_{mix}} = \phi (1-\phi)(\delta_{solvent} - \delta_{solute})^2 \tag{2}$$

Herein, V_{mix} is the volume, δ are the respective solubility parameters and ϕ the volume fraction of the solute. Essentially, the enthalpy of mixing is minimized if solubility parameters of solvent and solute are similar or match. Under the assumption that polar and hydrogen bonding interactions are marginal with layered nanomaterials like graphite,

the solubility parameters can be expressed by the surface energies γ of solute and solvent respectively according to equation 3.[85]

$$\frac{\Delta H_{mix}}{V_{mix}} \approx \frac{2}{h}\left(\sqrt{\gamma_{Solvent}} - \sqrt{\gamma_{Nanosheet}}\right)^2 \phi \quad (3)$$

h is thereby the nanosheet thickness. Surface energy and surface tension of a solvent are directly linked and therefore the solvent surface tension is used to experimentally assess the dispersive solubility parameter. Plotting the concentration of dispersed nanosheets as a function of the solvent surface tension of different solvents reveals a Gaussian shape centered around surface tensions of roughly 40 mJ/m^2 (figure 8, A-D).[85] This should correlate to a surface energy of 70 mJ/m^2 and is comparable to experimentally derived surface energies for group VI TMDs.[85] Interestingly, the aforementioned calculations assumed negligible contribution of polar and hydrogen interactions. However, significant scatter of data points is observed and concentrations of dispersed nanomaterials are significantly below the Gaussian envelope fit for some solvents. This indicates that additional contributions need to be considered. The Hildebrandt solubility parameter δ_T of the solvent can be divided into dispersive (D), polar (P) and hydrogen bonding (H) interactions individually described by Hansen solubility parameters according to equation 4.[64, 85]

$$\delta_T^2 = \delta_D^2 + \delta_P^2 + \delta_H^2 \quad (4)$$

The enthalpy of mixing is minimized when all three solubility parameters of solvent and solute match. Again, a Gaussian shape of dispersed nanomaterial concentration as a function of the individual Hansen solubility parameters is observed (figure 8, E-H).[85]

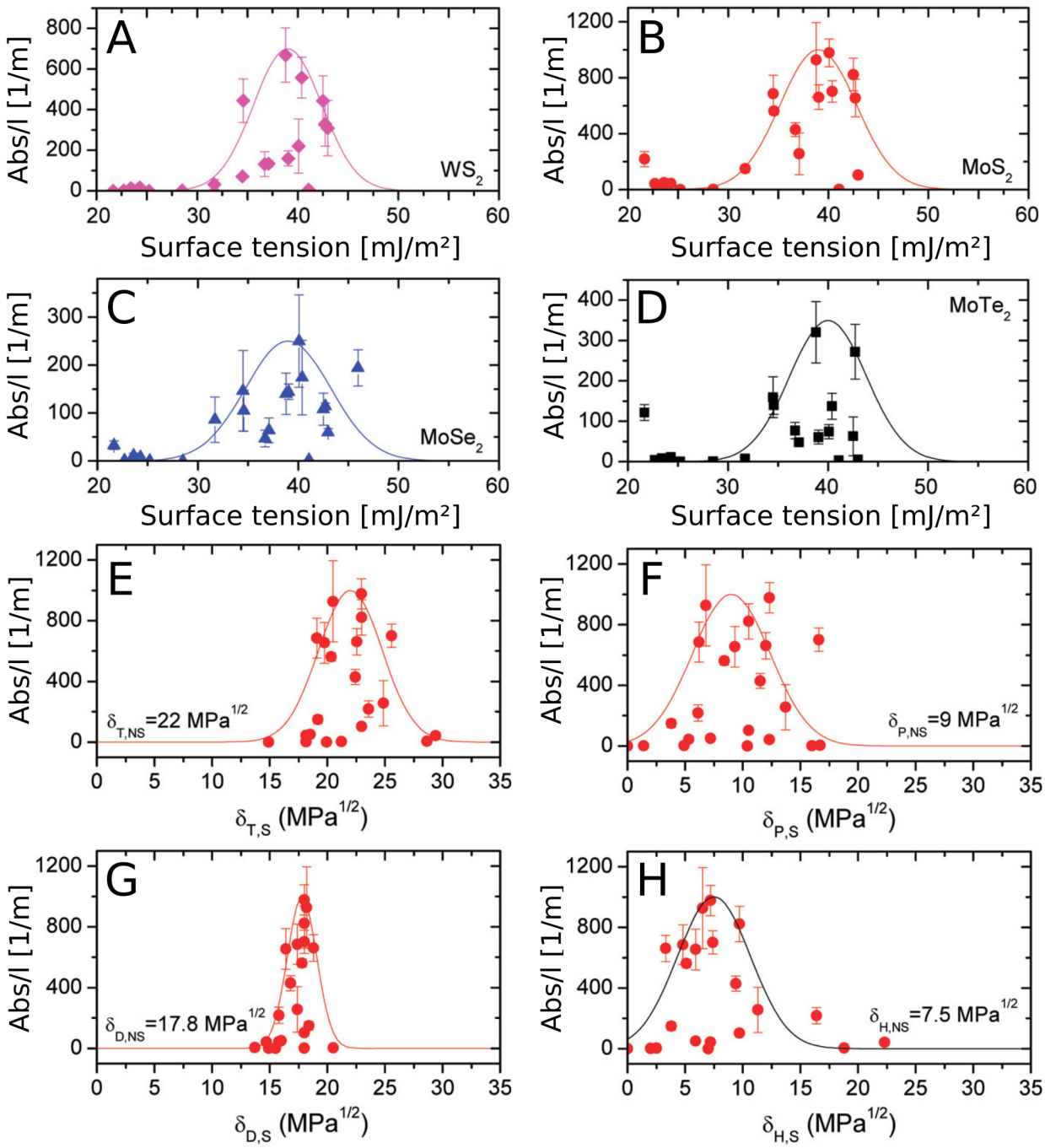

Figure 8: A-D) Dispersed nanosheet concentration (expressed as optical density) of different TMDs as function of the solvent surface tension. E-H) Dispersed nanosheet concentration (expressed as optical density) of MoS_2 as function of Hildebrand (E) and polar (F), dispersive (G) and hydrogen bonding (H) Hansen solubility parameters. Reprinted with permission from ACS Nano, 6, 4, 3468-3480. Copyright © 2012 American Chemical Society.[85]

This means good solvents should possess a dispersive parameter of roughly 18 $MPa^{1/2}$, a polar parameter of 9 $MPa^{1/2}$, and a hydrogen bonding Hansen solubility parameter of 7.5 $MPa^{1/2}$, as all three parameters need to match simultaneously. Furthermore, it indicates that neither polar nor hydrogen bonding contributions are zero in layered nanomaterials, possibly due to introduction of oxidized species during exfoliation

or other, yet unknown influences.[64] Based on these findings, dimethylformamide,[86] *N*-methyl-2-pyrrolidone (NMP) and *N*-cyclohexyl-2-pyrrolidone (CHP),[85] and cyclopenta- and -hexanone[87] were identified as suitable solvents for additive free stabilization of nanosheets in dispersion. Unfortunately these solvents usually feature high boiling points and viscosities and pose significant health hazards. While low-boiling point solvents like isopropanol (IPA) or water can be used to disperse nanosheets, achievable concentrations are typically low and the nanomaterial tends to aggregate quickly.

In order to work in an aqueous environment, additives are required to promote stabilization. Suitable stabilizers typically employed are either ionic or non-ionic amphiphiles or macromolecules.[64] Structures of ionic amphiphiles that can be employed in stabilization of layered nanomaterials are shown in figure 9.[88-90] In general terms, an amphiphile consists of a hydrophilic functional group of high polarity on one end and a hydrophobic functional group of low polarity on the opposing end of the molecule. Classic amphiphiles are usually linear with a small polar head group in form of negatively charged sulfates or positively charged ammonium groups linked to long alkyl chains as hydrophobic groups. At interfaces between media of different polarity, for example between hydrophobic nanosheets and the surrounding aqueous medium, surfactants will align accordingly and adsorb at the interface with the low polarity group on the nanosheet. At high concentrations, higher than the so-called critical micelle concentration (CMC), self-assembly of surfactant molecules in solution or on surfaces can occur and forms small aggregates (micelles) in which hydrophilic groups face the solution interface and hydrophobic groups face each other. Furthermore, amphiphiles are not restricted to a linear shape: facial amphiphiles consist of a rather flat structure with hydrophilic functional groups on one face and hydrophobic groups on the opposing face. Typical facial amphiphiles employed are sterane derivatives from the bile salt family, where the sterane-based backbone separates hydrophilic and hydrophobic faces.[64] Owing to differences in their chemical structures, interactions with the nanosheet upon adsorption differ for linear and facial amphiphiles. Adsorption of linear amphiphiles above the CMC occurs as hemicylindrical micelles with random orientation of alkyl chains lying flat on the sheet surface while polar head groups bend towards the electrolyte.[91-93] This adsorption geometry enables a rapid exchange of free and physisorbed surfactants on e.g. MoS_2 surfaces.[92, 94]

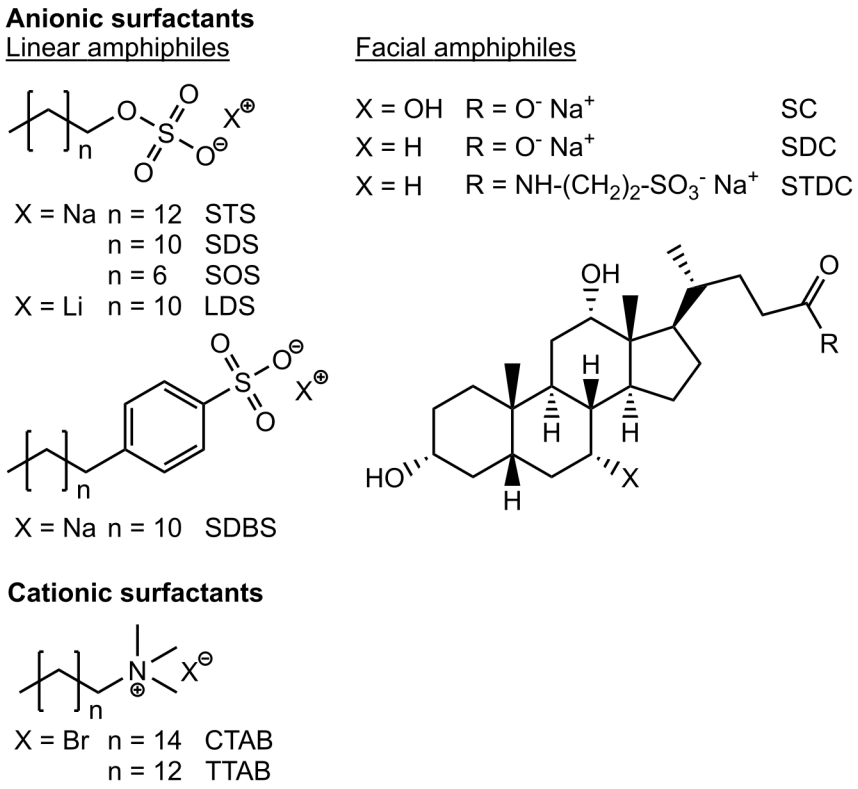

Figure 9: Chemical structures of anionic (top) and cationic (bottom) surfactants typically used for stabilization of layered nanomaterials. On the left, linear amphiphiles are shown, facial amphiphiles are depicted on the right. Abbreviations read as sodium tetradecyl sulfate (STS), sodium dodecyl sulfate (SDS), sodium octyl sulfate (SOS), lithium dodecyl sulfate (LDS), sodium dodecyl benzene sulfonate (SDBS), sodium cholate (SC), sodium deoxycholate (SDC), sodium taurodeoxycholate (STDC), cetyltrimethylammonium bromide (CTAB), and tetradecyltrimethylammonium bromide (TTAB).

For facial amphiphiles, such as sodium cholate (SC) on the other hand, the hydrophobic side faces the nanosheet surface and the hydrophilic side faces the electrolyte.[95-96] In conjunction with the possibility for hydrogen bonding on polar faces, side-to-side aggregation of individual molecules is favorable and is able to reduce the exposure of the hydrophobic face to the solution.[94, 96] These differences in adsorption tendencies are proposed to result in different behaviors of the surfactant-nanosheet system, which is discussed in more detail in chapter 4.2.

Adsorption of ionic surfactants on layered nanomaterials introduces a layer of charges on the nanosheet surface with counter ions in the surrounding solution to compensate the effective charge of the adsorbed layer.[97] This forms an electrochemical double layer around the nanosheet which is schematically illustrated in figure 10. While the charges of surfactants are bound to the nanomaterial, counter ions may be partially mobile.[97] These counter ions shield the charges on the nanosheet and as a result, a potential drop from the charged surface into the electrolyte occurs and distinct layers in the counter ion distribution can be differentiated based on the shape of the potential drop.[97]

Directly in front of the charged surface, counter ions are considered static and the respective layer of static charge distribution is called Helmholtz layer (1 in figure 10), which can be further subdivided: the layer closest to the surface contains only solvent molecules and specifically adsorbed anions, that stripped off either parts of or their entire solvation layer. It is located at a distance of an ion radius from the charged surface and the plane at this distance is called inner Helmholtz plane.[97-98]

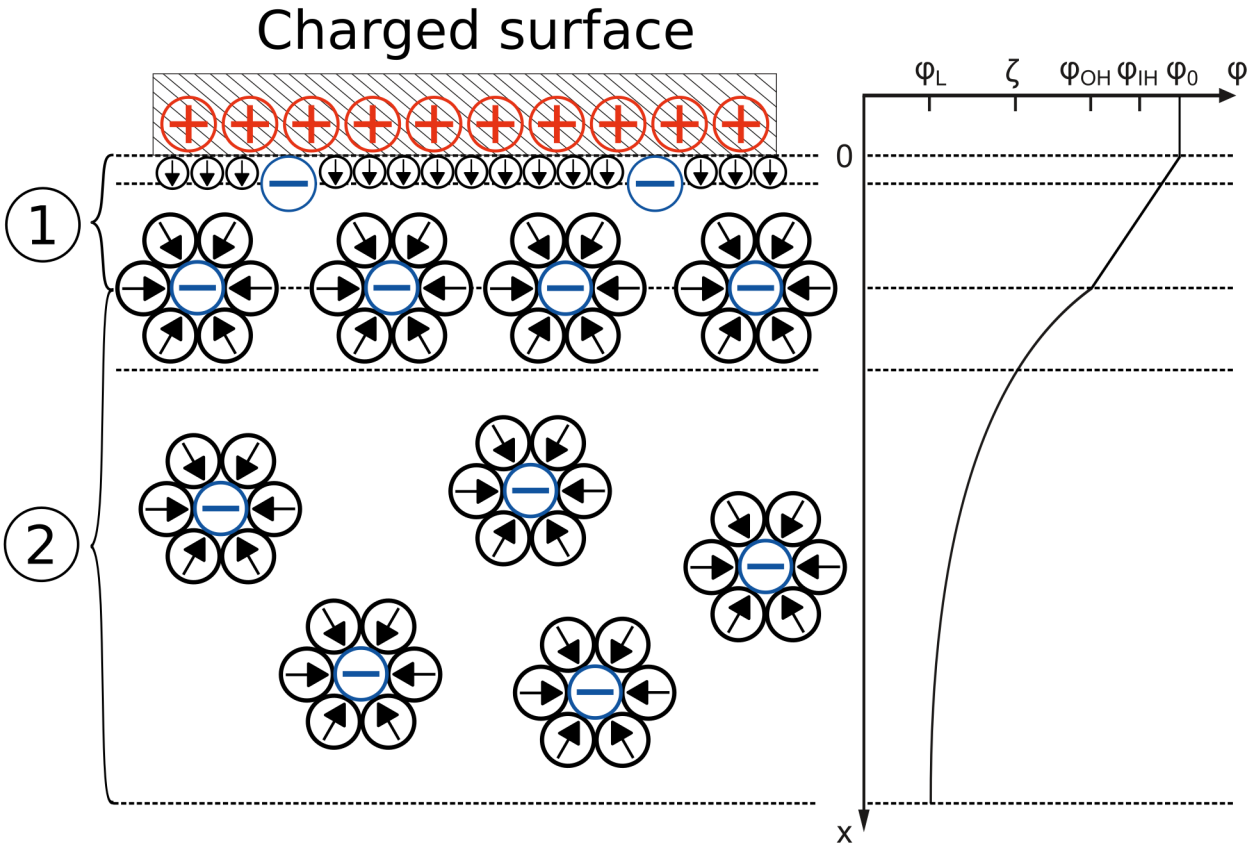

Figure 10: Left: Schematic illustration of the counter anion distribution in the electrolyte in front of a positively charged surface in accordance with the Stern-Gouy-Chapman model. Anions are illustrated with blue minuses and solvent molecules as black arrows indicating dipole orientation. Solvent molecules at the surface are reduced in size to increase readability. The Helmholtz layer is labeled with 1 and the diffuse layer with 2. Right: Electrostatic potential evolution as function of distance to the charged surface. Distances of interest are highlighted with dashed lines.

The electrostatic potential drops linearly as a function of distance, as the electric field in the Helmholtz layer is homogeneous due to the static nature of the counter ion distribution.[97, 99] Solvated ions on the other hand can approach the charged surface only to a finite distance, called the outer Helmholtz plane. At distances beyond the Helmholtz layer, counter ions are not regarded static any longer and charge distribution varies over time due to thermal motion.[97] This layer is referred to as Gouy-Chapman or diffuse layer.[97] The ion concentration along the axis perpendicular to the surface can be described by a Boltzmann distribution and as such electrostatic potential drops as an exponential decay in

the diffuse layer. The thickness of the double layer plays a key role in stabilization of nanoparticles and is related to the Debye length $1/\kappa$ of the ion cloud (equation 5).[97]

$$1/\kappa = \sqrt{\frac{\epsilon_r \epsilon_0 k_B T}{2 e^2 N_A \Lambda}}, \quad with \quad \Lambda = \frac{1}{2}\sum_{i=1}^{k} c_i \sigma_i^2 \tag{5}$$

The Debye length depends on the square root of the permittivity of the solvent expressed as the product of relative permittivity ϵ_r and vacuum permittivity ϵ_0 divided by the ionic strength of the electrolyte Λ and further the Boltzmann constant k_B, the temperature T, the elementary charge e and the Avogadro constant N_A. If working in aqueous environments at ambient conditions, the Debye length therefore predominantly depends on the ionic strength of the electrolyte, i.e. half of the sum of individual concentration of the ionic species c_i multiplied with the square of its charge σ_i.[97] Electrolytes with higher ionic strength, either through increases in concentration or through presence of ions with higher charge, lead to a sharper exponential decay of the electrostatic potential in the electrolyte and the size of the electrochemical double layer decreases. Another valuable metric is the so-called ζ (zeta) potential. This potential can be considered as the result of the loss of charge neutrality if the charged particle is set in motion: the counter ion cloud is disrupted and partially sheared off.[97] The ζ potential is the potential at this shear plane, whose position is at least a solvated ion radius outside of the outer Helmholtz plane. It can be described as the effective potential responsible for electrostatic particle stabilization in dispersion and is experimentally readily accessible, in contrast to the real surface charge. Therefore, it is often used in place of the surface charge.[97] The impact of these parameters on the colloidal stability of nanoparticles can be understood via the Derjaguin-Landau-Verwey-Overbeek (DLVO) theory.[97, 100] The total interaction potential φ_T of two dispersed spherical nanoparticles can be described by the sum of attractive φ_A and repulsive potentials φ_R in simplified form shown in equation 6.[97]

$$\varphi_T = \varphi_A + \varphi_R = -\frac{A_H r}{12 d} + B e^{-\kappa d} \tag{6}$$

The attractive potential is directly proportional to the particle radius r and inversely proportional to the distance of the two dispersed nanoparticles d for small distances of the particles ($d << 2r$).[97] The exact form of the attractive potential depends on the particle geometry and for nanoparticles with anisotropic shape further depends on the orientation of the respective particles with respect to each other, which renders a general description for all particle shapes inaccessible.[101] The parameter A_H is the so-called Hamaker constant and specific for the type of material and medium used.[97] The attractive contribution is especially dominant at low particle distances d and mainly related to van-

der-Waals forces. The repulsive part is related to the electrostatic repulsion of particles of the same charge.[97] When two charged particles approach each other, schematically illustrated in figure 11, A, the counter ion clouds of the particles overlap. This leads to an increase in concentration of ions of the same charge in between the particles, which in turn produces an osmotic pressure acting in the opposite direction and drives the particles apart.[97]

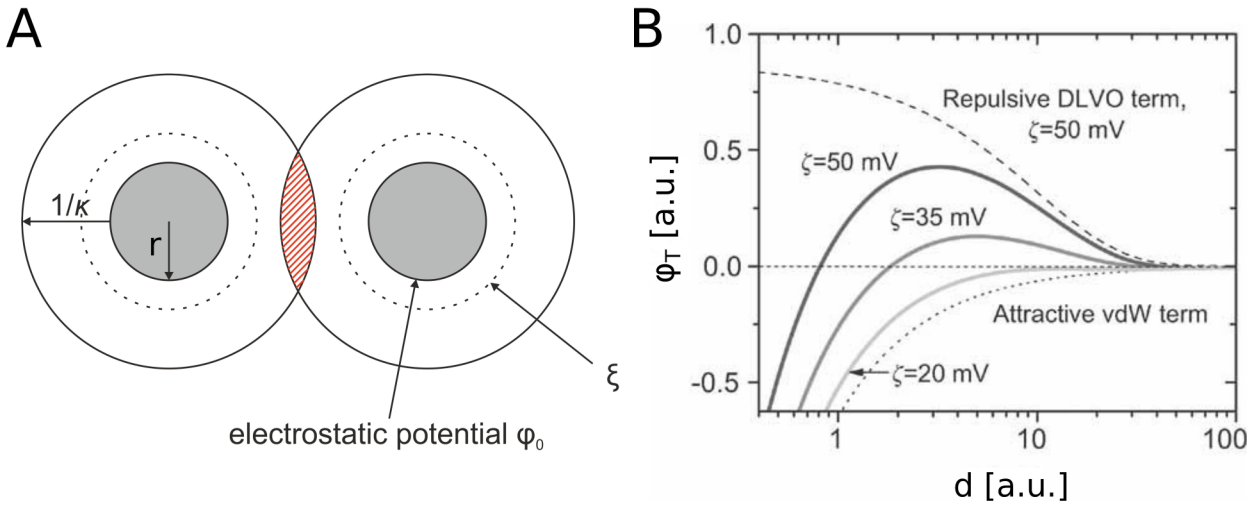

Figure 11: A) Illustration of two electrostatically stabilized spherical nanoparticles of radius r, illustrated as grey circles, approaching each other. The Debye screening length $1/\kappa$ is indicated as solid circles while the shear plane is indicated using dashed lines. Overlapping ion clouds are illustrated in red. B) Total interaction potential φ_T of two nanoparticles as function of nanoparticle distance for different ζ potentials. Individual repulsive and attractive parts are shown as dashed lines. Panel B is reprinted with permission from Advanced Functional Materials, 19, 23, 3680 – 3695. Copyright © 2009 John Wiley and Sons.[101]

As a result, the electrostatic stabilization strongly depends on the size of the electrochemical double layer and, therefore, the Debye length $1/\kappa$, and the magnitude of the surface potential, which can be approximated by the ζ potential.[101] The exact form of B depends on the geometrical properties and orientation of the nanoparticles similar to the attractive potential. For spherical particles, B can be approximated as $2\pi\epsilon_r\epsilon_0 r\zeta^2$ with the ζ potential being used in place of the real surface potential.[97] However, for other geometric properties like tubes or spherical discs, an expression for B can get quite complicated.[102-103] For parallel sheets, the total interaction potential can be approximated as equation 7.[90]

$$\varphi_T \approx -\frac{A A_H}{2\pi d^4} + 4 A \epsilon_r \epsilon_0 \kappa \zeta^2 e^{-\kappa d} \qquad (7)$$

Here, A is the nanosheet area. Strikingly, the Debye screening length also factors into the preexponential factor in the repulsive term and the scaling of the attractive term shows

an increased exponent with distance. In order to illustrate the general behavior of the interaction potential, it is plotted for crossed tubular structures for varying nanoparticle distances d and ζ potentials in figure 11, B.[90] At very low distances, the total interaction potential becomes negative, as the attractive van-der-Waals forces dominate the interaction. Consequently, aggregation occurs. However, if particles approach from a far distance, the interaction potential transitions through a maximum at intermediate distances as a result of the repulsive electrostatic contribution.[97, 101] This forms a potential barrier able to prevent aggregation of particles. The barrier height increases with increasing ζ potentials, highlighting the importance of the latter in electrostatic stabilization of dispersed nanoparticles. It is important to note, that electrostatic stabilization is purely kinetic, as an aggregated phase is thermodynamically favorable.[97] It was shown in the past that the amount of graphene stabilized in dispersion depends on the type of surfactant employed as it can directly be correlated to the ζ potential of the surfactant solutions although differences across different surfactants are typically small.[88, 90]

The key advantage of using ζ potentials is their experimental accessibility as it can be calculated from electrophoresis. If an electric field is applied to charged particles in an electrolyte, the particles are set in motion and move in the direction of the electric field depending on their charge. The electrophoretic mobility μ_E is then given by the particle velocity v normalized to the electric field strength U_E (equation 8).

$$\mu_E = \frac{v}{U_E} \tag{8}$$

The electrophoretic mobility is the measured quantity in electrophoresis, e.g. in laser doppler or phase analysis light scattering experiments and ζ potentials are calculated based on the mobility.[97] For a constant particle velocity in an electric field, viscous drag F_R and the electrophoretic force F_E are equal. If spherical particles are considered, then the viscous drag is given by the Stokes drag and can be expressed by equation 9.[104]

$$\begin{aligned} F_E &= F_R \\ \rightarrow U_E \cdot Q &= 6\pi r \eta_S v \end{aligned} \tag{9}$$

Hereby, Q is the charge of the particle, r its radius and η_S the solvent viscosity. The potential of a charged sphere according to Gauss' law can then be used as an expression for the particles charge and upon introduction of equation 8 yields an expression for the ζ potential (equation 10).[104]

$$\zeta = \frac{3}{2} f(\kappa r) \frac{\mu_E \eta}{\epsilon_r \epsilon_0} \quad (10)$$

The term $f(\kappa r)$ is the so-called Henry function and varies between 1 at $\kappa r = 0$, if the double layer is thick compared to the particle size (Hückel approximation), and 2/3 at $\kappa r = \infty$, if the double layer is thin (Smoluchowsky approximation).[104] This correction is necessary to compensate for the impact of electrical forces acting on ions in the double layer in the Smoluchowsky case which is especially relevant for working in aqueous solution and with layered nanoparticles.[90, 105] However, it should be noted that the Stokes drag is only applicable to spherical particles and, hence, inaccuracies in calculated ζ potentials are expected for different particle shapes. In essence, ζ potentials can serve as a readily available probe to investigate surface charges on a particle and, therefore, surfactant adsorption on layered nanosheets. This is presented in further details in chapter 4.2.

In general, charges present in the polar head groups are no prerequisite for efficient stabilization and several examples of non-ionic surfactants like Triton X-100 or Tween-20 or polymeric macromolecules like poly(methyl methacrylate) (PMMA) or polystyrene (PS) are commoly found in literature.[90, 106] However, the stabilization mechanism changes, as steric hindrance is now the main source of stabilization and bulky molecules are favorable. The macromolecule adsorbs on the nanosheet surface at various adsorption sites in a randomized fashion and the ends of the adsorbed chain stretch away from the surface by a significant distance.[97] If nanoparticles approach each other, interaction of the adsorbed polymer chains occurs and compression of the polymer layers leads to formation of a repulsive potential driving the particles apart.[97] The efficiency of this stabilization effect depends on the surface coverage of the polymer, the adsorption strength, the employed solvent and the concentration of free polymer in solution.[97] The advantage of steric stabilization lies in its compatibility with non-polar solvents and insensitivity to the presence of salts with possibly high valency counter ions in contrast to electrostatic stabilization.[97] However, the drawbacks are electronic interactions between particles and polymers, potential difficulties with polymer removal for certain processing steps and the possible occurrence of depletion and bridging interactions, which in turn can severely destabilize dispersions if the polymer-particle-solvent system is ill-chosen.[64, 97] In general, electrostatic stabilization of nanosheets is the dominant technique in the field and polymer stabilization of layered nanomaterials is not as well-studied in comparison.[64]

2.5 Size selection techniques

As outlined in chapter 2.3, dispersions of layered nanomaterials produced from sonication assisted liquid phase exfoliation contain nanosheets of a mostly constant

average lateral size to thickness ratio. However, sheets are intrinsically polydisperse in these dimensions, with lengths ranging from 50 to 500 nm and layer numbers from 1 to 10 for as-exfoliated MoS_2 dispersions.[7] As optical properties of layered nanomaterials show a pronounced size-dependence, means of size selection are necessary for resolution of size-dependencies in dispersions. Among various methods like nanopore filtration,[70] size-selective precipitation by addition of salts,[7] or column chromatography,[107] centrifugation-based approaches quickly became the dominant methods for size selection.

In centrifugation, particles sediment from the dispersion in a centrifugal force field. The centrifugal force F_c is acting on the particle and promotes sedimentation[1] while the buoyant force F_b and the frictional force F_f counteract it.[108] The buoyant force results from the displacement of solvent molecules in the liquid medium and the frictional force is generated by particles migrating through the liquid.[108] These forces are all (anti)parallel with respect to each other. The effective force F_{eff} acting on a particle in dispersion in sedimentation direction is then given by equation 11.[108]

$$F_{eff} = F_c + F_f + F_b = mr\omega^2 - vf - V_N \rho_S r \omega^2 \tag{11}$$

Here, r is the radius of the rotation, ω the angular velocity, m the mass and v the velocity of the particle in motion. Furthermore, f represents the frictional coefficient, V_N the particle volume and ρ_S the density of the medium. The frictional term is only relevant if the particle is moving, hence particles only start to accelerate if the centrifugal force overcompensates the buoyant force. The sedimentation coefficient ***s*** is then defined by the ratio of sedimentation speed and applied acceleration and can be derived by rearrangement of equation 11 in case of constant sedimentation velocity and yields equation 12.[108]

$$s = \frac{v}{r\omega^2} = \frac{m(1 - \bar{V}_N \rho_S)}{f} \tag{12}$$

The quantity $\bar{V}_N$ is the partial specific volume derived as the ratio of particle volume and mass and can be used to predict the buoyancy of a particle. It is equivalent to the inverse density of the sedimenting particle if hydration effects are neglected.[109-110] The unit of the sedimentation coefficient commonly employed is Svedberg (Sv, $1\ \mathrm{Sv} = 10^{-13}\ \mathrm{s}$).[108] The frictional coefficient depends on both the particle shape as well as on the viscosity of the solvent.[64, 108] As a consequence, sedimentation efficiency decreases for increasing solvent viscosities, and increases with increasing particle mass, and additionally depends

1 The gravitational force F_g can also promote sedimentation, but is usually small compared to the centrifugal forces employed and therefore can be neglected.

significantly on the particle shape. Therefore, in a polydisperse mixture of nanosheets, sedimentation efficiencies will depend on the respective nanosheet mass and separation of high-mass nanosheets with large lateral sizes and high layer numbers from small and thin nanosheets is feasible if the relative centrifugal force F_c (RCF in units of the earth gravitational field, *g*) is chosen accordingly or if the solvent density ρ_S changes during the sedimentation. Furthermore, separation efficiency also depends on the distance traveled during sedimentation and as such on the centrifugation time and the height of the liquid column in the centrifugation vial.[111] For charged particles, the ionic strength plays an additional role: the counter ion cloud that moves along with the particle increases in size for low ionic strength electrolytes and hence, the effective radius of the particle increases and the sedimentation coefficient decreases accordingly. This decrease of sedimentation velocities at low ionic strength is called primary charge effect.[108]

As mentioned above, nanosheet separation by mass can be either achieved through changing the relative centrifugal force employed or through variations in the solvent density during sedimentation. The latter principle is exploited in the so-called density gradient ultracentrifugation (DGU). Centrifugation is performed in media with a density gradient aiming at matching centrifugal and buoyant forces acting on the particles at a certain height in the vial.[112] The effective particle density in solution including solvation effects, namely the buoyant density as the inverse of the partial specific volume, is expected to change based on the layer number of a particle.[112-113] Sedimentation will then occur until the solvent density matches the buoyant density of the nanosheets (the so-called isopycnic point, where the sedimentation coefficient s reaches 0) and material is separated based on its buoyant density. Typical gradient media employed are either salts like CsCl or molecules like sucrose or iodixanol in aqueous solutions or 2,4,6-tribromotoluene in chlorobenzene.[113-116] This density gradient is usually prelayered in the vial by stepwise variation of the gradient medium composition. Furthermore, adsorbed species can be exploited to direct the buoyant density of a particle in a beneficial way for effective separation. The successful separation by layer number using density gradient ultracentrifugation of graphene (aided by SC) and MoS_2 nanosheets (aided by a block copolymer) was demonstrated in the past.[112-113] Especially in the latter case, the presence of a polymer was necessary as the intrinsic density of MoS_2 was higher than the density of the gradient medium.[113] The result of this centrifugation technique is the formation of distinct material bands in the centrifugation vial, which can then be collected fraction by fraction. The drawbacks of this method are that it is complicated and the optimization is tedious. On top of that, it requires specialized equipment, such as an ultracentrifuge equipped with a swinging bucket rotor and the yield of material after separation is typically in the *μg* regime strongly limiting the potential for experimental design or applications.[64]

An alternative approach, which is compatible with higher concentrations of dispersed nanomaterials, is liquid cascade centrifugation. Here, a variation in relative centrifugal forces acting on the nanoparticles is employed to achieve separation by nanosheet mass. For that, a dispersion is centrifuged multiple times in a sequence with iteratively increasing relative centrifugal forces. The sediment is isolated at each step and redispersed in fresh dispersant while the supernatant is subjected to the next step of the sequence. As such, material is isolated between two steps of varying relative centrifugal forces and labeled accordingly (e.g. 400 - 1 000 *g* describes material from a supernatant resulting after centrifugation at 400 *g*, that is isolated in the sediment after centrifugation at 1 000 *g*). A schematic drawing illustrating a typical centrifugation cascade is shown in figure 12, A. Each fraction contains nanosheets with different average lateral length $<L>$ and layer number $<N>$ with larger and thicker nanosheets being isolated at lower centrifugal acceleration and smaller and thinner nanosheets being isolated at elevated acceleration.[8] Usually the sediment isolated in the first step of the cascade as well as the supernatant after the last step are discarded in order to remove incompletely exfoliated material and highly defective nanosheets as well as impurities produced from exfoliation. A power-law scaling of $<L>$ and $<N>$ with the centrifugal force applied was identified in literature and hence, in liquid cascade centrifugation, $<L>$ and $<N>$ are correlated (figure 12, B-C).[8] This method is advantageous as it is compatible with high concentrations of layered nanomaterials, wastage of exfoliated material is low, it does not rely on additives of any sort, and the concentration or even dispersant of the sedimented nanomaterial can be adjusted to the desired outcome upon redispersion.[64] Furthermore, the cascade design is highly flexible: it is applicable to a large set of different materials[78] and the number of size-selected samples can be adjusted based on the experimental requirements. On the downside is to note that centrifugation times for each step need to be sufficiently long (usually about two hours for liquid column heights of about 10 cm) to ensure sufficiently completed sedimentation. Additionally, the intrinsic correlation of $<L>$ and $<N>$ does not allow for efficient enrichment of large, and at the same time thin nanosheets, and that manual decanting of the supernatant in its entirety without disturbing the sediment depends on the personal level of experience, which is therefore prone to inconsistencies across different researchers.[8, 64]

The successful separation of layered group VI TMDs by nanosheet size is directly reflected in their optical properties. This will be discussed in the following using the examples of WS_2 and MoS_2. When discussing the optical behavior of liquid dispersions of nanomaterials in transmission experiments, absorption and scattering contributions need to be considered for a complete description of size-dependent trends.

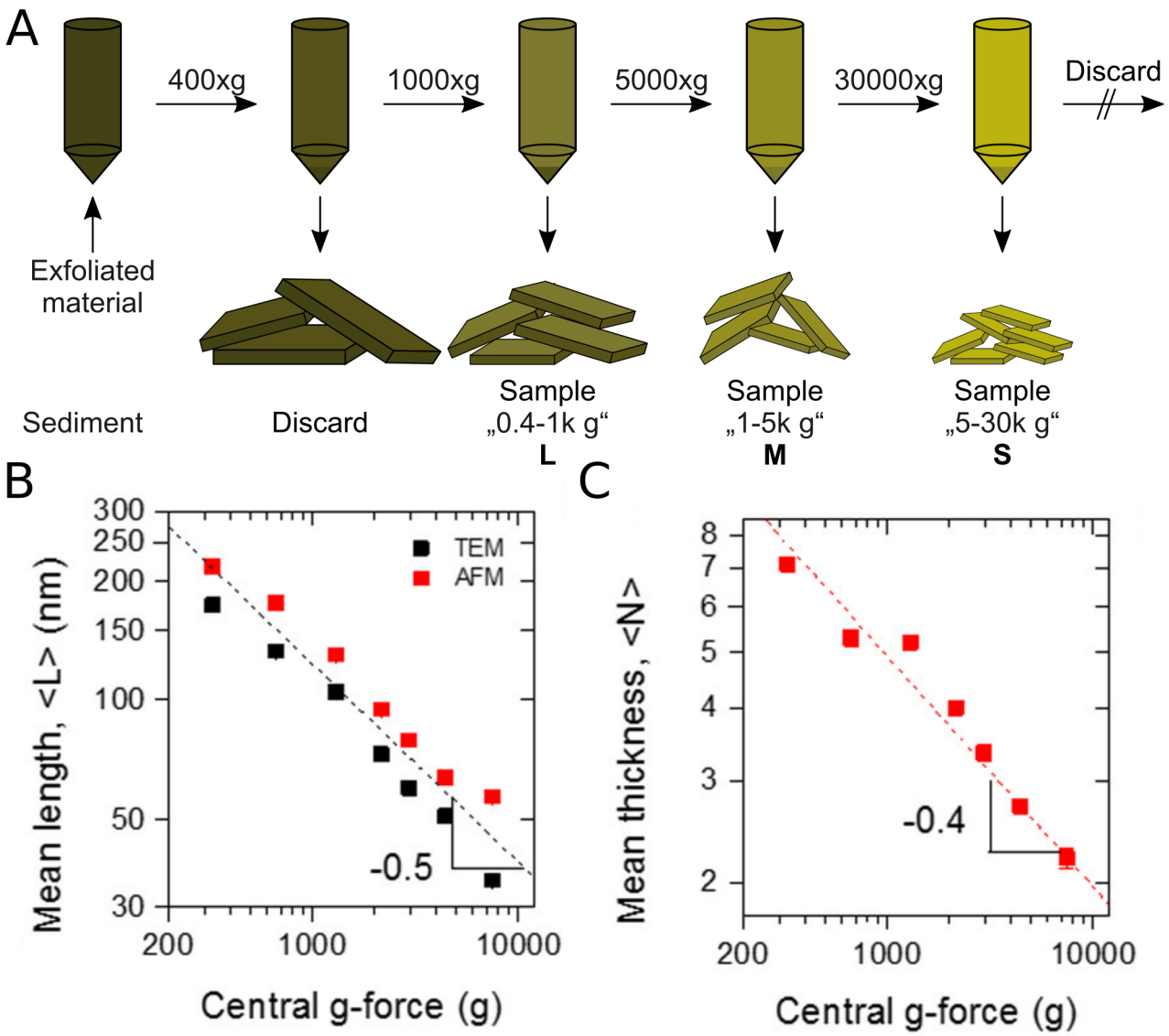

Figure 12: A) Schematic illustration of a typical centrifugation cascade. The sediment is isolated at each step of the centrifugation cascade while the supernatant is subjected to the next step in the cascade. The sediment is labeled according to the relative centrifugal force applied in the respective steps before and after sedimentation. B) Mean WS_2 nanosheet length <L> determined by statistic AFM and transmission electron microscopy (TEM) for different relative centrifugal forces. C) Mean WS_2 nanosheet layer number <N> determined by AFM for different relative centrifugal forces. Panel B and C are reprinted with permission from ACS Nano, 10, 1, 1589-1601. Copyright © 2016 American Chemical Society.[8]

The quantity extinction (Ext) usually measured in transmission UV-Vis spectroscopy is due to the wavelength-dependent (λ) attenuation of the incident light, when light travels through the medium. The transmittance of light τ is comprised of both absorption and scattering components according to equation 13.[117]

$$\log_{10}(\tau) = -\mathrm{Ext}(\lambda) = -\varepsilon(\lambda)\,c\,d = -\left(\mathrm{Sca}(\lambda) + \mathrm{Abs}(\lambda)\right) \tag{13}$$

According to Lambert-Beers law, extinction is equivalent to the product of the length of the light path in the medium d, concentration c and the wavelength-dependent extinction coefficient ε of a species.[117] The wavelength dependence of the extinction coefficient of WS_2 and MoS_2 for different nanosheet sizes derived from liquid cascade centrifugation are shown in figure 13.[15]

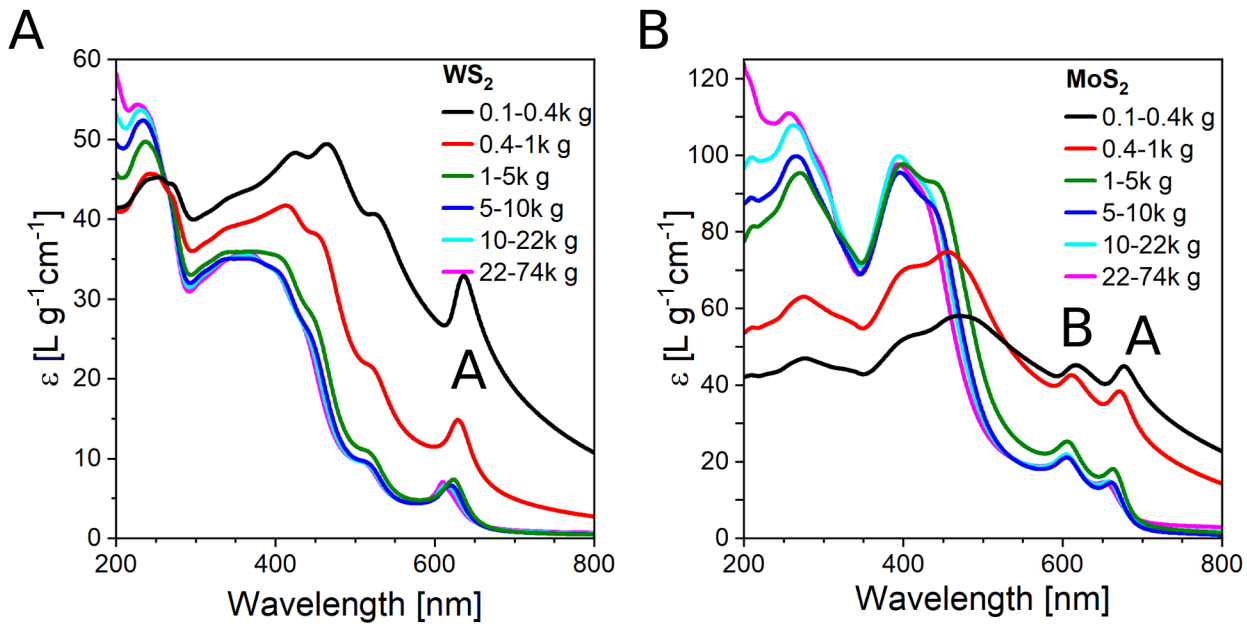

Figure 13: Wavelength dependence of the extinction coefficient for WS_2 (A) and MoS_2 (B) for varying nanosheet sizes derived from liquid cascade centrifugation. A and for MoS_2 B excitonic transitions are labeled accordingly. Reprinted and adapted with permission from Chemistry of Materials, 31, 24, 10049-10062. Copyright © 2019 American Chemical Society.[15]

For WS_2 (figure 13, A), the extinction coefficient decreases with decreasing nanosheet sizes until it reaches an almost constant level for small nanosheet sizes. Strikingly, at 235 nm extinction coefficient spectra converge irrespective of size. The extinction coefficient $\varepsilon(235\ nm)$ is therefore largely size-independent and can be used to estimate the WS_2 concentration in dispersions.[8] For MoS_2 on the other hand, such a convergence is not observed for all sizes in figure 13, B. For estimation of the nanomaterial concentration of MoS_2, a size-dependent equation for the extinction coefficient is necessary (see chapter 7.5 for an example).[15] Characteristic features of both materials are the ground state A excitonic transitions at the *K* point, highlighted by the capital letter A in figure 13.[7-8] On closer inspection, a pronounced blue-shift of this transition is evident for increasing relative centrifugal forces, i.e. smaller nanosheets for both materials. This shift can be understood if the role of scattering is explored in more detail. This is for example possible by measuring absorption spectra in an integration sphere, where, in contrast to extinction measurements, scattered light is collected and attenuation is solely based on the material's absorption.[15] The difference of absorption

and extinction spectra therefore results in the scattering spectrum. An example of deconvolution of these influences for WS_2 is shown in figure 14.[8]

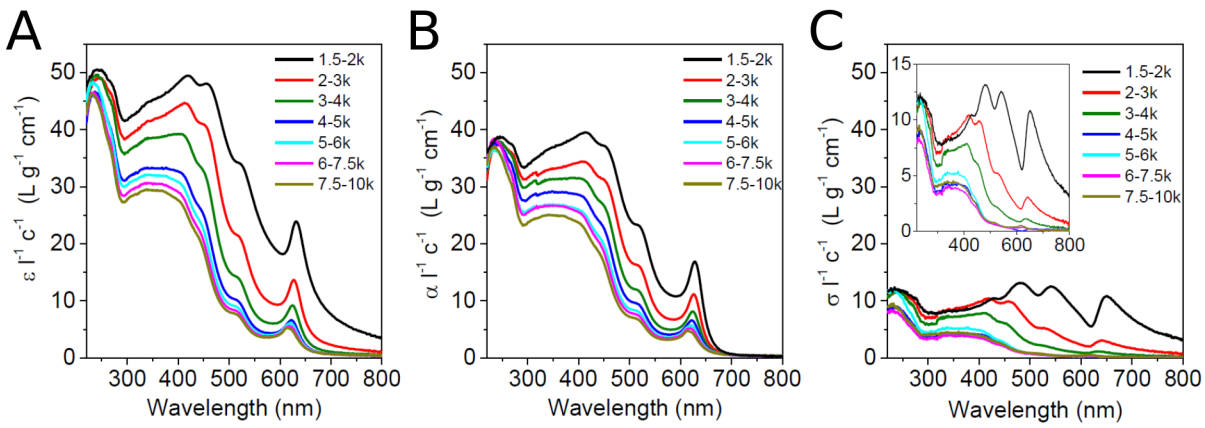

Figure 14: Extinction (A), absorption (B) and scattering (C) coefficient spectra of WS_2 in aqueous SC solution after liquid cascade centrifugation. The legend refers to the relative centrifugal forces as multiples of g. Reprinted with permission from ACS Nano, 10, 1, 1589-1601. Copyright © 2016 American Chemical Society.[8]

Extinction and absorption spectra (A and B in figure 14 respectively) follow similar trends although the blue-shift of the A exciton resonance is far less pronounced in absorption compared to extinction for samples isolated at low centrifugal forces. This is due to contributions from scattering shown in figure 14, C. The scattering contribution is largely red-shifted at high wavelengths and becomes negligible for dispersions smaller in size than the 3 - 4k *g* sample i.e. smaller than 100 nm.[8] The strong decrease of the red-shifted scattering contribution for smaller nanosheets is therefore the main contributor for the blue-shift of the A exciton signal in extinction for larger nanosheet sizes. However, at small sizes shifts can be attributed to changes in absorption due to quantum confinement effects. Importantly, as absorption and extinction are almost similar in shape, information in absorption spectra is largely retained in extinction spectra and, therefore, renders extinction spectroscopy a reliable method for nanosheet characterization.[8] Similar observations have also been made for MoS_2 nanosheet dispersions prepared by liquid cascade centrifugation.[7]

For the sake of simplicity, in the following the term *A exciton signal* will be employed to describe changes and shifts in extinction spectra. However, it is crucial to remember that contributions of both scattering and absorption factor into this signal.

Although relative precise determination of size and thicknesses is possible using statistical evaluation of microscopy images, e.g. atomic force microscopy (AFM) or transmission electron microscopy (TEM), these methods require manual counting and measurement of a large set of individual nanosheets, which renders these methods

extremely laborious and time consuming. As optical properties of the layered nanomaterials strongly depend on the size of the nanosheets, size information must be available from optical spectra. It is demonstrated in literature, that such size information can be extracted from extinction spectra for WS_2[8] and MoS_2[7] and later generalized for liquid phase exfoliated group VI TMDs.[15] This was achieved through correlation of statistical data derived from AFM imaging and corresponding extinction spectra. It was found that the average length $<L>$ of a TMD nanosheet dispersion in aqueous SC solution can be described by the ratio of two extinctions at different wavelengths in the spectrum according to equation 14.[15]

$$\frac{Ext(\lambda_1)}{Ext(\lambda_2)} = \frac{A_1 <L> + B_1}{A_2 <L> + B_2} \tag{14}$$

Parameters A and B are obtained from fitting of the experimental data and summarized in table 2.

Table 2: Parameters from equation 14 for different group VI TMDs. Reprinted with permission from Chemistry of Materials, 31, 24, 10049-10062. Copyright © 2019 American Chemical Society.[15]

	λ_1 [nm]	λ_2 [nm]	A_1 [1/nm]	B_1	A_2 [1/nm]	B_2
MoS_2	270	345	0.0144	1.97	0.0160	1
$MoSe_2$	280	390	0.0117	1.83	0.0154	1
WS_2	235	295	0.0159	2.20	0.0166	1
WSe_2	235	347	0.0143	2.20	0.0200	1

Such a size-dependence of extinction ratios was previously assigned to different absorption coefficients of nanosheet edges and basal planes respectively and length-dependent scattering effects.[7, 117] The relation given in equation 14 is valuable for estimation of nanosheet dimensions derived from exfoliation and size selection through facile extinction spectroscopy. Furthermore, no concentration information is necessary prior to length estimation and, hence, determination of concentrations for the case of size-dependent extinction coefficients is feasible as mean length $<L>$ can be estimated from the same spectrum.[15] Additionally, estimation of the mean layer number $<N>$ is also possible and detailed in the following: as outlined in chapter 2.2, the bandgap of TMDs depends on the layer number and optical bandgaps in TMDs are largely related to the ground state excitonic transitions. Both the free-particle bandgap E_g as well as the exciton binding energy E_B, due to the effects of quantum confinement and dielectric screening, are expected to change with decreasing layer numbers and hence, a dependence of the A exciton signal on the mean layer number $<N>$ is expected.[15] This is illustrated by plotting

the second derivative of the A exciton region with respect to the energy of the incident light in figure 15, A.

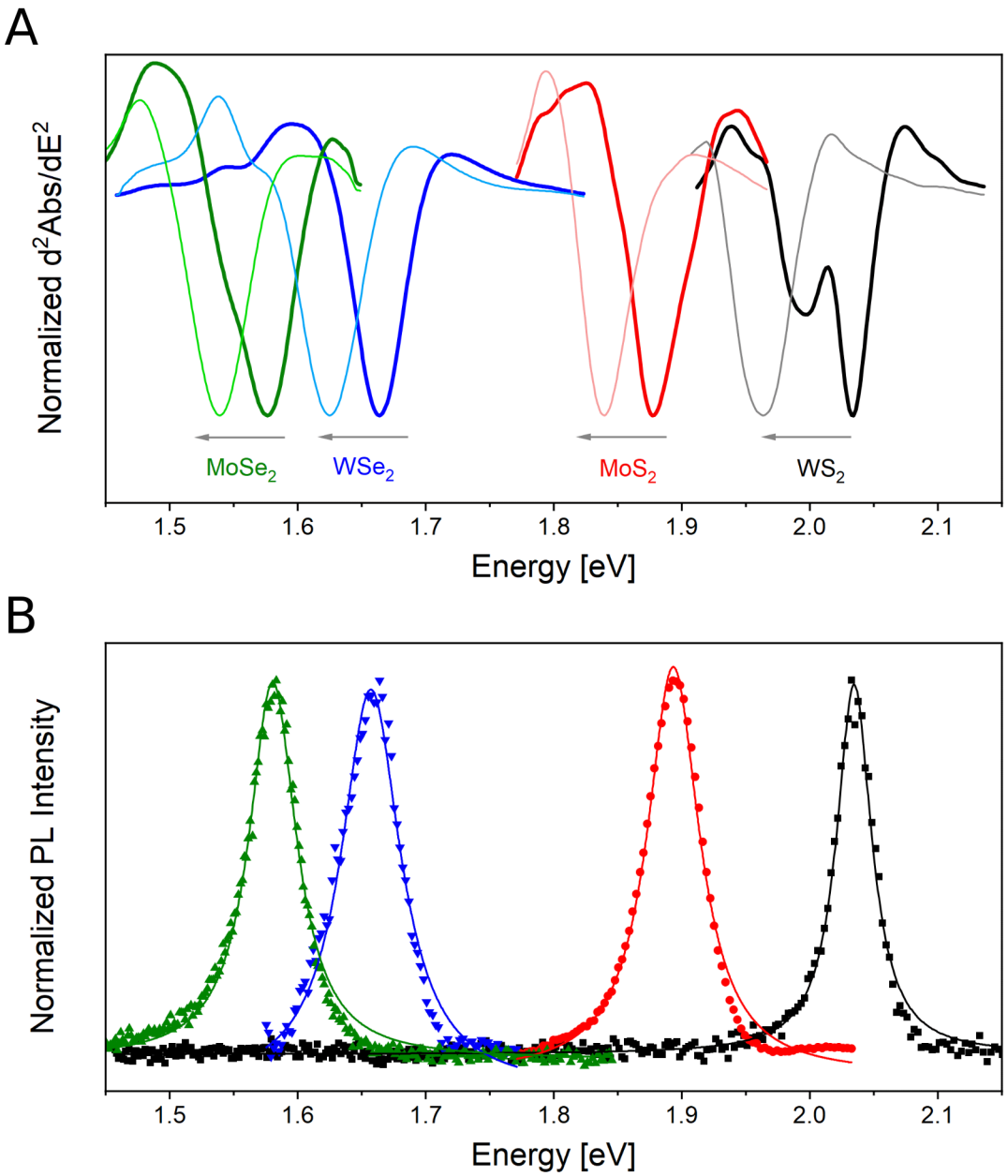

Figure 15: A) Second derivative of absorption around the A exciton region with respect to the photon energy of the incident light for $MoSe_2$ (green), WSe_2 (blue), MoS_2 (red) and WS_2 (black) in dispersion. Darker traces contain thin (10 - 22k g) and lighter traces thick (0.4 - 1k g) nanosheets. B) PL spectra of materials in dispersion for high monolayer contents. Reprinted and adapted with permission from Chemistry of Materials, 31, 24, 10049-10062. Copyright © 2019 American Chemical Society.[15]

In dispersions, a certain distribution of layer numbers even in size-selected samples leads to ensemble signals comprised of the weighted averages across all individual nanosheet contributions. To increase the resolution of individual components, the second derivative can be used as it considerably narrows component peaks.[15] Again, a significant red-shift of the A exciton signals is evident when going from thin to thick nanosheets

(figure 15, A). As absorption was measured in this case, no contributions from scattering are expected. In the case of thin WS_2 nanosheets, a well resolved fine structure is visible, with the lower energy contribution related to few-layer absorption and the higher energy contribution assigned to monolayer absorption.[8] Similar behavior is expected for the other materials (indicated by a small shoulder for $MoSe_2$), but not visible due to the inherently narrower line width of WS_2 in comparison to the other materials.[15, 118-119] However, the expected pronounced changes of the A exciton transition for decreasing layer numbers are comparatively small in the experiments. This is due to the fact, that the significant changes in free-particle bandgaps are partially compensated by comparable changes in exciton binding energy and the resulting shifts of the A exciton signal position going from the bulk to monolayered samples are therefore modest (on the order of 49 - 56 meV for Mo-based and 65 - 67 meV for W-based TMDs).[15] The layer number dependence of the A excitonic transition E_A is given by an exponential decay function in equation 15.[15]

$$E_A = E_{A,bulk} + \left(E_{A,ML} - E_{A,bulk}\right) \cdot e^{-\frac{\left(<N>_{V_f} - 1\right)}{N_0}} \tag{15}$$

Hereby, $E_{A,bulk}$ and $E_{A,ML}$ are the energies of the excitonic transitions of bulk and monolayered samples respectively, $<N>_{Vf}$ is the mean layer number weighted by the volume fraction of each nanosheet, and N_0 is an empirical decay constant. A sample is considered monolayered when $<N>_{Vf}$ reaches 1 and E_A in equation 15 is then equal to $E_{A,ML}$. Parameters for different TMDs are given in table 3.

Table 3: Exponential decay fit parameters for different materials in equation 15. Reprinted with permission from Chemistry of Materials, 31, 24, 10049-10062. Copyright © 2019 American Chemical Society.[15]

	$E_{A,ML}$ [eV]	$E_{A,bulk}$ [eV]	N_0
MoS_2	1.895	1.846	3.37
$MoSe_2$	1.599	1.544	2.80
WS_2	2.033	1.966	3.72
WSe_2	1.692	1.626	3.29

This enables calculation of the volume fraction weighted layer number using the A exciton signal position from spectroscopy. Note that equation 15 was derived from absorption spectra to avoid influences of scattering, which may lead to inaccuracies if the exciton position is extracted from extinction spectra as a significant scattering contribution is expected for large and thick nanosheets. Similar relations for MoS_2 and WS_2 derived from extinction spectra can be found elsewhere.[7-8]

As TMDs become direct bandgap semiconductors in the monolayer limit, efficient emission is expected for liquid dispersions and photoluminescence intensity is expected to depend on the monolayer content of a dispersion. The normalized PL intensity for different TMDs is shown in figure 15, B. Such measurements are usually carried out with dedicated spectrofluorometers. However, detection of TMD photoluminescence (PL) is also possible with the additional sensitivity of a Raman spectrometer.[8] This not only eases routine PL characterization, but also makes information from vibrational modes accessible in the same measurement.[8] Raman spectra of liquid exfoliated and size-selected WS_2 and MoS_2 dispersions are shown in figure 16.

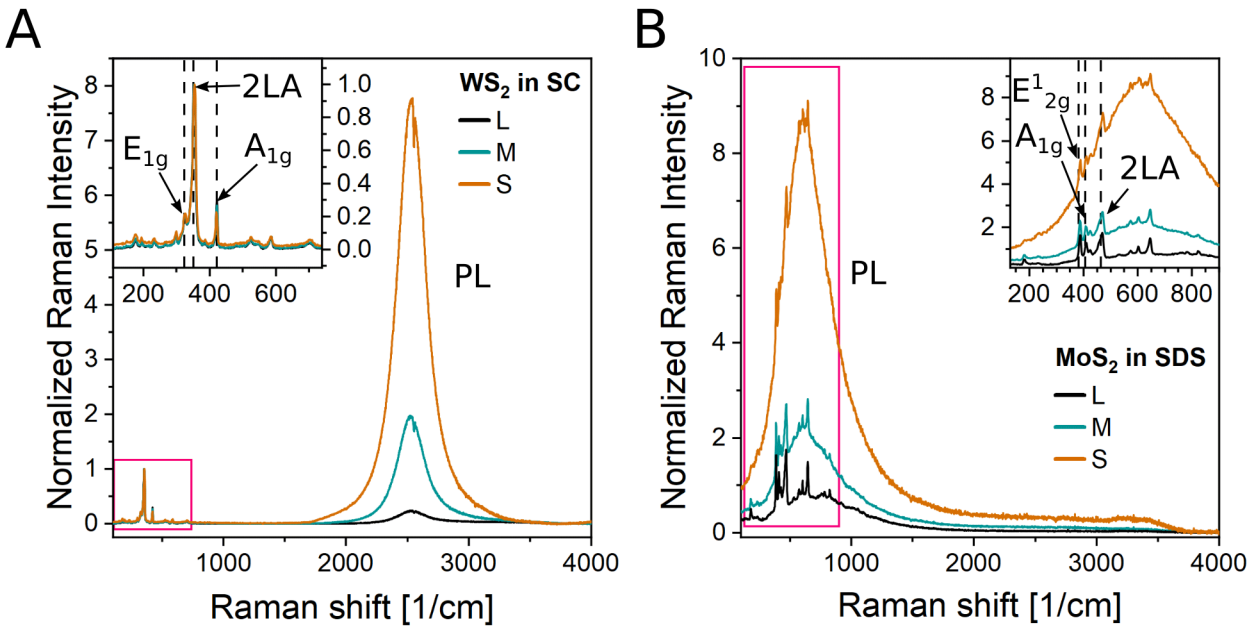

Figure 16: Normalized Raman spectra of WS_2 in aqueous SC solution (A, λ_{exc} = 532 nm) and MoS_2 in aqueous SDS solution (B, λ_{exc} = 633 nm) for different nanosheet sizes measured on a droplet of dispersion. Vibrational modes are enlarged in the inset and the three most pronounced features are labeled. Peak assignment was conducted according to literature.[120]

In the bulk crystals, four vibrational modes are Raman active: out-of-plane E_{1g}, E^1_{2g}, E^2_{2g} and in-plane A_{1g} vibrational modes.[121] Additionally, certain modes are disorder activated for nanosheets like the longitudinal acoustic mode LA and its second order mode 2LA.[122] Alongside these vibrational modes, PL of monolayers in dispersion is well visible. For WS_2 at laser wavelengths of 532 nm (figure 16, A) PL is visible at high wavenumbers and shows narrow linewidth and a clear increase with decreasing layer number. For MoS_2 at laser wavelengths of 633 nm (figure 16, B), PL manifests as an increasing background in the region of the MoS_2 vibrational modes. PL intensity in Raman spectra can be normalized with respect to the height of a vibrational mode to derive a metric often referred to as *PL/Raman ratio*. Such a ratio, for example the PL/2LA intensity ratio, can be used to quantitatively discuss the PL intensity and, therefore, the quality of dispersions in terms of monolayer content or defectiveness. In principle, these ratios can be exploited to

determine the monolayer content of samples as demonstrated for WS_2.[8] However, the metrics used for this are less robust compared to extinction metrics, as PL is highly sensitive to defects and starts to decrease for very small nanosheets due to edge-mediated non-radiative recombination pathways.[123-125]

2.6 Functionalization of layered group VI TMDs

Although properties of layered materials are highly promising and a certain amount of control is feasible by size selection, these methods can face limitations if a particular application is envisioned. As such, further means of additional influence exerted on the properties of the material are necessary. This can be accomplished by so-called functionalization, i.e. the directed surface modification of the nanomaterials. In literature, functionalization is often separated between non-covalent and covalent functionalization, although the terms physisorption and chemisorption may be equally employed.

In non-covalent functionalization, certain chemical species are physisorbed on the material and a certain effect on material properties is envisioned, often due to electronic interactions or electrostatic screening effects. In fact, nanosheet stabilization with ionic or non-ionic surfactants can be considered as a form of non-covalent functionalization with the aim of enhancing colloidal stability. As no covalent bonds are formed between particle and adsorbate, usually no structural changes[2] are induced in the material and adsorption is often reversible. In contrast to substitutional doping conventionally employed for Si based semiconductors, doping in TMDs can be accomplished without the necessity of altering the crystal lattice. Due to the susceptibility of the optical properties of TMDs to environmental influences, adsorbate effects can be divided into dipolar and charge transfer interactions. Molecules with a permanent dipole moment for example are capable of modulating the local charge carrier density through interactions with electric fields in excitons and therefore result in p- or n-type doping of semiconducting nanosheets depending on the dipole orientation, e.g. for material deposition on substrate supported self-assembled monolayers produced with alkylsilanes (figure 17), with Fermi level shifts up to 0.45 eV attainable.[126-128] Additionally, doping can be accomplished through adsorption of redox active electron donor or acceptor molecules, where the type of doping depends on the relative position of redox potentials of the adsorbate redox couple and the Fermi level of the nanosheet. This leads to injection of charges into the nanosheet lattice and can induce formation (or depletion) of charged excitons, commonly referred to as trions, with shifted transition energy.[129-130] The trion/exciton ratio in nanosheets thereby depends on the degree of doping.

2 It has to be noted that electron donors or acceptors inducing reduction or oxidation of the material can induce structural changes of group VI TMDs due to reasons outlined in chapter 2.2.

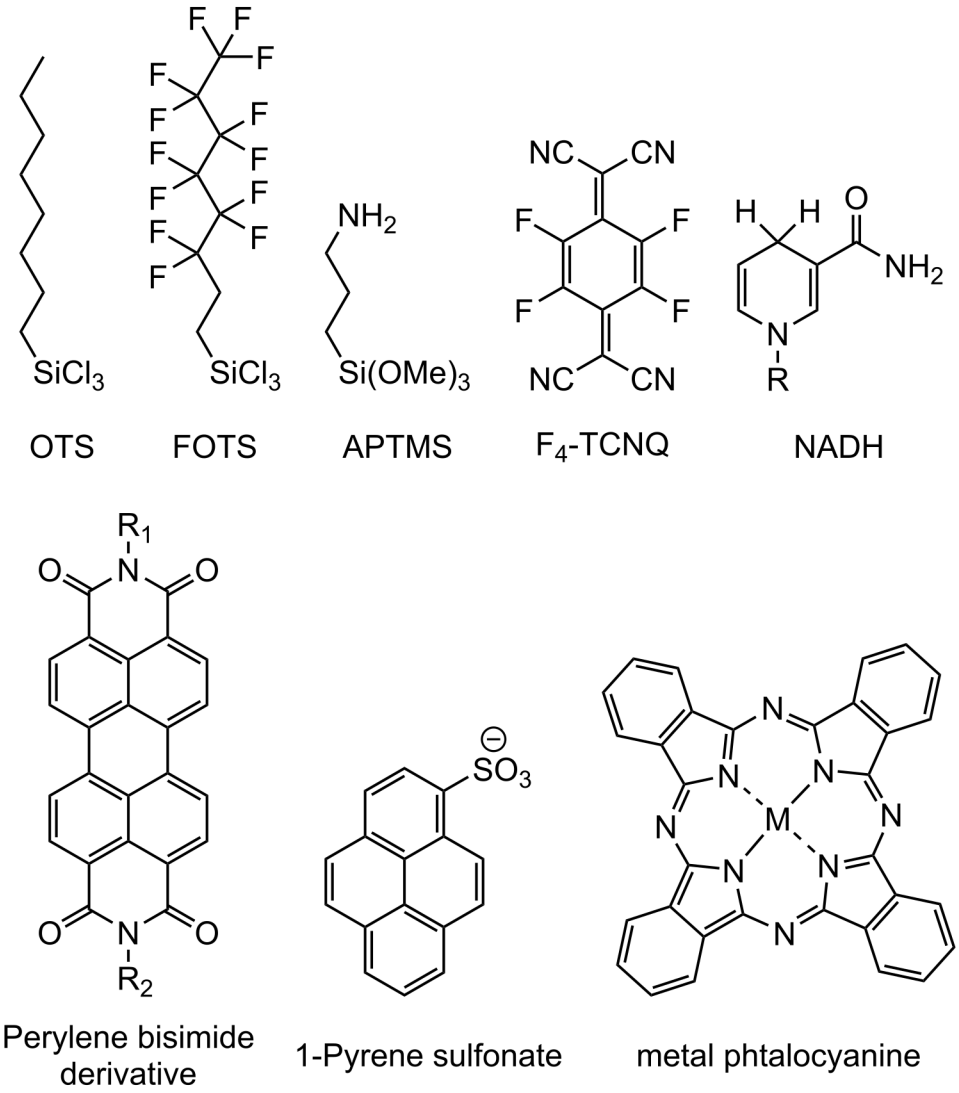

Figure 17: Chemical structures of molecules employed for non-covalent functionalization in literature. These can be roughly divided into self-assembled monolayers with trichlorooctylsilane (OTS), 1H,1H,2H,2H-perfluorooctyltrichlorosilane (FOTS), or 3-(aminopropyl)trimethoxysilane (APTMS), into redox active compounds with 2,3,5,6-Tetrafluoro-7,7,8,8-tetracyano-quinodimethane (F_4-TCNQ), or reduced nicotinamide adenine dinucleotide (NADH) and into organic dyes like perylene bisimide derivatives, pyrene sulfonates or metal phthalocyanines.

Redox active adsorbates which were used in the past were for example F_4-TCNQ as electron acceptors (p-type doping) or NADH as electron donors (n-type doping, figure 17).[129-130] Photoinduced charge transfer is also feasible using metal phthalocyanines with varying redox potentials based on the metal centers.[131-133] Other chromophores were also used in the past with graphene, where non-covalent functionalization is often facilitated using polycyclic aromatic systems like perylene or pyrene derivatives (figure 17), in order to exploit strong π-π-interactions for physisorption, and in conjunction with suitable functional groups enable solubilization of the nanomaterials in dispersion.[134-138] Furthermore, spontaneous adsorption of these compounds on materials like WS_2, MoS_2 or

black phosphorus is also observed, although no *π*-*π*-interactions are expected, presumably due to hydrophobic interactions.[136, 139-141] Due to the fact that these polycyclic aromatic compounds are usually strong chromophores, charge as well as energy transfers between nanosheet and adsorbates are possible, which has been exploited in perylene derivative mediated n-type doping of MoS_2 to enhance the photoresponse in photodetectors.[142-144]

Non-covalent functionalization of WS_2 in the solid state using a perylene bisimide derivative and two tetraazaperopyrene derivatives as well as their impact on the nanosheet properties is discussed in chapter 5.2 of this thesis.

In contrast, covalent functionalization occurs upon direct chemical reaction of adsorbate and material leading to the production of a covalent bond between the two. This is usually accompanied by local changes in the structure of the material and can lead to new material properties, as demonstrated recently for defect emission in carbon nanotubes.[145] The main obstacle to overcome for layered nanomaterials is the inertness of the pristine surface, as graphene or MoS_2 lack dangling bonds on the basal plane. Therefore, many functionalization approaches utilize defects such as sulfur vacancies or edges in the material to enable functionalization. Other approaches utilize a charge transfer prior to the functionalization or in general very reactive reagents. Covalent functionalization additionally bears the advantage that functional groups can be introduced that enable further chemical reactions possibly leading to supramolecular chemistry.[146-147] Sulfur vacancies as anchor points for covalent functionalization can be introduced selectively by e.g. argon ion bombardment of the MoS_2 crystal among other techniques.[148-149] Resulting defects show increased reactivity due to the presence of dangling bonds and can be used as target structures for functionalization. Especially prominent is the reaction of such defect sites with molecules containing a thiol group like alkyl thiols[150] or 1,2-dithiolane derivatives (figure 18).[133, 146, 151] This mechanism is often referred to as *repairing* as the sulfur bearing group of the reagent replaces the vacant sulfur site in the lattice.[152] Another possible route to enable functionalization is via introduction of charges: Upon treatment of e.g. MoS_2 with organolithium reagents like *n*-butyllithium intercalation of lithium in the interlayer space of the material takes place. Intercalation is accompanied by an electron transfer to the material and MoS_2 is transformed locally to its octahedral polytype (often referred to as *1T*-MoS_2, although formally a reduction took place, see chapter 2.2 for details).[45, 83] This is accompanied by the loss of the semiconducting nature of MoS_2 and a metallic character is adopted instead.[83] This reaction was already exploited to enhance electrocatalytic activity of WS_2 nanosheets[153] and can further be used to facilitate functionalization of the material due to the presence of charges on the nanosheets. Electrophilic agents like organic halides, such as iodomethane and 2-

iodoacetamide,[45] iodobenzenes,[154] or diazonium salts like 4-methoxyphenyldiazonium tetrafluoroborate[155] can be used to promote a nucleophilic substitution type reaction (figure 18).

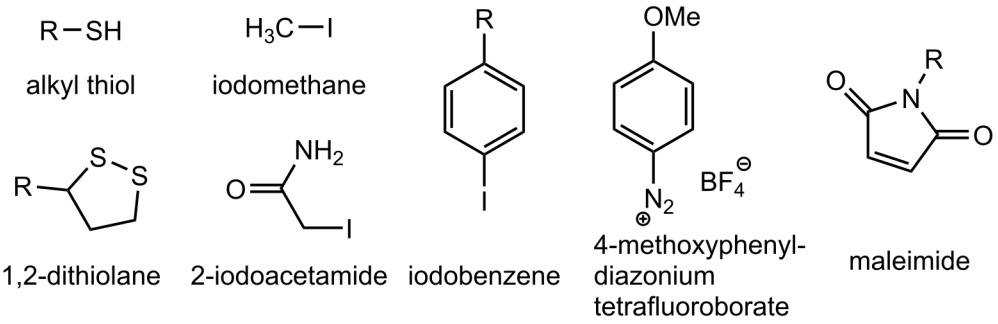

Figure 18: Chemical structures of molecules employed for covalent functionalization.

Additionally, grafting of organic functional groups on the TMD surface allows for subsequent chemistry with these groups and enables anchoring of other functional compounds.[156-157] Although *2H*-Mo/WS_2 is relatively inert, some functionalization strategies exist that do not rely on preprocessing of materials by introduction of defects or reductive exfoliation. These include, for example, coordination of transition metal compounds like nickel(II)acetate,[158] Michael addition of maleimide derivatives (figure 18),[147, 159] or noble metal nanoparticle decoration.[160-161] For the latter case though, functionalization approaches employed throughout literature are diverse. Metal nanoparticles reductively generated in-situ can be adsorbed at functional groups previously introduced on the nanomaterial surface[162-165] or directly attached to the surface. For direct adsorption, additional reducing agents[166-172] can be employed to achieve reduction of the metal precursors, although spontaneous formation of these particles was observed,[160-161, 173-174] both on *1T*-Mo/WS_2 produced from chemical exfoliation[173-174] as well as on *2H*-Mo/WS_2.[160-161] These methods allow for decoration of Pt, Pd, Au, or Ag nanoparticles on the nanosheet surface and enable further metal nanoparticle chemistry with these hybrid structures.[174-175] Direct reaction with the TMD surface in the case of *1T*-Mo/WS_2 can readily be explained by the presence of negative charges on the TMD, but not in the case of *2H*-Mo/WS_2, without addition of any additional reducing agents. According to these observations, it appears as if the metal precursor (chloroauric acid in literature[160-161]) is reduced by the material itself. In the case of gold nanoparticle functionalization of WS_2, a pronounced regioselectivity of gold nanoparticle decoration is observed and the production of selectively edge-functionalized WS_2 nanosheets has been demonstrated.[160] In this study, liquid dispersions of WS_2 as derived from sonication assisted liquid phase exfoliation and subsequent liquid cascade centrifugation were treated with varying amounts of chloroauric acid and spontaneous formation of gold nanoparticles occurred. A workup by centrifugation can be conducted to remove unreacted chloroauric acid as well

as aggregates that formed during the reaction (figure 19, A).[160] A dependence of gold nanoparticle diameters is observed based on the amount of chloroauric acid employed (figure 19, B-E).

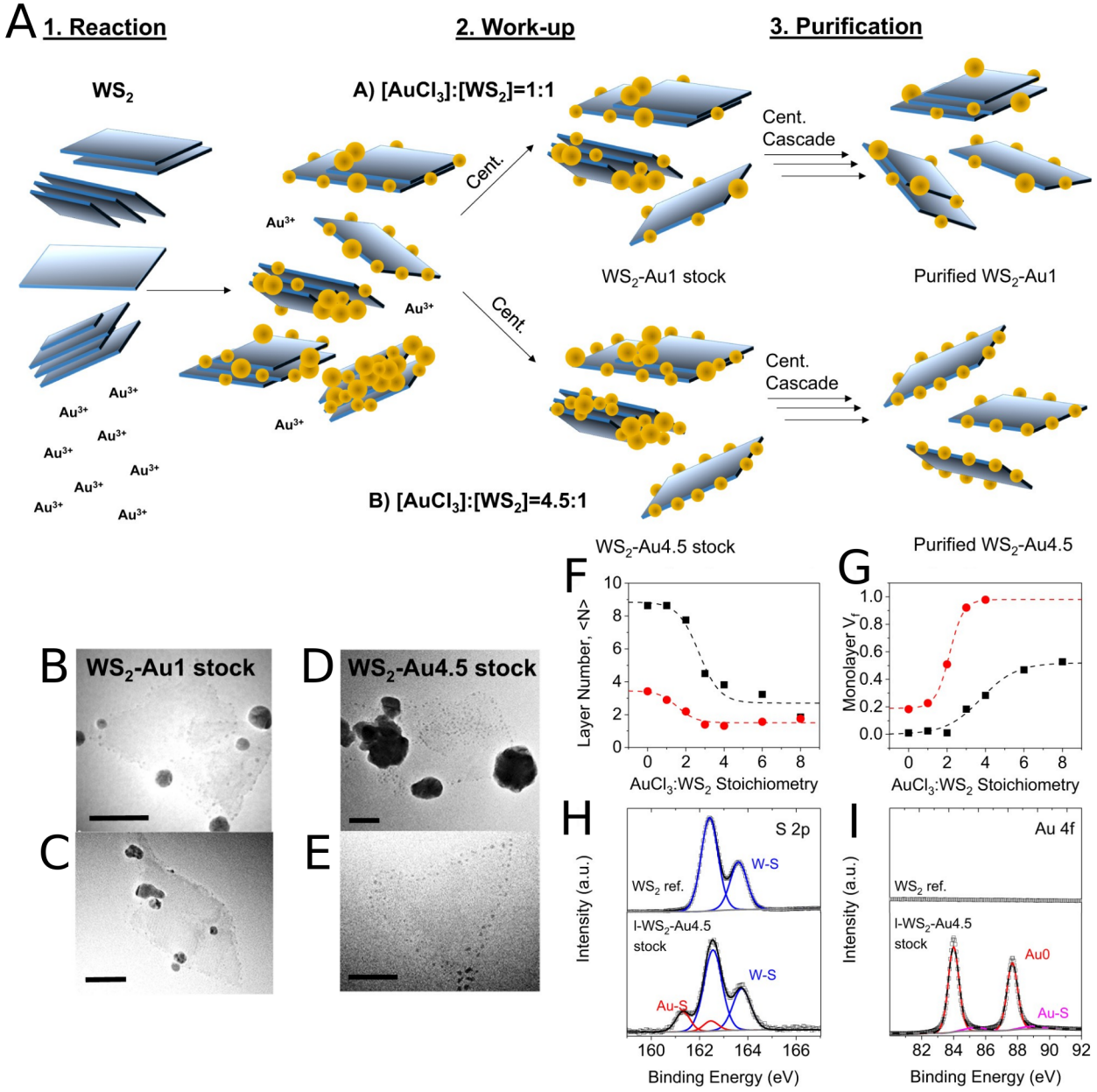

Figure 19: A) Schematic representation of the functionalization reaction, reaction workup and purification by centrifugation for 1 and 4.5 equivalents of chloroauric acid employed. B-D) TEM images of gold nanoparticle functionalized WS_2 nanosheets treated with 1 (B-C) and 4.5 (D-E) equivalents of chloroauric acid. F) Mean layer number and G) monolayer volume fraction of dispersions upon functionalization and purification with various amounts of chloroauric acid. H-I) X-ray photoelectron spectroscopy (XPS) measurements of S 2p (H) and Au 4f (I) core levels for pristine (upper layer) and functionalized (lower layer) WS_2 nanosheets. Reprinted under Creative Commons CC BY license from npj 2D Materials and Applications ***2017****, 1, 43, 1-9.*[160]

Furthermore, a second cascade centrifugation after gold nanoparticle functionalization can be employed to remove big gold aggregates and produce highly

monolayer enriched dispersions with the degree of enrichment possible depending on the stoichiometric ratio of chloroauric acid to WS_2 (figure 19, F-G).[160] According to XPS, the enriched monolayers are selectively edge-decorated and show no significant signs of oxidation, but indications for covalent bonding between gold and sulfur species are evident from X-ray photoelectron spectroscopy (XPS, figure 19, H-I). Mean length $<L>$ of the nanosheets in dispersion was retained upon monolayer enrichment.[160] In turn, formation of disulfides at the nanosheet edges and an influence of defects in general was hypothesized and linked to an increase in electrocatalytic activity of the nanosheets towards the hydrogen evolution reaction.[160] However, the reasons for both the increase in electrocatalytic activity as well as the regioselectivity of functionalization were not unambiguous in this study. Mechanistically, the formation of gold nanoparticles through the reduction of chloroauric acid on the nanosheet transitions through a surface intermediate, which was identified to be a linear Au(I) complex ($[(MoS_2)AuCl_x]$) in the case of substrate-supported CVD MoS_2.[176] In a first step, Au(III) is spontaneously reduced to Au(I) on the MoS_2 surface, before an Au-S coordination bond forms.[176] In the absence of water, e.g. in ethanol, this complex is stable. However, in an aqueous environment, disproportionation of Au(I) into Au(III) and Au(0) occurs, with the latter then aggregating to form gold metal nanoparticles. As gold reduction transitions through a surface intermediate, a significant dependence of the overall reaction on the surface chemistry is expected, e.g. for surfactants present at the solution-nanosheet interface. A similar complex was observed for Ag(I).[176] However, no disproportionation of Ag(I) is expected in an aqueous environment and, hence, no silver metal nanoparticles can be formed spontaneously along this reaction path.[6]

Regioselectivity of the functionalization reaction is discussed in more detail throughout chapters 4.1 and 4.2, while possible origins of an increased electrocatalytic performance is discussed in chapter 5.3.

2.7 Film deposition techniques

For various experimental designs as well as integration in functional devices, solid samples are required. Such samples are accessible by e.g. CVD methods as outlined in chapter 2.3. However, solution processing bears additional advantages, such as scalability of production,[80] size selection,[7-8] facile production of composites by mixing of dispersions,[177] or wet-chemical modification prior to deposition with methods described in the previous chapter. Therefore, means for processing of layered materials from the liquid phase into films are necessary. Various methods for film deposition for layered materials in the liquid phase have been explored in the past and printing of 2D material networks has resulted in demonstrations of device applications, such as transistors,[178-179] photodetectors,[180-181] and (super)capacitors.[182-184] A plethora of deposition techniques exists in literature, each with

their individual advantages and disadvantages. Some basic, non-contact deposition techniques are droplet deposition methods, such as drop casting,[185] spin coating,[186-187] and spray coating[178-179], while nozzle-based printing techniques, such as inkjet,[139, 179] and aerosol-jet printing approaches[188-189] allow for complex patterning of films. Furthermore, film transfer approaches, such as Langmuir-Blodgett type deposition techniques exist.[190-192] These methods usually utilize low-concentration, low-viscosity inks for printing.[193]

For high-throughput printing approaches, usually highly concentrated inks of elevated viscosity are required.[193] These approaches entail screen printing,[194] blade coating,[195] gravure,[196] and flexographic printing,[197] that have all been successfully applied for formation of nanosheet networks. They bear great potential for large scale printing and continuous roll-to-roll production of thin-films.[198] However, a significant downside of these approaches often is, that the formulation of inks compatible with these techniques is complex, as binding agents, additional solvents, or other additives are required to tailor the rheology of the inks or impede aggregation or precipitation.[198] This also applies to inkjet printing and,[198] as such renders these methods unappealing as a facile go-to method for film deposition in academic research.

In contrast, spray and drop casting approaches are readily accessible, as the deposition can be accomplished with dispersions as derived from LPE after size selection. However, control over the film morphology with these methods is poor.

In drop casting, a nanoparticle dispersion is deposited on the substrate of choice followed by evaporation of the solvent. In spite of its simplicity, films produced from this method can be integrated in applications, where the homogeneity of the films is less important, e.g. for use as electrodes in batteries[185]. However, the films are often inhomogeneous in thickness and morphology due to different evaporation rates across the deposited droplet. This so-called coffee ring effect[199] results in enhanced material deposition at the edges of the droplet compared to the center. If control over the film morphology is necessary, more elaborate methods are required for deposition.

Spray coating is a technique that uses spraying of a nanoparticle ink through a narrow nozzle. The liquid is finely dispersed at this nozzle by a high-pressure propellant gas stream,[178] ultrasound,[200] or an electric field,[201-202] and sprayed on a substrate, where the solvent evaporates. This technique is capable of evenly coating large substrates and requirements for the rheological ink properties are minimal compared to other printing techniques.[198] However, optimization of the spraying setup is tedious, as a multitude of processing parameters, such as solvent type, viscosity, flow rate, spraying distance, and evaporation rate on the substrate need to be controlled for optimal results.[200, 203-206]

A different method, that relies on film formation prior to the removal of the solvent are Langmuir-Blodgett type deposition approaches. For this method, the material ink is injected onto a liquid column, the so-called subphase and through self-assembly, a film is formed at the liquid-air interface.[207] The produced films are usually confined in one dimension due to the formation at the interface. Classically, amphiphilic molecules are used to establish the self-assembly at this interface.[207] However, polymers,[208-209] extended conjugated organic molecules,[210-211] and inorganic nanomaterials, such as fullerenes,[212] graphene,[213] and TMDs[214-215] can be used in this approach, with self-assembly at the interface, e.g. through hydrophobic interactions with a water subphase. Additionally, the Langmuir troughs, in which the deposition takes place, can be equipped with mobile barriers, usually made from polytetrafluoroethylene (PTFE), that can be used to further compress the film prior to transfer.[207] The preformed film is then transferred to a substrate by lifting it through the film orthogonal to the surface or at an angle.[207] If the substrate is immersed and retracted parallel to the film, then the method is referred to as Langmuir-Schaefer deposition.[207] Usually, a monolayer of the film is deposited on the substrate, but multiple deposition runs are possible to increase the number of deposited layers.[207] Furthermore, film formation is not restricted to liquid-air interfaces and successful film production from group VI TMDs at liquid-liquid interfaces was demonstrated.[190, 192, 216] Especially for layered nanomaterials, this method bears great potential for production of highly ordered tiled networks due to the confinement of the nanomaterial films at the two-dimensional liquid-liquid interface. This confinement further suppresses restacking of isolated nanosheets upon film formation and enables production of a monolayered, large-scale 2D network aligned parallel to the substrate.[190] Liquid-liquid interfaces employed in literature entail water/*n*-hexane with TMDs in IPA,[190] DMF/octadecene with TMDs in DMF,[192] or ethylene glycol/*n*-hexane with TMDs in hexylamine.[216] The film formation is thereby driven by a reduction of the interfacial energy at the liquid-liquid interface and, hence, immiscible solvents with high interfacial tension are best suited for this approach.[190] Applications of this method were demonstrated for field-effect transistors[190] and photoelectrochemical hydrogen production,[216] while film patterning was demonstrated by a combination of liquid-liquid interface film deposition and patterned hydrophobic coatings on the substrate by photolithography.[192] Due to the presence of a liquid-liquid interface instead of the liquid-air interface for Langmuir-Blodgett or -Schaefer type film deposition, the term *modified Langmuir-Blodgett or -Schaefer* method will be used throughout this thesis.

Airbrush spray and modified Langmuir-Blodgett and -Schaefer thin-film deposition techniques will be used throughout chapter 5 of this thesis for fabrication of WS_2 thin-films with varying film morphology.

3 Objectives

In this thesis, two distinct research questions are in the focus of the experiments detailed herein:

1) What is the origin of the regioselectivity in the heterogeneous reaction of chloroauric acid with WS_2?

2) What is the impact of film morphology on the optical and electrocatalytic properties of WS_2 nanosheet films?

Initially, these research questions were motivated by a publication[160] and my master thesis from 2018,[217] where the electrocatalytic activity of airbrush sprayed films made from surfactant-stabilized gold-functionalized WS_2 nanosheets were investigated. Nevertheless, many open questions about the exact origin of regioselectivity were left unanswered, e.g. if the surfactant plays a role in the reaction. Functionalization reactions take place directly on the nanosheet surface. However, that is also where the adsorption of surfactants takes place. It seems intuitive that the surfactant layer has a certain impact on chemical reactions with the surface. Therefore, a third research question is formulated:

3) Is there an influence of the surfactant layer on the gold nanoparticle functionalization of WS_2?

The objective of the first part of this thesis therefore lies in gaining a deeper insight into the mechanism of the gold nanoparticle functionalization of WS_2 (and other TMDs) and hopefully, into heterogeneous functionalization reactions of layered materials in general. Throughout chapter 4, it will be demonstrated that the answers to the research questions 1) and 3) are inherently linked.

In order to analyze the electrocatalytic activity of these materials, fabrication of (solid) working electrodes through film deposition is necessary. However, the impact of the film morphology on the hydrogen evolution reaction performance of gold-functionalized WS_2 thin-films was not analyzed in previous work.[160, 217] Furthermore, a pronounced degradation of the optical size-dependent properties of layered materials, such as WS_2 usually accompanies film deposition due to restacking effects in these films. Hence, for various applications, and especially for those concerned with the optical properties of layered materials, retention of size-dependent properties in films is necessary for reliable

data interpretation and integration in devices. Therefore, a fourth research question is formulated:

4) Which thin-film morphology is best suited to avoid restacking effects and how can such thin-films be produced from LPE layered materials such as WS_2?

The objective of the second part of this thesis therefore lies in the identification and characterization of a thin-film morphology, that is capable of translating size-dependent properties of layered materials in dispersion to film properties, on the example of LPE WS_2. Suggestions for research questions 2) and 4) will be discussed throughout chapter 5.

4 Gold nanoparticle functionalization

In this chapter, the functionalization of layered nanomaterials with gold nanoparticles and the influence of surfactants on such heterogeneous reactions is discussed. Results of this chapter have been partially published in *Angew. Chem. Int. Ed.* **2020**, 59, 13785 - 13792.[94] Furthermore, additional data will be presented and discussed.

Functionalization reactions producing gold nanoparticles exploit the high nobility of gold as an element and the subsequent high reactivity of gold in its oxidized form to perform reactions on the surface of the functionalization target material. Commercially available gold compounds, such as chloroauric acid ($H[AuCl_4]$), show a pronounced tendency to produce such particles. Gold nanoparticles are frequently used in research due to their well-studied optical properties and ease of synthesis. Furthermore, they can be used to probe functionalization reactions, as they are readily observable in electron microscopy techniques as well as in extinction or absorption measurements using visible light due to their intense surface plasmon resonance. This enables observation and analysis of reaction products which is often difficult using functionalization approaches with commonly used organic moieties. In this chapter, the functionalization of various layered nanomaterials using chloroauric acid is investigated in order to gain a deeper insight into heterogeneous functionalization of layered nanomaterials as a whole.

4.1 Functionalization of LPE tungsten(IV)sulfide in SC

For the functionalization of tungsten(IV)sulfide nanosheets, dispersions of this material are produced using liquid phase exfoliation. In brief, the material is sonicated in aqueous surfactant solution with surfactants, such as sodium cholate. In a first step, an relatively short sonication sequence is used to solubilize impurities which are then discarded together with the surfactant solution and the material is redispersed in fresh surfactant solution. For exfoliation, a second sonication step with increased duration is then employed in order to produce well-dispersed WS_2 nanosheets. Since these dispersions are intrinsically polydisperse in length and thickness of the nanosheets, liquid cascade centrifugation can be employed to selectively separate the material by mass and therefore produce size-selected dispersions with the average length and thickness decreasing with increasing centrifugal force. This enables the observation of size-dependent effects as can be seen in figure 20, A. The normalized extinction spectra show a clear trend with size as can be seen in a decrease of the normalized extinction, an increase in the extinction ratio $Ext(235\ nm)/Ext(294\ nm)$ as well as a blue-shift of the A exciton signal with decreasing lateral size $\langle L \rangle$ and thickness $\langle N \rangle$. Furthermore, a

splitting of the A exciton signal can be observed in the inset in figure 20, A. This splitting can be resolved more clearly in the second derivative of the spectral region around the A exciton signal with respect to the photon energy of the incident light (figure 20, B). Two distinct peaks can be observed for sample *S* whereas only the lower energy peak at around 1.97 eV is visible in sample *L*. In sample *M*, the lower energy peak is the dominant contribution and a shift of the lower energy peak to higher energies can be observed with decreasing thickness $<N>$, whereas no size-dependent changes are expected for the higher energy contribution at 2.03 eV.[8]

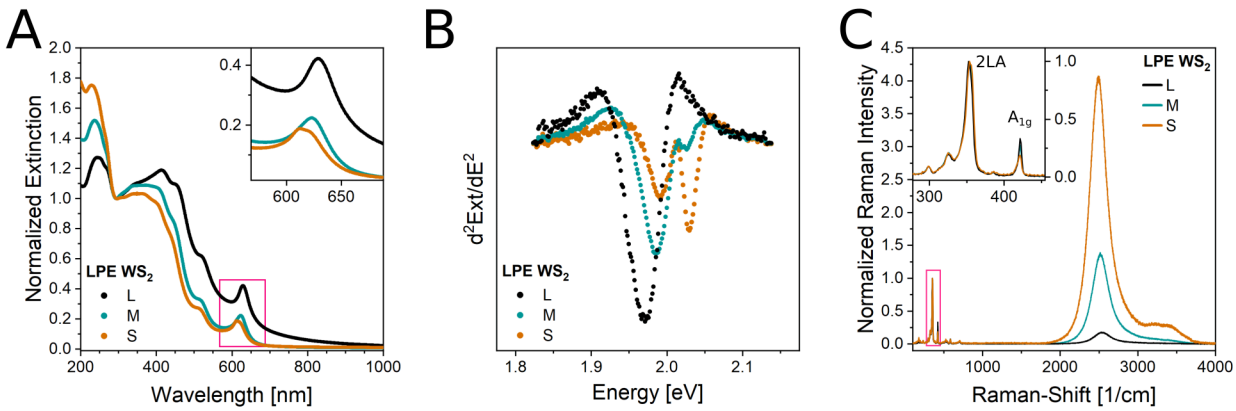

Figure 20: A) Extinction spectra of WS_2 after liquid phase exfoliation and subsequent liquid cascade centrifugation normalized to the extinction at 294 nm. Inset: enlarged view on the spectral region around the A exciton signal. B) Second derivative of the spectral region around the A exciton signal in A with respect to the photon energy of the incident light. C) Raman spectra of WS_2 dispersions measured on a droplet of the dispersion (λ_{exc} = 532 nm). Three spectra are averaged each, a baseline was subtracted and the spectra were normalized with respect to the 2LA mode. The inset shows an enlarged view on the spectral region around the 2LA and A_{1g} mode as indicated. Samples are labeled with L for large (0.4 - 1k g, $<L>$ = 158 nm, $<N>$ = 10), M for medium (1 - 5k g, $<L>$ = 66 nm, $<N>$=5) and S for small (5 - 30k g, $<L>$ = 34 nm, $<N>$ = 2) in order to illustrate changes in relation to the average lateral size $<L>$ and average layer number $<N>$ of the WS_2 dispersion. $<L>$ and $<N>$ were determined from extinction spectra using published metrics.[8]

These two contributions to the A exciton signal in extinction can be assigned to the absorption of the monolayered material in case of the high energy peak and the individually not resolvable absorption of bi- and few-layers for the low energy peak. The layer number-dependent exciton energy is believed to arise from a combination of confinement and dielectric screening effects.[8, 15] It should be noted that extinction spectra consist of absorption and scattering contributions which were not deconvoluted here (see chapter 2.5 for details). Since monolayered tungsten(IV)sulfide nanosheets possess a direct bandgap, photoluminescene can be observed in dispersions with sufficient monolayer content (figure 20, C). This can be efficiently measured in Raman spectrometers when matching the excitation energy to the absorption and emission of the TMD. In order to assess the PL intensity independent of the dispersion concentration, spectra are normalized to a vibrational mode of WS_2, namely the 2LA mode. A clear

increase in PL intensity is visible with decreasing average layer number $<N>$, indicating a significant increase in monolayer content through liquid cascade centrifugation.

In the following, tungsten(IV)sulfide produced from liquid phase exfoliation is reacted with chloroauric acid to produce gold nanoparticles. As a result, WS_2 is oxidized during the reaction. The WS_2 dispersion of medium size *M* is fixed to a concentration of 2 mmol/l in aqueous sodium cholate solution (c_{surf} = 0.46 mM) and stirred on an ice bath. The same volume of an aqueous chloroauric acid solution is added dropwisely. After resting at 4 °C overnight, the reaction outcome can be readily seen from a change in color of the reaction mixture producing a deep red colored dispersion due to the formation of gold nanoparticles on the nanosheet surface. The reaction mixture is then worked up through centrifugation. First, a high speed centrifugation step is employed in order to sediment all material in the reaction mixture and therefore separate it from unreacted chloroauric acid and soluble oxidation byproducts in the supernatant. This can be readily seen from extinction spectroscopy in figure 21, A (black trace). The characteristic absorption peaks of the square planar d^8 complex $[AuCl_4]^-$ at 226 nm and 313 nm respectively can be seen. Afterwards, a low speed centrifugation is used to remove any aggregated material which is not colloidally stable in dispersion (figure 21, A, teal trace). The supernatant of this low speed centrifugation step is denoted as *Stock* sample (figure 21, A, dark green trace) and used for further purification.

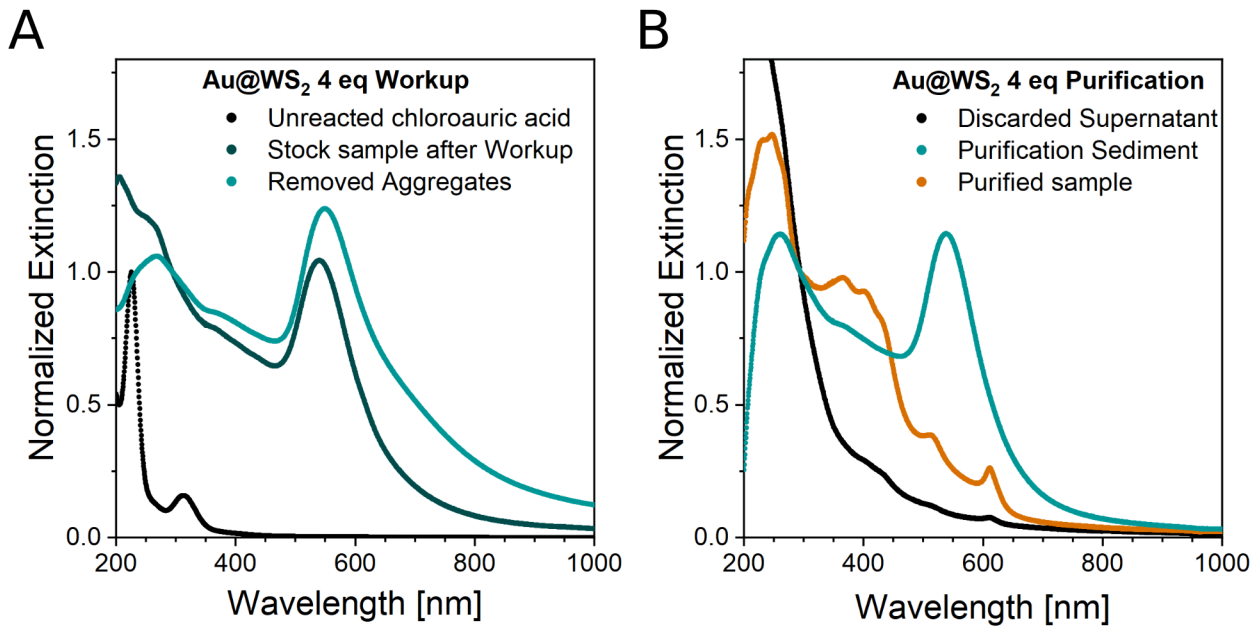

Figure 21: A) Extinction spectra of typical samples of M-WS_2 produced after reaction with chloroauric acid during workup. The trace denoted as Unreacted chloroauric acid was normalized to the extinction at 226 nm, all other traces were normalized to the extinction at 294 nm. B) Extinction spectra of samples produced during purification, normalized to the extinction at 294 nm.

In the extinction spectra of the *Stock* sample as well as the removed aggregates, the spectral profile of WS_2, as seen in figure 20, A is not clearly observed. The spectra are dominated by a broad absorption peak assigned to the surface plasmon resonance of the formed gold nanoparticles, with a peak maximum between 500 and 600 nm in figure 21, A. In order to reveal the spectral profile of WS_2, the removal of big gold nanoparticles is necessary, as the intensity and position of the surface plasmon resonance depend on the size of gold nanoparticles.[218] This step will be referred to as *purification*. An additional cascade centrifugation step is employed on the *Stock* sample with removal of big gold nanoparticles at a relative centrifugal force (RCF, in units of the earth gravitational field, *g*) of 4 000 *g* and sedimentation of the purified sample at 16 000 *g*. These RCF parameters can be adjusted for other nanosheet sizes.[160] Alternatively, an extended liquid cascade centrifugation can be employed in purification as discussed in appendix 8.1. The sediment is redispersed in fresh surfactant solution. The effect of this purification step can be readily seen from extinction spectroscopy (figure 21, B). In the spectrum of the purified sample (orange trace) the spectral profile of WS_2 is well discerned while the spectrum of the material removed in the lower RCF centrifugation step (teal trace) is still dominated by the surface plasmon resonance of big gold nanoparticles. The supernatant shows only light traces of WS_2 and/or Au nanoparticles with a mostly featureless extinction (black trace). The extinction spectra of pristine *M*-WS_2, and the purified samples using two different stoichiometry ratios of WS_2 and chloroauric acid are compared in figure 22, A.

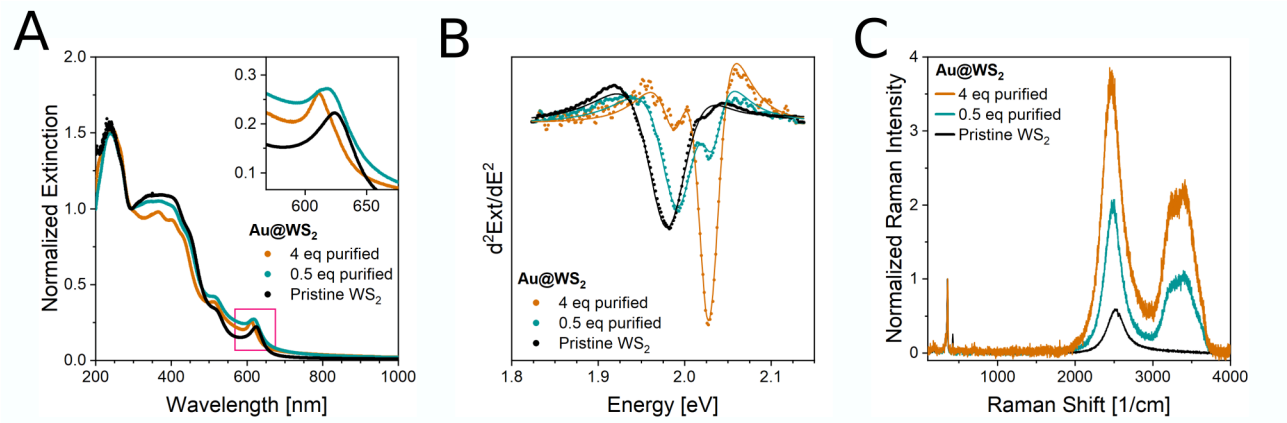

Figure 22: A) Extinction spectra of gold-functionalized M-WS_2 treated with 4 and 0.5 equivalents of chloroauric acid as well as of the starting material. All spectra are normalized to the extinction at 294 nm. The inset shows an enlarged view of the spectral region around the A exciton signal. B) Second derivative of the spectral region around the A exciton signal in A with respect to the photon energy of the incident light. The curves are fitted with the second derivative of the sum of two Lorentzians (solid lines). C) Raman spectra of functionalized and pristine WS_2 dispersions measured on a droplet of the dispersion (λ_{exc} = 532 nm). Three spectra are averaged each, a baseline was subtracted and the spectra were normalized with respect to the 2LA mode. The broad signal with high intensity around 3500 1/cm is attributed to the Raman response of water.

In agreement with literature,[160] the extinction ratio $Ext(235\ nm)/Ext(294\ nm)$ is not changed after purification revealing no significant changes in average lateral nanosheet size $<L>$ for functionalized nanosheets compared to the starting material and is therefore assumed constant. However, a noticeable change after purification can be seen in the A exciton signal: an increasing blue-shift of the signal with increasing chloroauric acid equivalents employed accompanied by narrowing of the exciton resonance (figure 22, A) is visible. Since the A exciton signal conveys information about the average layer number of the probed WS_2 nanosheet ensemble, this blue-shift indicates an increase in monolayer content in the dispersion after purification (see chapter 2.5 for details). This effect can be quantified through deconvolution of the constituting peaks in the second derivative of the A exciton signal (figure 22, B). By assessing the contribution of the monolayer signal to the total A exciton signal by fitting to the second derivative of the sum of two Lorentzians, an estimation of the monolayer content is possible.[8] While estimation of the monolayer volume fraction for pristine WS_2 dispersion gives a relatively low value of 0.7 %, the purified sample treated with 0.5 equivalents of chloroauric acid already contains 10 % of monolayered material. With 4 equivalents, a monolayer volume fraction of 88 % was achieved which renders this dispersion predominantly monolayered. Such a significant monolayer enrichment should be well visible in photoluminescence of the dispersion which is evident from Raman/PL spectroscopy (figure 22, C): The PL is increased roughly 4-fold and 8-fold for functionalization in 0.5 and 4 equivalents respectively. In agreement with literature,[160] it is therefore evident that the gold decoration in sodium cholate in conjunction with purification through centrifugation enriches the treated dispersion in monolayers. This can be directly observed via transmission electron microscopy of gold nanoparticle functionalized nanosheets after purification in comparison to the material removed during purification. In figure 23, A-D, transmission electron microscopy images of the material removed during purification is shown. The removed nanosheets are heavily functionalized with big gold nanoparticles sitting on the basal plane of the nanosheets while on close inspection also very small nanoparticles are visible, predominantly found around nanosheet line defects as edges and terraces, best seen in figure 23, C. Statistical evaluation of gold nanoparticle diameters found during TEM corroborates the distinct differences in nanoparticle diameters (figure 23, E): Two well resolved distributions can be identified which are fitted using Gaussians. While the diameter distribution of the small particles is relatively sharp with particle diameters of 2.78 ± 1.41 nm, the second distribution is significantly broader with larger diameters of 20.11 ± 9.92 nm. The fact that two distinct distributions can be identified implies that different growth mechanisms are involved in the formation of large and small nanoparticles.

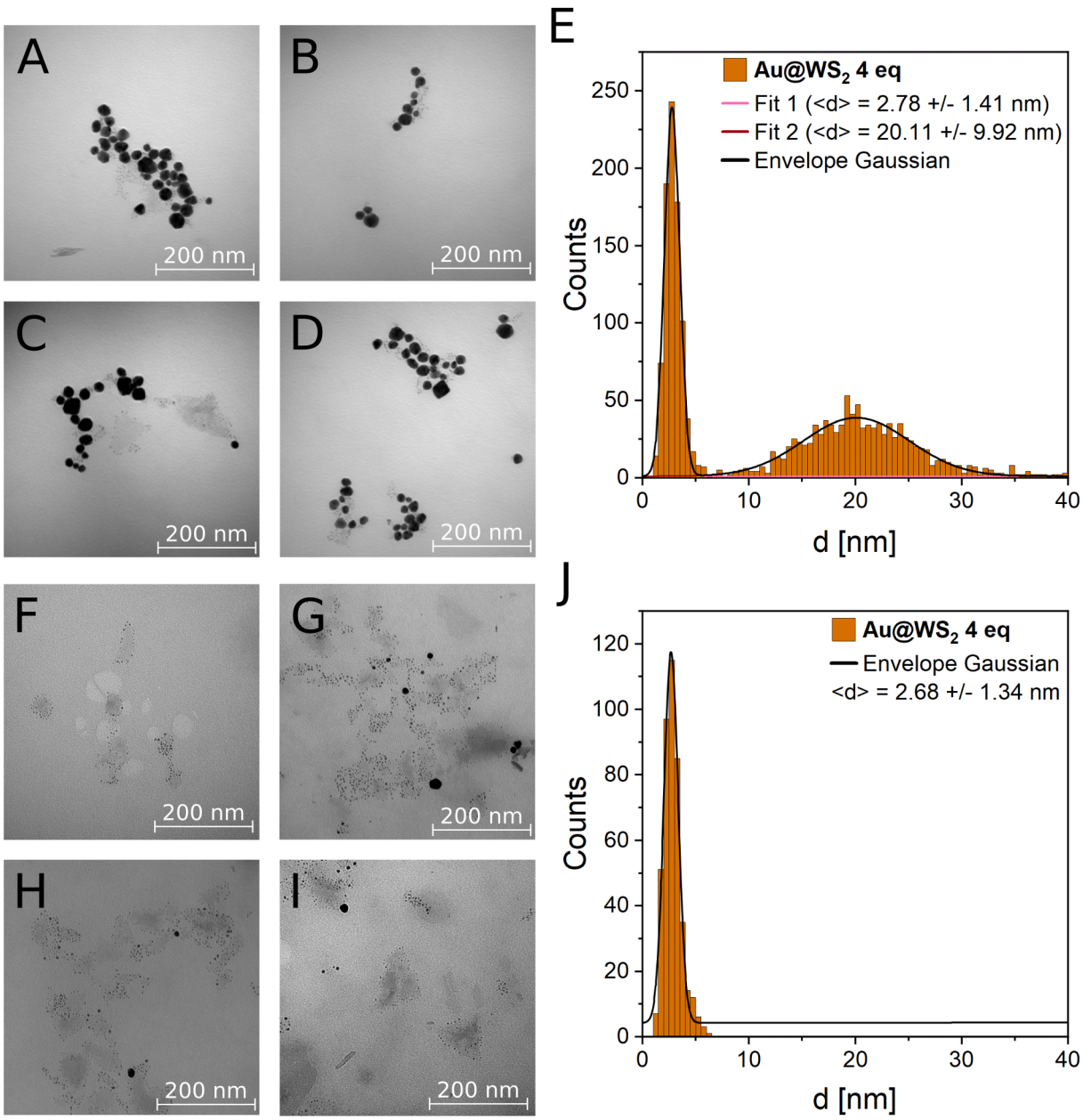

Figure 23: A-D) Transmission electron microscopy images of gold-functionalized M-WS_2 nanosheets removed during purification for 4 equivalents of chloroauric acid. E) Statistical evaluation of gold nanoparticle diameters in A-D. F-I) Transmission electron microscopy images of gold-functionalized M-WS_2 nanosheets after purification. J) Statistical evaluation of gold nanoparticle diameters in F-I. All shown images were recorded with 120 kV acceleration voltage at x50 000 magnification. Statistical data are fitted with one or two Gaussians respectively. Peak centers of the individual Gaussians were taken as average gold nanoparticle diameter <d> and full width at half maximum was taken as standard deviation.

After purification however, only small nanoparticles remain in dispersion as can be seen in transmission electron microscopy (figure 23, F-I). These are still found predominantly along line defects, whereas most of the big gold nanoparticles are removed. This is further corroborated via the statistical analysis, where only the peak of the small diameter particles can be seen in the distribution histogram without any significant

changes to peak center or width (figure 23, J). Bigger nanoparticles have a significantly increased mass and in conjunction with the clear separation of these two distributions leads to efficient separation via centrifugation during purification.

The importance of a clear separation of the distributions for purification becomes apparent when analyzing gold nanoparticle decoration with 0.5 equivalents of chloroauric acid. In the TEM images of material removed during purification no clear distinction between nanoparticle diameters can be made by bare eye (figure 24, A-D). The nanoparticles are smaller than the big nanoparticles found for the functionalization using 4 equivalents. In agreement with the functionalization using 4 equivalents, they are often found along line defects of the nanosheets as well as on the basal plane. The statistical evaluation reveals a seemingly monomodal distribution albeit being slightly asymmetric at the small diameter tail. This can be interpreted as a shoulder due to the presence of two, largely overlapping distributions. Fitting two Gaussian distributions reveals a small diameter distribution with comparatively few counts at 2.63 ± 1.95 nm, which is very similar to the small diameter distribution for the 4 equivalent functionalization. The larger diameter distribution however is significantly shifted to smaller diameters and narrowed compared to the 4 equivalent analysis, with an average diameter of 6.74 ± 3.45 nm. Due to the large overlap of the two distributions, no efficient separation is to be expected through centrifugation. This can be readily seen from TEM images recorded on the material after purification (figure 24, F-I). With bare eye, the nanosheets after purification are almost indistinguishable in TEM from the nanosheets removed during purification. Only in the statistical analysis, the aforementioned shoulder in the statistical data is now more intense and clearly distinguishable as a second separate distribution (figure 24, J). Position and width of the small diameter distribution is virtually unchanged in all statistic evaluations indicating that the formation of these small diameter nanoparticles is largely independent of the amount of chloroauric acid added. Since the observation, that the small diameter nanoparticles are predominantly found around nanosheet edges or terraces, was found in the case of the functionalization with 4 equivalents chloroauric acid and also published earlier,[160] it is very well possible that the small particles are solely the product of reactions of the chloroauric acid with edge regions of the nanosheets. These apparently reach a finite size after which no significant further growth takes place. Since the nanoparticles stay attached to the nanosheet, passivation of the edge region is the most likely cause for this, resulting in a monodisperse distribution with small diameters. The diameter distributions of the larger nanoparticles however show a pronounced dependency on the amount of chloroauric acid used, with the diameter of the nanoparticles as well as the width of the diameter distribution increasing for increasing amounts of chloroauric acid. Since the small nanoparticles are assumed to be the result of an attack of the WS_2 edge

region by the oxidant, it seems intuitive that a basal plane attack of the oxidant is the source of the large diameter nanoparticles.

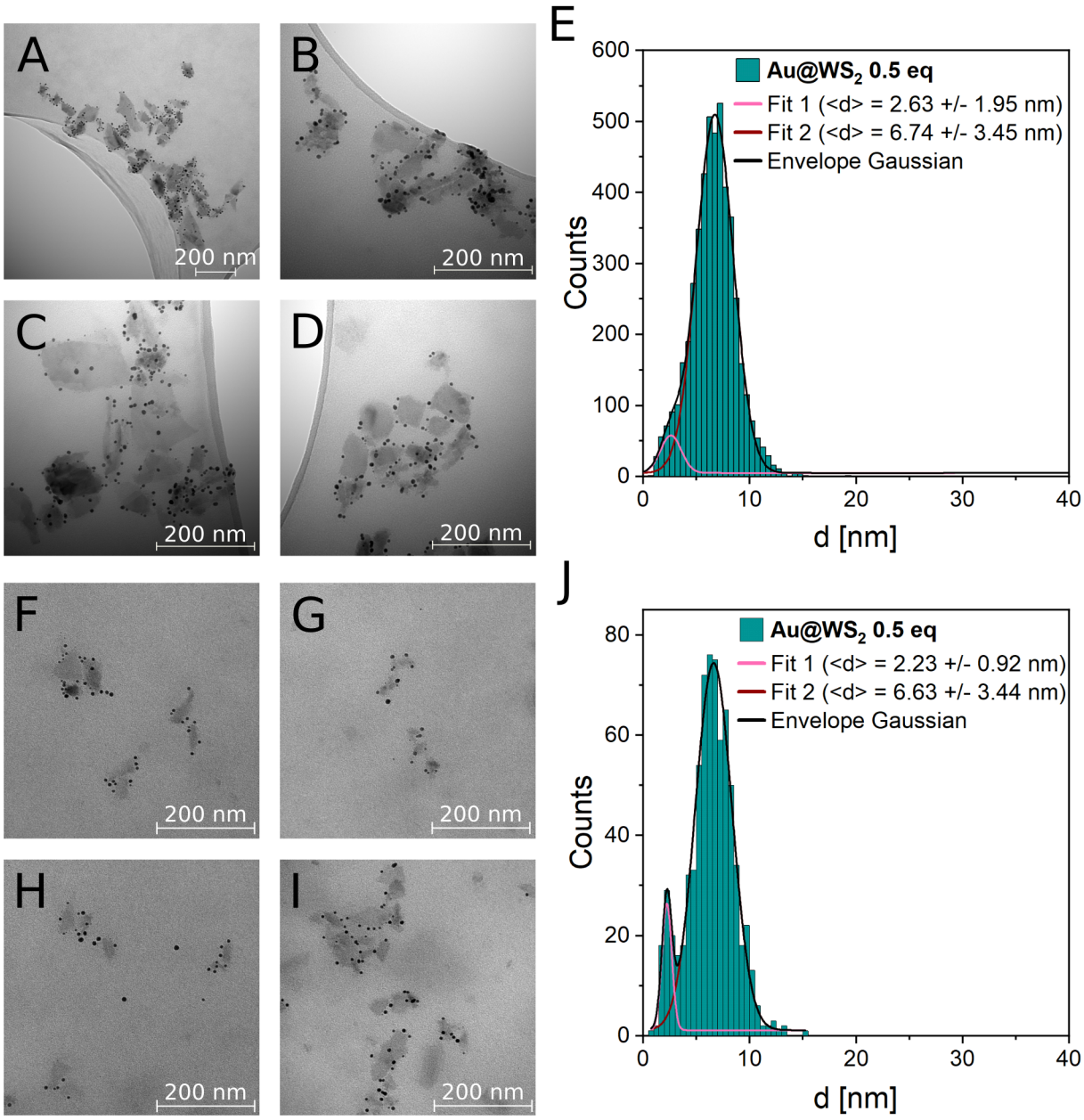

Figure 24: A-D) Transmission electron microscopy images of gold-functionalized WS_2 nanosheets removed during purification for 0.5 equivalents of chloroauric acid. E) Statistical evaluation of gold nanoparticle diameters in A-D. F-I) Transmission electron microscopy images of gold-functionalized WS_2 nanosheets after purification. J) Statistical evaluation of gold nanoparticle diameters in F-I. All shown images except A were recorded with 120 kV acceleration voltage at x50 000 magnification. A was recorded with 120 kV acceleration voltage at x20 000 magnification. Statistical data are fitted with two Gaussians. Peak centers of the individual Gaussians were taken as average gold nanoparticle diameter $\langle d \rangle$ and full width at half maximum was taken as standard deviation.

As mentioned above, the efficiency of monolayer enrichment visible in the optical properties after purification increases with increasing amounts of chloroauric acid

employed and therefore apparently coincides with the removal of nanosheets functionalized with big gold nanoparticles. It appears as if monolayers do not experience the formation of larger gold nanoparticles on their basal plane and are therefore not removed during the purification process. However, this seems counter intuitive as the reactivity of a nanoparticle increases with decreasing size and increasing surface area to volume ratio. With this in mind, monolayers contained in the dispersion should be more prone to the oxidation. In contrast, it was previously shown that the gold decorated monolayers separated after purification show no significant signs of oxidation.[160] In order to explain the possible link between all these observations, further factors have to be taken into consideration as is discussed below.

4.2 Influence of surfactants

When working with dispersions of layered materials, a common issue is often dispersion stability. Among various different stabilization techniques known in literature, surfactant stabilization is a prominent method able to impede restacking of exfoliated layered nanomaterials. The surfactant molecules enable this through adsorption to the nanosheets surface and therefore they must be a point of consideration when discussing heterogeneous functionalization reactions. For surfactants typically employed for stabilization, two different types of surfactants are commonly utilized: linear and facial amphiphiles.

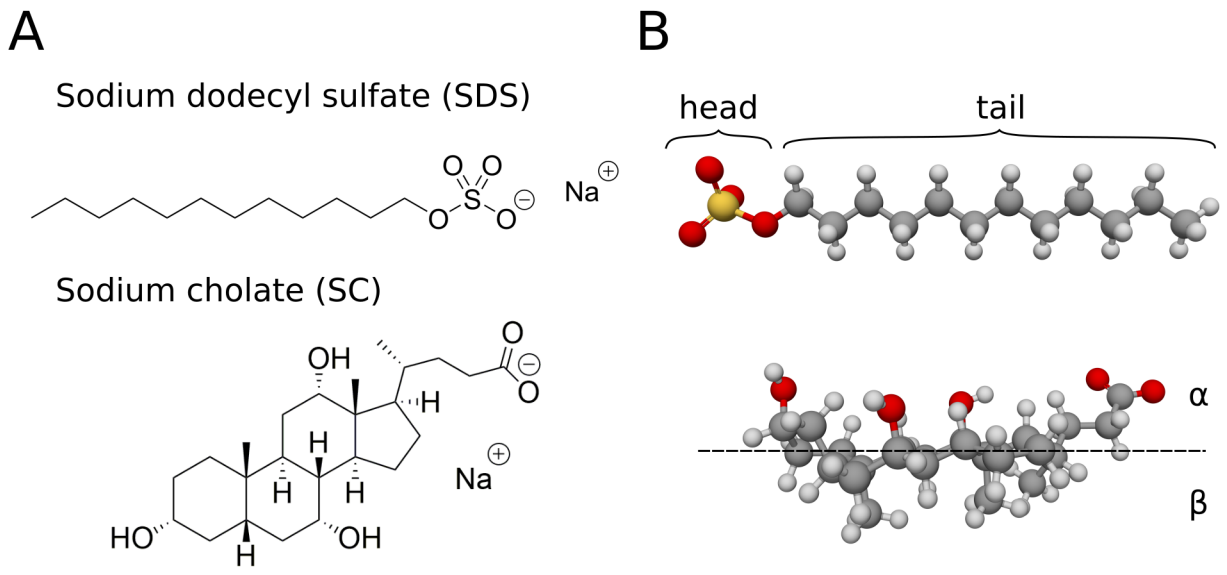

Figure 25: A) Molecular structures of sodium dodecyl sulfate (SDS, top) and sodium cholate (SC, bottom). B) Schematic to visualize structural motifs of linear and facial amphiphiles. Head and tail for linear amphiphiles as well as α and β face for facial amphiphiles are emphasized. Counter ions are omitted for clarity.

Linear amphiphiles, such as sodium dodecyl sulfate (SDS, figure 25, A, top) usually feature a structural unit of high polarity (typically sulfate or carboxylate groups), commonly

referred to as *head* and another structural unit of lower polarity referred to as tail, typically composed of long alkyl chains (figure 25, B, top). In contrast, facial amphiphiles, such as sodium cholate show a more planar structure, commonly derived from cyclopentanoperhydrophenanthrenes (or sterane compounds, figure 25, A, bottom) where the change in polarity occurs across the plane in the molecular structure (figure 25, B, bottom). One face of the sterane carbon backbone features multiple hydroxide groups, rendering this so-called *α face* highly polar, whereas on the opposing face only methyl groups are found. Therefore the so-called *β face* is of lower polarity.

Due to the high anisotropy present in two-dimensional nanomaterials, differences in surfactant interactions with the nanomaterial can be hypothesized in particular when comparing different types of surfactants. In order to probe this behavior, the gold functionalization reaction was applied in the following on WS_2 nanosheets exfoliated from aqueous SDS solution and the results compared to the functionalization in SC. The experimental procedure for functionalization was kept comparable, although only one WS_2 dispersion (0.4 - 30k g) was produced by liquid cascade centrifugation for decoration instead of three size-selected dispersions (*L*, *M*, and *S*) investigated above. After addition of chloroauric acid to a WS_2 dispersion in SDS solution a change of color to dark blue can be observed which is in stark contrast to the intense red for functionalization in aqueous SC solution. Extinction spectroscopy of the material removed after workup in figure 26, A (teal trace) reveals a pronounced and extremely broad peak ranging from 500 to 1000 nm that can be assigned to the surface plasmon resonance of gold nanoparticles. The red-shifted plasmon compared to the results obtained in SC, suggests that the gold nanoparticle diameter must have increased significantly. Furthermore, due to the increased peak width, either aggregation of the particles occurs or much broader size distributions are produced, which overall results in the blue color observed for the dispersion. After removal of the aggregated material the spectral profile of WS_2 is not reproduced in the S*tock* samples (dark green trace) and no sharp surface plasmon resonance peak of defined gold nanoparticles is visible. Furthermore, there is a significant onset of extinction in the UV region of the spectrum for the removed reaction mixture supernatant (figure 26, A, black trace) which cannot be assigned to the characteristic chloroauric acid absorption but rather to water soluble oxidation products after functionalization. Even after purification, the characteristic profile of WS_2 cannot be resolved in the extinction spectra after functionalization using 4 equivalents (figure 26, B, orange trace). Instead, there is an increase in extinction in the UV region usually observed when significant oxidation of the material takes place. This is especially visible in direct comparison with the starting material (black trace). Although there are slight differences in extinction ratios for the material removed during purification and the purified material, the

overall shape of the extinction spectrum does not change much (comparison orange and teal trace).

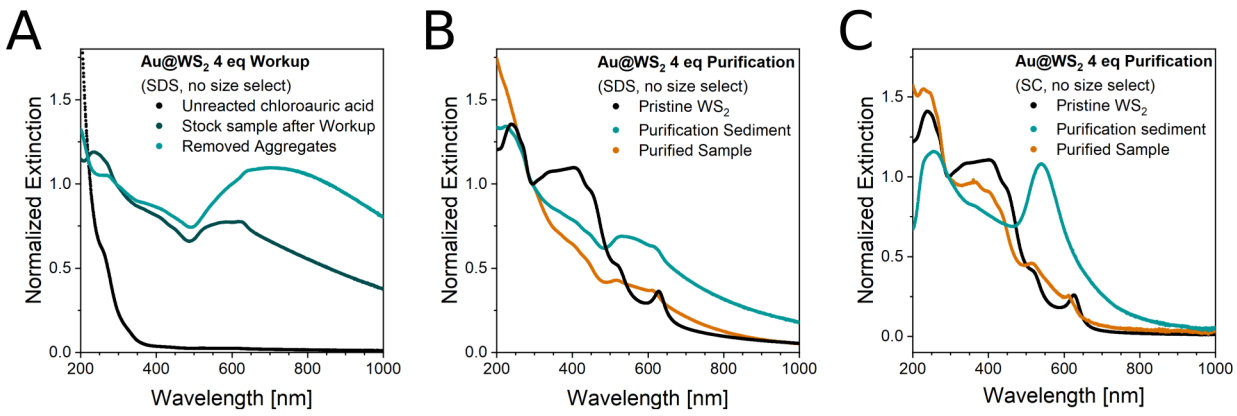

Figure 26: A) Extinction spectra of samples produced during workup of the reaction mixture after functionalization in SDS. The trace denoted as Unreacted chloroauric acid was normalized to the extinction at 226 nm, all other traces were normalized to the extinction at 294 nm. B) Extinction spectra of samples produced during purification of functionalization in SDS, normalized to the extinction at 294 nm. C) Extinction spectra of samples produced during purification of functionalization in SC, normalized to the extinction at 294 nm.

Since no size selection was performed for the starting material in SDS, average length $<L>$ and layer number $<N>$ for the sample should differ from what was outlined in the previous chapter for SC. For direct comparison, functionalization of non-size-selected material in SC (0.4 - 30k *g*) was therefore conducted and the corresponding extinction spectra are displayed in Figure 26, C. Again, the spectral profile of WS_2 can be efficiently reproduced after purification (comparison orange and black trace) while a relatively sharp surface plasmon resonance peak is visible for the material removed after purification (teal trace). This can be seen as a clear indication that the surfactant employed during functionalization has a significant impact on the functionalization reaction.

For further investigation, the impact of gold functionalization on the WS_2 nanosheets is visualized using electron microscopy. In figure 27, A-B transmission electron microscopy images of gold-functionalized nanosheets removed during purification can be seen. Gold particles can be clearly distinguished from WS_2 due to differences in contrast. As expected from the position and width of the plasmon resonance, the nanoparticle size is increased and big, ill-defined gold clusters are seen alongside WS_2 nanosheets that appear multilayered and disrupted at edges. Edge disruption is more easily visible in scanning electron microscopy (figure 27, C): multiple gold clusters can be identified and holes are visible in the nanosheet structure. This points towards oxidative damage at the nanosheets upon functionalization and a breakdown of the mechanism that produces small, monodisperse gold nanoparticles around nanosheet edges, which was observed in the case of SC. Transmission electron microscopy of nanosheets after purification shows

mostly free gold nanoparticles likely solubilized by SDS surfactant (figure 27, D), with intermediate diameters and a seemingly monomodal distribution (figure 27, E). Nanosheets however are barely visible in the purified material. This explains signs of oxidation and the lack of WS_2 nanosheet signals in extinction spectroscopy.

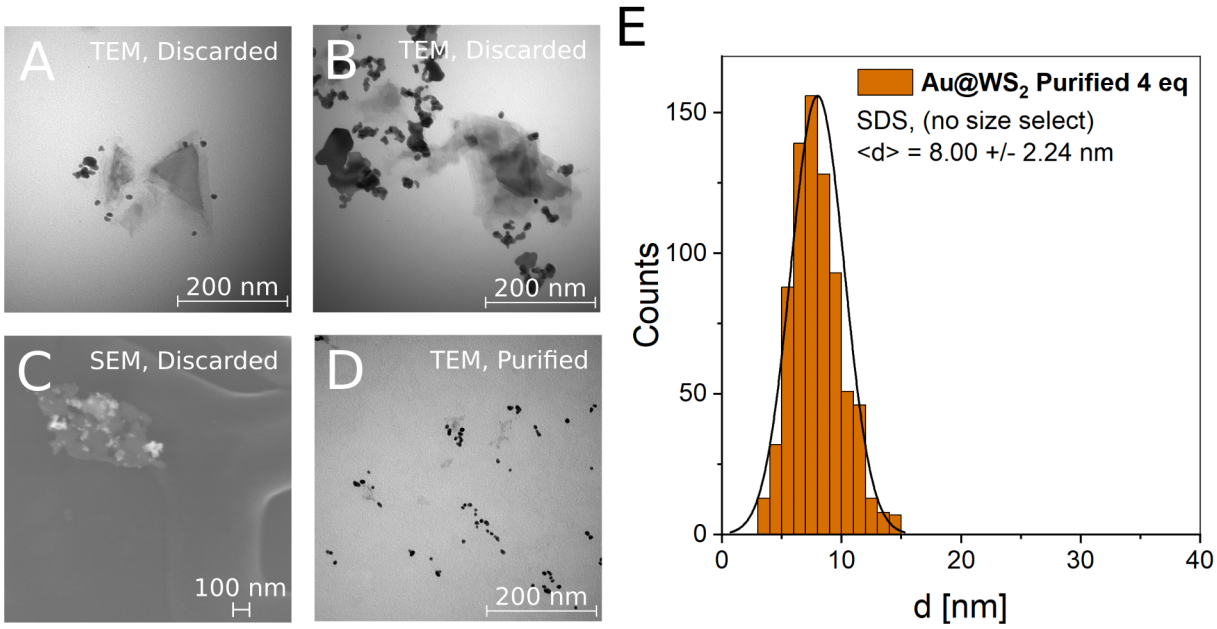

Figure 27: A-B) Transmission electron microscopy images of gold-functionalized WS_2 nanosheets removed during purification for functionalization in SDS with 4 equivalents of chloroauric acid. C) Scanning electron microscopy images of gold-functionalized WS_2 nanosheets removed during purification for functionalization in SDS with 4 equivalents of chloroauric acid. D) Transmission electron microscopy images of gold-functionalized WS_2 nanosheets after purification for functionalization in SDS with 4 equivalents of chloroauric acid. E) Statistical evaluation of gold nanoparticle diameters in D. All TEM images were recorded at 120 kV acceleration voltage with x50 000 magnification. The SEM image was recorded at 15 kV acceleration voltage with x50 000 magnification.

In order to confirm oxidation as a possible source of degradation, X-ray photoelectron spectroscopy (XPS) was employed to determine oxidation states of the elements in question. In figure 28, A an XPS survey spectrum of gold-functionalized WS_2 in SDS prior to workup is shown. The core levels of interest gold (B), sulfur (C) and tungsten (D) are extracted and fitted using doublets with a fixed peak area ratio. As expected, only gold in the oxidation state 0 is found, due to the formation of elemental gold nanoparticles and removal of chloroauric acid through washing. In the sulfur *2p* core level spectrum, however, multiple peaks are visible, which can be deconvoluted into three doublet pairs. The doublet pair with the lowest binding energies (figure 28, C, brown fits, $2p_{3/2}$ at 161.1 eV and $2p_{1/2}$ at 162.3 eV) corresponds to sulfur in the oxidation state -II and can be assigned to pristine WS_2. The overall low intensity of this signal indicates that a large portion of the initial material is converted on the surface. Shifted to slightly higher binding energies are sulfur cores bound to gold atoms (red fits, $2p_{3/2}$ at 162.4 eV and $2p_{1/2}$ at 163.6 eV), which is expected due to the high bond strength of the Au-S-bond. The last

doublet pair can be assigned to highly oxidized sulfur species in the oxidation state +VI (orange fits, $2p_{3/2}$ at 168.8 eV and $2p_{1/2}$ at 170.0 eV) based on the high binding energy of the signal. This signal clearly dominates the spectrum in intensity and therefore shows that severe oxidation of sulfur atoms took place.

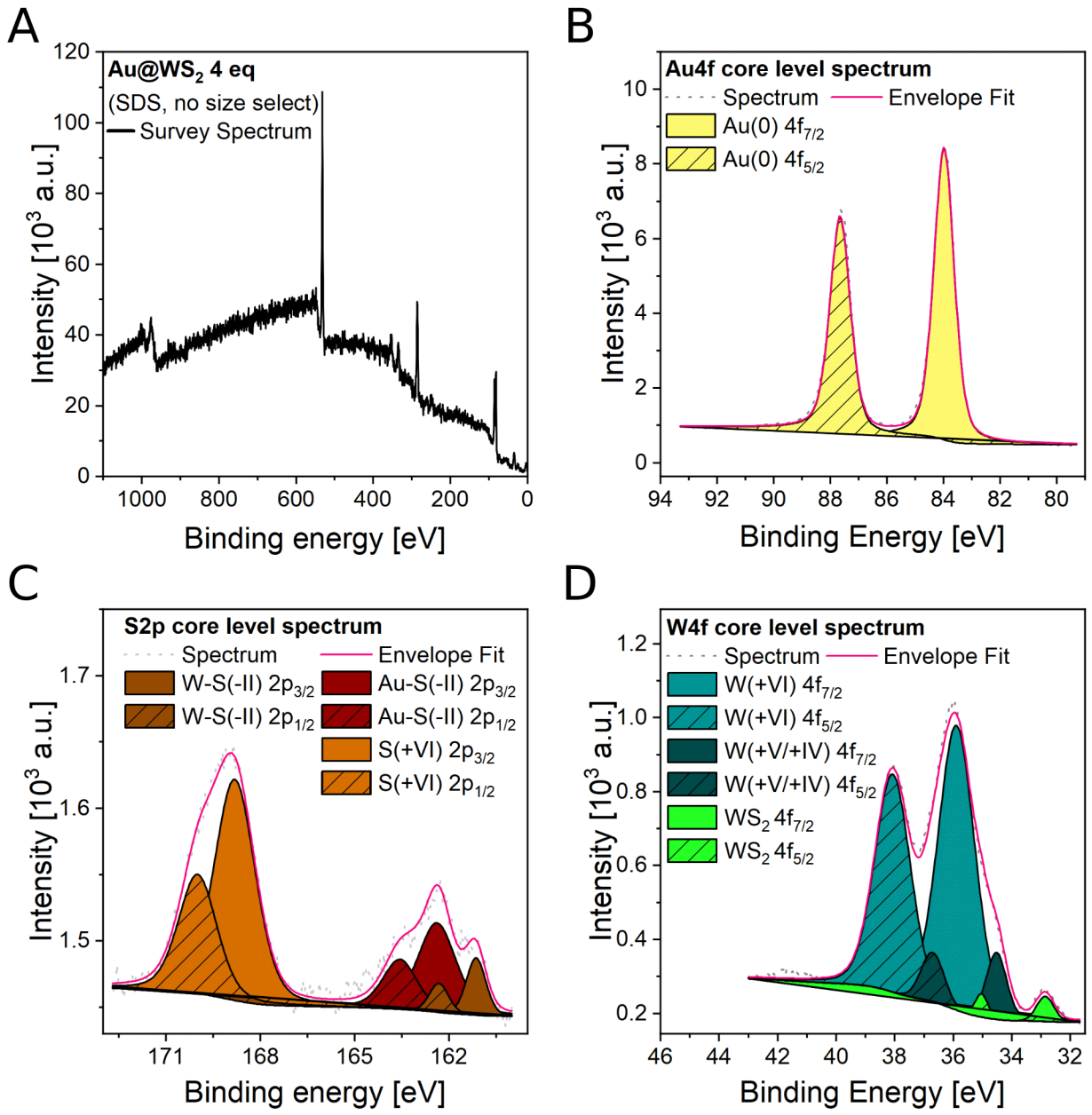

Figure 28: A) XPS survey spectrum of gold-functionalized WS_2 filtered from 20 ml of the reaction mixture prior to workup in SDS and consecutive intense washing with water. The spectrum was measured using a monochromated Al Kα line (1486.7 eV). B-D) Regions of core levels of gold (Au 4f core level, B), sulfur (S 2p core level, C), and tungsten (W 4f core level, D). Respective peaks were fitted using doublets with a fixed peak area ratio.

Similar observations can be made for the tungsten core level spectrum (figure 28, D). The contribution of the lowest binding energy doublet pairs assigned to tungsten in pristine WS_2 (bright green fits, $4f_{7/2}$ at 32.9 eV and $4f_{5/2}$ at 35.1 eV) is in the

clear minority, in contrast to the dominant signal at highest binding energies (teal fits, $4f_{7/2}$ at 36.0 eV and $4f_{5/2}$ at 38.1 eV) corresponding to heavily oxidized tungsten in the oxidation state +VI. In literature, oxidized Mo(+VI) species were identified after chloroauric acid treatment of chemically-exfoliated MoS_2 and the production of molybdic acid was suggested as a possible compound formed during oxidation.[173] The doublet at intermediate binding energies (dark green fits, $4f_{7/2}$ at 34.5 eV and $4f_{5/2}$ at 36.7 eV cannot be assigned unambiguously, but owing to its binding energies it may be assigned to an intermediate, not completely oxidized tungsten species. Similar assignments have been made previously for CVD synthesis of WS_2 nanosheets from WO_3 precursors.[219] It is therefore evident from XPS that severe oxidation of the material took place, indicating that the reduction of chloroauric acid is fueled by significant oxidation of the WS_2 starting material.

In order to assess the degree of oxidation of the starting material, a screening of various amounts of chloroauric acid with a fixed amount of WS_2 is conducted. This allows for estimation of the reactant consumption as well as visualization of the effects of progressing oxidation on the starting material using extinction spectroscopy. For that, small scale functionalization reactions were performed with a fixed amount of WS_2 and varying amounts of chloroauric acid in different surfactant solutions. The reaction supernatant is removed via centrifugation and extinction spectroscopy conducted on it (figure 29, A-B). At high amounts of oxidant the characteristic absorption peaks of chloroauric acid are visible (figure 29, A-B, 6, 7 and 8 eq) increasing in intensity with increasing stoichiometry ratios. At lower chloroauric acid equivalents, where chloroauric acid absorption is absent, an increasing onset in the UV region, most probably owing to water soluble oxidation products, is observed. According to Lambert-Beers law, determination of molecular concentrations is possible once the extinction coefficient at a given wavelength is known and with this information, the amount of chloroauric acid consumed can be calculated. Therefore the extinction coefficient in chloroauric acid is determined as outlined in Appendix 8.2. Consumption is then expressed as portion of reacted in percent based on equation 16.

$$P = \left(1 - \frac{c}{c_0}\right) \cdot 100\,\% \tag{16}$$

P is the portion of reacted, c the concentration measured from extinction and c_0 the starting concentration of the reactant calculated from reaction volume and amount of chloroauric acid added. The result of this calculation from extinction spectra shown in figure 29, A-B are displayed in figure 29, C-D using both SC (figure 29, A, C) and SDS (figure 29, B, D) as surfactant.

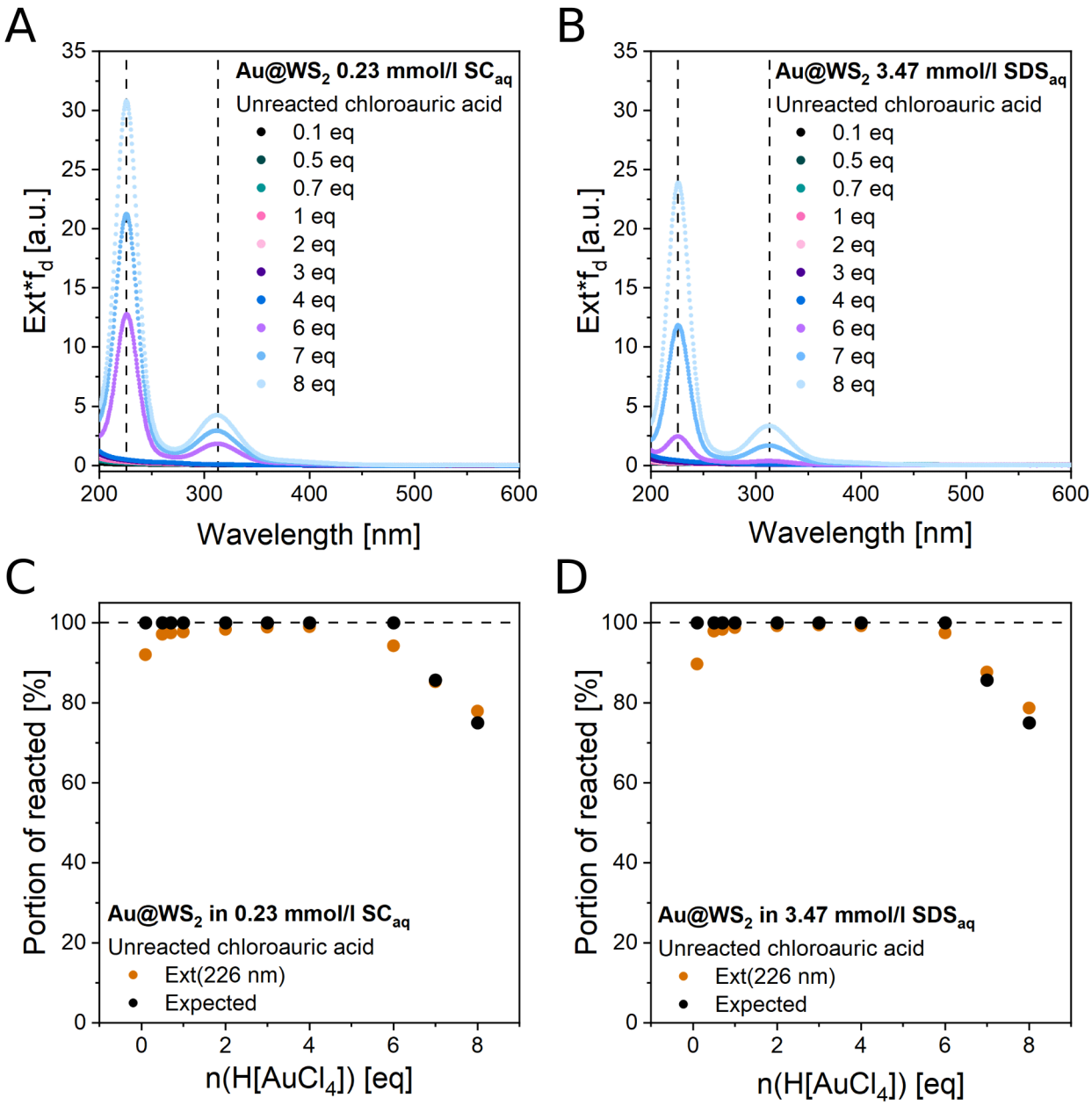

Figure 29: A-B) Extinction spectra of unreacted chloroauric acid in the removed reaction mixture supernatant for reaction in aqueous SC (A) and SDS (B) solution multiplied with the dilution coefficient f_d for varying amounts of chloroauric acid used. Extinction maxima are indicated using dashed lines. C-D) Quantification of the portion of reacted derived from the extinction at 226 nm in A for SC (C) and in B for SDS (D) respectively (orange traces in C and D) as well as consumption based on theory (black traces in C and D). Complete conversion is indicated using dashed lines.

Consumption of chloroauric acid is near unity up to 6 equivalents of chloroauric acid used after which consumption drops for both surfactants. Based on this behavior, 6 equivalents of chloroauric acid is identified as stoichiometric point and a reaction formula derived from this information is hypothesized in figure 30.

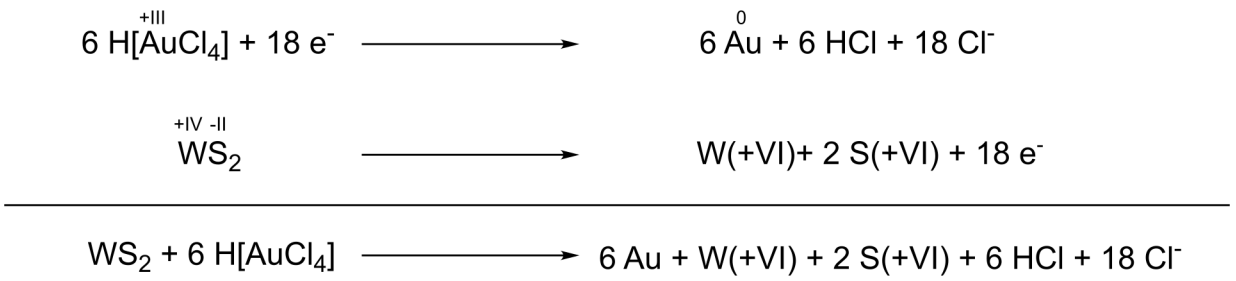

Figure 30: Reaction formula postulated for the gold functionalization reaction based on the information outlined above. Reduction and oxidation half reaction are detailed on the top and complete reaction on the bottom. W(+IV) and S(+IV) species are left blank since an assignment is not possible based on the available data.

This hypothesis entails complete oxidation of the valence shell electrons of tungsten and sulfur, respectively, in order to consume 6 equivalents of chloroauric acid. The produced W(+VI) and S(+VI) species are intentionally not specified since a precise assignment is not possible based on the experimental data available. However, formation of sulfates and tungstates seems likely in an aqueous environment and would explain the presence of water soluble species in extinction spectroscopy. For corroboration, the theoretical consumption based on this stoichiometry is added in figure 29, C-D, black traces. Remarkable agreement with the experimental portion of reacted derived from extinction spectroscopy is evident with the exception of low amounts of chloroauric acid where the concentration in solution is overestimated due to the onset of extinction in the UV region mentioned earlier.

Such an oxidation would result in a significant loss of WS_2 from the dispersion. Therefore, *Stock* samples after workup as well as the removed aggregated material are investigated in extinction spectroscopy (figure 31). Extinction spectra of S*tock* samples after workup in aqueous SC are displayed in figure 31, A. With increasing amounts of chloroauric acid, the surface plasmon resonance of gold nanoparticles becomes increasingly dominant (see Appendix 8.3), whereas the extinction at low wavelengths (between 200 and 500 nm) decreases indicating minor loss of the underlying WS_2 material. The spectral profile in that region becomes less pronounced indicating progressing oxidation. For SDS however, intense loss of material can be observed with increasing amounts of chloroauric acid until almost no material remains in the S*tock* sample after workup (figure 31, B). The spectral profile of WS_2 quickly deteriorates as well, while no pronounced gold nanoparticle surface plasmon resonance is visible. Apparently both *Stock* dispersions increasingly lose material upon increasing oxidation with chloroauric acid, more pronounced for SDS compared to SC. In comparison, the aggregated material removed after functionalization in SC shows an inverse trend with increasing amounts of material removed for increasing amounts of chloroauric acid

(figure 31, C). It can be concluded, that material lost in the S*tock* sample is mostly transferred to the removed aggregates.

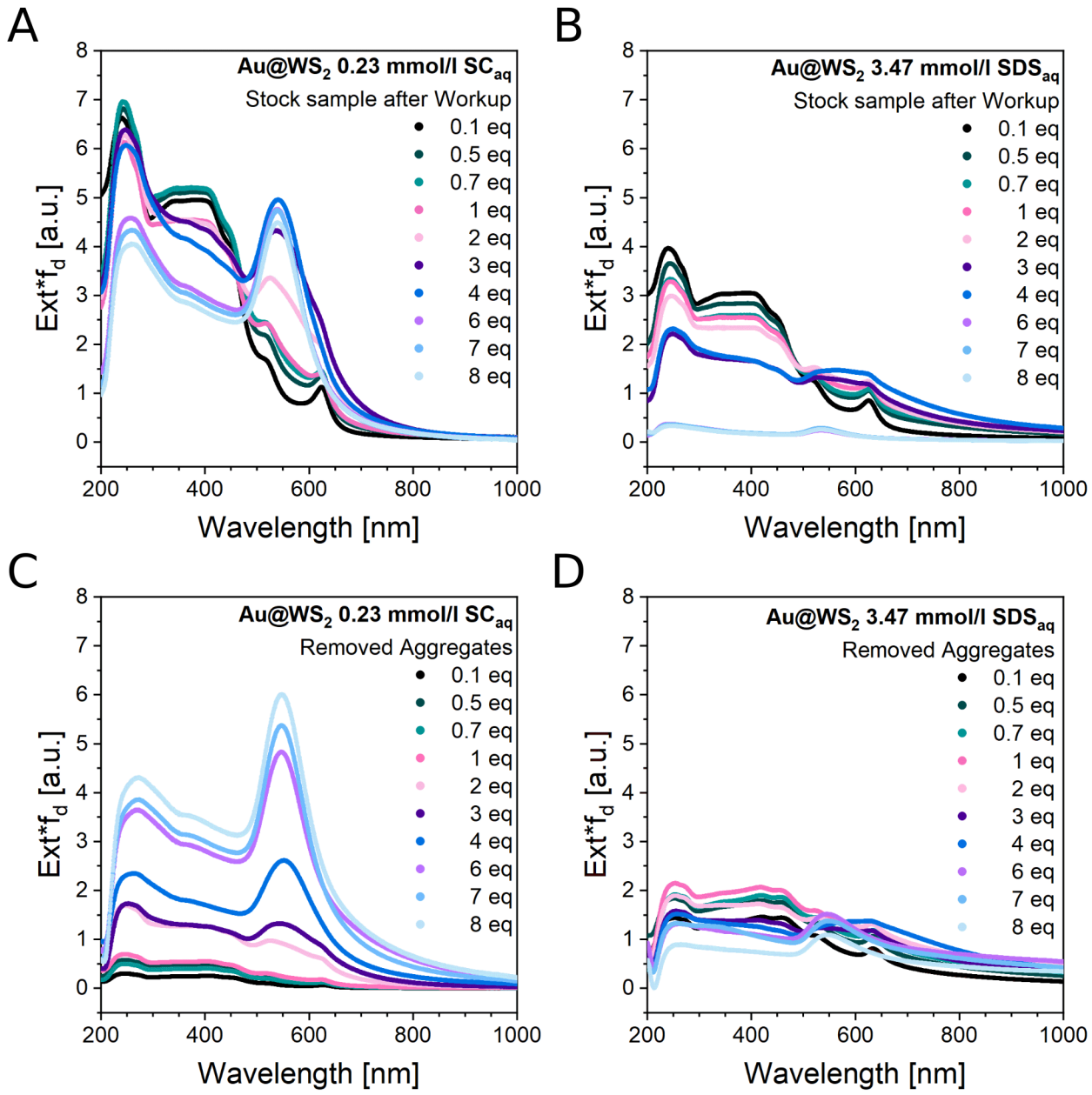

Figure 31: Extinction spectra multiplied with dilution coefficient for Stock samples after workup in SC (A) and SDS (B) as well as removed aggregated material in SC (C) and SDS (D) for varying amounts of chloroauric acid employed.

For SDS however, the material removed during purification increases slightly for amounts of chloroauric acid up to one equivalent before it decreases again with increasing amounts of chloroauric acid. This suggests that in SDS much more material is lost and solubilized in comparison to SC. It appears that the oxidation pathway differs for different surfactants, with some degree of structural integrity maintained in SC, whereas structural degradation is pronounced in SDS.

Since the surfactants themselves adsorb to the nanosheet surface and the reaction itself is most probably the same for both surfactants as shown in figure 29, kinetic control of the surfactants employed can be hypothesized, in which the surfactant type, either facial or linear, governs the dominant reaction pathway and therefore impacts the result of the functionalization. This hypothesis is schematically shown in figure 32.

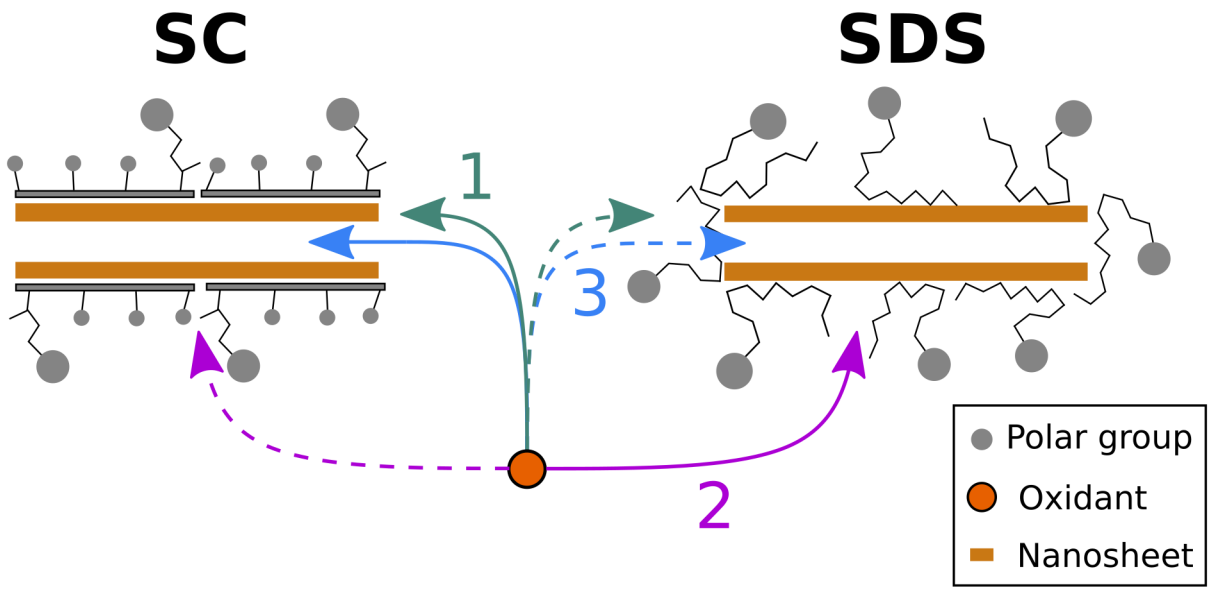

Figure 32: Schematic of the hypothesized reaction mechanism model. The dominant reaction pathways are indicated with solid lines while the suppressed pathways are indicated with dashed lines.

A molecular reagent has multiple pathways along which a heterogeneous attack to the surface of a surfactant covered nanosheet can occur: either on the nanosheet edges (figure 32, pathway 1) or the basal plane, whereas for the latter attack of the basal plane exposed to the aqueous environment (figure 32, pathway 2) or the basal plane in the intralayer space (figure 32, pathway 3) can be distinguished. Attacks to the basal plane in the intralayer space can only occur with bi- and fewlayered material (if the reactant can penetrate the intralayer space) and can therefore be distinguished from monolayered material. From a structural point of view, sodium cholate with its rigid carbon backbone is better suited for basal plane adsorption whereas SDS might be less restricted with its adsorption preferences. If we assume dense packing of SC on the basal plane of a WS_2 nanosheet (figure 32, left) then attacks to the basal plane along pathway 2 get suppressed and pathway 1 and 3 become dominant. The reaction products are exclusively edge-decorated monolayers as well as basal plane and edge-decorated bi- and fewlayered nanosheets, which can then be efficiently separated through centrifugation. In SDS however, edges are more easily covered while basal plane coverage becomes less efficient (figure 32, right). This results in oxidation pathway 1 and 3 being suppressed and pathway 2 becoming the dominant reaction pathway and therefore significant basal plane

oxidation without distinguished functionalization of mono- and multilayered nanosheets and reduced edge decoration. For basal plane oxidation, structural degradation is more likely compared to edge decoration as passivation effects through adhesion of gold nanoparticles impede further edge oxidation.

The basic assumption for this hypothesis is that different surfactants employed show different adsorption preferences. However, visualization of physisorbed organic molecules through imaging methods is not trivial and therefore an indirect approach is necessary to confirm this. The adsorbed surfactants are ionic in nature which leads to electrostatic stabilization of the nanosheets. The charges introduced to the WS_2 nanosheet surface respond to external electrical fields and therefore can be probed in ζ potential measurements. For that, WS_2 dispersions were exfoliated in aqueous SC solution and transferred into either aqueous SC or SDS solution before measurement. This procedure serves the purpose of producing comparable dispersions in different surfactant solutions and prevention of batch-to-batch variations in exfoliation.

Normalized extinction spectra of such transferred samples are shown in figure 33, A-B. At first glance, the progression with size is comparable across surfactants with negligible differences in both sample sets. This suggests that the transfer approach is suitable for the production of comparable dispersions. On closer inspection of the spectral region around the A exciton signal shown in the insets, minuscule peak shifts are visible which are more pronounced for smaller nanosheets. To resolve these shifts more clearly, the second derivative of the extinction in the spectral region around the A exciton signal with respect to the photon energy of the incident light is shown in figure 33, C-D.

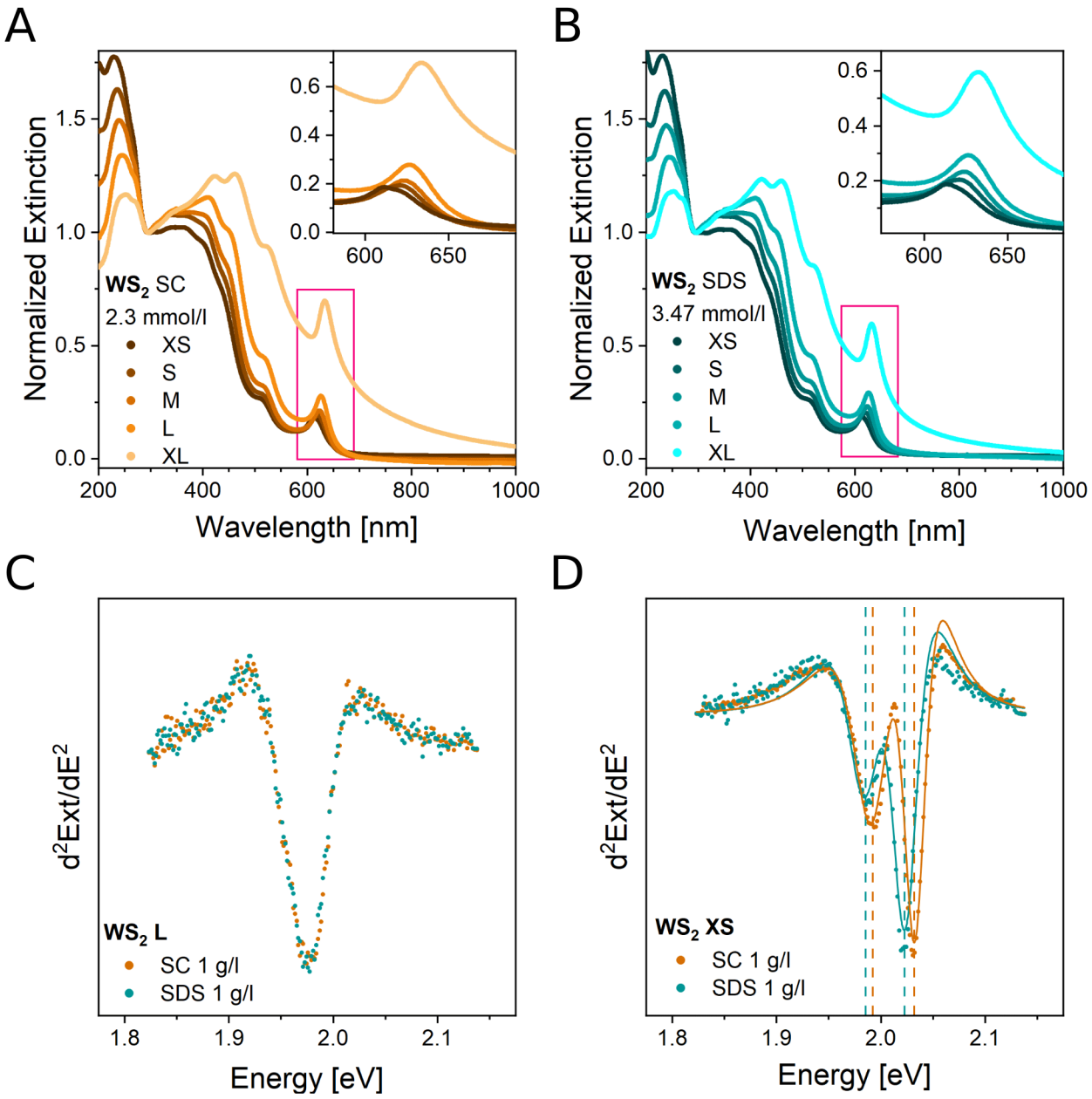

Figure 33: A) Extinction spectra of WS_2 nanosheets in 2.3 mmol/l aqueous SC solution for varying nanosheets sizes normalized to the extinction at 294 nm. Inset: enlarged view of the spectral region around the A exciton signal. B) Extinction spectra of WS_2 nanosheets in 3.47 mmol/l aqueous SDS solution for varying nanosheets sizes normalized to the extinction at 294 nm. Inset: enlarged view of the spectral region around the A exciton signal. C) Second derivative of the spectral region around the A exciton signal with respect to the photon energy of the incident light for nanosheets of size L for SC and SDS. D) Second derivative of the spectral region around the A exciton signal with respect to the photon energy of the incident light for nanosheets of size XS for SC and SDS. Samples are labeled with XL for extra-large (0.1 - 0.4k g, $\langle L \rangle = 305$ nm, $\langle N \rangle = 16$), L for large (0.4 - 0.8k g, $\langle L \rangle = 134$ nm, $\langle N \rangle = 7$) M for medium (0.8 - 2k g, $\langle L \rangle = 75$ nm, $\langle N \rangle = 5$), S for small (2 - 6k g, $\langle L \rangle = 49$ nm, $\langle N \rangle = 3$) and XS for extra-small (6 - 30k g, $\langle L \rangle = 34$ nm, $\langle N \rangle = 2$) in order to illustrate changes in relation to the average lateral size $\langle L \rangle$ and average layer number $\langle N \rangle$ of the WS_2 dispersion. $\langle L \rangle$ and $\langle N \rangle$ were determined from extinction spectra in 2.3 mmol/l aqueous SC solution using published metrics.[8]

Figure 33, C shows the second derivative of the A exciton region for *L* nanosheets in SC and SDS. The traces consist of a single peak each, indicating a marginal monolayer content in *L* samples. The curves also show no shift between SC and SDS. Due to the relatively large average layer number $<N>$ of 7, the majority of WS_2 material is located in the inner layers of the nanosheets and therefore does not come in direct contact with the surfactant. For material with significantly reduced average layer number $<N>$ however, significant peak shifts can be observed (figure 33, D). Traces in both surfactants clearly show two peaks assigned to bi- and fewlayered material for the lower energy peak and monolayered material for the high energy peak. Furthermore, traces for nanosheets in SC are clearly shifted towards higher energies, with the peak assigned to monolayered material experiencing a stronger shift compared to the lower energy peak.[3] The latter can be readily explained from the fact, that monolayered material has two faces of the same nanosheet layer in contact with adsorbed surfactants and therefore the peak shift is maximized. The shift itself is most probably related to changes in the dielectric environment of the nanosheets as excitonic transitions are especially susceptible to such changes. However, further interpretation of these shifts is not possible based on the data presented herein: differences in adsorption preferences could cause such shifts as well as different packing densities or intrinsic properties of the molecular structures of surfactants.

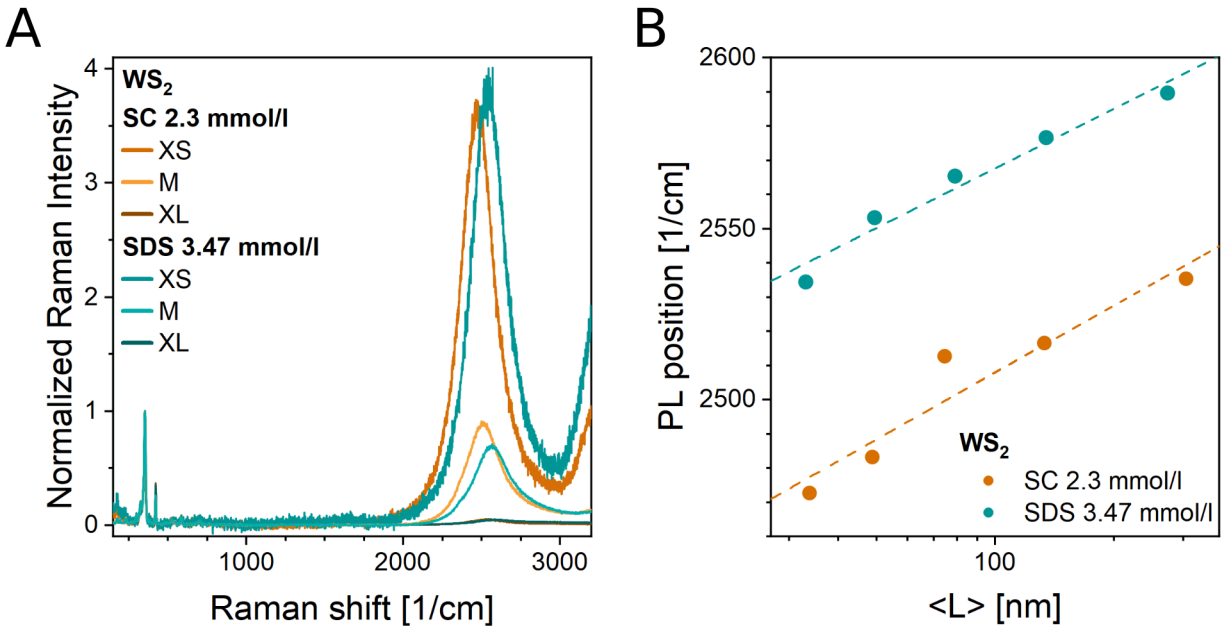

Figure 34: A) Raman spectra (λ_{Exc} = 532 nm) of selected WS_2 nanosheet dispersions in aqueous SC (orange traces) and SDS (teal traces) with varying sizes. Three spectra are averaged each, a baseline was subtracted and the spectra were normalized with respect to the 2LA mode. B) Position of PL peak maximum from Raman spectroscopy plotted versus the logarithm of the average length of nanosheets in dispersion derived from extinction spectroscopy.

3 These solvatochromatic shifts render estimation of monolayer content with metrics developed for SC unreliable in SDS.

Similarly, shifts visible in absorption are transferred to emission as well. Raman/PL spectra of WS_2 nanosheets, excited using a 532 nm laser and normalized to the intensity at the 2LA vibrational mode, are shown in figure 34, A. The PL intensity is roughly the same across the two surfactants again underlining the suitability of the transfer approach in ensuring sample comparability. As expected based on the extinction spectroscopy data described above, the PL peak maximum is shifted for SDS compared to SC consistent across all sizes. This can be readily visualized by plotting the PL peak maximum position against the logarithm of the average lateral nanosheet size (figure 34, B): A powerlaw scaling of PL position plotted versus the logarithm of nanosheet size is evident. The comparable peak shift across all sizes can be rationalized by the fact that only monolayered material is a direct semiconductor with appreciably PL quantum yield. Thus, in contrast to absorption, only monolayered WS_2 is probed. The shift itself can be quantified to a difference of 60 cm^{-1} or 2.25 nm (8 meV) at $<L> = 100\ \mathrm{nm}$.

In order to find a suitable surfactant concentration for ζ potential measurements, a screening of various surfactant concentrations with two different nanosheet sizes was conducted and is shown in appendix 8.4. In order to be able to visualize surfactant selectivity, a sufficiently low concentration was selected where saturation of adsorption sites is not expected. Therefore, surfactant solution concentrations were fixed to 0.23 mmol/l to ensure comparability of SC and SDS dispersions while enabling the observation of size-dependent trends.

For ζ potential measurements, WS_2 dispersions with varying sizes in different surfactant solutions were measured and the cell equilibrated between each measurement. ζ potential distributions averaged across three measurements are depicted in figure 35, A for SC and B for SDS. Distributions are mostly of Gaussian shape (with the exception of sample *XS* in SC, where distribution width is increased significantly) with decreasing intensity for decreasing size due to a decrease in scattering efficiency[4]. In SC, shifts of the distribution maximum to less negative ζ potentials can be observed with decreasing size from *L* to *XS*, whereas in SDS the peak position is largely retained for decreasing nanosheet size. In both dispersions, *XL* samples deviate from this trend but due to the bulk like behavior of this sample and the broad size and thickness distribution, unknown effects may play an additional role.

To ensure precise evaluation of ζ potentials, all individual measurements were fitted with Gaussians (exemplary shown in figure 35, C) and positions of maxima extracted and averaged across three measurements.

4 Phase analysis light scattering is used for determination of the electrophoretic mobility of particles.

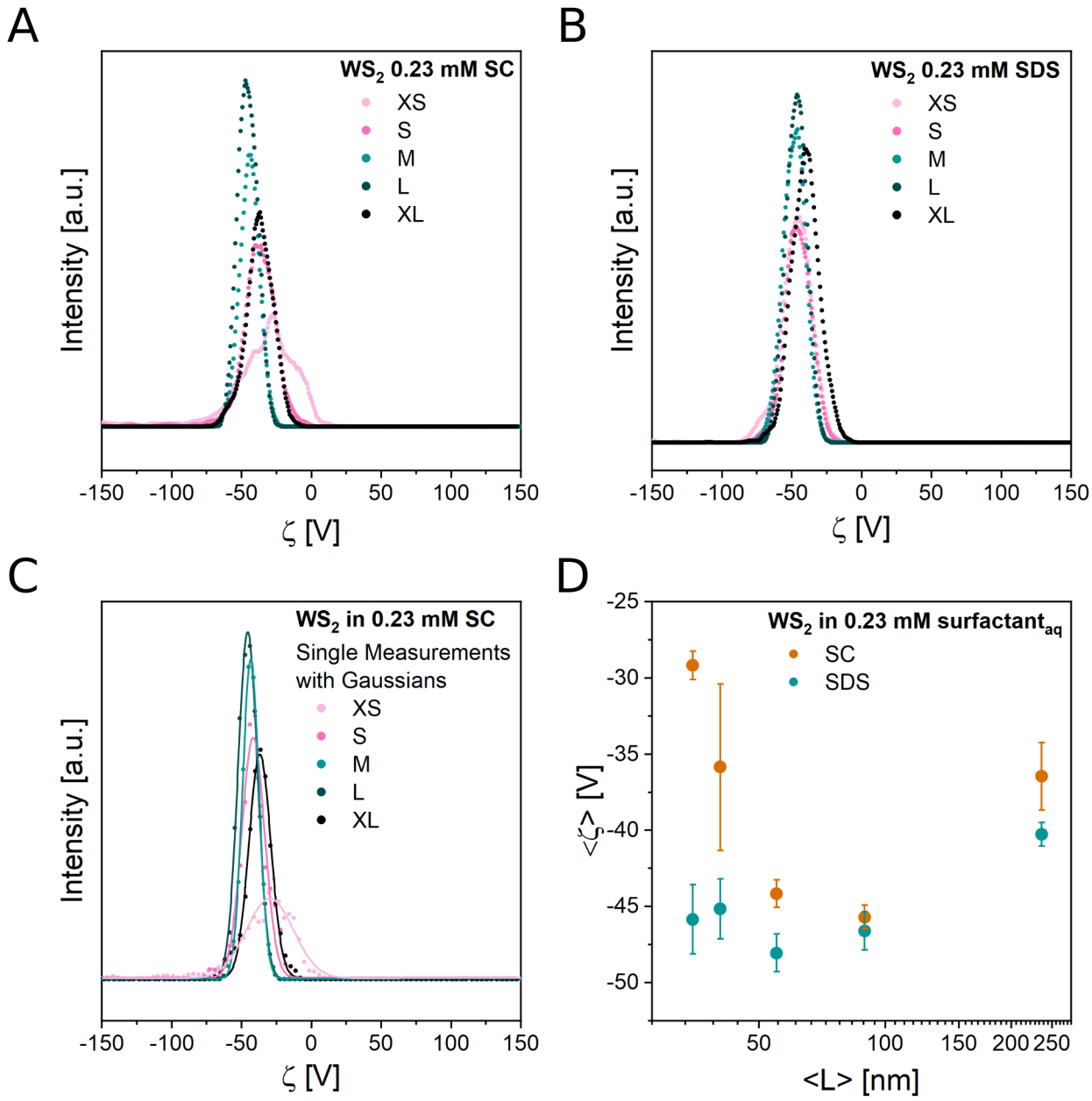

Figure 35: A) ζ potential distributions of WS_2 nanosheets in 0.23 mM aqueous SC solution for varying nanosheet sizes, shown as average of three measurements each. B) ζ potential distributions of WS_2 nanosheets in 0.23 mM aqueous SDS solution for varying nanosheet sizes, shown as average of three measurements each. C) ζ potential distributions of WS_2 nanosheets in 0.23 mM aqueous SC solution for varying nanosheet sizes, not averaged and fitted with Gaussians for extraction of the distribution center. D) Averaged ζ potential distribution maxima for WS_2 nanosheets in SC and SDS. Error bars indicate the standard mean deviation of averaged ζ potential distribution maxima. Samples are labeled with XL for extra-large (0.1 - 0.8k g, $\langle L \rangle = 237$ nm), L for large (0.8 - 2k g, $\langle L \rangle = 89$ nm) M for medium (2 - 4k g, $\langle L \rangle = 55$ nm), S for small (4 - 6k g, $\langle L \rangle = 40$ nm) and XS for extra-small (6 - 30k g, $\langle L \rangle = 35$ nm) in order to illustrate changes in relation to the average lateral size $\langle L \rangle$ of the WS_2 dispersion. $\langle L \rangle$ was determined from extinction spectra in 0.23 mmol/l aqueous SC solution using published metrics.[8]

The dependence of ζ potentials on the nanosheet size is shown in figure 35, D. In accordance with the observations outlined above, a clear trend for samples *L* to *XS* is

evident with samples *XL* deviating from this trend for both surfactants. With decreasing size, ζ potentials become less negative for SC while in SDS ζ potentials are largely independent of size. This behavior can be attributed to the response of the adsorbed surfactant layer to the increasing edge-to-basal plane ratio with decreasing nanosheet size. Basal plane adsorption becomes increasingly difficult and therefore material stabilized in SC, which preferentially adsorbs to the basal plane due to its rigid carbon backbone, suffers from surfactant desorption and the absolute ζ potential decreases accordingly with decreasing size. In contrast, SDS is less restricted with its adsorption preferences and therefore no significant response of the ζ potential to a change in nanosheet size is observed. This interpretation validates our basic assumption about preferential adsorption within the hypothesis depicted in figure 32, which in turn offers an explanation for the monolayer enrichment.

The size-dependent adsorption behavior of SC also suggests a size-dependent reactivity behavior. For sufficiently small WS_2, SC adsorption and the resulting protective basal plane coverage should diminish, and the extracted monolayers should become more defective. To probe this behavior, *S* sheets (5 - 30k *g*) were functionalized using the standard decoration approach and analyzed. Normalized extinction spectra of functionalized and pristine starting material are shown in figure 36, A (orange and black trace, respectively). In contrast to the previously analyzed WS_2 samples, it is evident that the spectral profile of WS_2 is barely visible after functionalization. Although the peak maximum can still be identified for the A exciton signal it appears very weak in comparison to the pristine sample. The observable peak maximum is further blue-shifted and the bi- and few-layer contribution to the signal has seemingly decreased. This is best visualized in the second derivative of the A exciton signal with respect to the energy of the incident light (figure 36, B). The lower energy contribution to the overall signal has decreased significantly upon functionalization rendering the material mostly monolayered. Estimation from area ratios in the second derivative results in a monolayer volume fraction of 93 % and center of mass A exciton position gives an average layer number $<N>$ of 1.003.[8] This increase in monolayer enrichment compared to experiments with *M* sheets described earlier is due to an increased monolayer content in the starting material and therefore expected. In contrast to earlier experiments though, photoluminescence of the material after purification suffers from a significant decrease in the 2LA normalized PL (figure 36, C). PL is a more sensitive probe towards the structural integrity of the basal plane of WS_2 nanosheets and is therefore significantly reduced when damages to the nanosheet occur.[123-125, 220-221] This can be seen as a first indicator that the surfactant mediated basal plane protection fails for smaller nanosheets. For visualization of this damages, TEM images of the gold-functionalized dispersion after purification are shown in figure 36, D-F.

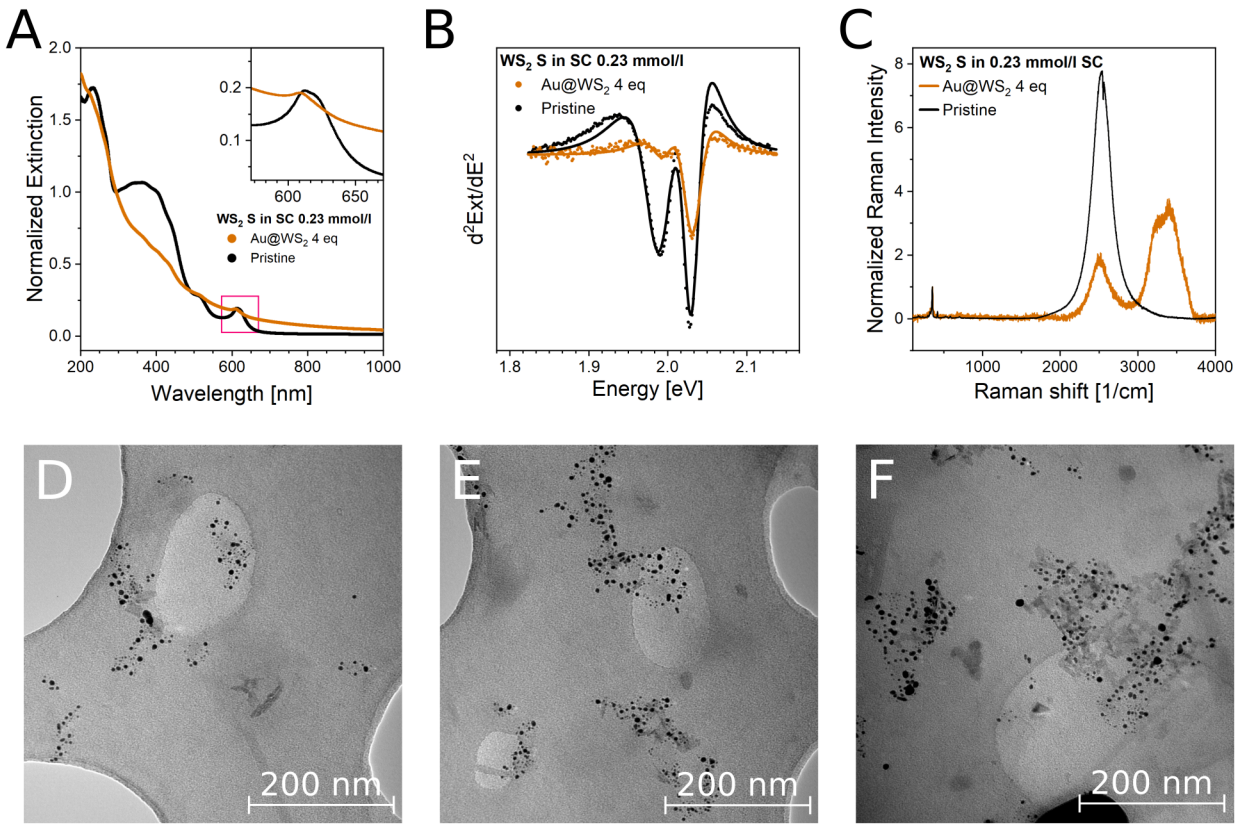

Figure 36: A) Extinction spectra of gold-functionalized S-WS_2 treated with 4 eq of chloroauric acid as well as of the starting material. All spectra are normalized to the extinction at 294 nm. The Inset shows an enlarged view of the spectral region around the A exciton signal. B) Second derivative of the spectral region around the A exciton signal in A with respect to the photon energy of the incident light. The curves are fitted with the second derivative of the sum of two Lorentzians (solid lines). C) Raman spectra of dispersions in A measured on a droplet of the dispersion ($\lambda_{exc} = 532$ nm). Three spectra are averaged each, a baseline was subtracted and the spectra were normalized with respect to the 2LA mode. Starting material labeled with S for small (5 - 30k g) was evaluated to contain $\langle L \rangle = 37$ nm and $\langle N \rangle = 2$. $\langle L \rangle$ and $\langle N \rangle$ were determined from extinction spectra using published metrics.[8] D-F) *TEM images of gold-functionalized S-WS_2 after purification recorded at 120 kV acceleration voltage with x50 000 magnification.*

Although the material is mostly monolayered according to optical spectra, big gold nanoparticles alongside small nanoparticles at edges are frequently found on the nanosheets. Based on the observations detailed in chapter 4.1 the presence of nanoparticles belonging to the large diameter distribution can be seen as an indicator for basal plane oxidation. Therefore, it is evident that the monolayered material for size S is attacked at the basal plane and therefore protection due to SC coverage failed. This is most likely tied to the observation of decreasing ζ potentials with decreasing size for SC and corroborates the hypothesis.

In order to further validate this model, additional experiments are necessary. In the case of SC, basal plane attack along pathway 2 in figure 32 should be suppressed. However, if the formation of larger gold nanoparticles was indeed an indicator for basal

plane oxidation, then basal plane attack must occur in the interlayer space of the nanosheet. This requires mobility of chloroauric acid in the interlayer space of the nanosheet and should also result in gold nanoparticles growing between individual layers of bi- or fewlayered nanosheets. With microscopy imaging, however, visualization of such a behavior is difficult since methods are either surface sensitive (SEM, AFM) or transmissive (TEM), where in the latter case depth information with the necessary resolution is lost for basic imaging. However, gold nanoparticle growth in the interlayer space should have a significant impact on the crystal structure of WS_2 and result in an expansion of the interlayer space as schematically shown in figure 37.

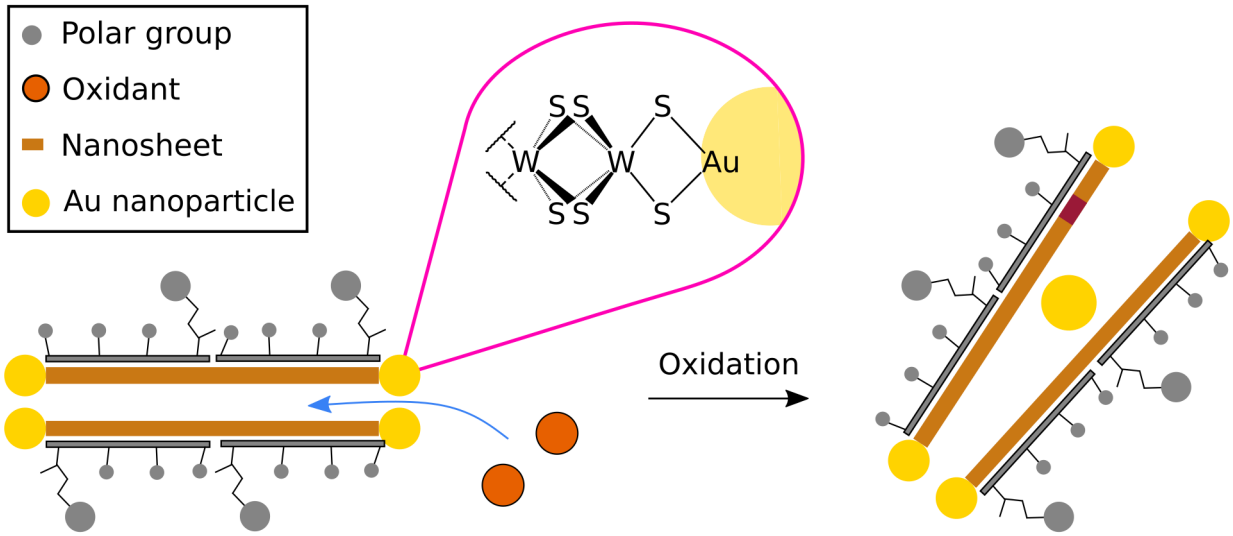

Figure 37: Schematic of the hypothesized reaction mechanism model. Penetration of the oxidant in between two layers of a nanosheet leads to production of gold nanoparticles and subsequent expansion of the interlayer space.

Such an interlayer expansion should be visible in the crystal structure of the decorated material and therefore powder X-ray diffraction (XRD) measurements were conducted. In order to avoid significant damage to the basal plane, which in itself would heavily impact XRD measurement of the material, low amounts of chloroauric acid (0.5 equivalents) were employed for the functionalization. The produced material was washed multiple times with water to remove any surfactants present, transferred to IPA and then dried in vacuo. The respective powder XRD is displayed in figure 38. At first glance, all reflections characteristic for WS_2 (dashed black lines in figure 38) are present in the gold-functionalized sample (orange trace) along with reflections assigned to elemental gold (*face centered cubic*, pink solid lines) without any significant shifts to their glancing angles. However, peak broadening in the gold-functionalized trace is visible.[68, 222] Peak intensities on the other side seem to change relative to each other, as some reflections drop in intensity while others appear unusually enhanced in functionalized WS_2 compared to the reference material after liquid phase exfoliation (teal trace). In general, loss in

intensity alongside peak broadening is expected after exfoliation of layered nanomaterials and directly visible going from non-exfoliated to exfoliated WS_2 (comparison pink and teal trace).[68]

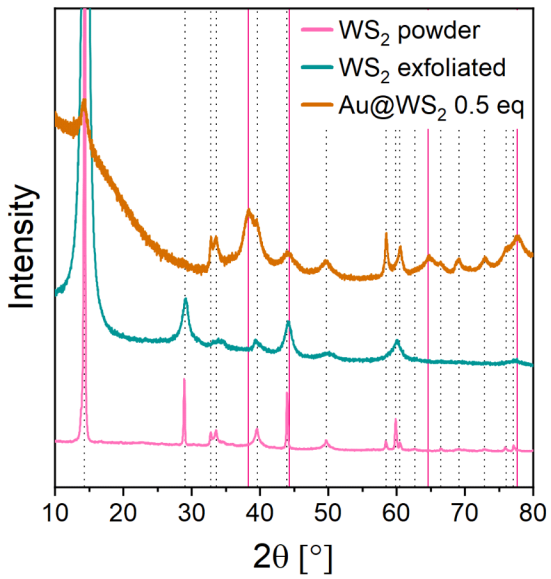

Figure 38: Powder XRD spectra of commercially available WS_2 powder, exfoliated WS_2 and gold-functionalized WS_2. Reference data (pink and teal trace) was provided by Zahra Gholamvand.

Reflections at 32.88° and 33.68° are hard to distinguish in exfoliated WS_2 in contrast to WS_2 powder and gold-functionalized material, with the latter showing even increased intensity. These reflexes may be attributed to the presence of tungsten oxides, which are initially present in the unprocessed bulk material due to atmospheric oxidation and removed during the purification step in liquid phase exfoliation. Oxidation during gold functionalization reintroduces these oxides and therefore reflections with increased intensity reappear. Peak broadening in the spectrum of functionalized WS_2 even surpasses broadening due to exfoliation as readily observable with the (006) reflection at a glancing angle of 44.08°. Furthermore, a significant measurement background is visible for the functionalized material, especially pronounced for low glancing angles. This background is absent in non-exfoliated WS_2 and only slightly visible for exfoliated WS_2. This effect is related to non-Bragg scattering and was previously assigned to the existence of single and fewlayered particles upon mechanical exfoliation.[68] However, this rational cannot be applied here, since the monolayer content in the starting material for functionalization is very low and low amounts of chloroauric acid are not expected to perform any monolayer enrichment, especially not without the purification process. Therefore, this background is attributed to degradation of the crystal lattice due to gold nanoparticles growing in the interlayer space and subsequent decoupling of individual layers of the nanosheets. This is only achievable if chloroauric acid is capable of moving into the interlayer space and hence validates the hypothesis in figure 37. In conclusion, it should be noted that gold

nanoparticles may as well contribute to the non-Bragg scattering background but the expected contribution is insufficient to solely explain these observations.[222]

In order to fully test the hypothesis outlined in figure 32, a final experiment was conducted. If the mechanism that leads to production of defined gold nanoparticles relies on adsorbed surfactants, increasing temperatures should have adverse effects on the reaction outcome in SC. Therefore, in analogy to the chloroauric acid concentration screening experiments described in figures 29 and 31, functionalization with varying amounts of chloroauric acid were carried out at 4 °C, 40 °C, and 60 °C. Again, unreacted chloroauric acid in the supernatant as well as aggregated material is removed and analyzed separately from the S*tock* sample. Note that reaction times were shorter for this experiment compared to the screening experiment presented earlier in order to avoid excessive damage to the WS_2 nanosheets through prolonged heating. Therefore, consumption is likely lower. In figure 39, A-C extinction spectra multiplied with the dilution factor are shown for the respective temperatures. In analogy to the concentration screening detailed above, the characteristic absorption of chloroauric acid is visible for reactant amounts starting from 4 equivalents. For increased temperatures, the amount of chloroauric acid remaining in dispersion is lower for comparable equivalents due to increased consumption in line with an elevated reaction speed at elevated temperatures. From extinction spectroscopy of unreacted chloroauric in the supernatant, the portion of reacted can be calculated according to equation 16. This is plotted versus the stoichiometry ratio in figure 39, D. The trace at 4 °C (teal trace) is clearly distinguishable from 40 and 60 °C, showing a significantly lower consumption which deviates from the theoretical consumption for 4 equivalents and above. Traces of 40 and 60 °C fall on the same curve but deviate from the theoretical consumption as well for 6 equivalents and above. Overall, no complete conversion to W(+VI) and S(+VI) is achieved under these reaction conditions, presumably due to the lower reaction times. However, importantly, even less chloroauric acid is consumed at lower temperatures compared to elevated temperatures. Note that it is not possible to distinguish between a slower reaction rate at decreased temperatures in general and a difference in the SC adsorption/desorption equilibrium due to the different temperatures.

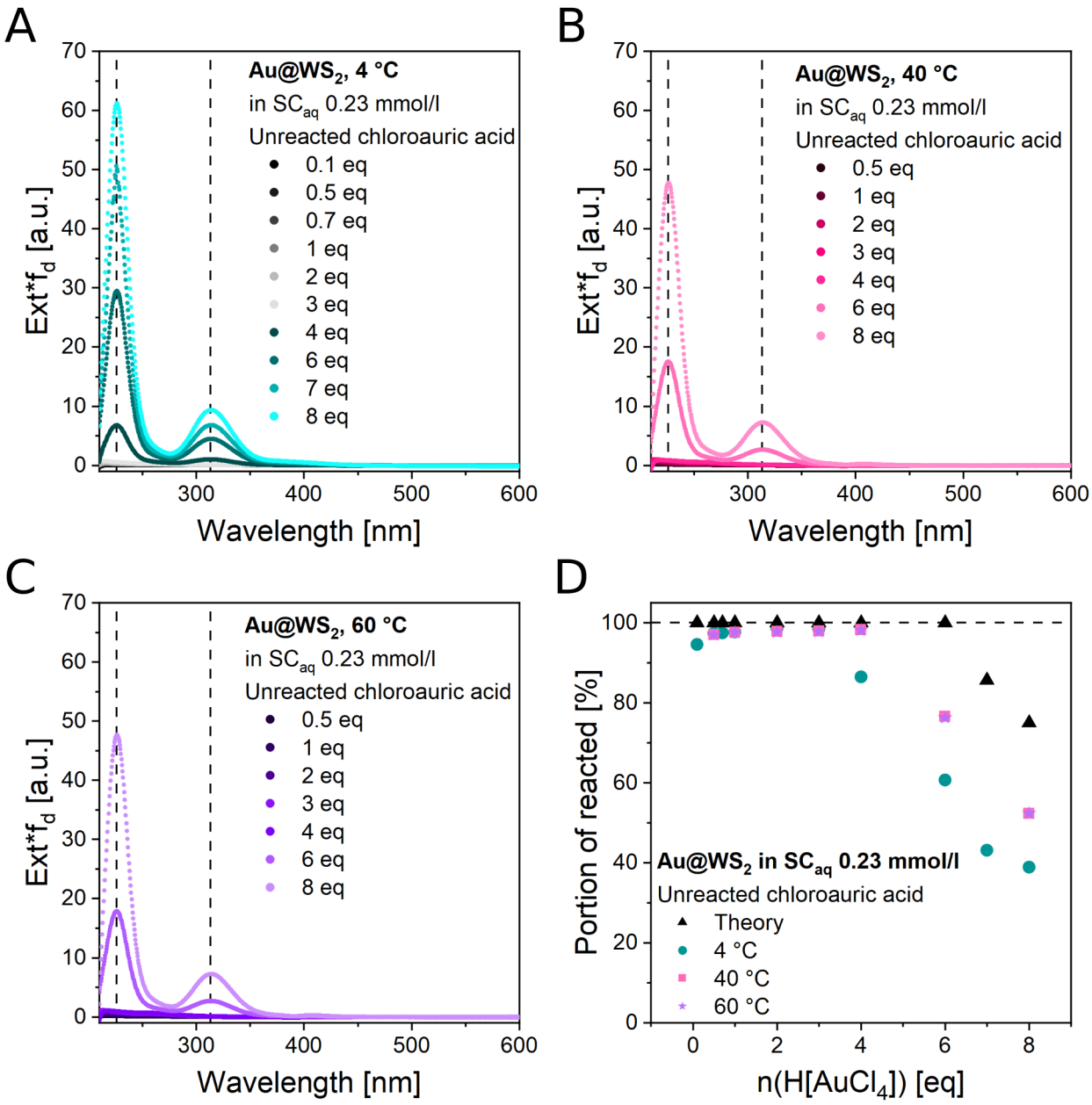

Figure 39: A-C) Extinction spectra of unreacted chloroauric acid in the removed reaction mixture supernatant for reaction in aqueous SC solution at 4 °C (A), 40 °C (B) and 60 °C (C) multiplied with the dilution coefficient f_d for varying amounts of employed chloroauric acid. Extinction maxima are indicated using dashed lines. D) Quantification of the portion of reacted derived from extinction at 226 nm in A-C for 4 °C, 40 °C and 60 °C respectively as well as consumption based on the theory (black trace in D) of full oxidation to W(+VI) and S(+VI). Complete conversion is indicated using a dashed line.

In addition to the supernatant after the workup, the *Stock* samples and workup sediments are also investigated by extinction spectroscopy. Extinction spectra of the *Stock* samples multiplied by the dilution coefficient are depicted in figure 40, A-C. For increasing amounts of chloroauric acid, more material is lost for all temperatures probed. However, this loss of material (i.e. lower extinction) in the *Stock* samples increases for increasing temperatures.

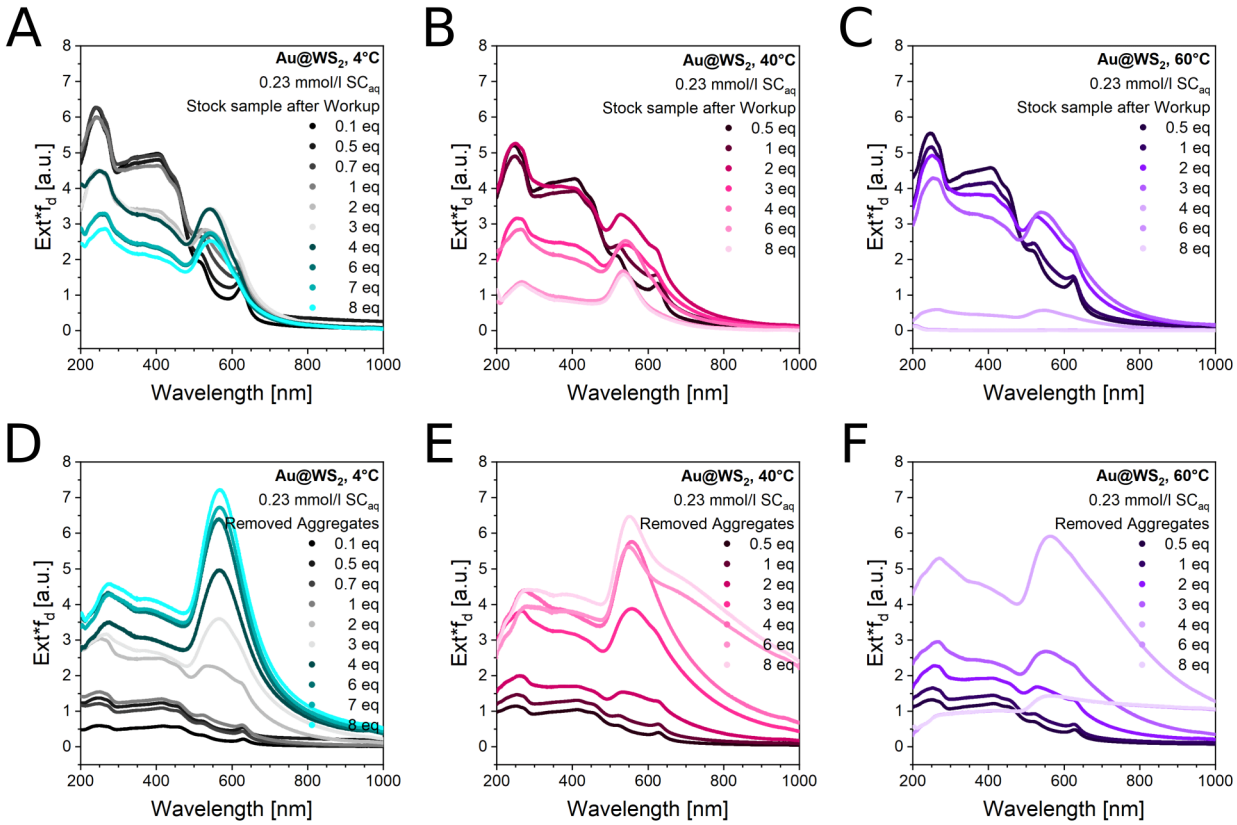

Figure 40: A-C) Extinction spectra of Stock samples after workup for reaction in aqueous SC solution at 4 °C (A), 40 °C (B) and 60 °C (C) multiplied with the dilution coefficient f_d for varying amounts of employed chloroauric acid. D-F) Extinction spectra of aggregated material removed during workup for reaction in aqueous SC solution at 4 °C (D), 40 °C (E) and 60 °C (F) multiplied with the dilution coefficient f_d for varying amounts of employed chloroauric acid. It has to be noted that aggregates removed for samples 6 and 8 eq at 60 °C dispersions were unstable resulting in underestimation of the amount of material in dispersion for the respective traces in F.

In the extreme case of 6 and 8 equivalents of chloroauric acid at 60 °C (C) the extinction even drops close to zero for the largest part of the spectral region measured, indicating near complete loss of material in dispersion upon workup. Further the surface plasmon resonance of the produced gold nanoparticles becomes increasingly dominant for increasing temperatures whereas the spectral shape of WS_2 is lost. This is best visualized using the normalized spectra shown in appendix 8.5, indicating that the material remaining in the S*tock* samples after workup suffers from stronger degradation for increasing temperatures. Comparably, for aggregates removed during workup the amount of material in dispersion increases at all temperatures (figure 40, D-F), in contrast to observations made with decoration in SDS in figure 31. The surface plasmon resonance thereby experiences significant broadening indicating an increased production of aggregated gold particles or the formation of larger gold nanoparticles.

It appears that the efficiency of surfactant control for this heterogeneous reaction depends to a certain degree on the reaction temperature. Interpretation here is less straightforward due to the complexity of parameters in this system. However, this observation could serve as an indication that temperature driven ad- and desorption events play a role. Since the enthalpy of adsorption for SC on WS_2 nanosheets is not known, it remains unclear whether an increase in temperature shifts adsorption equilibrium towards desorbed surfactant molecules or whether the increase in desorption event frequency for increasing temperatures may be the root of this behavior. This could also partially account for the fact that SDS is improperly protecting the material basal plane, as fast ad- and desorption of SDS on MoS_2 surfaces was reported in literature.[92] It has to be noted though that increasing temperatures also increase the likelihood of reaction for a given kinetic barrier.

Concluding, a clear dependence of the gold functionalization of WS_2 using chloroauric acid with respect to the surfactant coverage of the nanosheets was shown. The reaction outcome and morphology of the material retrieved after reaction workup and purification clearly depend on the type of the surfactant employed. It was shown that in SDS severe oxidation of the material in dispersion takes place, while in SC isolation of barely oxidized monolayered nanosheets is feasible.[160] It was further shown that the surfactant does not stop oxidation at a certain stage, but rather directs reactivity along competing reaction channels. A simple model was developed with three different trajectories along which an oxidant can attack a nanosheet. Whether a certain reaction channel is dominant depends on the kinetic barrier that arises along the respective trajectory due to preferential surfactant adsorption at different sites on the nanosheet. For example, if a surfactant efficiently shields basal plane oxidation by surface adsorption, the observed scenario of chemically widely inert monolayers can be explained. Preferential basal plane adsorption of SC as a facial amphiphile in contrast to SDS as a linear amphiphile was suggested by ζ potential measurement of WS_2 dispersions with varying sizes. The size-dependence of the SC coverage was further corroborated by exploring the chloroauric acid treatment of very small nanosheets which confirmed that small monolayers are not efficiently shielded. In order to probe the interlayer mobility of the reactant, powder XRD was conducted and yielded indications of an irregular expansion in the interlayer space and subsequent decoupling of the nanosheets presumably due to formation of polydisperse gold nanoparticles. Furthermore, the reaction was performed at various temperatures to probe the effects of surfactant desorption on the SC system which led to increased material degradation for increasing temperatures.

Overall, the experiments conducted strongly corroborate the model presented and surfactant adsorption is likely influencing heterogeneous reactions at the nanosheet-

solvent interface. It remains unclear to this point, whether this influence exerted by the surfactant layer depends on electrostatic or steric interactions between surfactant and reactant, but given the fact that surfactants and reactants are both of negative charge, electrostatic repulsion seems to be the most intuitive explanation.

4.3 Gold nanoparticle functionalization of molybdenum(IV)sulfide

Based on the observations outlined in chapter 4.2 a certain sensitivity of gold functionalization towards subtle differences in the material system, such as the surfactant coverage is evident. Previous experiments were conducted on WS_2 nanosheets which served as model substance due to the ease in spectroscopic characterization. The question arises if the mechanism outlined above applies for other group VI TMDs containing sulfur atoms. For MoS_2 especially, comparable reactivity is expected: due to lanthanide contraction, molybdenum and tungsten are chemically very similar which renders many properties, such as atom radii (1.41 Å for W and 1.40 Å for Mo) or enthalpies of formation (-240.8 kJ/mol for WS_2 and for MoS_2 -273.8 kJ/mol at 298.15 K) comparable for analogue compounds.[6, 223-224] Therefore, MoS_2 and WS_2 in their at room temperature thermodynamically stable *2H* polymorph are isostructural and further very comparable in bond lengths as illustrated in figure 41. The closest distance between two sulfur atoms across two layers with 353 pm for WS_2 and 347 pm for MoS_2 is very similar and hence the interlayer distance, which is measured orthogonal to both layers (296 pm for MoS_2) should be comparable for both compounds.[225] The metal-sulfur bond lengths are virtually identical for both compounds and sulfur-sulfur and metal-metal distances differ marginally. As such, no major discrepancies in chemical behavior are expected on exchange of the metal center, especially since the layer surface interacting with the environment is in both case primarily composed of sulfur atoms.

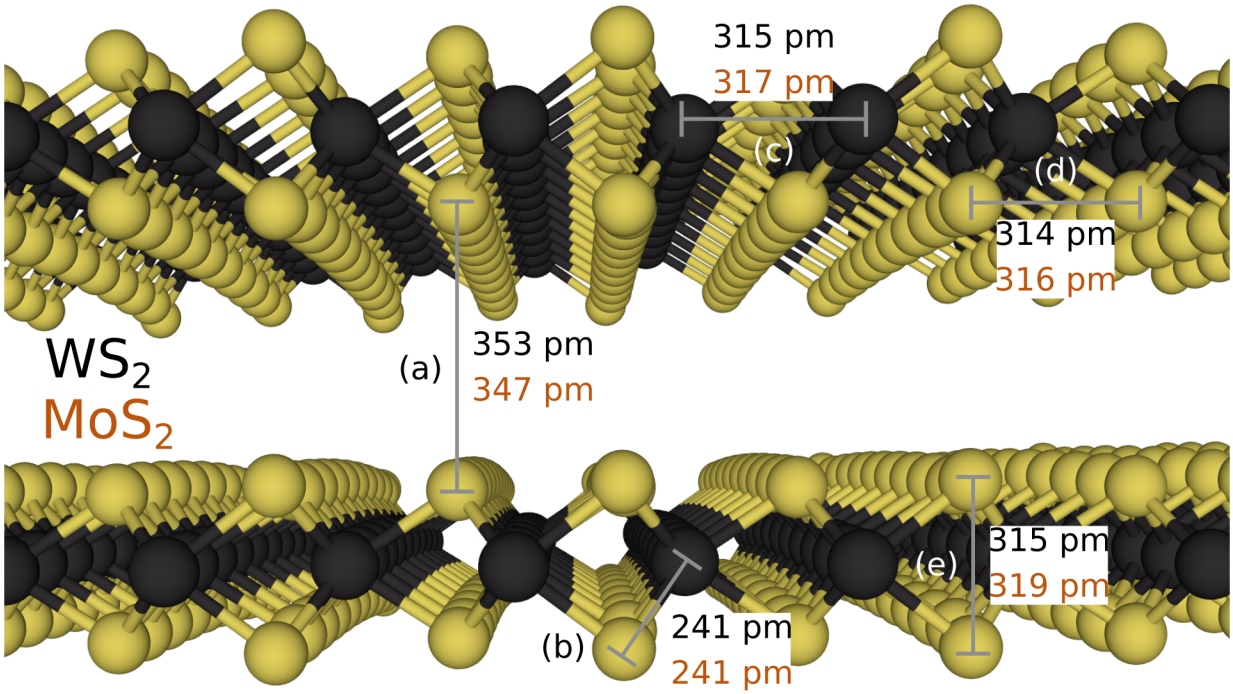

Figure 41: Schematic view of the hexagonal MS_2 (M = W, Mo) crystal structure with sulfur as yellow and M as black spheres. Selected atom distances are indicated using solid lines for WS_2 (black text) and MoS_2 (orange text). Bond lengths shown S-S distance across layers (a), M-S bond length (b), M-M distance (c) and parallel and orthogonal S-S distance (d and e respectively). Bond length values are taken from literature.[225-228]

In order to test this expected behavior for validity, gold functionalization of MoS_2 was conducted and the reaction products analyzed. For this, MoS_2 was exfoliated by tip sonication according to the standard liquid phase exfoliation protocol in aqueous SC and SDS solution and a consecutive liquid cascade centrifugation was employed in order to produce three dispersions each of varying sizes (*L*, *M*, *S*). Normalized extinction spectra of these dispersions are shown in figure 42, A. All samples show the characteristic spectral profile of MoS_2 with clear trends in extinction with size. The position of the A exciton signal blue-shifts as the average layer number $\langle N \rangle$ in dispersion decreases with decreasing sizes due to confinement and dielectric screening effects in analogy to WS_2 and as outlined in chapter 2.5. Furthermore, the ratio of the extinction intensity $Ext(270\ nm)/Ext(345\ nm)$ increases for decreasing sizes due to edge effects. Similar spectra are observed for exfoliation and size selection in both SC and SDS. For example, the second derivative of the spectral region around the A and B exciton with respect to the incident photon energy for S nanosheets is plotted in figure 42, B. In contrast to WS_2, no splitting of the A exciton in contributions from monolayers and fewlayers is observed due to an increased excitonic linewidth.[15, 118-119] Furthermore, no significant shifts are visible in the A exciton position when comparing MoS_2 exfoliated and stabilized in SC and SDS, respectively, but visible in the B exciton position. This can be more clearly resolved when

plotting the peak positions of the A and B exciton signals versus the average layer number <*N*> of the nanosheets (figure 42, C).

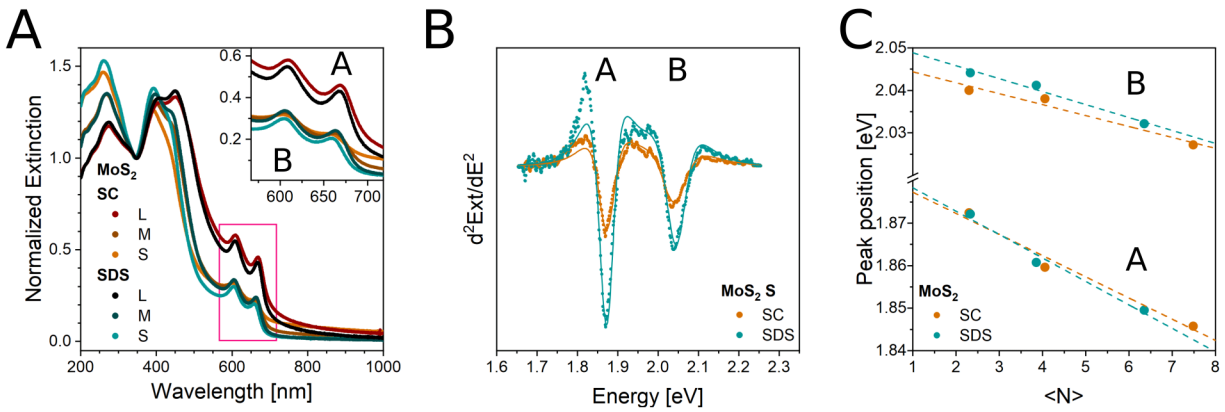

Figure 42: A) Extinction spectra of MoS_2 after liquid phase exfoliation and subsequent liquid cascade centrifugation normalized to the extinction at 345 nm. The inset shows an enlarged view of the spectral region around the A and B exciton signal. B) Second derivative of the spectral region around the A and B exciton signal in A with respect to the photon energy of the incident light. C) Dependence of peak maximum position of A and B exciton with respect to average nanosheet layer number for SC and SDS. Empirical linear fits are shown with dashed lines. A and B exciton are labeled in A-C. Samples are labeled with L for large (0.4 - 1k g, SC: <L> = 185 nm, <N> = 7, SDS: <L> = 167 nm, <N> = 6), M for medium (1 - 5k g, <L> = 87 nm, <N> = 4, SDS: <L> = 86 nm, <N> = 4) and S for small (5 - 30k g, <L> = 60 nm, <N> = 2, SDS: <L> = 47 nm, <N> = 2) in order to illustrate changes in relation to the average lateral size <L> and layer number <N> of the MoS_2 dispersion. <L> and <N> was determined from extinction spectra using published metrics.[7, 15]

Since the metrics used for the nanosheet size determination from extinction spectra were established for exfoliation in SC, <*L*> and <*N*> were calculated for WS_2 samples in SC and assumed to be comparable with the respective SDS samples in chapter 4.2. This was done in order to avoid inaccuracies of the size evaluation due to the observed shifts of the A exciton signal position in SDS compared to SC (see figure 33). In the case of MoS_2 however, no significant shifts in the A exciton signal position are observed irrespective of the used surfactant (figure 42, C). This observation enables transfer of metrics developed in SC to dispersions in SDS.[7, 15] Minor differences in nanosheet sizes across surfactants are evident, e.g. for <*N*> in *L* samples and <*L*> in *S* samples, however this is likely related to batch-to-batch-variations between different exfoliation runs and not due to inaccuracies in size determination stemming from the transfer of metrics. This is a downside of not using the transfer approach outlined in chapter 4.2, where sizes are always directly comparable across surfactants and batch-to-batch variations in the exfoliation process are avoided. However, direct exfoliation in SDS ensures absence of SC in samples for functionalization. As evident from figure 42, C size-dependent shifts in both A and B exciton are directly visible. The comparison across the two surfactants shows that the size-dependent A exciton position is widely independent of the surfactant used. However, a

blue-shift ranging from roughly 1 to 4 meV, depending on size, is visible for the B exciton in SDS compared to SC. This is in contrast to WS_2 where PL in SDS samples was consistently shifted to lower energies by 8 meV for the A exciton. However, at the current stage, no interpretation of this finding can be given. Possible batch-to-batch variations and increased intrinsic line width for MoS_2 compared to WS_2 can play a role.[15] This also applies to the interpretation of increased photoluminescence in Raman spectroscopy for samples exfoliated in SDS (Appendix 8.6). Furthermore, the influence of scattering to the extinction spectra was not assessed and as such unexpected shifts might also happen due to changes in the scattering contribution. Therefore, no reliable interpretation is possible based on the available data.

For gold functionalization, MoS_2 dispersions of medium size were fixed to a material concentration of 2 mmol/l in SC and SDS respectively and functionalized according to the standard protocol. To this end, chloroauric acid solution was added dropwisely to a dispersion stirred on an ice bath. Workup and purification were performed with comparable parameters used for the respective WS_2 experiments. Extinction spectra of MoS_2 dispersions were measured after functionalization and subsequent purification (figure 43, A-B). For unreacted chloroauric acid removed during workup, differences for SC and SDS can be observed (pink traces). For functionalization reactions in SC and SDS, the position of the oxidant absorption at 226 nm is shifted to higher wavelengths in SDS compared to SC, the lower intensity band of chloroauric acid at 313 nm is absent in both cases. Therefore, unambiguous identification of the molecular species remaining in the supernatant removed during workup is not possible. As no acidification was conducted prior to extinction measurement in this experiment pH dependent shifts due to ligand exchanges are the likely source of this spectral profile. It should be noted that the extinction multiplied with the dilution factor reveals a larger amount of unreacted reagent in dispersion in SC compared to SDS. This trend is explored in more detail later.

For the aggregated material removed during workup, a pronounced signal assigned to the surface plasmon resonance of gold nanoparticles is visible (figure 43, A-B, black trace). This signal clearly dominates the extinction spectrum in SC while in SDS certain features of MoS_2 extinction are still visible. For purification, again liquid cascade centrifugation was employed where material is removed during centrifugation at 4 000 *g* (*Sediment*, blue traces in figure 43, A-B) and the purified material dispersion is concentrated through centrifugation at 16 000 *g* (*Purified*, orange and teal trace in figure 43, A-B). For material removed during purification, the contribution of the gold nanoparticle surface plasmon resonance to the extinction spectrum is only weak and best seen in SC, while for SDS no distinct signal is observed in the as-measured spectra

suggesting that relatively few and small nanoparticles are associated with the MoS_2 surface in the purified sample.

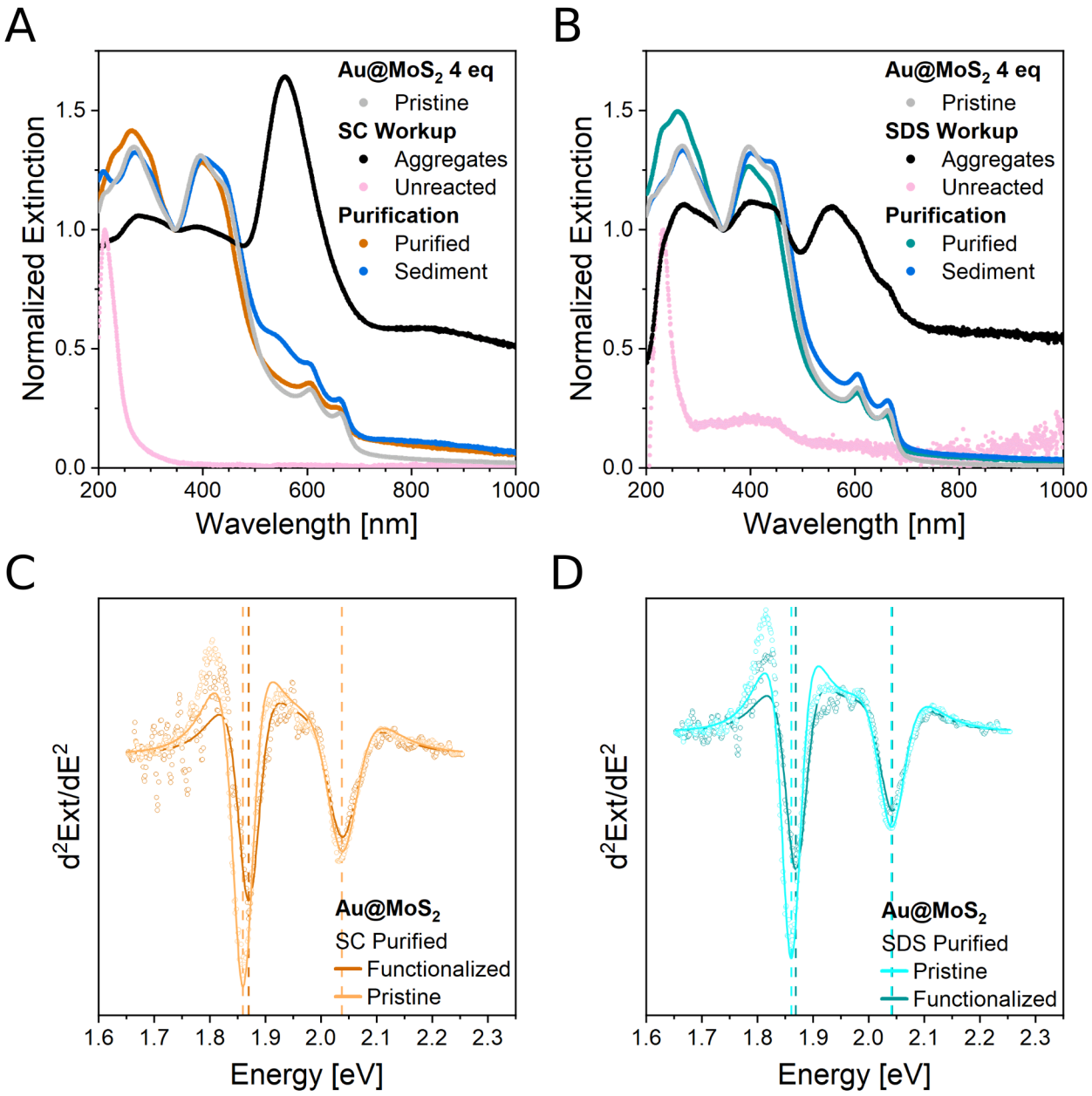

Figure 43: A-B) Extinction spectra of dispersions isolated during workup and purification of gold-functionalized M-MoS_2 for reaction in SC (A) and SDS (B) normalized to extinction at 345 nm, except for traces labeled Unreacted which were normalized to the extinction at the peak maximum of the trace. C-D) Second derivative of the spectral region around the A and B exciton signal for purified dispersions in A and B respectively with respect to the photon energy of the incident light. The curves are fitted with the second derivative of the sum of two Lorentzians (solid lines).

Apparently, most of the material decorated with big gold nanoparticles is already removed during workup. Upon centrifugation-based purification, the spectral signature of pristine MoS_2 in the A and B exciton region are completely restored in the purified (orange and teal traces) samples indicating successful purification in both SC and SDS. This is in

contrast to the functionalization of WS_2, where purification in SDS was not successful due to severe structural degradation of the nanosheets. Furthermore, a change in the extinction intensity ratio $Ext(270\ nm)/Ext(345\ nm)$, which is used to estimate the average nanosheet length $<L>$ in dispersion, is visible.[15] In comparison to the starting material, the extinction intensity ratio increases in both cases, but more pronounced in SDS compared to SC. This can be seen as a reduction of $<L>$ through functionalization, workup, and purification and is again in stark contrast to functionalization of WS_2 where $<L>$ did not change significantly.[15, 160] For a closer inspection of the spectral region around the A and B excitons, the second derivative of extinction with respect to the energy of the incident light is calculated (figure 43, C-D). In both cases a shift of the A exciton to higher energies is visible upon functionalization and purification suggesting a moderate reduction of the average layer number $<N>$ in dispersion.[7, 15] For WS_2 this was only achievable in SC and not in SDS and therefore this behavior underlines a difference in reactivity between WS_2 and MoS_2 which was not expected prior to these experiments. For the B exciton, no significant shifts can be observed upon functionalization although the established shifts across surfactants still persist (comparison figure 42).

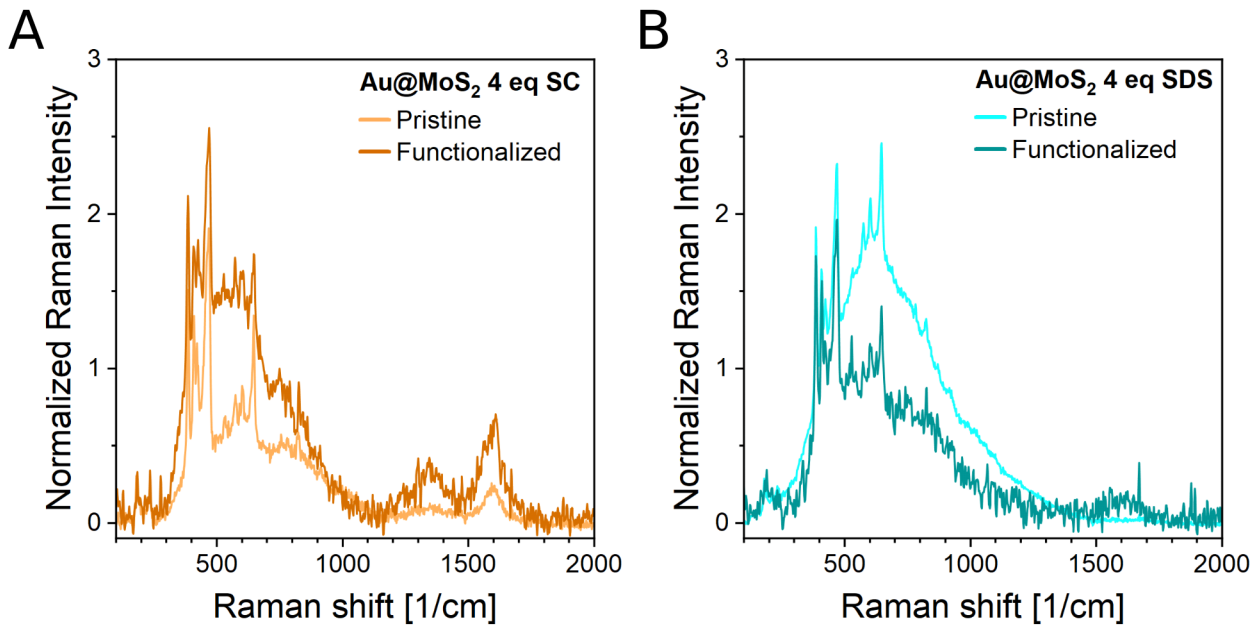

Figure 44: A-B) Raman spectra of gold-functionalized MoS_2 dispersions after purification measured on a droplet of the dispersion ($\lambda_{exc} = 633\ nm$) in SC (A) and SDS (B) and respective starting materials. Three spectra are averaged each, a baseline was subtracted and spectra were normalized with respect to the height of the E^1_{2g} mode. Careful smoothing was performed to remove excessive noise in the data and increase readability.

A decrease in the average layer number $<N>$ should result in an increase in PL for samples if no significant structural damages to the nanosheets occurred. Therefore, Raman/PL spectra were measured and are shown in figure 44, A-B. In contrast to WS_2, it is not easily possible to separate the PL peak from the Raman signal in MoS_2: With

532 nm excitation, which is ideally suited for WS_2, the MoS_2 PL expected at 655 nm would be centered at ~3500 1/cm and thus overlap with the Raman signal of water. Therefore, an excitation wavelength of 633 nm was chosen. However, for this excitation energy, the Raman modes are superimposed on the PL of MoS_2 which renders a precise analysis more difficult. Nonetheless, qualitatively, it can be observed that the PL is roughly doubled after functionalization and purification in SC compared to the starting material in agreement with the expectation of a reduction in $<N>$. In contrast, in SDS, the PL is roughly decreased by a factor of ~2. Since extinction spectroscopy suggests that $<N>$ decreases for both dispersion types, some degree of structural damage can be inferred for the functionalization in SDS. Furthermore, for SC, additional peaks at ~1350 and ~1600 1/cm are visible which increase in relative intensity upon functionalization. In SDS, these are less pronounced and solely the peak at 1600 1/cm is weakly visible in the purified, functionalized sample. These peaks are very characteristic in shape and position for amorphous carbon. While this spectral region is typically not analyzed in publications focussing on MoS_2, the amorphous carbon signature on CVD MoS_2 samples was frequently observed by members of the working group. Since the signal is associated with the surface of MoS_2, a reduction in flake dimensions is expected to result in an increased relative contribution after the functionalization and purification. It should be noted that such an amorphous carbon layer can strongly impact the reactivity of MoS_2 compared to WS_2, where this is typically not observed.

In order to validate the decreased nanosheet dimensions inferred by extinction and Raman spectroscopy, AFM measurements and statistical evaluation of the nanosheet dimensions were conducted. To this end, line profiles were manually taken across individually deposited nanosheets and the longest lateral dimension of a nanosheet, referred to as length L, the lateral dimension orthogonal to L called width W and sheet thickness h were recorded. From this data, distribution histograms were constructed for nanosheets before and after functionalization (figure 45). Representative AFM images are shown in the appendix 8.7.

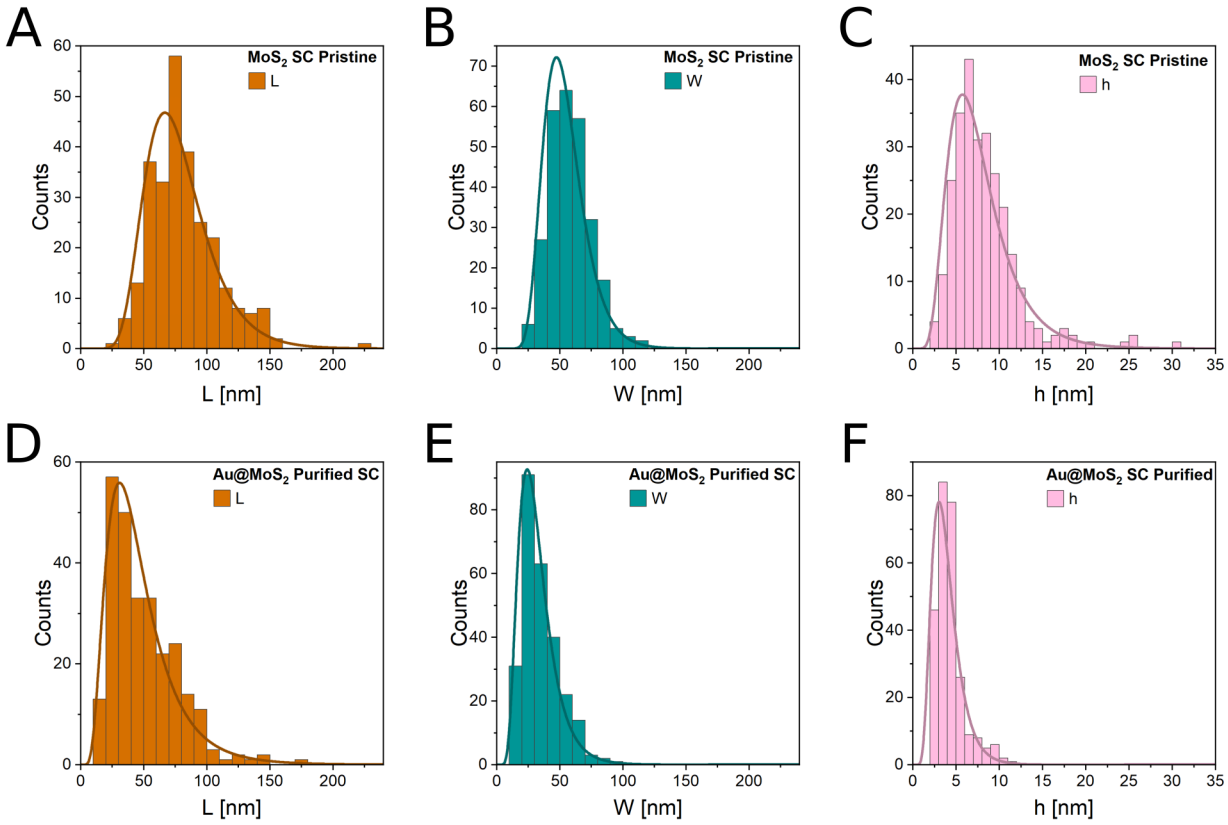

Figure 45: Statistical evaluation of sheet dimensions of nanosheets derived from AFM images for pristine starting material in SC before (A-C) and after the chloroauric acid treatment and subsequent purification (D-F). Dimensions evaluated are the longest lateral dimension L (A, D), the lateral dimension orthogonal to it W (B, E) and thickness h (C, F). Lognormal distributions are indicated by the solid lines.

It is evident from comparison of the nanosheet dimensions before (figure 45, A-C) and after functionalization (figure 45, D-F) in SC that the nanosheets are smaller in all dimensions after the chloroauric acid treatment and subsequent centrifugation-based purification. This is in accordance with the expectations based on the analysis of the extinction spectra. It should be noted that this is not necessarily a mere result of the functionalization reaction, but that the sizes can also be influenced by the centrifugation applied for the purification. The centrifugation parameters were initially optimized for gold-functionalized WS_2 in SC to efficiently remove nanosheets decorated with larger gold nanoparticles from the edge-decorated WS_2. However, for a different size and density of nanoparticles, different centrifugation boundaries might be more suitable. Overall, for a direct comparison of the effect of the functionalization, it would have been required to perform the identical workup and purification on the reference sample prior to AFM analysis.

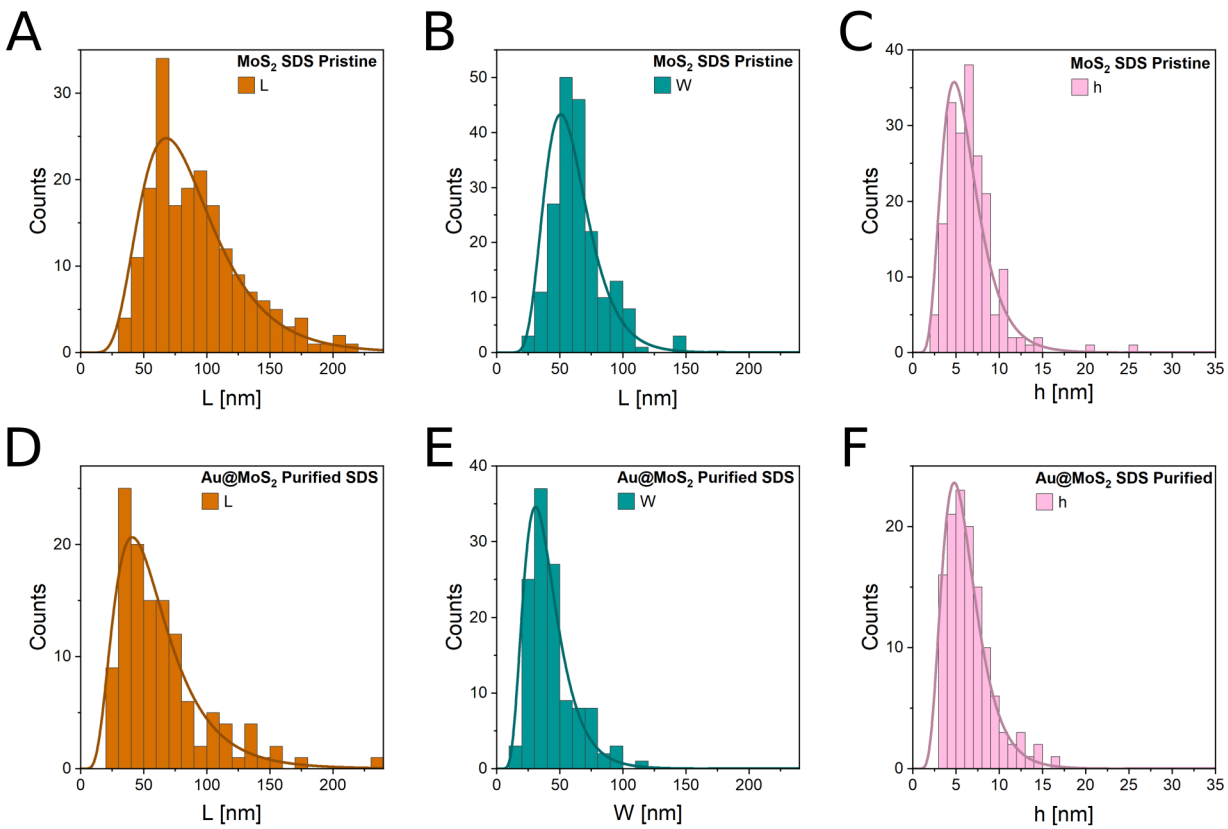

Figure 46: Statistical evaluation of sheet dimensions of nanosheets derived from AFM images for pristine starting material in SDS before (A-C) and after the chloroauric acid treatment and subsequent purification (D-F). Dimensions evaluated are the longest lateral dimension L (A, D), the lateral dimension orthogonal to it W (B, E) and thickness h (C, F). Lognormal distributions are indicated by the solid lines. To ensure comparability of deposition methods, samples were transferred to SC solution prior to deposition.

For SDS, the result of the statistical evaluation is visualized in figure 46. After functionalization and purification in SDS, a decrease in the lateral nanosheet sizes is visible in dimensions $<L>$ (comparison A and D) and $<W>$ (comparison B and E) compared to pristine starting material. However, in thickness no significant changes can be observed in SDS in contrast to SC. This observation seems to be a contradiction to the analysis of the extinction spectra, where a blue-shift of the A exciton was observed, which is typically attributed to reduced nanosheet layer numbers. However, it should be noted that the apparent AFM height cannot readily be converted into layer numbers, in particular in the case of the gold-functionalized nanosheets. Even if the gold nanoparticles were predominantly bound at the edges of the sheets, they would also contribute to the height, as the nanosheets no longer lie flat on the substrate surface.

The average nanosheet dimensions as well as derived parameters such as average sheet area and aspect ratios were extracted by fitting a lognormal function to the respective distributions. The center position of the individual distribution fits are summarized in table 4.

Table 4: Average nanosheet dimensions derived from AFM statistics as center positions of a lognormal fit of the respective distributions.

	$\langle L \rangle$ [nm]	$\langle W \rangle$ [nm]	$\langle h \rangle$ [nm]	$\langle A \rangle$ $(L \cdot W)$ [nm^2]	$\langle k \rangle$ (L/W)	$\langle k_\perp \rangle$ (A/h) [nm]
SC Pristine	78.0	57.2	7.5	4224	1.34	553
SDS Pristine	83.7	60.2	6.3	4412	1.36	757
SC Functionalized	43.8	31.4	3.9	1275	1.35	313
SDS Functionalized	51.0	37.4	5.9	1583	1.31	239

Pristine MoS_2 exfoliated in SC and SDS shows small differences in $\langle L \rangle$[5] and $\langle h \rangle$. Interestingly, the MoS_2 in SDS is slightly larger laterally, but thinner than the nanosheets in SC. A larger area $\langle A \rangle$ with simultaneously lower average layer number $\langle N \rangle$ could be the origin of the more efficient PL emission of monolayered MoS_2 in dispersions exfoliated in SDS compared to SC. This is best seen from the area-thickness aspect ratio $\langle k_\perp \rangle$, which can be used as a parameter for the exfoliation efficiency and dispersion quality. Note that previous work has suggested that the length/thickness aspect ratio achievable from LPE is a material parameter determined by the in-plane to out-of-plane binding strength ratio of the bulk crystal.[78] As such, the aspect ratios of LPE nanosheets are typically not tunable by the exfoliation conditions or the quality of the starting material.[78-79, 229] While the majority of work in this area focuses on exfoliation using only SC as surfactant, a comparison of the exfoliability in different surfactants has shown that the aspect ratio is also independent of the surfactant type when using standard linear and facial amphiphiles.[88] However, recent work suggested that the balance between nanosheet exfoliation and scission, which determines the length/thickness aspect ratio, can indeed be influenced by certain surfactants, such as aromatic molecules.[230] Unfortunately, only limited data is available for TMDs, but in the case of graphene, so-called *π*-surfactants as stabilizers produce thinner nanosheets, that are laterally smaller than nanosheets produced from exfoliation in solvents in the absence of stabilizers.[230] As such, it is extremely surprising that the area/thickness aspect ratio of the pristine, as-produced MoS_2 in SDS is larger than for SC. A possible rational is the presence of amorphous carbon on the surface of the MoS_2 nanosheets, which was clearly detected in the Raman spectra of pristine MoS_2 in SC and which would also contribute to the apparent AFM height of the nanosheets in this sample. This hypothesis is backed by the average layer number extracted from extinction spectroscopy,[7] where $\langle N \rangle$ for pristine *M*-MoS_2 in SC and SDS are very close, with 4.06 and 3.86 respectively. In addition, as previously mentioned, this difference might be the result of batch-to-batch variations in liquid phase exfoliation and generalization requires

5 Note that $\langle L \rangle$ estimated from extinction spectroscopy was 87 nm in SC (86 nm from SDS), i.e. in agreement with the results from statistical AFM analysis.

additional data of multiple exfoliation runs. Overall, the AFM analysis shows that the two dispersions used for functionalization are slightly different in nanosheet sizes, which needs to be factored in when comparing results after functionalization.

Upon functionalization and purification, the nanosheet area $<A>$ decreases significantly for both surfactants by 64 % in SDS and by 70 % in SC. The aspect ratios of length and width are barely affected. The area/thickness aspect ratio $<k_{\perp}>$ decreases by 68 % in SDS but only by 43 % in SC. Even though the apparent height is likely influenced by the presence of gold nanoparticles (which effectively leads to a reduction of the area/thickness aspect ratio), the data suggests that the dispersion quality in SC suffers less from oxidative functionalization than in SDS. Further visualization of the trends observed is feasible using a scatter plot of area as function of thickness as displayed in the appendix 8.7. These show that larger/thicker nanosheets are removed in both dispersions treated with chloroauric acid which could be a result of the centrifugation steps applied for the purification. In addition, the scatter plots reveal that the thinnest nanosheets found in gold-functionalized MoS_2 in SDS have a larger apparent AFM height than in SC or the samples prior to functionalization. This points to the presence of larger Au nanoparticles formed on MoS_2 in SDS.

Since it was not possible to draw conclusions on the gold nanoparticle size based on the extinction spectra due to a negligible signal from the gold surface plasmon resonance, the samples were subjected to TEM imaging. In addition, imaging of the material removed during purification was performed (figure 47).

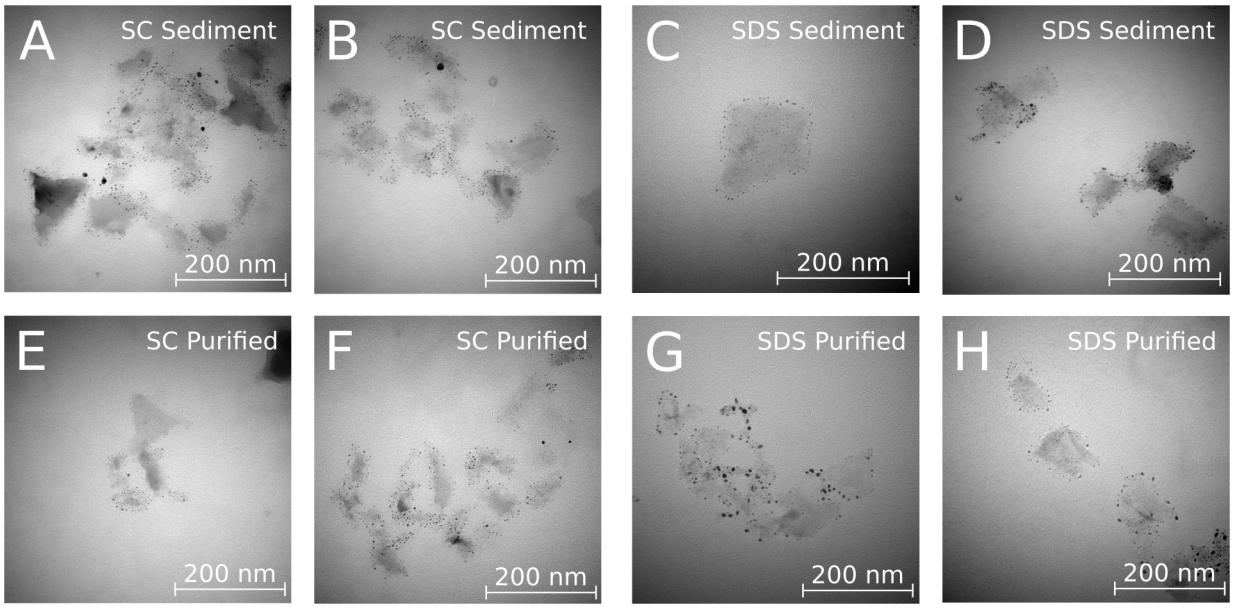

Figure 47: TEM images of M-MoS_2 nanosheets after functionalization in SC (A-B, E-F) and SDS (C-D, G-H). Material removed during purification is labeled Sediment (A-D) and material after purification is labeled Purified (E-H). All images were recorded at 120 kV acceleration voltage and x50 000 magnification.

In the sediment removed during purification after functionalization in SC (figure 47, A-B), nanosheets appear with intense variations in contrast revealing changes in the layer number of nanosheets imaged. This agrees with the AFM analysis that showed that larger/thicker nanosheets were removed from the purified dispersion. Few big gold nanoparticles are visible corroborating the hypothesis based on the extinction spectra that most of the big gold nanoparticles are already removed during workup. Furthermore, small gold nanoparticles are found predominantly around line defects, such as edges, comparable in appearance to the results of WS_2 functionalization. In the purified material (figure 47, E-F), differences in contrast across the imaged nanosheets diminish due to a decrease in the nanosheet thickness polydispersity as expected from AFM. Fewer big gold nanoparticles are visible compared to the sediment, albeit the difference is far less pronounced than in the case of WS_2 (see chapter 4.1). This shows that the purification is still successful for MoS_2 in SC, even though centrifugation parameters were not optimized for this system which resulted in the loss of the larger and thicker nanosheets, respectively.

In SDS a striking difference can be observed compared to WS_2: not only is the material structurally relatively intact and small to intermediate size gold nanoparticles are found predominantly around edges, but also many small gold nanoparticles are found on random spots of the basal plane. This clearly shows that basal plane attack occurs in SDS whereas it is suppressed in SC. This may also serve as an explanation for the lower PL/Raman ratio in gold-functionalized MoS_2 in SDS compared to pristine MoS_2 in SDS, as

PL is expected to decrease upon damage to the basal plane. In contrast to WS_2 in SDS, the small Au nanoparticles at the edges and terraces of MoS_2 in SDS suggest that SDS is not able to suppress edge oxidation sufficiently in the case of MoS_2. This was likely masked in WS_2 due to material degradation or a larger share of basal plane oxidation in WS_2.

Overall, the basal plane protection in SC-based dispersion is apparent in both WS_2 and MoS_2 and therefore again validates our model of shielding of the basal plane by the facial amphiphile. However, in SDS, MoS_2 appears less prone to basal plane degradation than WS_2. The reaction outcome in SDS can be rationalized using the simplest case of parallel reaction kinetics. If chloroauric acid, coined reactant O, is capable of performing three distinguishable reactions, exterior and interior basal plane attack as well as edge attack, a threefold parallel reaction can be postulated (figure 48).

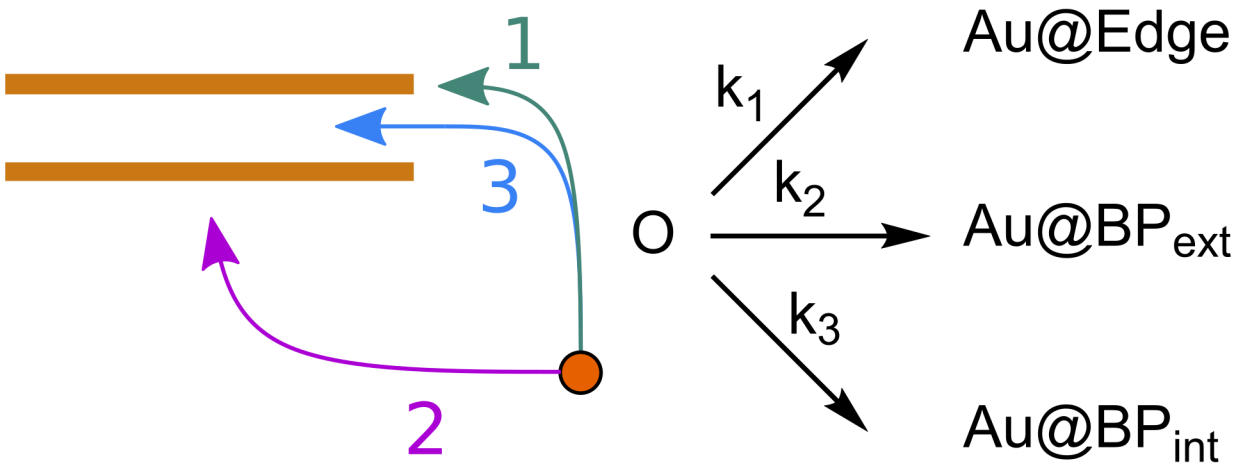

Figure 48: Schematic of the parallel reaction for the three reaction pathways. The TMD concentration is assumed constant for ease of visualization. This is purely illustrative, and no first order kinetics are assumed for the actual reaction.

The production speed of the reaction outcome i (either Au@Edge, Au@BPext or $Au@BP_{int}$ in figure 48) can then be formulated as equation 17.

$$\frac{dc(i)}{dt} = k_i^r c(O) \tag{17}$$

With k^r_i being the rate constant of reaction i, t as time and c as concentration of the oxidant. The consumption of reactant O can be described by equation 18.

$$\frac{dc(O)}{dt} = -(k_1^r + k_2^r + k_3^r) c(O) \tag{18}$$

This can be directly integrated to acquire a time dependent term for $c(O)$.

$$c(O) = c(O)_0 \cdot e^{-(k_1^r + k_2^r + k_3^r)t} \tag{19}$$

With this information, integration of equation 17 is possible and yields equation 20.

$$c_i = \frac{k_i^r}{k_1^r + k_2^r + k_3^r} \cdot \left(1 - e^{-(k_1^r + k_2^r + k_3^r)t}\right) \tag{20}$$

The relative share of each reaction outcome is then given by equation 21.

$$\frac{c_i}{c_{total}} = \frac{k_i^r}{k_1^r + k_2^r + k_3^r} \quad . \tag{21}$$

Equation 21 shows that the relative share of each reaction product depends on its individual rate constant. On the one hand, these are intrinsically different, e.g. an attack on basal planes exposed to the environment should be faster than attacks on basal planes from the interlayer space where diffusion has to occur first. On the other hand, the individual rate constants can be influenced by the chemical reactivity of certain reaction sites in MoS_2 compared to WS_2, but also affected by molecules adsorbed to the nanosheet surface. If a certain reaction pathway is suppressed, the relative amount of products for this individual species decreases and concomitantly, the relative amount of products of other pathways increases.

It should be noted that this example is purely illustrative in nature. First order kinetics cannot be postulated based on the available data and are used solely for facile demonstration. Nonetheless, we can use this knowledge to justify the presence of small gold nanoparticles at edges for functionalization of MoS_2 in SDS: If the basal plane attack is intrinsically slower in MoS_2 than in WS_2, the relative share of other reaction products increases. Hence, small gold nanoparticles at edges are visible for MoS_2 in SDS, but not for WS_2. This means that minor differences in the reactivity of WS_2 and MoS_2 can be visualized using gold functionalization. Whether this is an intrinsic property of the TMD, or related to different types of defects or even additional factors such as the presence of amorphous carbon on the surface cannot be rationalized based on this data.

In order to gain a more complete picture of the MoS_2 system, a concentration screening in analogy to the experiments described in chapter 4.2 was conducted. To this end, small amounts of MoS_2 dispersions with a fixed concentration were treated with varying amounts of chloroauric acid. For reaction workup, unreacted chloroauric acid was removed in the supernatant after initial centrifugation and analyzed using extinction

spectroscopy (figure 49, A-B). The characteristic absorption bands of chloroauric acid are well visible with negligible shifts. This corroborates the hypothesis that the observed peak shifts in chloroauric acid absorption seen in figure 43 happened due to changes in pH, as no shifts are visible after acidification.

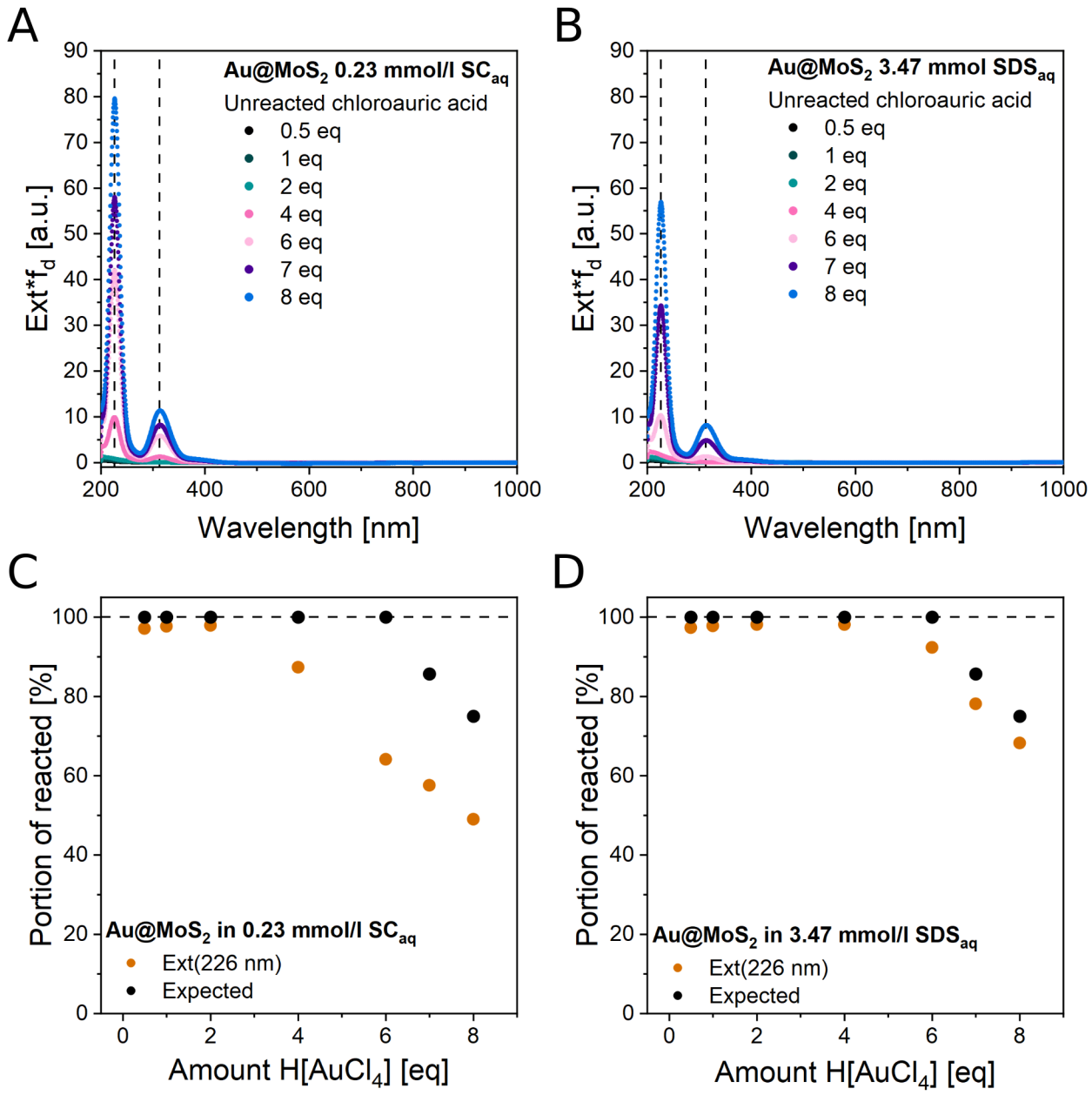

Figure 49: A-B) Extinction spectra multiplied with the dilution coefficient f_d of unreacted chloroauric acid in the reaction mixture supernatant that was removed for the reaction with M-MoS_2 in aqueous SC (A) and SDS (B) solution for varying chloroauric acid-MoS_2 stoichiometry ratios. Extinction maxima are indicated using dashed lines. C-D) Quantification of portion of reacted derived from extinction at 226 nm in A for SC (C) and in B for SDS (D) respectively (orange traces in C and D) compared to the theoretical consumption of chloroauric acid for complete oxidation to Mo(+VI) and S(+VI) (black traces in C and D). Complete conversion is indicated using dashed lines.

There is also a clear increase in the leftover reactant with increasing amounts of chloroauric acid added to the MoS_2 dispersions. Interestingly, above 2 equivalents, the amount of unreacted chloroauric acid in solution is higher for SC (A) than it is for SDS (B). This suggests that oxidation is less complete using the facial amphiphile SC compared to the linear amphiphile SDS. To analyze this further, the extinction multiplied with the dilution coefficient at 226 nm is used to calculate chloroauric acid concentrations with the aid of the extinction coefficients derived in Appendix 8.2 and converted to portion of reacted using equation 16 (figure 49, C-D). For functionalization in SC, the consumption is severely impeded and deviates strongly from the theoretical full oxidation to Mo(+VI) and S(+VI) (black data points in figure 49, C) above 2 equivalents added. In contrast, for functionalization in SDS, the chloroauric acid consumption is comparable to the consumption in the case of WS_2 (D). Since the reaction time was identical for SC and SDS, the reactivity of MoS_2 in SC is apparently reduced compared to SDS. In turn, the average reaction rate of MoS_2 in SDS is fast enough to achieve complete conversion similar to WS_2 in SC and SDS. To complement this analysis, the other constituents from the reaction workup were also investigated. After removal of unreacted chloroauric acid during workup, a low-speed centrifugation step is employed for removal of aggregated material while the *Stock* dispersion remains in the supernatant. Extinction spectra multiplied with the dilution coefficient of aggregated material, as well as the *Stock* dispersions are shown in figure 50. For *Stock* dispersions after workup (A-B) a decrease in the dilution corrected extinction is visible in both surfactants, with increased loss of material visible in SDS (B) compared to SC (A). This agrees with a more complete oxidation of MoS_2 concluded from the increased reactant consumption in the case of SDS. In SC the characteristic spectral profile of MoS_2 is maintained for all equivalents indicating no significant material degradation for the fraction of material isolated in the *Stock* dispersions. In SDS, pronounced degradation of the spectral profile is visible for reactant amounts larger than 6 equivalents. This is best seen in the normalized spectra in Appendix 8.8. It is evident that reaction in SDS has a bigger impact on extinction spectra of the material isolated as *Stock* than for SC. This can be linked to the mild basal plane oxidation happening in SDS which is suppressed in SC, as indicated through the presence or absence of gold nanoparticles on the basal plane respectively (comparison figure 47).

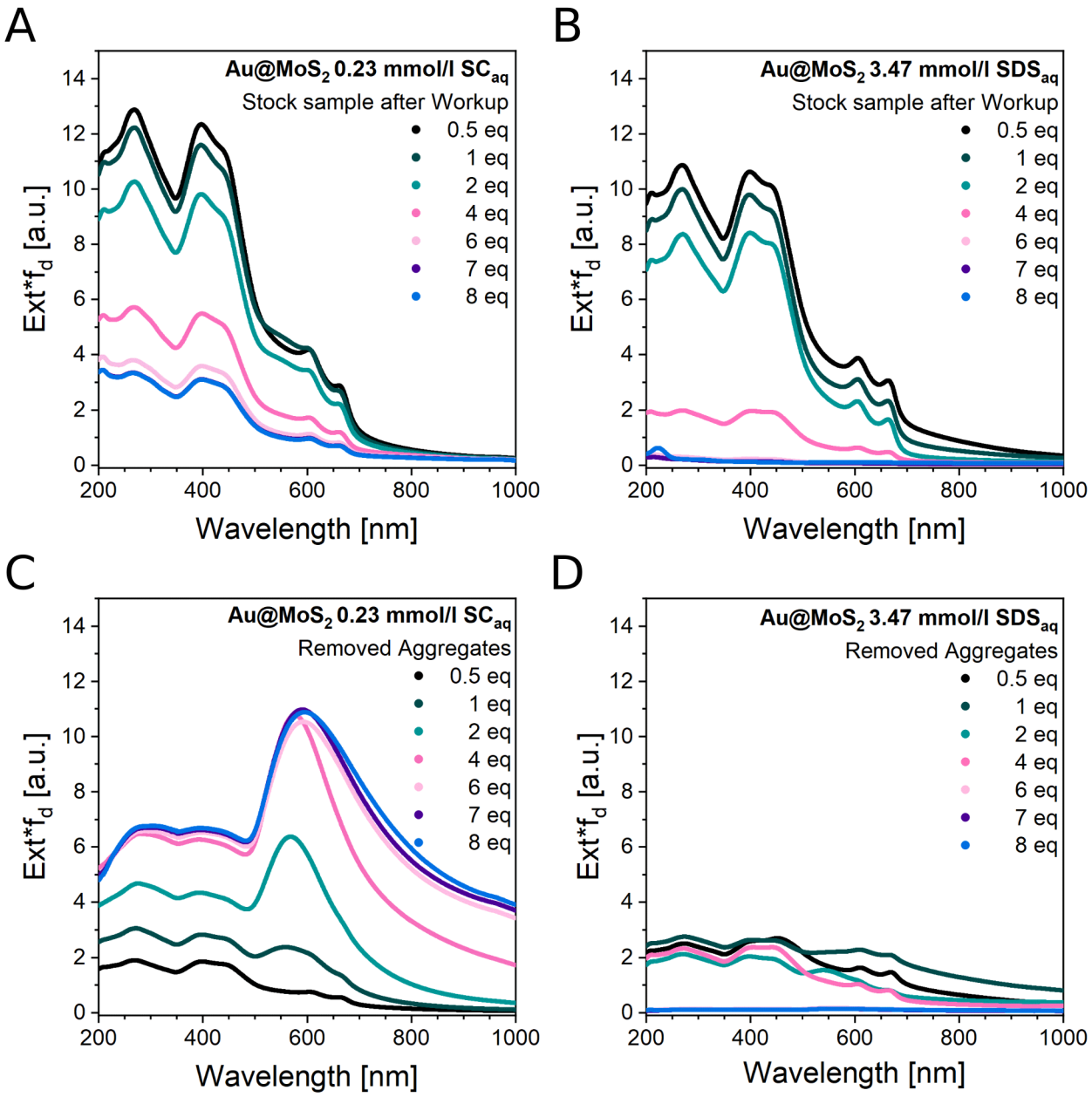

Figure 50: Extinction spectra multiplied with the dilution coefficient f_d for M-MoS_2 Stock samples after chloroauric acid treatment and workup for varying amounts of chloroauric acid in SC (A) and SDS (B) as well as the aggregated material in SC (C) and SDS (D) which was removed during workup. Dispersions for traces 6 to 8 eq in D were of insufficient colloidal stability and therefore the material removed during workup is likely underestimated.

The extinction spectra multiplied with the dilution coefficient of the portion of aggregated material removed during workup are shown in figure 50, C. In the case of SC, the spectra are dominated by the Au plasmon for high chloroauric acid/MoS_2 stoichiometry ratios. Furthermore, with increasing amounts of chloroauric acid used (figure 50, C), the overall extinction intensity subsequently increases, which is to be expected from the decreased extinction in the portion of isolated *Stock* material. In SDS however, the portion of material removed as sediment from the *Stock* dispersion does not increase significantly

up to 6 equivalents with increasing amounts of chloroauric acid (D). Possibly, stabilization of (partially) oxidized MoS_2 occurs in SDS which is likely the origin of the onset of extinction in the UV region of the extinction spectra of the *Stock* material (figure 49, B). Interestingly, although less chloroauric acid was consumed during functionalization in SC, the gold nanoparticle surface plasmon resonance is more pronounced in the spectra compared to SDS, best seen in Appendix 8.8. This could be related to the production of ill-defined nanoparticles polydisperse in size in SDS, in analogy to observations made for WS_2.

To conclude, the basal plane reactivity of MoS_2 is apparently significantly lower compared to WS_2. In WS_2, the basal plane attack was the dominant reaction pathway leading to a full oxidation to W(+VI) and S(+VI) when a sufficiently large amount of chloroauric acid was used as oxidant. Depending on the surfactant, the basal plane attack occurred on both the exterior surface and through the interlayer space (SDS), or predominantly through the interlayer space (SC). Hence, monolayer-enrichment was easily possible for WS_2 in SC. The basal plane degradation was evident from the presence of larger Au nanostructures polydisperse in size and shape. The reaction pathway at edges had a relatively low share to the overall oxidation reaction since neither did the size of gold nanoparticles bound to the edges change with the amount of chloroauric acid used, nor did the nanosheet size decrease significantly (at least after careful optimization of the centrifugation-based reaction workup and purification).

In MoS_2 however, the basal plane oxidation is less severe and hence no complete conversion to Mo(+VI) and S(+VI) is observed when using a sufficiently large amount of oxidant, in particular when using SC as surfactant. In this case, monolayer enrichment is also observed, as evident by a blue-shift of the A exciton, as well as an increased PL/Raman ratio. For MoS_2 in SC, this was confirmed by AFM statistics which showed that nanosheets were smaller in all dimensions after reaction with chloroauric acid and subsequent purification. However, it should be noted that the workup and purification was not adjusted to the sample type so that the decreased nanosheet dimensions could be a result of the employed centrifugation. For MoS_2 in SDS, the degradation of nanosheets is less apparent compared to WS_2 in SDS: Widely intact sheets are observed for intermediate equivalents of chloroauric acid that are functionalized with well-defined small gold nanoparticles at edges, terraces and at the basal plane. In contrast to WS_2 in SDS, the basal plane nanoparticles are well-defined in appearance and shape pointing to an overall more inert basal plane of MoS_2 compared to WS_2. In contrast to MoS_2 in SC, the PL/Raman ratio in purified MoS_2 in SDS decreased which is indicative of basal plane degradation in agreement with the presence of Au nanoparticles on the basal plane for MoS_2 in SDS that are widely absent for MoS_2 in SC. Thus, the study with MoS_2 confirms an

additional shielding of the basal plane oxidation through chloroauric acid treatment in the presence of the facial amphiphile surfactant SC in agreement with the work on WS_2.

The reason for the decreased basal plane reactivity of MoS_2 compared to WS_2 however remains unknown and contradicts expectations based on the chemical structure. Therefore, a contribution of basal plane defects present in commercially available powders or introduced through liquid phase exfoliation may be hypothesized which can significantly alter the intrinsic reactivity of the material. Furthermore, additional factors such as the presence of amorphous carbon in MoS_2 might play a role. Based on the available data presented here, no final conclusion can be drawn and the origin of the observed differences in reactivity remains elusive.

4.4 Gold functionalization of tungsten(IV)sulfide nanotubes

Another aspect of WS_2 reactivity towards gold functionalization not yet explored is changes in morphology. Until now, only nanosheets were used. However according to the developed model, the nanomaterial structure defines the possible reaction pathways. In analogy to their carbon relative graphene, different morphologies, such as fullerenes or nanotubes exist for layered group VI transition metal dichalcogenides.[231-233]

To test the impact of the morphology of the starting material towards the oxidation with chloroauric acid, multi-walled, tube shaped WS_2 (supplied by the group of Reshef Tenne) has been selected. Functionalization of WS_2 nanotubes with chloroauric acid is reported in literature, although functionalization was carried out in boiling chloroauric acid solution with nanotubes deagglomerated in acetone, i.e. without any additional additives, such as surfactants.[233] Gold nanoparticles are deposited around the nanotube perimeter and especially the tube ends, with the average particle size tuneable by the molar chloroauric acid to WS_2 ratio. Furthermore, film deposition at a liquid-liquid interface as well as integration in a photoresistive NO_2 sensor were demonstrated in separate works for these hybrid structures.[234-235] The presented functionalized nanotubes appeared mostly intact in shape in SEM images and a spatial separation of reduction and oxidation was hypothesized to explain the lack of structural degradation.[233] However, the harsh reaction conditions in combination with the lack of post-reaction workup and the absence of any surfactants hampers comparability to the mechanism for functionalization of TMD nanosheets developed above. Furthermore, no evidence for the proposed spatial separation of oxidation and reduction is presented: although complete oxidation of WS_2 to W(+VI) and S(+VI) is proposed and production of WO_3/H_2WO_4 was observed from XRD analysis of the reaction mixture, no oxidized species are found on the intact tube surface in this study.[233]

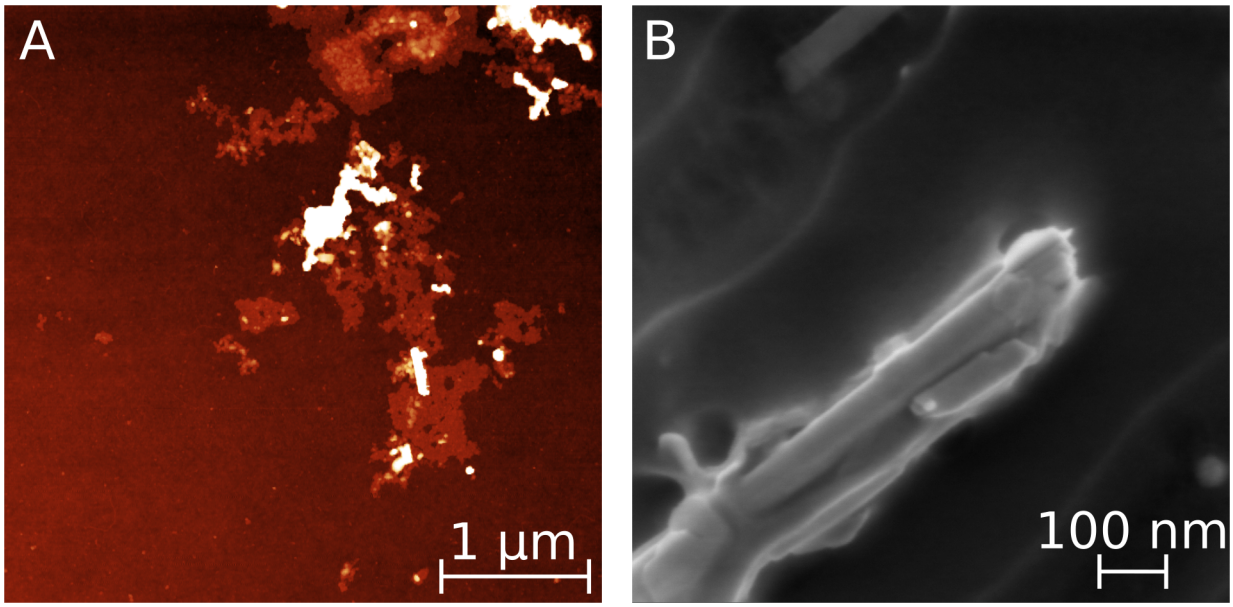

Figure 51: A) AFM image of WS_2 nanotubes on SiO_2 after treatment with a sonic probe. Structural degradation is visible as only highly defective nanosheets are found. B) SEM image of a WS_2 nanotube on GC after extended bath sonication. Image was acquired with 1 kV acceleration voltage at x100 000 magnification.

In first instance, a protocol for the production of dispersions needs to be developed. Standard sonic probe exfoliation with high sonication times as employed for WS_2 nanosheets leads to severe degradation of the tubular structure and produces sheet-like structures of 2 to 3 nm height rich in defects as visible from the AFM images of such a sample shown in figure 51, A. This degradation resembles the nanosheet tearing observed for nanosheets upon sonication-assisted liquid phase exfoliation and is probably enhanced due to strain arising from the tubular structure of WS_2 nanotubes.[78] In order to retain the tubular structure, an alternative approach for the production of dispersions is required. Since extended bath sonication of 5 h sonication time also led to structural damage and defective nanotubes (see figure 51, B), the devised protocol entails short bath sonication of the WS_2 nanotube powder in surfactant solution for 90 minutes with an hour of stirring after the first 30 minutes of sonication. Subsequent liquid cascade centrifugation is employed to produce the final nanotube dispersion after removal of aggregated material at 100 *g*. Relative centrifugal forces necessary to completely sediment nanotubes are significantly lower for high mass multi-walled nanotubes compared to nanosheets. Extinction spectra of the WS_2 nanotube dispersions produced this way are displayed in figure 52, A for dispersions in aqueous SC and SDS solution, respectively.

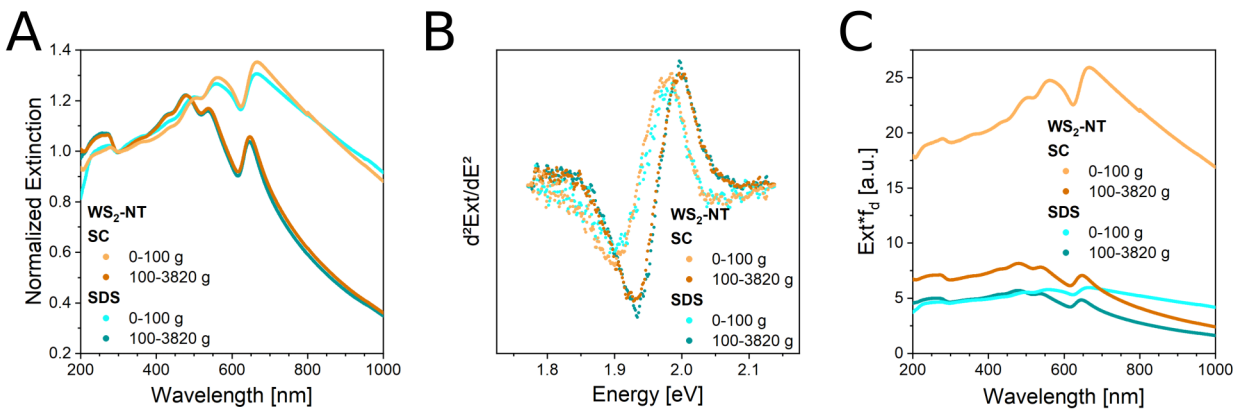

Figure 52: A) Extinction spectra of WS_2 nanotubes normalized to the extinction at 294 nm produced by bath sonication in aqueous SC and SDS, respectively, and subsequent trapping between two sets of centrifugal accelerations compared to the sediment removed in the low-speed centrifugation. B) Second derivative of the extinction around the A exciton signal in A with respect to the photon energy of incident light C) Extinction spectra of the same dispersions multiplied with the dilution coefficient.

Extinction spectra of nanotube dispersions are dominated by the scattering contribution as is evident from the large background in all traces which is discerned as powerlaw scaling in the nonresonant regime.[117] An apparent blue-shift of the A exciton signal is visible when comparing the high mass fraction removed as sediment at low centrifugal acceleration (0 - 100 *g,* light traces) to the final dispersions (100 - 3820 *g*, bold traces). However, this is likely related to a larger contribution from scattering to the spectra and only minor shifts in A exciton absorption are expected, comparable to WS_2 nanosheets with large mean layer number. The characteristic spectral profile of WS_2 is well discerned in the final dispersions for both surfactants. On closer inspection of the spectral region around the A exciton signal using the second derivative, no significant shifts of the A exciton position is observed for the two surfactant systems (figure 52, B). This in contrast to WS_2 nanosheets, but can be explained by the polydispersity of the sample (and thus relatively broad A exciton) in combination with a relatively large scattering contribution. Upon inspection of the extinction multiplied with the dilution coefficient in figure 52, C, the extinction in SC is generally higher than in SDS for comparable dispersions. This suggests that SC is able to stabilize WS_2 nanotubes more efficiently compared to SDS. For further characterization, Raman spectra were measured and shown in Appendix 8.9 alongside a brief discussion. All vibrational modes expected for WS_2 and those associated with the tubular structure especially are visible. SEM imaging was performed to finally validate the production of intact WS_2 nanotubes (figure 53). In figure 53, A, bundled nanotubes are visible and the tubular structure is well retained across all nanotubes visible. Individual nanotubes show no significant defects and lengths of roughly 1 µm (B) indicating successful production of intact nanotubes in dispersion without excessive shortening due to sonication. Therefore, the protocol is adopted for all further works.

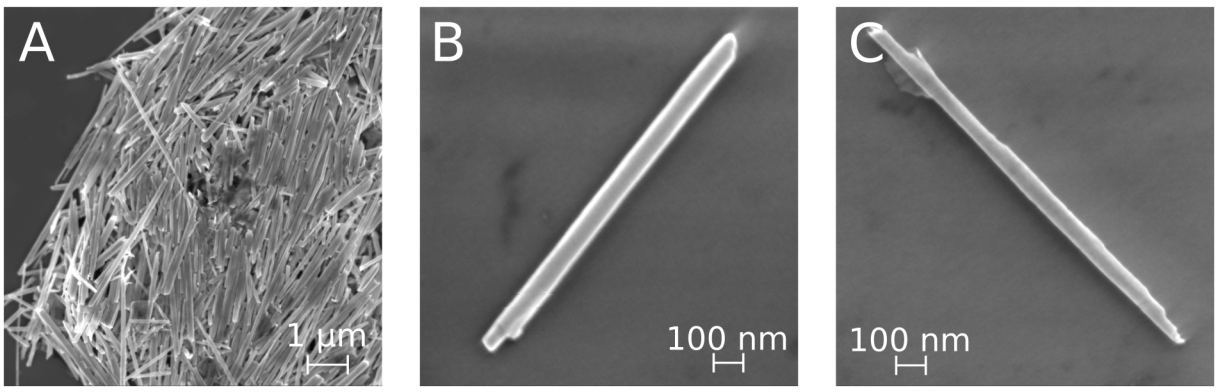

Figure 53: SEM images of WS_2 nanotubes produced by bath sonication in SC after deposition on Si. Image acquisition was performed with 5 kV acceleration voltage at x9 500 magnification in A and 1 kV acceleration voltage at x70 000 magnification in B-C.

For gold nanoparticle functionalization, WS_2 nanotube dispersions were treated with chloroauric acid as outlined previously for WS_2 nanosheets. For efficient monolayer enrichment with nanosheets, 4 equivalents of chloroauric acid were employed previously. As no reliable extinction coefficient for WS_2 nanotubes is known, assessing molar equivalents is not straightforward. Therefore, in order to estimate the molar equivalents, no liquid cascade centrifugation was performed prior to functionalization and the starting concentration of WS_2 nanotubes prior to the production of the dispersion was used for calculation. Decoration was then performed with 2 and 4 equivalents of chloroauric acid in SC. Such high amounts of chloroauric acid lead to the production of predominantly lose and aggregated gold nanoparticles which indicates that severe oxidation occurred (figure 54). Since the nanotubes visible still appear mostly intact, oxidation must be fueled by a specific portion of dispersed constituents, e.g. thin, individual nanotubes opposed to bundles or thick structures.

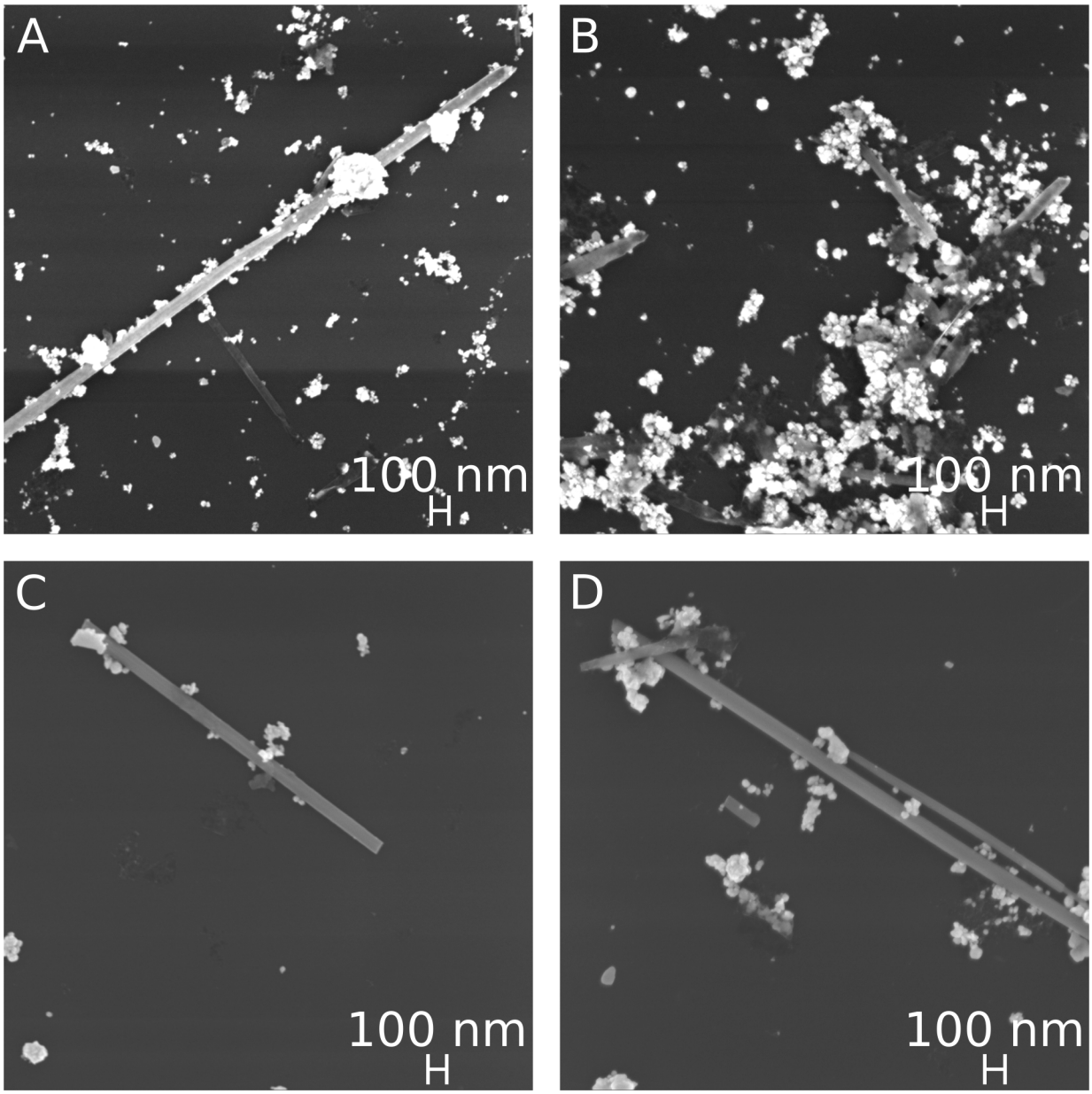

Figure 54: SEM images of gold-functionalized WS_2 nanotubes on Si with 2 (A-B) and 4 equivalents (C-D) of chloroauric acid employed. Image acquisition was performed with 5 kV acceleration voltage at x30 000 (A), x40 000 (B-C) and x43 000 (D) magnification.

To ensure that oxidation is not driven by degraded material in dispersion from sonication (which is normally removed in the liquid phase exfoliation step) and to gain deeper insights on the reaction pathways involved, functionalization with lower amounts of chloroauric acid was attempted on dispersions after liquid cascade centrifugation. The downside to this strategy is that molar equivalents cannot be calculated anymore. To nonetheless describe the system and ensure reproducibility across different dispersions, another relative substance amount ratio is calculated termed *extinction equivalents* in the following. Extinction equivalents are calculated by dividing the amount of chloroauric acid

concentration employed by the optical density of the WS_2 nanotube dispersion at 235 nm according to equation 22.

$$eq_{ext} = \frac{c(H[AuCl_4])}{OD(235\,nm)} \tag{22}$$

This type of equivalents is directly proportional to the molar ratio equivalents used earlier[6] and is easily converted to molar equivalents once an extinction coefficient at 235 nm is known for WS_2 nanotubes. Gold functionalization of nanotube dispersions after liquid cascade centrifugation was performed using 0.01 and 0.04 eq_{Ext} with the optical density of the nanotube dispersion fixed to $OD(235\ nm) = 2\ 1/\mathrm{cm}$. Normalized extinction spectra of the samples obtained after workup are shown in figure 55.

For functionalization in SC (A), no difference between 0.01 and 0.04 extinction equivalents is directly visible, as respective curves overlap largely. It is evident that the scattering contribution is decreased for *Stock* dispersions and increased in the removed aggregates compared to the starting material. This leads to apparent blue-shifts in the A exciton signal for dispersions after workup and red-shifts for the aggregated material. Similarly, the extinction ratio $Ext(235\ nm)/Ext(294\ nm)$ increases for *Stock* samples while it decreases for removed aggregates in comparison to the pristine starting material.

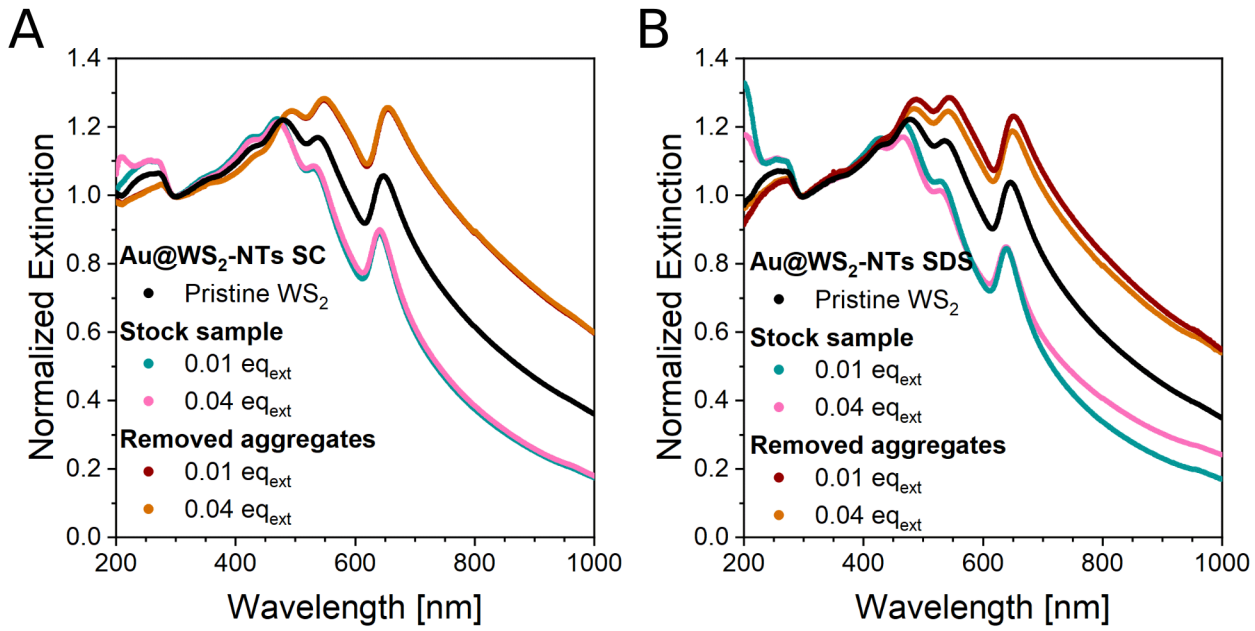

Figure 55: Extinction spectra normalized to the extinction at 294 nm of gold-functionalized WS_2 nanotubes obtained after treating WS_2 dispersions after LCC (100 - 3820 g) with 0.01 and 0.04 extinction equivalents of chloroauric acid and subsequent workup in SC (A) and SDS (B).

6 Since dispersion and reactant volume are maintained equal for all functionalization reactions presented.

In the case of TMD nanosheets, an increase in this extinction ratio is usually interpreted as a reduction in nanosheet size – a rational that cannot be directly applied here. However, it is noted that this trend was also visible within a multistep liquid cascade centrifugation employed for nanotube dispersions (see figure 52, A). Size-dependent trends in the optical spectra of WS_2 nanotubes sorted by liquid cascade centrifugation are reported in literature and similar changes in the extinction ratio $Ext(235\ nm)/Ext(294\ nm)$ were discerned although not discussed in detail.[236] In the published work, no change in nanotube length was reported upon size selection through liquid cascade centrifugation, only changes in tube diameter. Therefore, an interpretation of this extinction ratio needs more systematic experiments to properly correlate extinction ratios to nanotube dimensions, in particular it will be required to measure absorbance spectra with contributions from scattering removed, which can also impact extinction intensity ratios in the case of 2D materials.[21] The extinction spectra for functionalization in SDS show a similar behavior as in SC with marginal shifts of spectral features (figure 55, B). With these minor differences, functionalization appears to be similar across the two surfactant systems.

For further characterization, scanning electron microscopy images were recorded and are shown in figure 56. As no direct difference in functionalization behavior was evident for different chloroauric acid concentrations tested, only 0.04 eq_{ext} dispersions will be discussed in the following section.

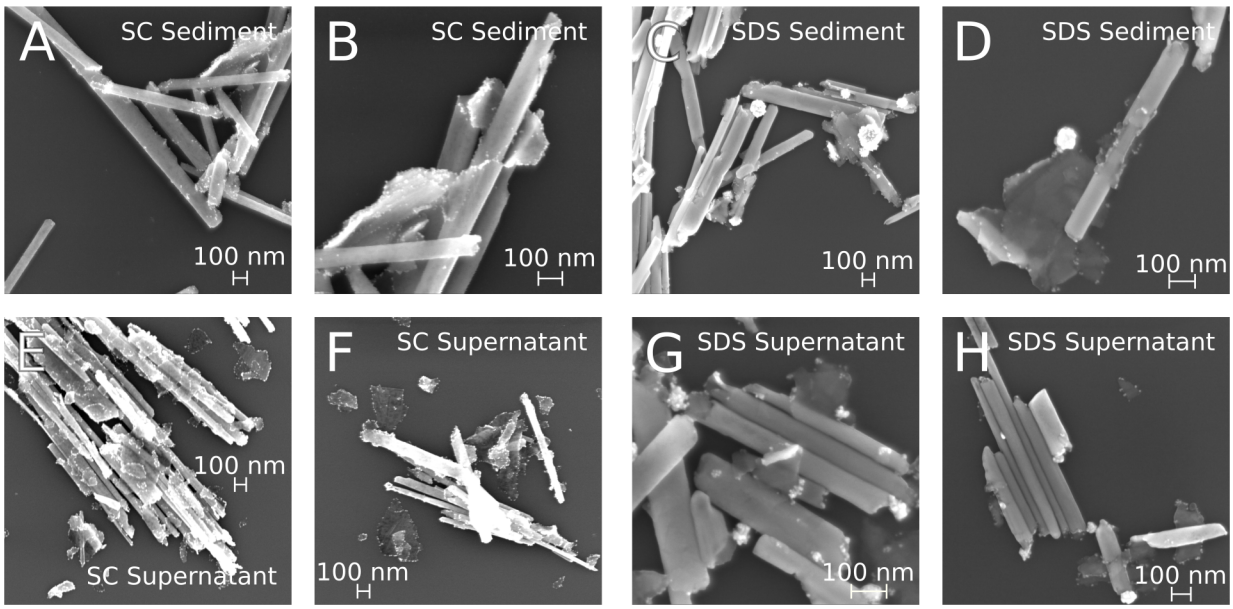

Figure 56: SEM images of gold-functionalized WS_2 nanotubes obtained after treating WS2 dispersions after LCC (100 - 3820 g) in SC (A-B, E-F) and SDS (C-D, G-H) with 0.04 extinction equivalents of chloroauric acid and subsequent workup. Both the removed aggregated material (A-D) and Stock dispersions (E-H) are shown. Imaging was performed with 5 kV acceleration voltage and varying magnifications.

In the material removed during workup after functionalization in SC (A, B) gold nanoparticles are visible on the surface of the WS_2 nanotubes. The tubular structure seems mostly intact although delamination of outer walls is visible occasionally in SC, best seen in B in figure 56. The delaminating layer shows small bright dots around the edges attributed to the formation of small gold nanoparticles in analogy to functionalization of nanosheets. Furthermore, sparse gold nanoparticle decoration is visible on the tubular structures. The delaminating layers visible in B do not appear to be monolayered based on the contrast, therefore, production of fewlayered nanosheets seems to occur during delamination. These products can be readily seen from SEM images of the *Stock* nanotube dispersion nanotubes shown in figure 56, E and F. Alongside WS_2 nanotubes, that appear to be relatively free of gold nanoparticles around the perimeter of the tubular structure, many nanosheet structures functionalized with gold nanoparticles are visible on the substrate and on the surface of the tubular structures. The basal plane of these nanosheets is largely free of gold nanoparticles, indicating that the protective function of SC as a surfactant also occurs for nanosheets delaminated from the tubular structures due to the oxidative treatment. Formation of such nanosheet structures was not observed in literature,[233] possibly due to oxidative degradation of delaminated nanosheets by the oxidant in absence of the surfactant.

This delamination mechanism visible in SC is seen in SDS as well. In figure 56, C and D, aggregated material removed during workup after functionalization in SDS is displayed. Similar to SC, production of edge functionalized nanosheets is visible (best seen in D), while in contrast to SC, larger gold nanoparticle clusters are present on the surface of the tubular structures as well as on the delaminated nanosheets. Formation of such structures is apparently suppressed in SC, but not SDS indicating that the outer wall surface – shielded in SC – is involved in the production of clusters. It should be noted that albeit molar equivalents are unknown, the amount of chloroauric acid added should be significantly lower compared to the amount employed for decoration of WS_2 nanosheets in SDS (4 equivalents). Therefore the severe nanosheet degradation observed in initial experiments in SDS might not be visible here and instead, the formation of clusters indicates the onset of heavy degradation for these lower equivalents of chloroauric acid. Furthermore, the production of delaminated nanosheet structures is apparently reduced in SDS as a lower number of nanosheets is visible. However, this was not quantified and can therefore not be assumed without doubt. This could be related to the consumption of a large share of the oxidant for the production of the gold clusters and therefore reduction in the number of delaminated nanosheets. This is further corroborated by a decrease in the nanoparticle density around nanosheet edges in SDS compared to SC.

In order to assess the precise position of gold nanoparticles on the tubular structures, TEM imaging was performed. The images are shown in figure 57. For functionalization in SC, nanotubes are found along with predominantly edge-functionalized nanosheets with the latter being significantly larger than what is typically derived from functionalization of LPE WS_2 nanosheets (figure 57, A).

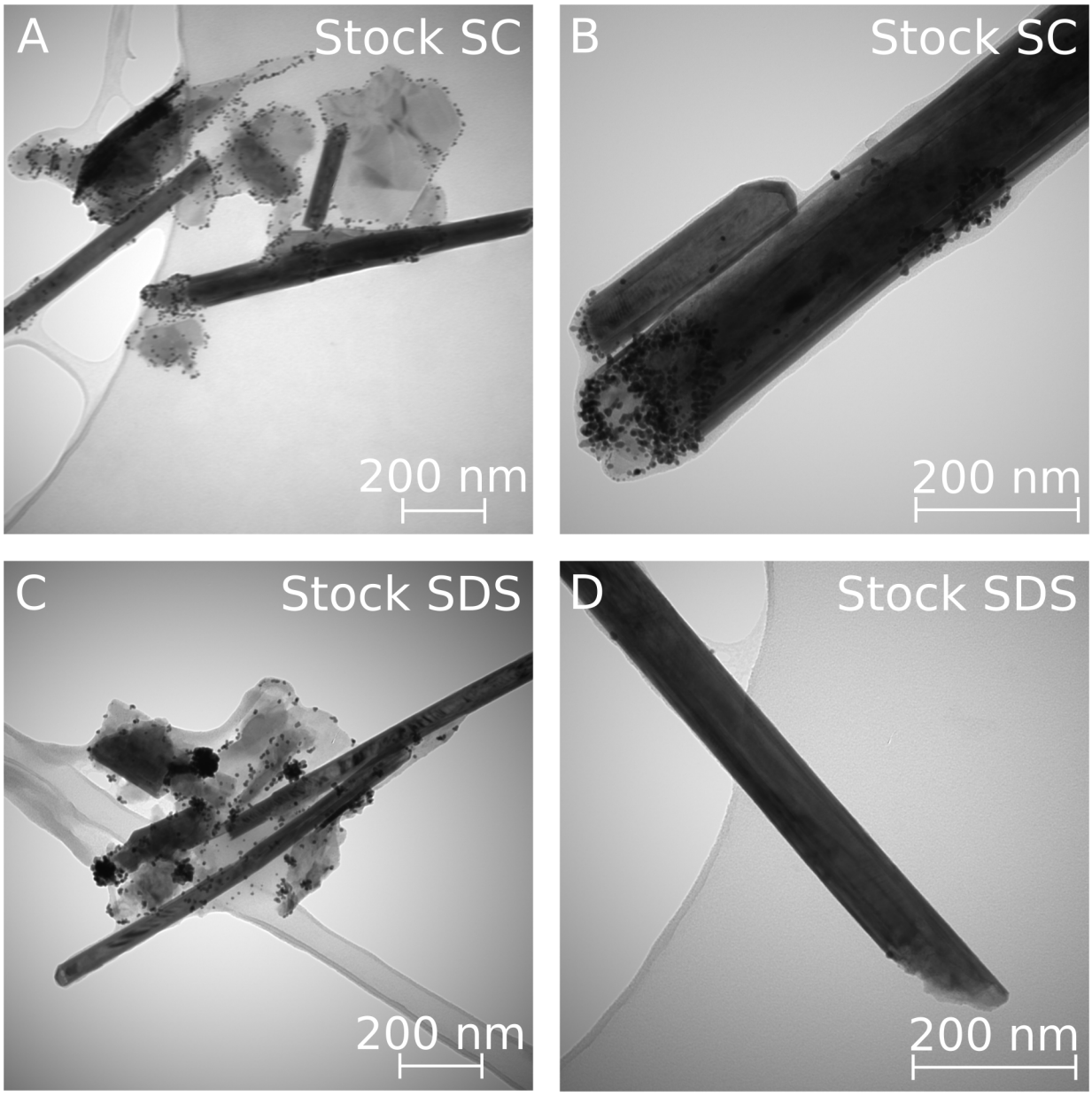

Figure 57: Transmission electron microscopy images of gold-functionalized WS_2 nanotubes after workup (Stock samples) for functionalization in SC (A-B) and SDS (C-D). All images were recorded using 120 kV acceleration voltage and x20 000 (A, C) and x40 000 (B, D) magnification.

In contrast to SEM, TEM is less surface sensitive and therefore features on the inside of nanotubes are visible. More small gold nanoparticles are visible in comparison to SEM imaging which are partially overlapping with the nanotube contrast, best seen in figure 57, B. Thus, many of the visible gold nanoparticles appear to be on the inside of the

nanotube. As depth information is lost with basic TEM imaging, this is hard to distinguish from gold nanoparticles on the outside of the tubular structure, but the lack of visibility of these gold nanoparticles in SEM imaging as well as the close proximity of the individual gold nanoparticles strongly suggests location on the interior of the nanotube. As nanotubes are multiwalled, each tubular layer has a separate WS_2 edge region on the ends of the tube which can be attacked by the oxidant. Furthermore, gold nanoparticles are not only found at tube ends, but also in regions further towards the center of the tube as evident from figure 57, B. This could serve as an explanation for the observed delamination of gold decorated nanosheets, as the production of gold nanoparticles in the interlayer space facilitates delamination through an increase in the interlayer distance and produces predetermined points for cleavage of nanosheets induced by the oxidation.

For functionalization in SDS, images are shown in figure 57, C - D. Again, gold-functionalized nanosheets are visible in addition to the tubular structures. Furthermore, the gold nanoparticle clusters are visible as black contrast in panel C. Nanosheet edge functionalization is much sparser compared to functionalization in SC in agreement with SEM imaging. Strikingly, functionalization at tube ends appears to be less pronounced than for functionalization in SC, as fewer nanoparticles are found on the tube ends that are hard to discern due to the different contrast in transmission. It appears that oxidative attacks in the interlayer space and around line defects dominate the functionalization in SC, but not in SDS, where an attack to surfaces exposed to the environment dominate. However, the exact origin of the gold nanoparticle clusters is unknown at this point and a link to an oxidation at the exposed surface area on the tube can only be hypothesized.

Since gold functionalization in SC produces relatively large amounts of larger gold-functionalized WS_2 nanosheets than accessible from LPE, a new route for the production of WS_2 nanosheets might be established based on this functionalization reaction. However, many nanotubes remain in dispersion after the employed functionalization protocol due to the low amounts of chloroauric acid used. Since higher molar equivalents of chloroauric acid do apparently not lead to the production of nanosheets (comparison figure 54), a protocol for the separation of nanotubes and nanosheets is required. Since figure 56 revealed an enrichment of WS_2 nanosheets in the *Stock* sample after workup, the removal of WS_2 nanotubes might be feasible using additional low-speed centrifugations. Therefore, purification through centrifugation at 200 *g* for 1 h is attempted on the *Stock* sample. SEM imaging was conducted to assess the share of nanotubes remaining in dispersion and respective images are shown in figure 58.

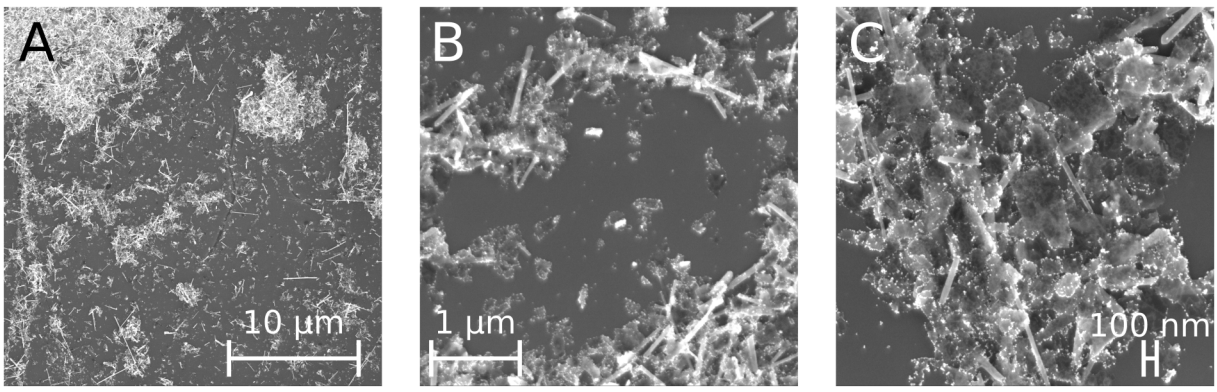

Figure 58: SEM images of gold-functionalized WS_2 nanotubes on Si after functionalization with 0.04 eq_{ext} and purification at 200 g for 1 h. Images were recorded with 5 kV acceleration voltage and x3 000 (A), x22 000 (B) and x40 000 (C) magnification.

In low magnification images (A) a significant portion of nanotubes is visible in addition to the targeted nanosheets. Although nanosheets with gold nanoparticles on the edges are visible on higher magnification (B - C), a significant portion of the sample is still composed of the higher mass multi-walled nanotubes. Thus, a higher selectivity of the purification is necessary. Therefore, purification was repeated[7] by centrifuging the dispersion twice at 200 *g* for 2 h and the sedimented material was removed after both steps. This was chosen as an alternative to centrifugation at increased centrifugal speeds as this will also remove large nanosheets. The efficiency of the separation was again judged based on SEM images shown in figure 59.

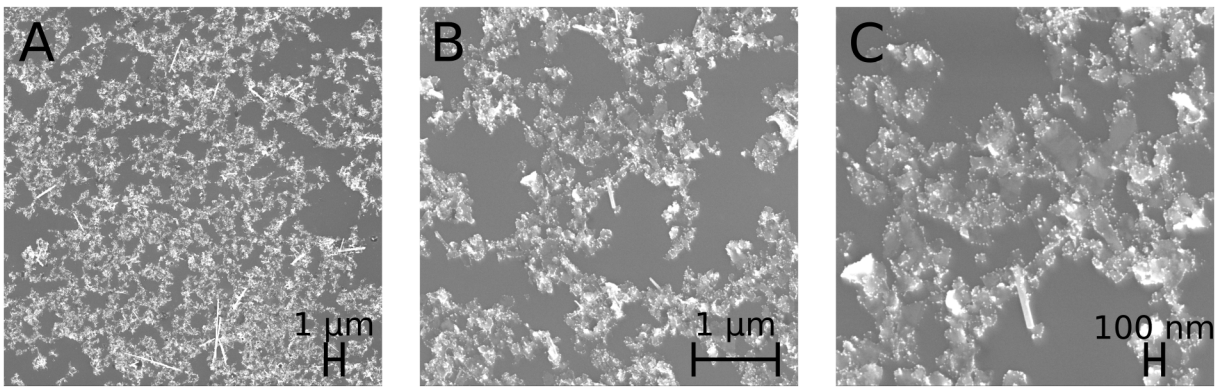

Figure 59: SEM images of gold-functionalized WS_2 nanotubes on Si after functionalization with 0.04 eq_{ext} and purification at 2 x 200 g for 2 h each. Images were recorded with 5 kV acceleration voltage and x4 000 (A), x20 000 (B) and x40 000 (C) magnification.

A significant decrease in nanotube content is evident from imaging at low magnifications (A), while a large number of nanosheets is retained. There are still nanotubes visible, however, as centrifugation is not able to selectively remove a single

7 To ensure comparability, fractions of the material previously separated during purification were reunified

species entirely. The nanosheets isolated are relatively large in lateral dimensions and gold nanoparticles are predominantly found along edges as observed before (B-C).

In order to assess the optical properties of the dispersion enriched in nanosheets, extinction spectra of the dispersions were measured and shown in figure 60, A. The characteristic spectral profile of WS_2 nanosheets is well discerned for the purified samples (pink and orange trace) and the scattering contribution is progressively reduced going from pristine nanotubes (black trace) to material removed during purification (teal trace) after nanoparticle decoration to purified samples enriched in nanosheets which show the lowest scattering contribution for the dispersion centrifuged twice (orange trace). Similarly, the extinction ratio $Ext(235\ nm)/Ext(294\ nm)$ increases with the described sequence. While a change in the lateral dimensions of the nanosheets cannot be excluded at this stage, such a pronounced change in the extinction intensity ratio would be related to a significant change in the nanosheet dimensions, if the sample was merely composed of the 2D objects. This is not apparent from the electron microscopic inspection so that it appears that this extinction ratio is generally larger for nanosheets than for nanotubes and the visible effect is related to progressive removal of tubular structures in the dispersions. Furthermore, blue-shifts in the A exciton signal in line with a decrease in the scattering contribution are visible and best visualized using the second derivative of the spectral region around the A exciton (figure 60, B).

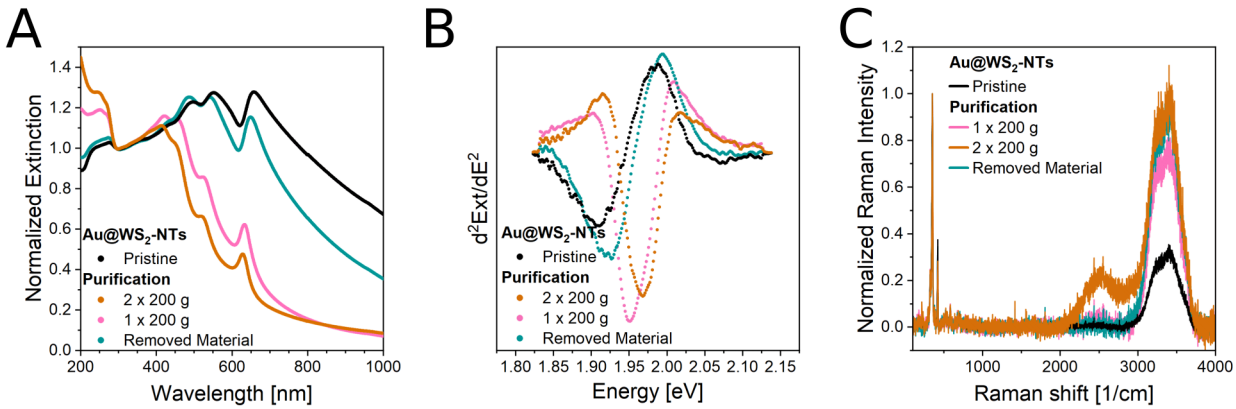

Figure 60: A) Extinction spectra of gold-functionalized WS_2 nanotubes for initial chloroauric acid treated dispersions as well as for dispersions produced during purification by centrifugation normalized to the extinction at 294 nm. B) Second derivative of the spectral region around the A exciton signal in A with respect to the photon energy of the incident light. C) Raman spectra ($\lambda_{exc} = 532\ nm$) of the same gold-functionalized WS_2 nanotube/nanosheet dispersions measured on a droplet of dispersion normalized to the intensity of the combined contributions of 2LA and E^1_{2g} mode of nanosheets and nanotubes respectively at 352 1/cm.[237-238] *The signal centered at 2500 1/cm is attributed to the photoluminescence of monolayered nanosheets, while the broad feature centered around 3500 1/cm is related to the Raman response of water.*

The A exciton is blue-shifted for functionalization and increasing nanosheet enrichment in purification. No splitting in the A exciton signal is visible, most probably due

to the presence of some remainig nanotubes in dispersion. However, as the monolayer content of the nanosheets in the dispersion is unknown, it may well be too small to resolve the monolayer contribution. To further investigate the optical properties of nanosheets after functionalization and purification, Raman spectra of the dispersions were measured and are shown in figure 60, C. Note that the broad signal between 3000 and 4000 1/cm is assigned to the Raman response of water. Raman modes expected for WS_2 are visible. The A_{1g}/E^1_{2g} ratio decreases from pristine nanotubes (black trace) over material removed during purification (teal trace) to purified samples with the lowest ratio for the dispersion centrifuged twice (orange trace). In the latter sample, PL of nanosheets is visible (centered at ~2500 1/cm), albeit weak. This indicates the production of intact monolayered nanosheets even though the volume fraction might be low. Different interpretations are possible to rationalize the PL/Raman ratio that is lower than in most LPE WS_2 dispersions after size selection. Either the monolayer colume fraction is small (compared to fewlayered nanosheets or nanotubes), or the structural integrity of the nanosheets delaminated from the nanotubes is impaired due to oxidation on the basal plane. To assess the actual monolayer content as well as average lateral nanosheet dimensions, statistical evaluation of AFM images is conducted and presented in figure 61, A-C. The arithmetic average nanosheet dimensions are summarized in table 5. A selection of AFM images used for statistical evaluation are shown in the appendix 8.10.

Table 5: Arithmetic average nanosheet dimensions derived from AFM statistics for WS_2 nanosheets isolated from delamination in a chloroauric acid treated nanotube sample compared to the WS_2 area to thickness aspect ratio from conventional LPE.

	$\langle L \rangle$ [nm]	$\langle W \rangle$ [nm]	$\langle h \rangle$ [nm]	$\langle A \rangle$ $(L \cdot W)$ [nm^2]	$\langle k \rangle$ (L/W)	$\langle k_\perp \rangle$ (A/h) [nm]
Tube delamination WS_2	122.9	85.1	7.9	13 391.6	1.5	2116.6
LPE WS_2	-	-	-	-	-	1085.7

The thickness distribution displayed in figure 61, C shows an average thickness of 7.9 nm and therefore confirms that nanosheets are predominantly fewlayered. This serves as an explanation for the low photoluminescence due to a low volume fraction of monolayers.

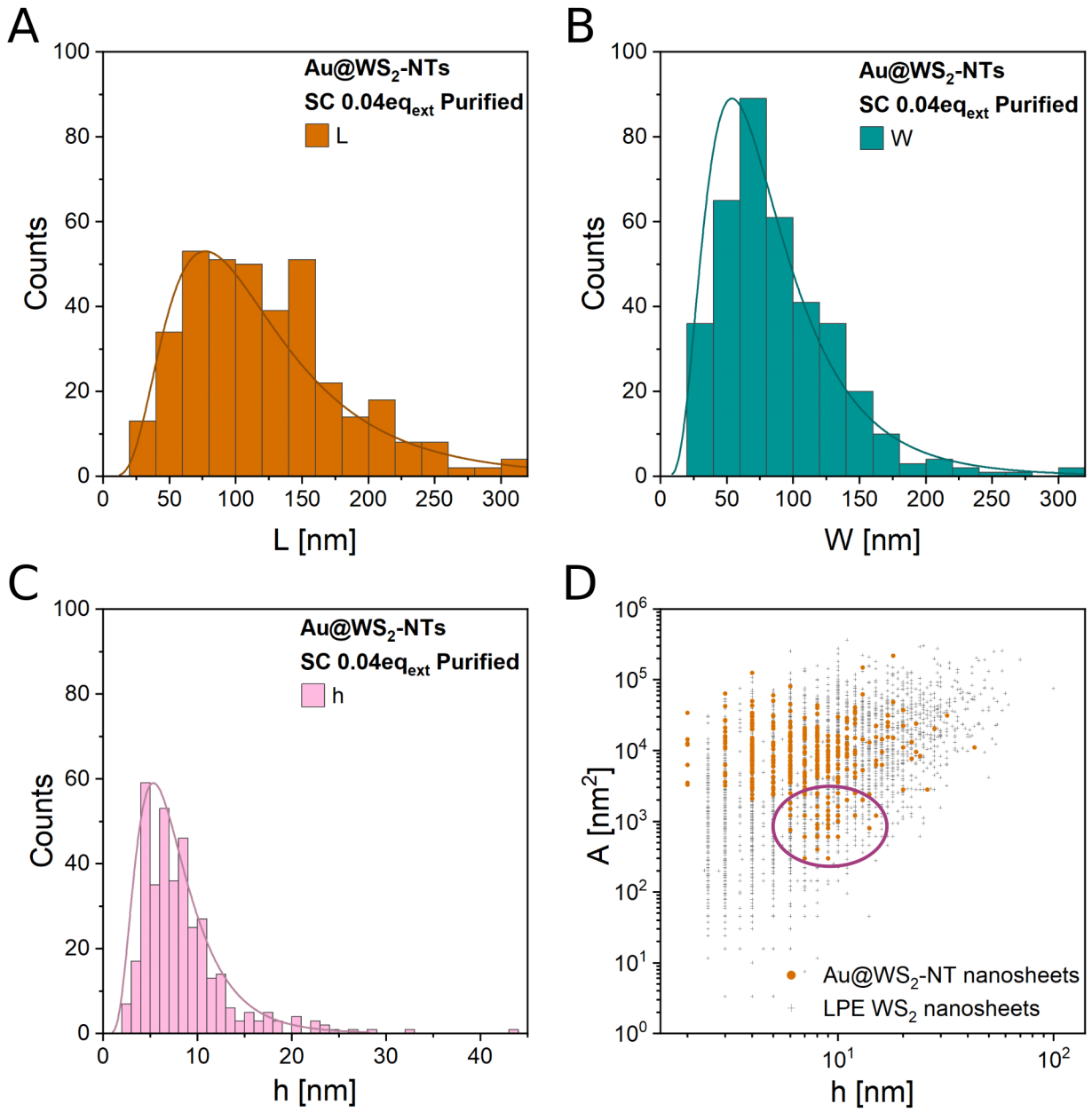

Figure 61: A-C) Results of the statistical analysis of nanosheet dimensions produced from chloroauric acid treated nanotubes based on an analysis of AFM images in terms of the longest dimension termed L (A), lateral dimension orthogonal to L termed W (B) and nanosheet thickness termed h (C). D) Scatter plot of nanosheet area calculated as $L \cdot W$ versus the sheet thickness h for nanosheets enriched from chloroauric acid treated WS_2 nanotubes in comparison to conventional WS_2 nanosheets produced through liquid phase exfoliation. Reference data was supplied by Claudia Backes and layer number was converted to thickness using $h = N \cdot 1.9\ nm + 0.5\ nm$. The elliptic shape highlights an anomaly in the scatter cloud.

An important parameter for 2D materials is the area to thickness aspect ratio. As discussed in the previous section, it is extremely difficult to increase this aspect ratio in conventional LPE. The visual inspection of the nanosheets delaminated from the nanotubes due to the oxidative attack of chloroauric acid suggested that the produced nanosheets are laterally larger than the typical dimensions of LPE nanosheets. It is thus of

great interest to investigate, whether they indeed have higher area to thickness aspect ratios. As summarized in table 5, the area to thickness aspect ratio $<k_{\perp}>$ is doubled for nanosheets derived from gold functionalization of nanotubes compared to LPE nanosheets. Note that this is a conservative estimate, as the Au nanoparticles increase the apparent AFM heigth, thus underestimating the aspect ratio compared to the conventional LPE WS_2. In terms of dimensionality, the nanosheet quality is improved for nanosheets derived from gold functionalization.

This is further corroborated by the scatter plots of nanosheet area versus thickness for gold-functionalized nanosheets from nanotube functionalization and LPE WS_2 as reference shown in figure 61, D. While very thin nanosheets < 4 nm are relatively scarce in the sample derived from chloroauric acid treatment of WS_2 nanotubes, the scaling of nanosheet area with thickness characteristic of LPE WS_2 is not apparent. Importantly, the lateral dimensions are widely independent of the nanosheet thickness, i.e. the thin nanosheets are laterally significantly larger than for conventional LPE WS_2. As such, the chloroauric acid treatment of nanotubes is capable of producing (gold-functionalized) WS_2 nanosheets with a higher area to thickness aspect ratio. This is important, as the area to thickness aspect ratio was recently identified as an important factor for the network conductivity of LPE materials.[193]

An anomaly in the data cloud is highlighted using a purple indicator that shows a separate data cloud forming at smaller nanosheet areas and intermediate thicknesses. This is most likely related to gold nanoparticle aggregates or small tube fragments not easily discernible in AFM imaging that can bias the statistics. These particles obviously reduce average nanosheet area in statistics and underline that more efficient means of dispersion purification are necessary. If an efficient purification protocol can be established in future works, this method can be considered as a potential method for production of high quality nanosheets. However, nanosheet yields are very low in general, presumably due to the trade-off between efficient delamination and severe destruction. In conjunction with the poor availability of WS_2 nanotubes compared to bulk layered material, the procedure is hard to justify economically at this point and only of interest for academia, for example to unravel fundamental aspects of the charge transport in networks. However, to achieve this, it is important to devise strategies for a reliable nanosheet deposition which will be addressed in the subsequent chapters of this thesis.

5 Film deposition

In order to judge the impact of certain modifications or processing techniques towards properties of layered materials for e.g. device applications, processing of films from nanomaterials in dispersion is usually required. In addition, film production from dispersed nanomaterials is often necessary in the academic field, as anisotropic properties are generally lost in dispersion due to a random orientation of the dispersed constituents. In fact, almost any application and most advanced characterization techniques require solid samples. However, film deposition of layered nanomaterials faces the intrinsic problem of sheet restacking which degrades the unique properties of exfoliated nanosheets and restores bulk-like behavior if it happens in excess. Therefore, a straightforward method for film production from dispersions of layered nanomaterials is sought for, which is capable of translating dispersion properties of isolated sheets in dispersion to properties in the film. Thin-films, where nanosheets form an extended network on a substrate with minimal basal plane overlap are of particular interest, especially in light of the fabrication of heterostructures from different 2D materials, as substrates to study on-substrate functionalization, or to improve the alignment of the nanosheets, which was shown to result in an increased network conductivity important for many application areas. In the following, two methods for film production will be discussed and compared.[193]

5.1 Airbrush Spray Deposition

A straightforward method for production of films from liquid dispersions is usually evaporation of the used solvent, often done by deposition on a substrate and heating of the underlying substrate. Since simple deposition of a liquid droplet with subsequent solvent evaporation produces so-called *coffee rings* and therefore films with very uneven coverage,[199] more elaborate methods for liquid deposition and subsequent solvent evaporation than drop casting are used. An example of such a method is airbrush spray deposition. In contrast to other printing strategies, requirements to the rheological properties of the ink are minimal.[198] In airbrush spraying, a liquid dispersion is sprayed on a heated substrate through a nozzle using a gas jet as propellant. Such airbrush guns are commercially available which aids the implementation of the method. As production of nanomaterial aerosols can pose significant health threats, an enclosure for airbrush spray deposition is necessary. The custom deposition setup used in this work is shown in figure 62, A-B. The enclosure is a ventilated box in which the airbrush gun is fixed in a bracket outside the enclosure (1) pointed at a heat stage (2) mounted on top of a lifting stage (4). The lifting stage enables an adjustable spraying distance (z direction) while movement in the x direction (left to right in A) is motorized. For motor control, limiter

switches are attached (3) to enable calibration of center position. Position along y direction is fixed and centered with respect to the airbrush gun bracket.

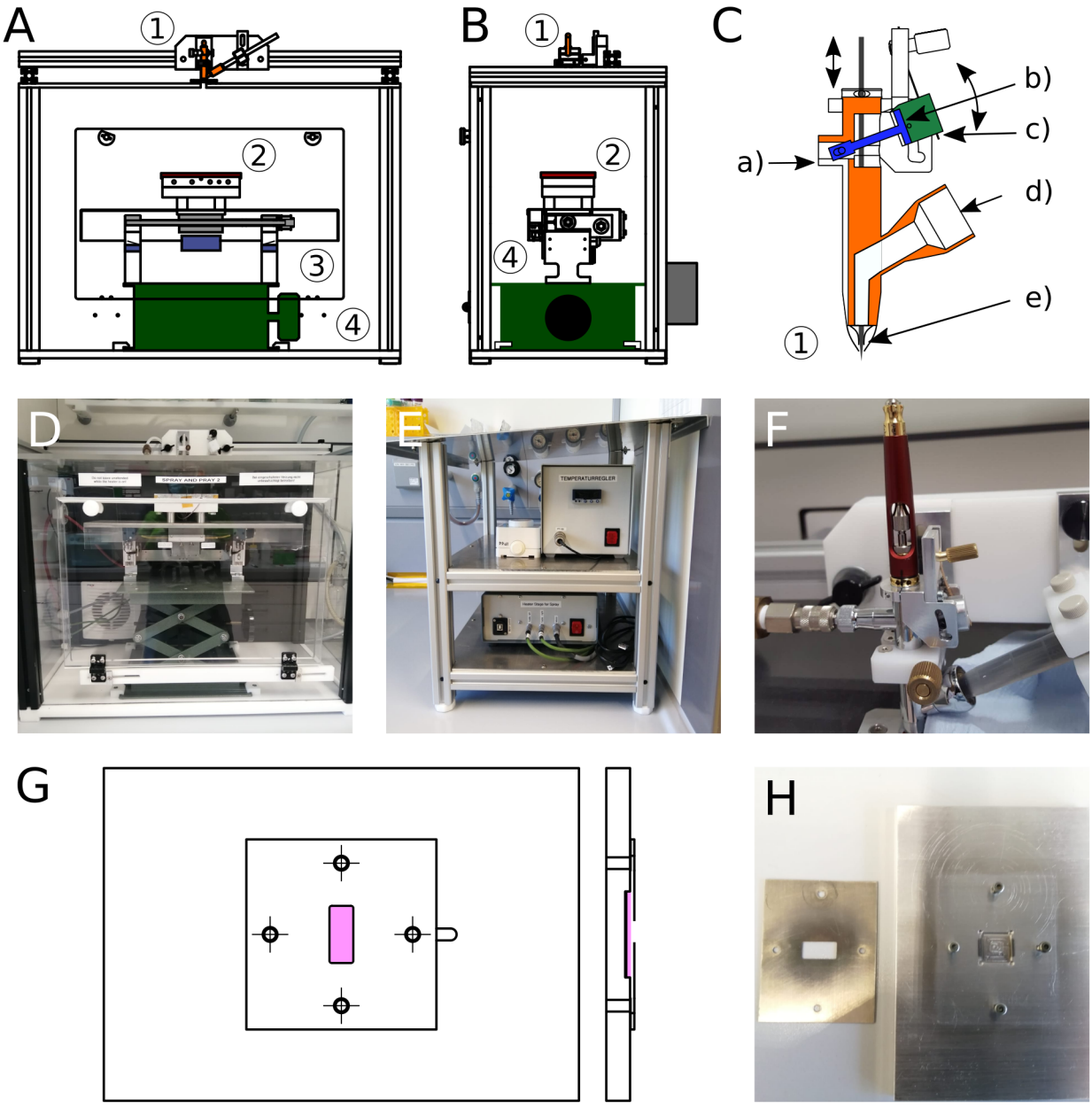

Figure 62: A) Schematic of the airbrush spray enclosure, front view. B) Schematic side view of the airbrush enclosure. Relevant parts are highlighted in color in A and B: airbrush guns (1, orange), heat stage (2, red), limiter switches (3, blue) and lifting platform (4, green). C) Schematic view of the airbrush gun interior, relevant parts are labeled: propellant inlet (a), gas vent trigger and needle lift (b, blue), home built auto fire button (c, green), ink inlet (d) and spray cone outlet (e). D) Photography of the built airbrush enclosure. E) Photography of the stage control tower. F) Installed airbrush gun equipped with home built auto fire button. G) Schematic top (left) and side view (right) of the shadow mask (12 x 4 mm opening) and substrate holder. H) Photograph of the shadow mask (stainless steel, left) and substrate holder (aluminum, right).

The commercially available airbrush gun uses a gaseous propellant (N_2 at 1 bar over pressure, a) in figure 62, C) entering through a trigger activated vent. When pushed in, the

trigger (b) can be moved upwards to raise the central needle (grey in C) which enables the dispersion to leave the ink reservoir (d). The dispersion then leaves through the nozzle (e) where the aerosol is immediately formed by the propellant jet. Deposition occurs in a spray cone and the size of the sprayed cone on the substrate depends on the propellant pressure as well as on the spraying distance. The needle opening is based on the movement range of the trigger (b) and therefore ink consumption can be adjusted. As commercial airbrush guns are usually handheld devices no option for continuous operation is built in. Therefore an auto fire button was built that fixes the spraying trigger in firing position (c in figure 62, C, green). Photographs of the home built enclosure are displayed in figure 62, D. Both stage temperature and stage movement are controlled from the outside control tower (figure 62, E). The installed airbrush gun equipped with the auto fire button is depicted in figure 62, F. The nanomaterial ink is continuously fed into the gun using a cut to size 10 ml plastic pipette tip. The substrate itself is placed on an aluminum substrate holder and a stainless steel shadow mask with 0.4 cm slit width is placed on top of the substrate (figure 62, G-H). The substrate stage is heated to 90 °C and performs a looped movement for a specific distance around the center. The developed script used for stage movement is found in appendix 8.11.

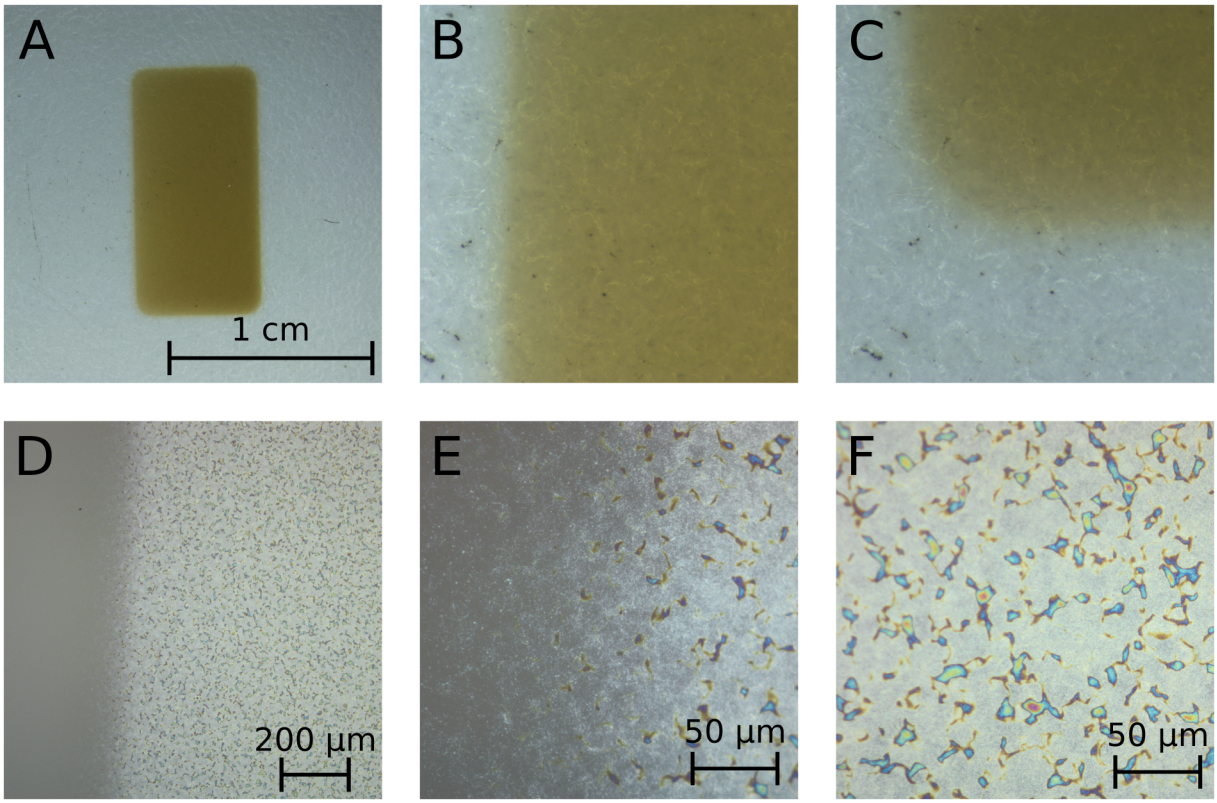

Figure 63: A-C) Digital microscopy images of WS_2 nanosheet (M) films deposited from IPA via airbrush spray on glass of the whole (A) and magnified parts of the film (B-C). D-F) Optical microscopy images of WS_2 nanosheet (L) films deposited from IPA via airbrush spray on glass with x10 (D) and x50 objective (E-F).

For assessment of optical properties of the films, spraying on glass substrates was conducted. WS_2 dispersions of varying sizes (*L*, *M*, *S*) were therefore transferred to IPA to enable deposition at 90 °C for this study. However, deposition directly from aqueous dispersion is possible and was conducted at 130 °C in other experiments. Example microscopy images of films sprayed from IPA onto glass substrates are shown in figure 63. Digital microscopy images of a WS_2 nanosheet film produced via airbrush spray deposition of medium-sized nanosheets in IPA are shown in figure 63, A-C. The shape of the shadow mask is well reproduced with good contrast (A) and the characteristic yellow color of diluted WS_2 dispersions is retained. Edges along the longitudinal direction are well defined with bare eye (B), but at corners a curvature is visible (C) due to the technique employed for shadow mask fabrication. For deposition on 10 x 10 mm substrates, for which the shadow mask was tailored, curved edges are absent due to overspray. Optical microscopy images of longitudinal edges in figure 63, D-E reveal a fade out effect of deposited material related to a certain degree of material migration under the shadow mask. This is likely caused by an imperfect contact of the shadow mask and the substrate and possibly impacted by thermal expansion, as substrate holder and shadow mask are fabricated of different metals and probably slightly deform upon heating. In figure 63, F an image of the inner film area with high magnification is shown and reveals continuously distributed iridescent features in the film. These are likely holes or aggregates, although this cannot be distinguished based on optical microscopy alone. However, a certain degree of microscopic inhomogeneity is expected due to the presence of such features. Presumably deposition at higher propellant pressures could alleviate this issue, as material is then more finely dispersed. However, no variation in propellant pressure was studied in this work.

In order to better resolve the observed features, films were deposited on conductive glassy carbon substrates to enable scanning electron microscopy imaging. Representative images are shown in figure 64. At low magnifications (A-C) the iridescent features observed in figure 63, D-E reappear as ruptures in the film surface. On closer inspection, these ruptures are partially filled with nanosheets, indicating formation during film deposition. As such, strain induced film segregation or insufficient dispersion during airbrush deposition may be hypothesized. However, the exact origin of these ruptures is not known. For higher magnifications on non-ruptured film regions, randomly orientated nanosheets are visible for all sizes, rendering the films porous with decreasing porosity for decreasing nanosheet sizes in accordance with literature.[177] Pore formation is possible due to the randomized nature of the deposition method and the relatively high area to thickness aspect ratios of layered nanomaterials.

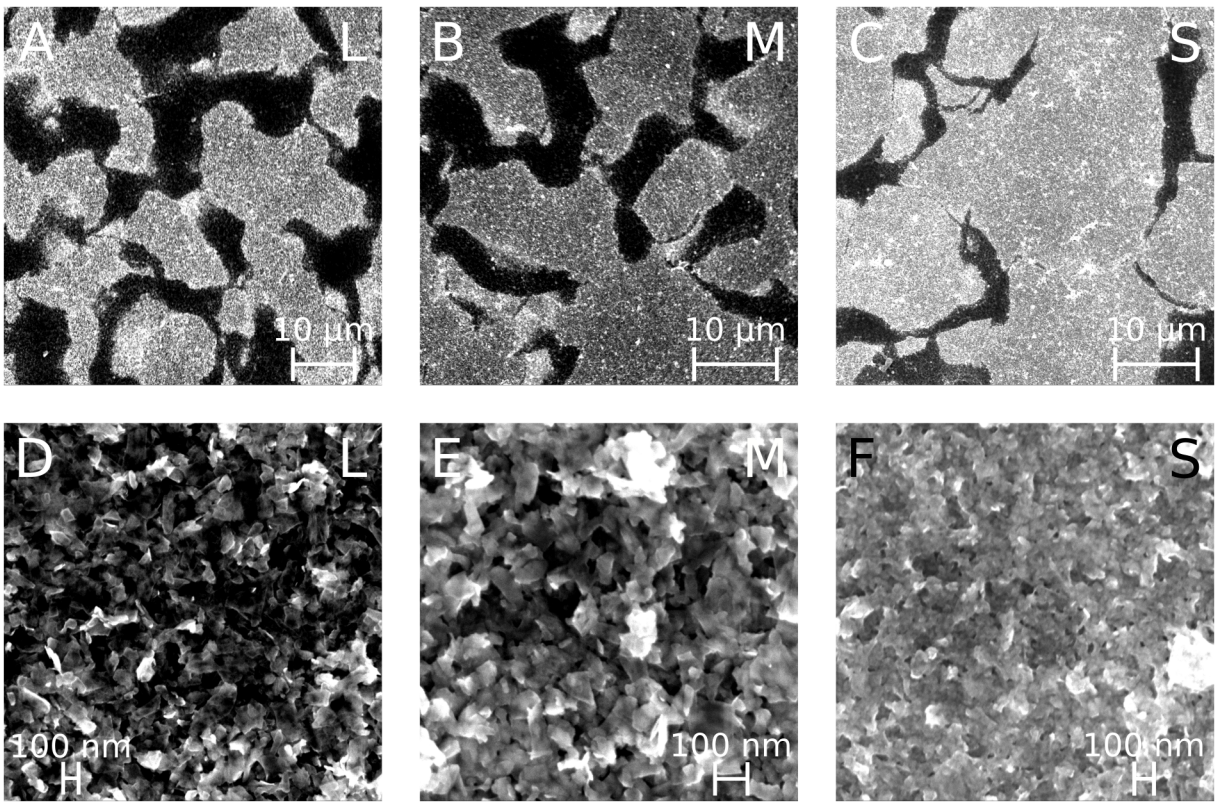

Figure 64: A-F) SEM images of WS_2 nanosheet films of varying sizes (L in A, D, M in B, E and S in C, F) deposited on glassy carbon via airbrush spray at low (A-C) and high magnifications (D-F). All images were recorded at 5 kV acceleration voltage and x1 500 (A), x2 000 (B-C), x40 000 (D), x50 000 (F) and x80 000 (E) magnification.

Due to random nanosheet deposition via airbrush spraying, random restacking of nanosheets is expected and therefore optical properties of exfoliated nanosheets should degrade and shift to a more bulk-like behavior. The optical properties of WS_2 films on glass were assessed using extinction as well as Raman spectroscopy and are shown in figure 65. In the extinction spectra of WS_2 dispersions transferred to IPA (A) size-dependent trends of WS_2 as observed for aqueous SC solution are well retained and for dispersions with high monolayer contents (S, orange traces in figure 65) the A exciton shows a peak and a shoulder in the raw spectra according to expectation. After airbrush spray deposition on glass slides at 90 °C, size-dependent trends become less pronounced as traces converge largely (figure 65, B). Only in the A exciton signal, a size-dependent blue-shift is still visible, however far less pronounced than for the nanosheets in IPA dispersion. Furthermore, the signal width increases, the A exciton response is red-shifted compared to the initial dispersion and no splitting in the A exciton signal is visible anymore for the sample containing small/thin nanosheets. In addition, the excitonic resonances are superimposed on a featureless background best discerned in the non-resonant region of the spectrum (> 700 nm).

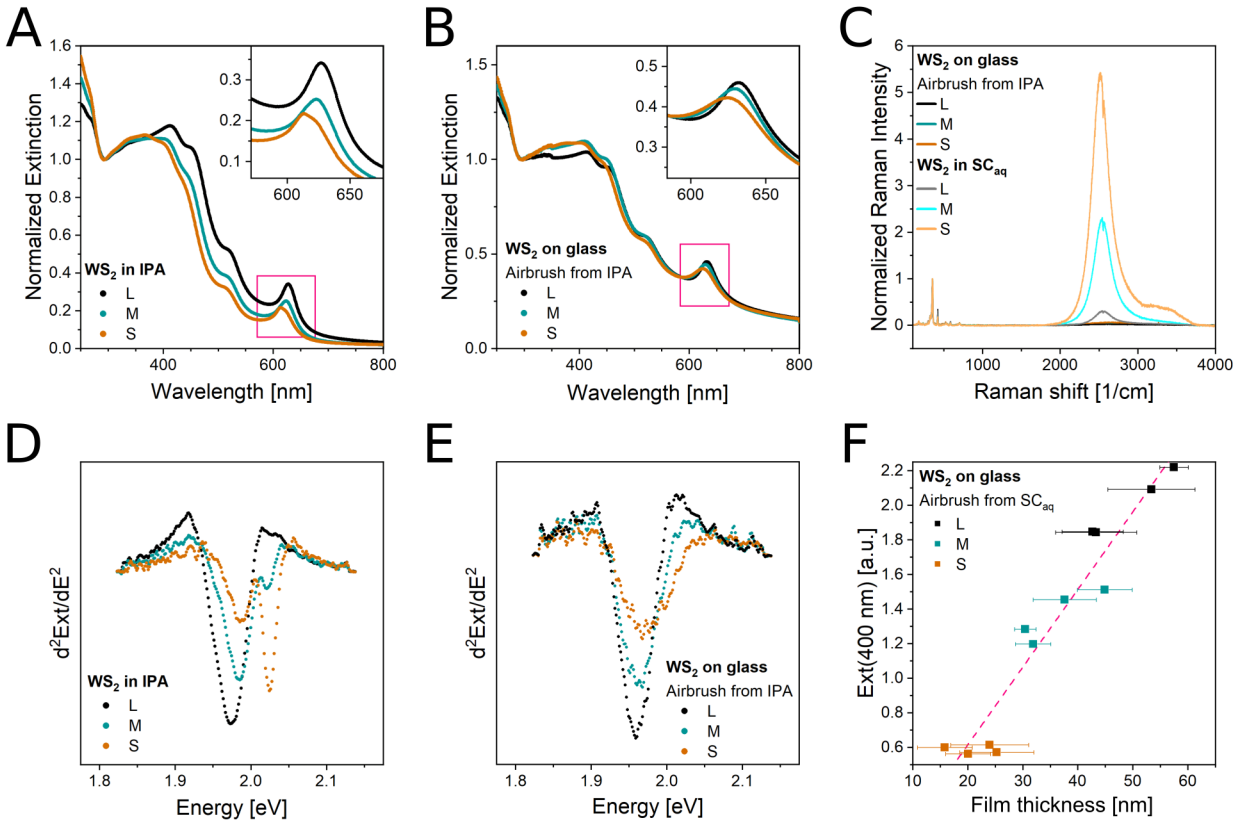

Figure 65: A) Extinction spectra of WS_2 nanosheets in IPA for various nanosheet sizes normalized to the extinction at 294 nm. Inset: enlarged view of the spectral region around the A exciton signal. B) Extinction spectra of WS_2 nanosheet films deposited from IPA via airbrush spraying of the size-selected dispersions normalized to the extinction at 294 nm. Inset: enlarged view of the spectral region around the A exciton signal. C) Raman/PL spectra of WS_2 nanosheet dispersions in aqueous SC solution (light traces) measured on a droplet of the dispersion and of films deposited from IPA via airbrush spray (bold traces) measured on the film surface (λ_{exc} = 532 nm). Five spectra are averaged each, a baseline was subtracted and the spectra were normalized to the 2LA mode. D) Second derivative of the spectral region around the A exciton signal in A with respect to the photon energy of the incident light. E) Second derivative of the spectral region around the A exciton signal in B with respect to the photon energy of the incident light. F) Extinction at 400 nm plotted versus film thickness derived from profilometry for various WS_2 films deposited from size-selected fractions in aqueous SC solution at 130 °C via airbrush spraying. Panel F is reproduced from literature and shown for reference.[217] *Samples in A-E are labeled with L for large (0.4 - 1k g, $\langle L \rangle$ = 141 nm, $\langle N \rangle$ = 7), M for medium (1 - 6k g, $\langle L \rangle$ = 68 nm, $\langle N \rangle$=5) and S for small (6 - 30k g, $\langle L \rangle$ = 40 nm, $\langle N \rangle$ = 2) and samples in F are labeled with L for large (0.4 - 1k g, $\langle L \rangle$ = 140 nm, $\langle N \rangle$ = 8), M for medium (1 - 6k g, $\langle L \rangle$ = 66 nm, $\langle N \rangle$=5) and S for small (6 - 30k g, $\langle L \rangle$ = 41 nm, $\langle N \rangle$ = 2) in order to illustrate changes in relation to the average lateral size $\langle L \rangle$ and average layer number $\langle N \rangle$ of the WS_2 dispersions. $\langle L \rangle$ and $\langle N \rangle$ were determined from extinction spectra in aqueous sodium cholate using published metrics and assumed to be constant after transfer to IPA.*[8]

The A exciton is further analyzed via the second derivative with respect to the photon energy of incident light. In contrast to the nanosheets in IPA dispersion (figure 65, D), no monolayer contribution to the A exciton signal can be discerned after deposition as thin-films (figure 65, E). Apparently, all monolayered material in dispersion loses its

characteristic properties upon deposition, most probably due to random restacking and electronic coupling of monolayers to other nanosheets in the film. Thermal degradation could pose another source of this behavior and although a certain thermal instability of WS_2 is known in literature,[239] complete oxidation of all monolayered material upon film deposition appears unlikely, as deposition takes only about 30 minutes.

If random restacking took place, its effect should be well visible as a significant decrease in photoluminescence from WS_2 nanosheets. Therefore, Raman spectra of nanosheet films were measured and are compared to the respective nanosheet dispersion in aqueous SC solution produced by liquid phase exfoliation and subsequent liquid cascade centrifugation (figure 65, C). Note that the IPA dispersions cannot be measured under comparable conditions due to the volatility of the solvent. Normalized photoluminescence is completely quenched in films deposited via airbrush spray. This further corroborates the idea of random restacking and is in agreement with the interpretation of the extinction spectra.

As thicknesses of films produced using airbrush spray deposition depend on the amount of material injected, film thickness is very well scalable. However, due to changes in film porosity, a certain impact of nanosheet sizes on the film thickness is expected. A correlation of film thickness and color was established in previous works after deposition of a fixed amount of nanosheets (700 mg) and subsequent profilometry (figure 65, F).[217] A clear linear correlation between film thickness and extinction at 400 nm is visible. Films produced from small nanosheets are significantly thinner compared to larger nanosheets. This is most probably related to changes in film porosity due to changes in average nanosheet size $<L>$ and not to changes in average layer number $<N>$ as orientation of nanosheets is randomized. A dependence on $<N>$ is only expected for aligned films however, as $<L>$ and $<N>$ are intrinsically correlated with liquid phase exfoliation and subsequent liquid cascade centrifugation, these effects cannot be discerned.

Overall, benefits of the airbrush deposition method are facile film production and the possibility of patterning of the produced films as well as straightforward production of composite films with other nanomaterials e.g. conductive carbon nanotubes[177, 217] or insulating *h*-BN nanosheets (see appendix 8.12). As such, film properties can be tailored. Even though airbrush spray deposition is a facile method for the production of films with scalable thickness, it is evident that optical properties of the original nanomaterial are not well transferred to the film and hence, other means of film deposition are explored in the following section.

5.2 Modified Langmuir-Schaefer film deposition

In recent years, modified Langmuir-Schaefer nad Langmuir-Blodgett deposition has evolved as promising film deposition method[190-191, 240] with numerous advantages: Due to the lack of substrate heating, thermally sensitive materials do not degrade. Furthermore, random restacking is suppressed as the stabilizing medium is usually removed after the film is already formed. With high aspect ratio nanomaterials, such as nanosheets, control over the alignment can be achieved which is beneficial for charge transport, as well as to retain the properties of the individual platelets in the film. A method for nanosheet film formation that fulfills all of the outlined criteria is film formation at a liquid-liquid interface which will be referred to as modified Langmuir-Blodgett or modified Langmuir-Schaefer deposition in the following, in contrast to conventional Langmuir-Blodgett procedures, where film formation happens at the liquid-air interface. For this, a small volume of a dispersion is either injected or mechanically transferred into the interface between two immiscible solvents with high interfacial tension. This method has been employed for film deposition of layered nanomaterials in the past with e.g. n-hexane/water or octadecene/dimethlyformamide interfaces.[190, 192] For preliminary tests, a small volume (25 ml) glass beaker was filled with 25 ml deionized water and 2 ml of *n*-hexane was layered on top. The WS_2 dispersion transferred to IPA is then added to the wall of the glass beaker and a yellow film forms at the interface. This is schematically shown in figure 66.

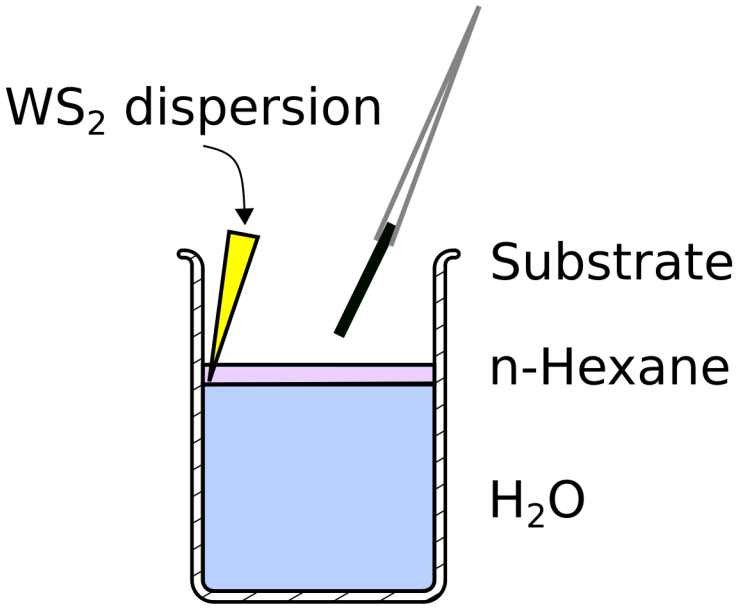

Figure 66: Schematic of the initial deposition setup to produce thin-films after preassembly of the nanosheets at the liquid-liquid interface.

The film is then transferred to a substrate by manual immersion of a glass slide orthogonal to the interface and retraction at an angle. Whether the method is termed modified Langmuir-Blodgett or modified Langmuir-Schaefer deposition depends on the alignment of the substrate relative to the preformed film. WS_2 was chosen for deposition

tests due to its well understood optical properties with clear indicators for changes in morphology. It was quickly found that complete removal of the *n*-hexane layer prior to transfer is beneficial for the film quality, as it improves adhesion to the substrate. Therefore, *n*-hexane is removed using a pipette as complete as possible after the film is formed and leftover solvent is evaporated at ambient conditions after transfer onto the substrate. Furthermore, dispersion volumes were ideally kept low (100 µl), as excessive IPA injection disturbed the formed interface and low volume, high concentration dispersions were best suited for deposition. An impact of the WS_2 concentration in dispersion on the film quality can be seen in figure 67. At low magnifications in digital microscopy, holes and cracks in the films are visible and large scale inhomogeneity is evident for both concentrations employed in digital microscopy (figure 67, A and D). For the film formation at the liquid-liquid interface, only some minor inhomogeneities were visible, but not to the extent after film transfer to the substrate. Therefore, manual immersion and retraction of the substrate may be seen as a possible source of macroscopic degradation of film quality.

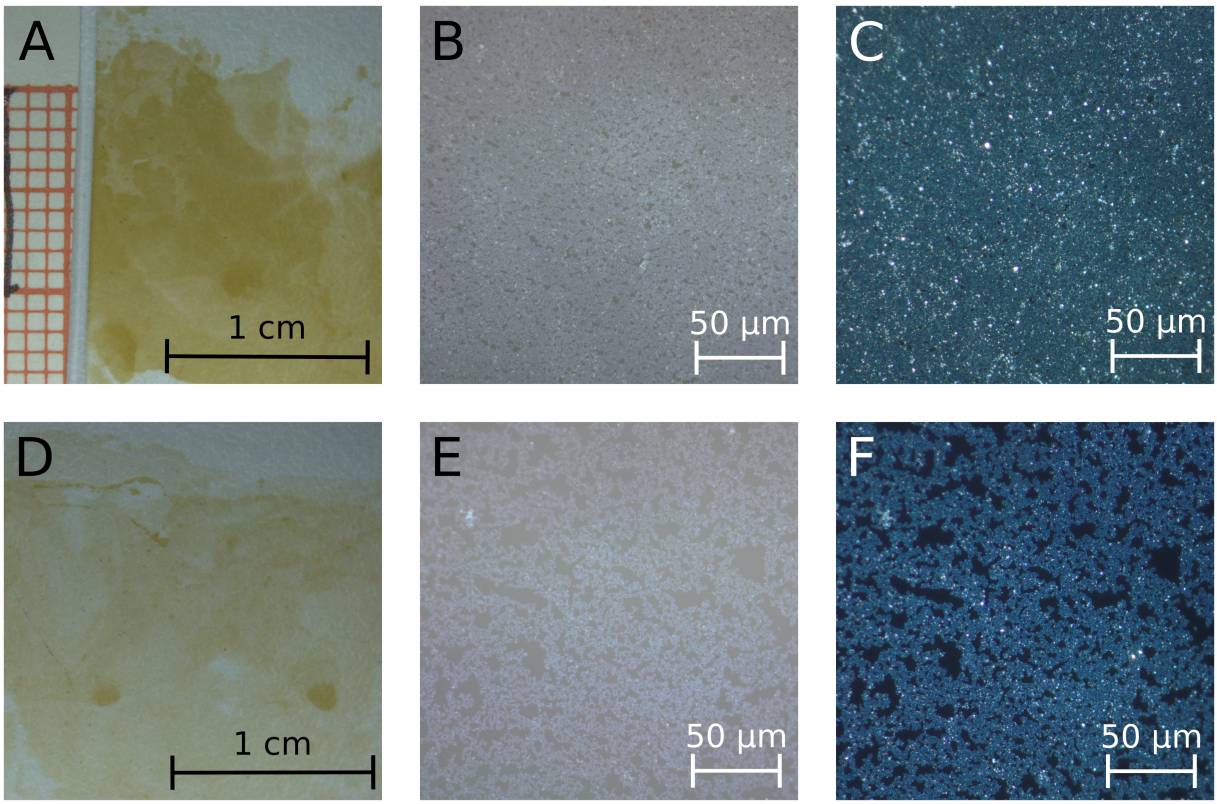

Figure 67: Digital (A, D), bright field (B-C) and dark field (E-F) optical microscopy images of WS_2 films on glass deposited via modified Langmuir-Blodgett deposition with the initial setup using L nanosheets (0.4 - 1k g). The concentrations of the dispersions used for the deposition are 1.6 mmol/l in A-C and 0.8 mmol/l in D-F. Optical microscopy images were recorded using a x50 objective.

At higher magnifications in optical microscopy on intact regions of the film (figure 67, B and E), the surface appears largely homogeneous. This is further corroborated by dark

field images at identical magnifications (figure 67, C and F), as contrast is relatively even and no bright reflexes are visible[8]. The effect of the ink concentrations is well visible, as holes in the film are small when using a higher concentration dispersion (B-C) and increase significantly in E-F for lower ink concentration. For an analysis of the optical properties of the films, extinction and Raman spectroscopy was performed on films produced from nanosheets of varying sizes (labeled *L*, *M* and *S*). The respective spectra are shown in figure 68. For extinction spectroscopy, two films are measured each to assess the reproducibility of the deposition (figure 68, A). Pronounced trends with nanosheet size are visible in the normalized extinction in contrast to films deposited via airbrush spray (compare figure 65, B). Films of equal nanosheet sizes nicely converge and therefore indicate good reproducibility of the method. Size trends in the extinction ratio *Ext(235 nm)/Ext(294 nm)* are inaccessible due to increasing absorption of glass substrates. The inset in figure 68, A shows a clear blue-shift of the A exciton signal with decreasing size and the characteristic lineshape of two distinguishable components can be observed for *S* nanosheets. For deconvolution of the respective contributions to the A exciton signal, the second derivative of the extinction with respect to photon energy is calculated and fitted using the second derivative of the sum of two Lorentzians. The A exciton response in the film is compared to the spectra of dispersions as exfoliated in aqueous SC solution and after transfer to IPA (figure 68, B). Monolayer and the sum of individually not resolvable bi- and few-layer contribution can be clearly distinguished in all traces indicating retention of uncoupled monolayered material and hence the absence of excessive nanosheet restacking upon film deposition. A minor red-shift of the A exciton signal is visible upon transfer from aqueous surfactant solution (black trace) to IPA (teal trace) indicating solvatochromic effects. A sizable red-shift of 11 meV is visible after film deposition (orange trace) compared to as exfoliated dispersions (black trace) possibly due to substrate effects and lack of the solvation shell. Such shifts are expected as excitonic transition in WS_2 nanosheets are especially susceptible to environmental changes.[47] To further assess the optical properties upon film deposition, the PL spectra of films (measured in a Raman spectrometer) are shown in figure 68, C and compared to the PL of exfoliated WS_2 in aqueous SC solution. A significant loss in the PL intensity after normalization to the WS_2 2LA Raman mode (not shown) is visible across all sizes. However, quenching is far less pronounced in comparison to airbrush spray deposition (comparison figure 65, C). For further visualization of size-dependent trends, the PL was fitted to a Gaussian and the area is plotted versus nanosheet thickness in figure 65, D. Note that the area was determined in this case rather than the previously used PL/Raman intensity ratio due to broadening of the PL response in the films.

8 In dark field imaging, rough surfaces and defects in the film surface appear as bright and smooth, reflecting surfaces as dark spots.

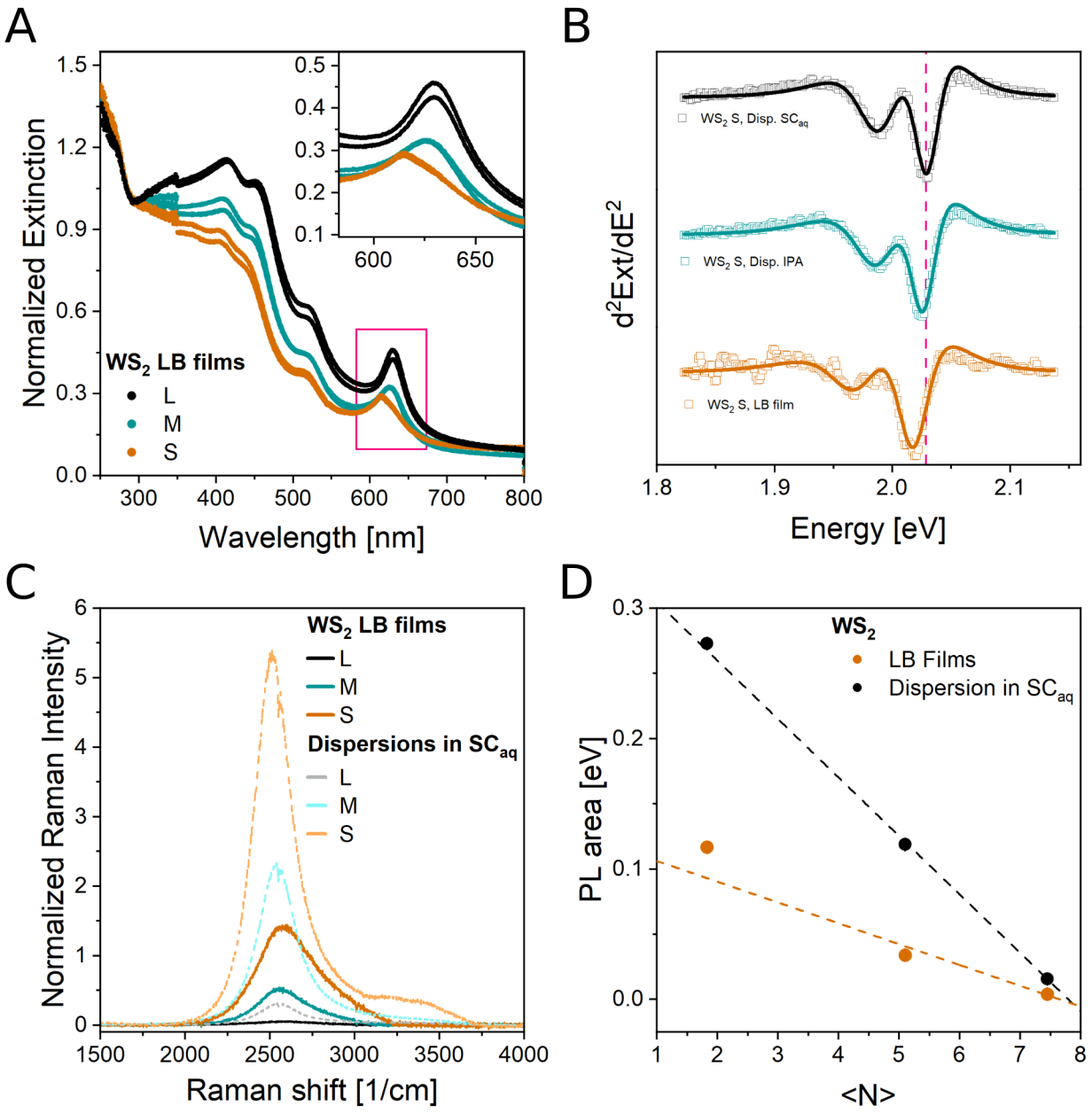

Figure 68: A) Extinction spectra of WS_2 films produced via the modified Langmuir-Blodgett technique with the initial setup normalized to the extinction at 294 nm. Inset: enlarged view of the spectral region around the A exciton signal. B) Second derivative of the spectral region around the A exciton signal with respect to the photon energy of the incident light for S dispersions as exfoliated in aqueous SC solution, after transfer to IPA and for films. C) Raman spectra of WS_2 nanosheet dispersions in aqueous SC solution (light traces) measured on a droplet of the dispersion and of films deposited from IPA via the modified Langmuir-Blodgett technique with the initial setup (bold traces) measured on the film surface (λ_{exc} = 532 nm) and centered on the PL peak. Five spectra are averaged each, a baseline was subtracted and the spectra were normalized with respect to the 2LA mode (not shown). D) PL area derived from Gaussian fitting of the PL signals in C plotted versus average nanosheet layer number. Samples are labeled with L for large (0.4 - 1k g, <L> = 141 nm, <N> = 7), M for medium (1 - 6k g, <L> = 68 nm, <N>=5) and S for small (6 - 30k g, <L> = 40 nm, <N> = 2) in order to illustrate changes in relation to <L> and <N> of the WS_2 dispersions. <L> and <N> were determined from extinction spectra in aqueous sodium cholate using published metrics.[8]

The PL area increases for decreasing nanosheet sizes for both films and dispersions according to expectation. A linear scaling is observed for dispersions as indicated by the dashed line. Importantly, this is retained in the films, albeit with slight deviations from linearity. The different slopes suggest that more non-radiative decay pathways are active in the film compared to the dispersion, either due to interaction with the substrate, substrate doping or some residual nanosheet restacking.

To assess the film morphology, films of nanosheets of varying sizes were deposited on conductive glassy carbon substrates and scanning electron microscopy was performed (figure 69). Low magnification images in figure 69, A-C show a dense network of nanosheets with only small holes visible and a minor population of aggregates. For higher magnifications (figure 69, D-F), individual nanosheets are resolved with a clear decrease in sheet size going from D to F according to the expectation from the size selection cascade. Important, sheets are largely aligned parallel to the substrate surface. Overlap of nanosheets is small and confined to edge regions. No deposition of a second layer is evident from the images shown in figure 69. The lack of significant sheet overlap in these films serves as an explanation for the retention of monolayer properties, such as PL emission and the preservation of size trends upon film deposition visible in figure 68. Overall, the morphology of these films is well-defined and nanosheets are aligned with no restacking visible.

From these results it is evident that the modified Langmuir-Blodgett method detailed above is capable of producing films with optical properties of the individual nanosheets widely retained. However, macroscopic film coverage is still insufficient and the process as a whole is unreliable. In particular, manual substrate immersion and retraction are prone to errors, which can be especially cumbersome if ink materials are of limited availability. Generally, for a go-to-method for film deposition in academic research, reliability, reproducibility and a minimum of subjective researcher interaction is desirable.

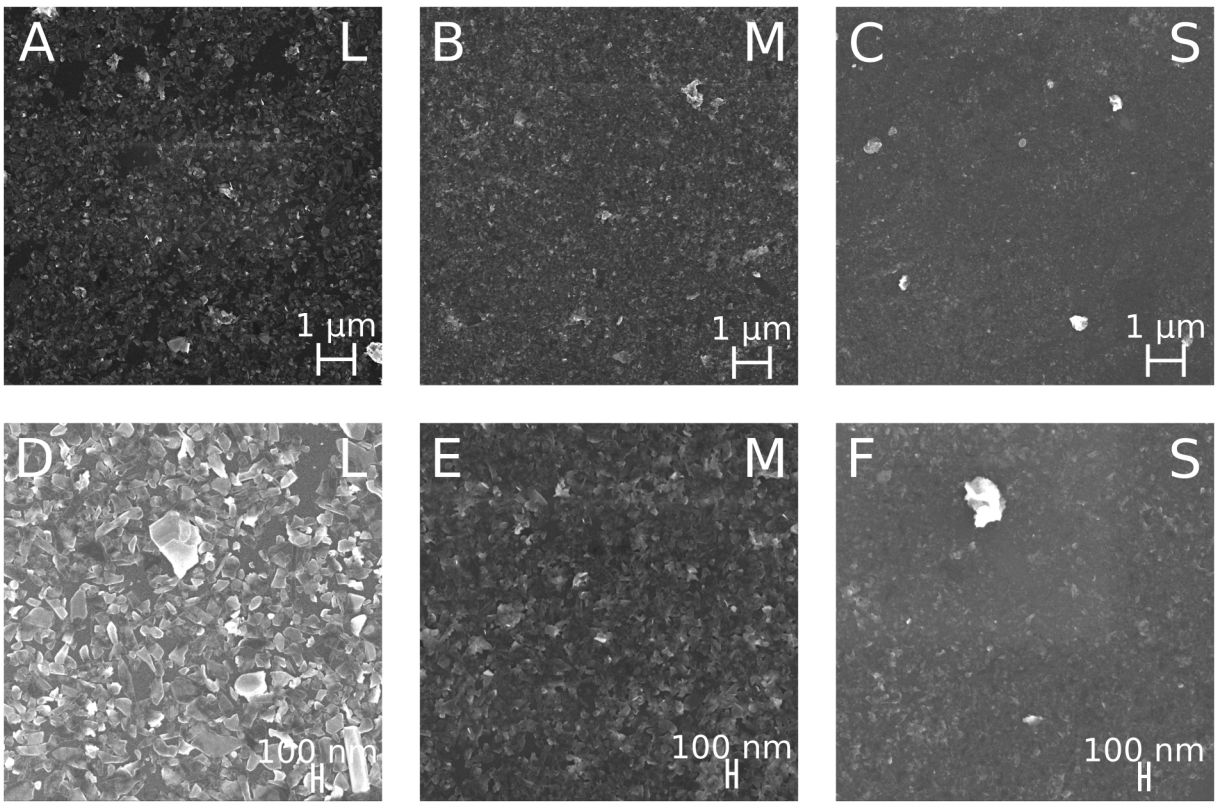

Figure 69: Scanning electron microscopy images of WS_2 nanosheet films produced via the modified Langmuir-Blodgett technique with the initial setup for nanosheet sizes L (A, D), M (B, E) and S (C, F). Images were acquired using 5 kV acceleration voltage and x10 000 (A-C) and x30 000 magnification (D-F).

In order to improve the reliability of the method, modifications to the deposition setup were necessary. The modified setup is shown in figure 70 and consists of three individual parts. The substrate is placed on the substrate mount (3 and 4 in figure 70) and the substrate mount is placed in the indentation of the base (1 in figure 70). Retrieving rods (2 in figure 70) are attached to the base for lifting of the substrate in order to form the retriever part. This modular design enables facile manufacturing and exchange of substrate mounts suited for varying substrate sizes without the need for an exchange of the retriever part. Holes are drilled in the bottom of the base to avoid turbulence in the liquid column upon lifting of the retriever. The assembled substrate mount and retriever are placed in a commercially available 250 ml glass beaker (6 in figure 70) and water is filled into the beaker until the substrate is completely covered. Afterwards, the film bucket (5 in figure 70) is inserted and rests on top of the beaker. *n*-Hexane is then added on top of the water column and the liquid-liquid interface is contained on the inside of the film bucket. This enables film formation and substrate lifting without penetration of the formed film prior to transfer to the substrate. The bucket size is a key aspect of film coverage as it governs the minimum amount of material necessary for closed coverage and therefore material

consumption. The bucket used in this work was 40 mm in diameter, but lower diameter buckets were fabricated for other experiments with limited material availability.

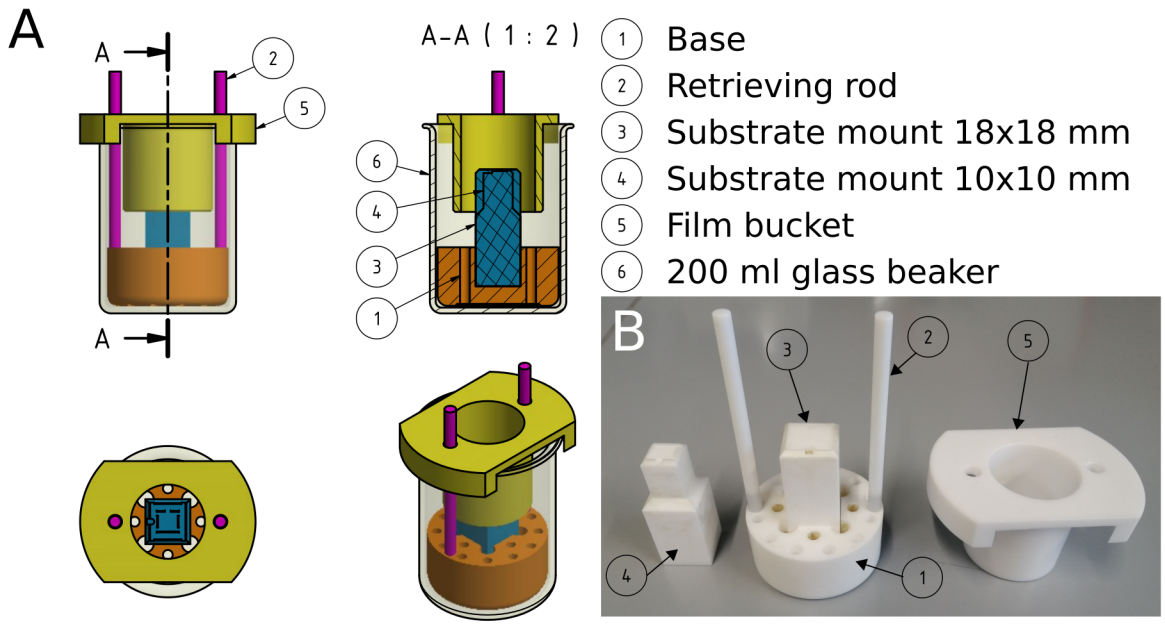

Figure 70: A) Schematic of the modified Langmuir-Schaefer setup in a commercially available glass beaker at different viewing angles and an intersection along the A-axis is shown. Individual parts of the setup are labeled accordingly. B) Photographs of the home-built setup fabricated from PTFE.

All parts of the setup were fabricated from poly(tetrafluoroethylene) (PTFE). This ensures not only chemical inertness of the parts in contact with organic solvents but maintains surface tension on the water surface due to its hydrophobicity. This can be seen as an analogy to Langmuir-Blodgett troughs, however the hydrophobic barriers used herein are fixed in position and compression of the formed film happens spontaneous through gradients in interfacial tension upon addition of the dispersion in IPA.[190] Furthermore, in contrast to the traditional Langmuir-Blodgett techniques, the substrate is not withdrawn perpendicular to the film, but parallel to it comparable to a Langmuir-Schaefer (LS) type approach. Thus, the term *modified Langmuir-Schaefer deposition* will be used to describe this methodology and distinguish it from the initial trials where the substrate was lifted through the preassembled film in an angle. For injection of the nanosheet ink into the liquid-liquid interface with as great precision as possible, a disposable glass Pasteur pipette is lowered using a lifting stage until the liquid is just capable of entering the pipette and the dispersion is then added on the top of the pipette. A schematic of the assembled setup is shown in figure 71, A. After complete injection of the ink, the film is left to settle until all *n*-hexane is evaporated. To minimize the time for the solvent evaporation, low volumes of *n*-hexane were employed (500 - 750 µl for the 40 mm bucket).

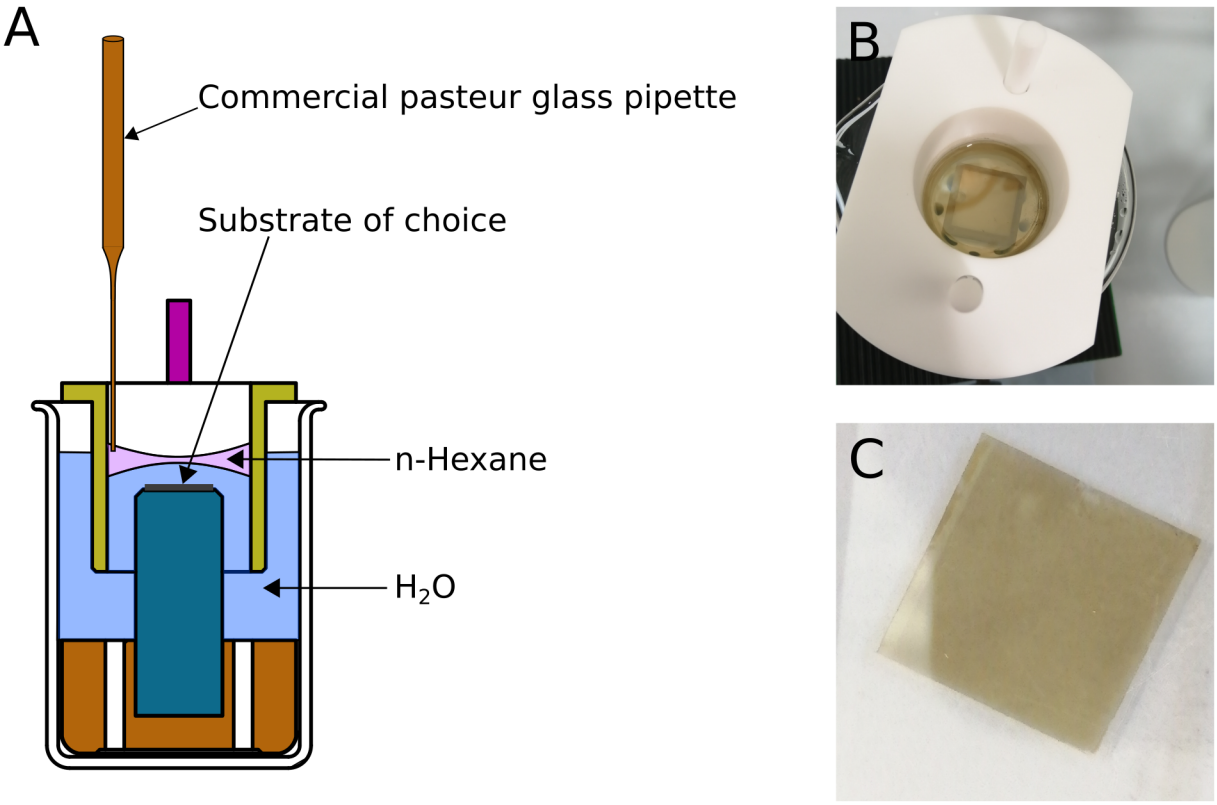

Figure 71: A) Schematic of the home-built deposition setup assembled for usage. B) Photograph of the formed WS_2 L (0.4 - 1k g) nanosheet film at the liquid-liquid interface. C) Photograph of a WS_2 L nanosheet film after transfer to a glass substrate (18 x 18 mm). The small rupture at the top of the film is due to handling with tweezers in the wet state.

An example image of such a film produced from *L*-WS_2 nanosheets is shown in figure 71, B. The mirror finish visible is indicative of the smooth nature of the produced film. After *n*-hexane evaporation, the substrate is lifted through the liquid-liquid interface for film transfer and the retriever is removed from the beaker together with the bucket. The film then rests on a cushion of water and is left to dry at ambient conditions. After drying, a continuous film of uniform visual appearance is deposited on the whole surface of the substrate (figure 71, C). This is more clearly resolved with digital microscopy images of the film after transfer and drying shown in figure 72, A. The film is of yellow color and transparent, as is evident from the visibility of drawings on the microscope stage underneath. Very minor fractures are visible in the film and a rectangular dent at the top, with the latter being the result of film handling in the wet state, where films are still very susceptible to vibrations or contact[9]. At substrate edges, a narrow line on the film is of deeper color due to folding of the film around the substrate edges upon removal of the substrate from the mount.

9 This could be alleviated by drying on the substrate mount. After drying, handling with tweezers does not leave such pronounced markings.

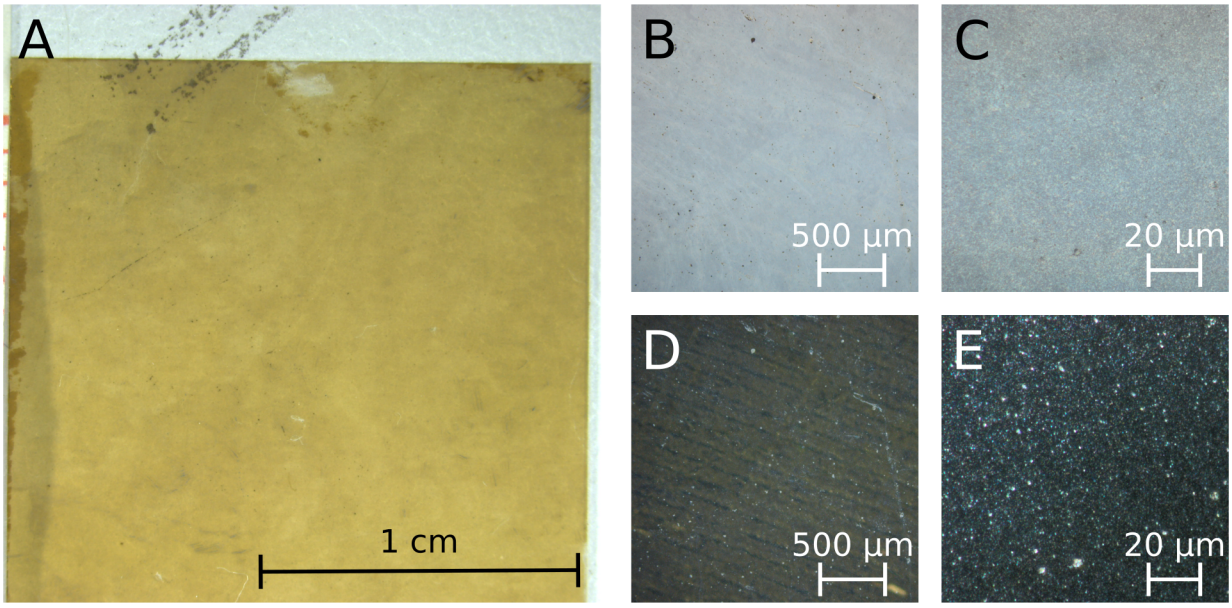

Figure 72: A) Digital microscopy image of an L-WS_2 nanosheet film on an 18×18 mm glass slide. B-E) Optical microscopy images of the film in A with x5 (B, D) and x100 (C, E) objective in bright (B-C) and dark field mode (D-E).

Upon closer inspection of the film surface in optical microscopy, barely any features are visible at low magnifications in bright and dark field mode (figure 72, B and D). Only at the highest magnification small grains in the film surface are visible in bright field mode and minor surface roughness can be expected from dark field imaging (figure 72, C and E).

Optical film properties were again assessed using extinction spectroscopy and spectra are shown in figure 73, A. Four films were fabricated per nanosheet size to judge the reproducibility of the method. Extinction across the films produced from the same sample varies slightly per nanosheet size, most pronounced for large nanosheets and barely at all for small nanosheets. Changes in extinction at a given wavelength for a specific nanosheet size can be interpreted as changes in film thickness. Therefore the extinction at 400 nm is plotted versus the average nanosheet layer number derived from the extinction spectroscopic metrics of the initial dispersion in aqueous SC solution in figure 73, B. A linear correlation of layer number $<N>$ and extinction at 400 nm is evident and extinction approaches 0 for a nanosheet size of 0 nm. This is in line with a dependence of film extinction on the film thickness. It may be argued that, in dispersion, extinction coefficients decrease for decreasing nanosheet sizes at this wavelength and that this effect can result in a similar trend. However, it should be noted that a linear correlation of nanosheet size and film thickness (in the range of ~3 to 8 nm) derived from AFM profilometry for $MoSe_2$ films produced from this method was shown in independent work.[241] Therefore it can be concluded that film thickness directly depends on the

nanoparticle dimensions and varies most for dispersions enriched in large nanosheets, which are also more polydisperse, and least for small nanosheets.

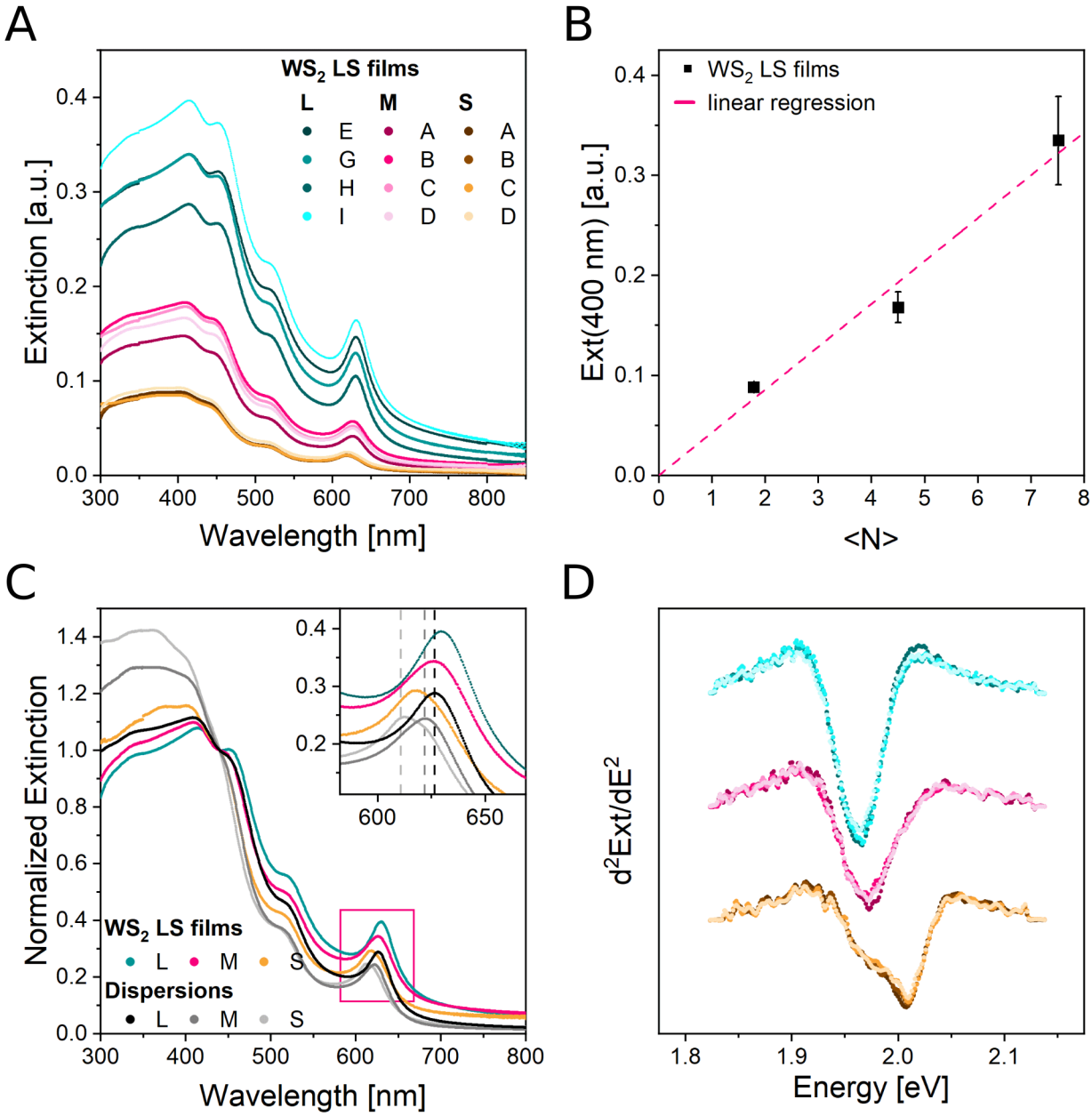

Figure 73: A) Extinction spectra of WS_2 films produced via the modified Langmuir-Schaefer technique for varying sizes and four films each. B) Plot of averaged film extinction at 400 nm versus the average nanosheet layer number. A linear fit is shown as a dashed line. C) Extinction spectra of WS_2 films produced via the modified Langmuir-Schaefer technique normalized to the extinction at 440 nm for varying sizes in comparison to the respective inks. Inset: enlarged view of the spectral region around the A exciton signal. The center of mass positions of the A exciton of the inks are highlighted using dashed lines. D) Second derivative of the spectral region around the A exciton signal with respect to the photon energy of the incident light for films produced from differently sized nanosheets. Legend in A applies to C-D as well. Samples are labeled with L for large (0.4 - 1k g, $\langle L \rangle = 123$ nm, $\langle N \rangle = 8$), M for medium (1 - 5k g, $\langle L \rangle = 59$ nm, $\langle N \rangle = 5$) and S for small (5 - 30k g, $\langle L \rangle = 33$ nm, $\langle N \rangle = 2$) in order to illustrate changes in relation to $\langle L \rangle$ and $\langle N \rangle$ of the WS_2 dispersions. $\langle L \rangle$ and $\langle N \rangle$ were determined from extinction spectra in aqueous sodium cholate using published metrics.[8]

Note that, in contrast to airbrush spraying, the film thickness is not expected to depend on the average lateral nanosheet size $<L>$ but on average layer number $<N>$ due to the nanosheet alignment parallel to the substrate surface. However, for size selection using liquid cascade centrifugation $<L>$ and $<N>$ are intrinsically correlated and therefore an apparent linear correlation with $<L>$ is visible as well. Furthermore, the minimum mass of nanosheets necessary for closed film formation should also depend on $<N>$ as will be derived below. For a closed film the liquid-liquid interface area A must at least match the sum of the nanosheet surface area along the basal plane on one face of the sheet A_f for all individual nanosheets. The sum can then be approximated by the product of the number of nanosheets β multiplied by the average nanosheet area $<A_f>$ (equation 23).

$$A = \pi r^2 = \sum_{i=1}^{B} A_{f_i} = \beta \langle A_f \rangle \tag{23}$$

The interface radius r is given by the dimensions of the bucket used in the experiments and is 20 mm for the bucket used in this study. The average nanosheet area can be calculated if the nanosheet shape is approximated to be rectangular. Then $<A_f>$ can be calculated directly from experimentally accessible nanosheet dimensions $<L>$ and $<W>$ (equation 24).

$$\langle A_f \rangle = \langle L \rangle \langle W \rangle \tag{24}$$

For estimation of the nanosheet number β, the ratio of total mass m and average individual nanosheet mass $<m_f>$ can be used. The mass of an individual nanosheet m_f is given by the layer number N and mass of individual layers m_L, whereas the layer mass depends on sheet dimensions L and W, density ρ and effective monolayer height $h_{0'}$ (equation 25).

$$\beta = \frac{m}{\langle m_f \rangle}, \quad with \ \langle m_f \rangle = \langle N \rangle \langle m_L \rangle = \langle N \rangle \langle V_L \rangle \rho = \langle N \rangle \langle L \rangle \langle W \rangle \rho h_{0'} \tag{25}$$

Equation 24 and 25 can be inserted in equation 23 and after rearrangement yields an expression linking average layer number of nanosheets to the total mass necessary for a closed film (equation 26).

$$m = \pi r^2 d_0 \rho \langle N \rangle \tag{26}$$

This shows that the nanosheet mass m and, as the dispersion volume is fixed to a low volume of 250 µl, the concentration for differently sized nanosheets needs to be

adjusted prior to deposition for optimal results (compare figure 67) based on the average layer number $<N>$ of the nanosheets in dispersion. This was further corroborated in an independent study by the deposition of $MoSe_2$ nanosheets for varying ink concentrations.[241] Note that this also implies that the film thickness cannot be increased using larger amounts of the material for deposition. Instead, to increase the film thickness, stacking of multiple layers has to be performed which was shown to be possible elsewhere.[241]

In the normalized extinction spectra visible in figure 73, C the thickness information is less distinct compared to the respective ink spectra (grey traces). The progression with size is retained in the films and a blue-shift of the A exciton signal with decreasing nanosheets sizes is visible for both films and dispersions. For comparable nanosheet sizes a red-shift of the A exciton signal is observed for films compared to dispersions, best seen in the inset in figure 73, C. Positions of the A exciton signal are highlighted using grey dashed lines. The shift in the A exciton signal position going from dispersion to films is roughly 4 nm for *L* and *M* and 5 nm for *S* nanosheets. Due to the minor restacking of the sheets in the films this shift is most probably related to changes in the dielectric environment of the nanosheets due to substrate effects and the lack of a solvation shell in comparison to dispersions. The expected splitting of the A exciton signal for small nanosheets is not obvious from the extinction spectra in figure 73, C. Therefore, the second derivative of the extinction in the spectral region around the A exciton signal is used to deconvolute individual contributions more clearly (figure 73, D). For *S* nanosheets, two distinct peaks can be identified with the higher energy peak assigned to monolayers being absent for *L* and *M* nanosheets. Hence, the monolayer character is widely preserved upon film deposition although the A exciton signal splitting is less apparent than in dispersion. As the optical properties of the nanosheets and the PL in particular depend on their direct environment, Raman spectroscopy with spatial resolution was conducted to resolve film inhomogeneities. To this end, 100 individual spectra were recorded evenly distributed on a 200×200 µm area for films of each size. Averages across all measured spectra per film and reference spectra for dispersions in aqueous SC solution are shown in figure 74, A. As expected, the PL increases significantly with decreasing nanosheet size going from *L* to *S* nanosheets for films (colored traces) and dispersions (grey traces). However, for comparable sizes, the PL normalized to the WS_2 2LA Raman mode is reduced in films compared to the signal in dispersions. Furthermore, the PL position is shifted to lower energies and appears broadened and slightly asymmetric compared to the dispersions. For *S* nanosheet films, spectra of four different films are shown to assess reproducibility of the film deposition technique. The PL/2LA ratio appears to vary slightly across the different films produced from the same dispersion indicating that reproducibility is not perfect for deposition of small nanosheets via the modified Langmuir-Schaefer approach. To resolve the spatial information, the PL response in the individual spectra is

fitted with Gaussians, while three individual Lorentzians were used for the E_{1g}, A_{1g} and 2LA Raman modes, respectively. The PL/2LA peak intensity ratio maps of films produced from the size-selected dispersions are shown in figure 74, B-D.

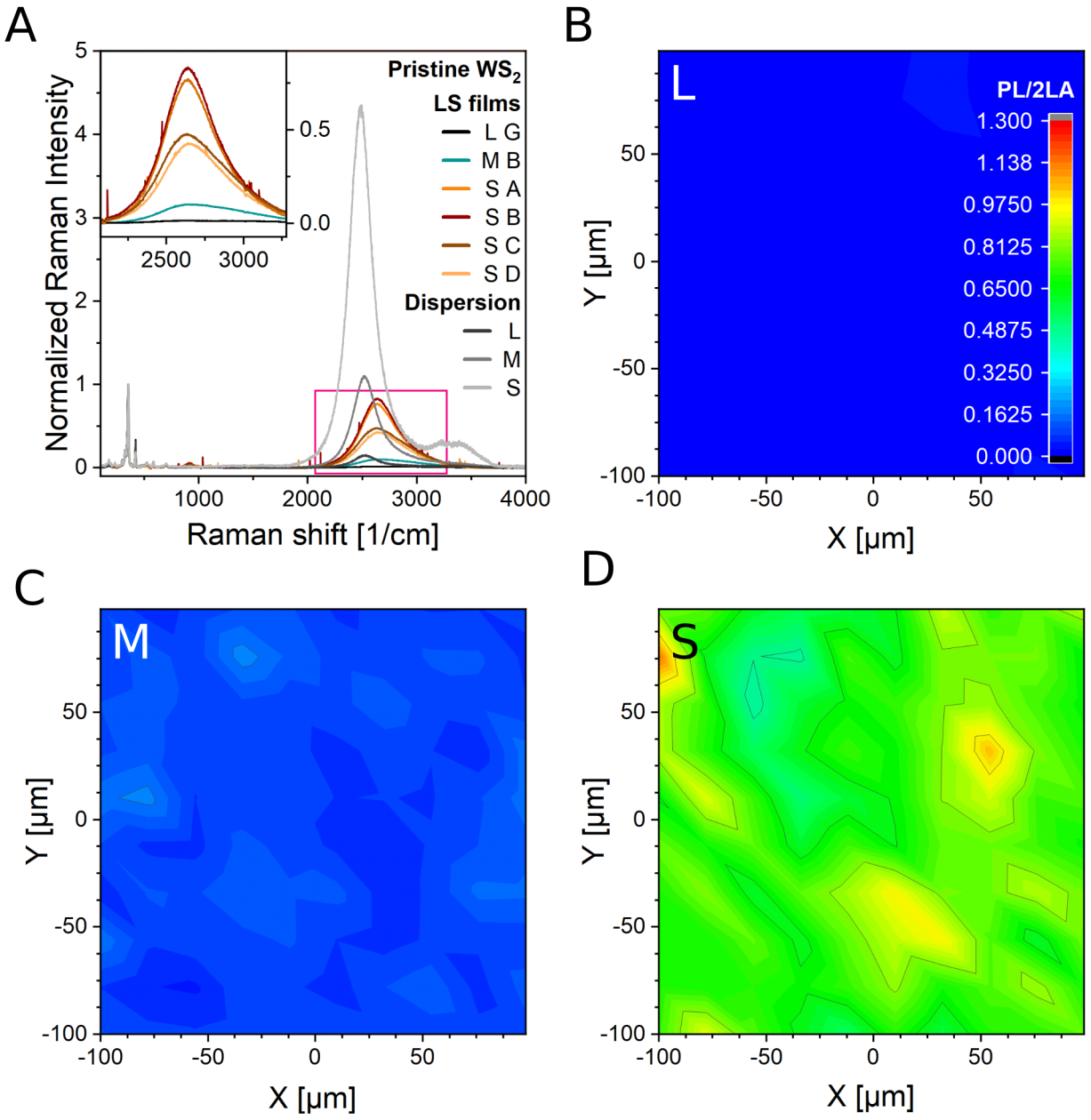

Figure 74: A) Averaged Raman spectra (λ_{exc} = 532 nm) of all measured spectra of individual nanosheet films produced via the modified Langmuir-Schaefer technique with the optimized setup compared to the reference spectra of the dispersions for varying nanosheet sizes. The inset shows an enlarged view of the spectral region around the PL signal. B-D) Raman/PL maps of the PL/2LA intensity ratio for films produced from L (film G in B), M (film B in C) and S (film B in D) nanosheets. Legend in panel B is valid for C-D as well.

Due to the low PL intensity of *L* nanosheets, no contrast is visible for the PL/2LA maps for *L* films in figure 74, B. For intermediate sized *M* nanosheets, a minor spatial variation of the PL/2LA ratios is observed in figure 74, C. Overall, with the resolution of the spectroscopic mapping, the PL/2LA ratios are relatively homogeneous in the measured

area and no specific features can be discerned. Overall, the spot-to-spot variation of the PL emission appears to be marginal. For films produced from the dispersion containing the smallest nanosheets, the PL/2LA ratio is increased compared to *L* and *M* nanosheets due to the higher monolayer content (in figure 74, D). The contrast is again relatively monotone indicative of a homogeneous film morphology. In order to visualize the spatial PL/2LA distribution, histograms of Raman maps for *L*, *M* and *S* nanosheet films are shown in figure 75, A and fitted using normal distributions. Good agreement of the data and normal fits can be seen, while the center position of the PL/2LA intensity ratio gradually increases for decreasing nanosheet sizes as expected.

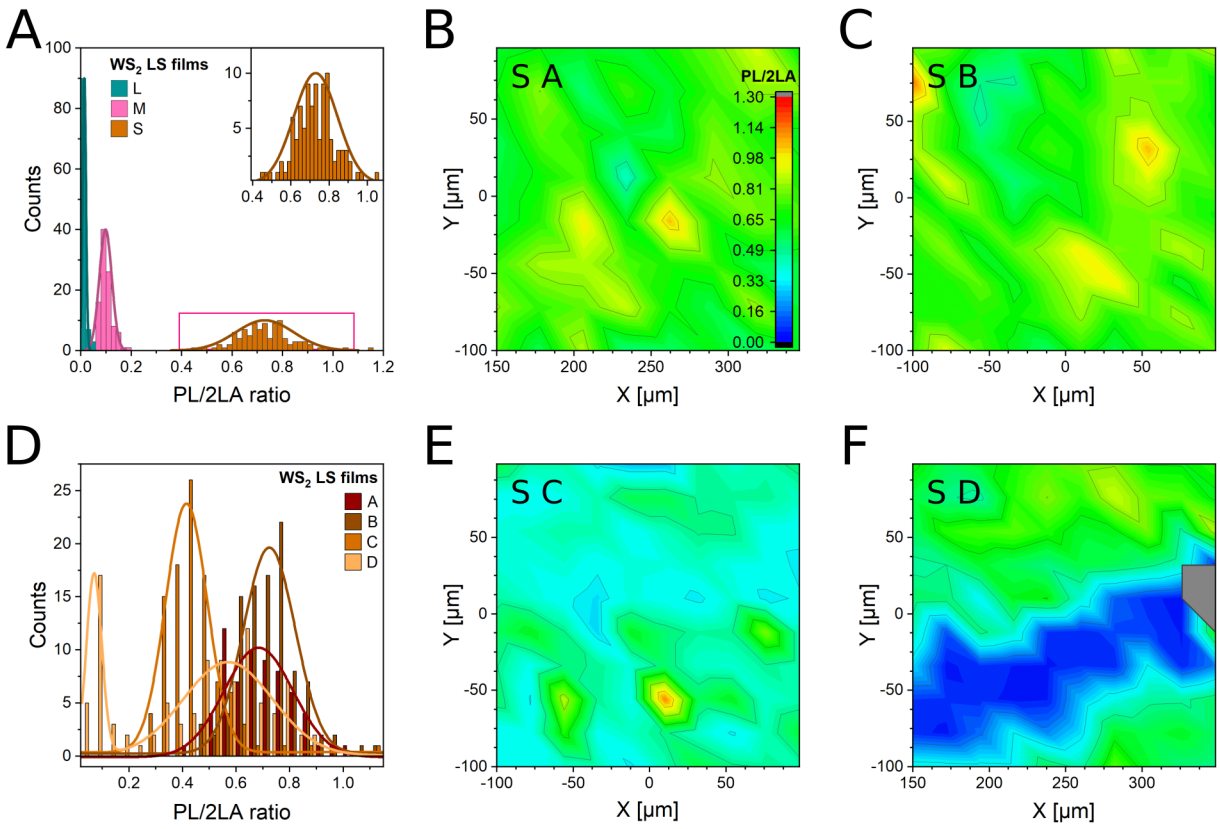

Figure 75: A) Histogram of the PL/2LA intensity ratios of WS_2 nanosheet films constructed from the Raman maps presented in figure 74. The distribution data is fitted with Gaussians. Inset: enlarged view of the S nanosheet film distribution. B-C, E-F) Raman maps of the PL/2LA intensity ratio for different films produced from S nanosheets. The legend in panel B is valid for C and E-F as well. D) Histogram of the PL/2LA intensity ratios of WS_2 S nanosheet films constructed from the Raman maps presented in B-C and E-F. The data is fitted with Gaussian distributions.

The distribution width can be interpreted as a measure for spot-to-spot variations in Raman/PL mapping and increases with decreasing nanosheet size. However, this may not necessarily mean that film formation is less defined for small nanosheets as lower average layer numbers $<N>$ increase the sensitivity of the optical properties to the environment. Therefore small inhomogeneities appear more pronounced for thinner nanosheets. As means to gain further insights into the origins of film-to-film variations visible from the

average spectra of films measured after deposition of the small nanosheets in figure 74, A, individual PL/2LA intensity ratio maps are shown in figure 75, B-C and E-F. The PL/2LA intensity ratio spans a similar value across the four films, resulting in a similar color in the presented maps. However, some differences in color tone are visible especially for film C (E in figure 75). The utility of the Raman mapping is directly evident from film D (F in figure 75): film defects, such as ruptures can be directly observed from such maps which can serve as quality control. These ruptures can be the result of vibrational damages to a film while it still rests on the cushion of water. By eye or optical microscopy, these are hard to spot on transparent substrates. In order to further assess the film-to-film variations, histograms of the PL/2LA intensity ratio of the four different *S* nanosheet films are shown in D in figure 75 and fitted using normal distributions[10]. The average PL/2LA ratio across the four films is 0.60 with a standard deviation of 0.14 and hence, deviates by 23 % around the average value. Therefore, a certain degree of film-to-film variation is expected for the modified Langmuir-Schaefer deposition technique based on the presented data. Thus, to ensure comparability, reference measurements of each individual film prior to any further experiments are advisable. Possible sources of such changes in PL are manifold as substrate-nanosheet as well as nanosheet-nanosheet interactions are complex and may cause such behavior. However, a possible culprit of uncontrolled changes in PL is always the surface roughness of films.

In order to exclude roughness as a possible issue, AFM imaging was conducted on each film and the root mean square roughness was extracted (figure 76). Example AFM images are shown in A-C and a clear decrease in nanosheet size is visible when using the size-selected inks, as expected. The film height is overall homogeneous and individual nanosheets can be discerned, in particular when using the nanosheets of larger size. Especially for *S* nanosheets, films appear very smooth and of uniform thickness. In order to improve the significance of the roughness determination four films per size were produced and imaged with two 5×5 µm images per film. The probed area is therefore 200 µm^2 per type of size-selected ink. The extracted root mean square roughness is plotted versus the average nanosheet layer number $<N>$ in figure 76, D. The root mean square roughness of all films is generally very low, well below 10 nm and decreases linearly with nanosheet size even reaching roughly 2 nm for *S* nanosheets. Note that this is comparable in margin to the average thickness expected for individual nanosheets. Furthermore, linear regression passes through the origin with a slope of 1.08 nm per average nanosheet layer number. The roughness is therefore likely associated with the nanosheet thickness itself: in a single layer of a tiled network, the substrate remains visible in AFM imaging and therefore the profile height ranges between the blank substrate and

10 For film D, the sum of two individual normal distributions was used to separate the influence of the visible film defect. The lower PL/2LA distribution in Film D was excluded for calculation of averages.

the nanosheet on the substrate. This is a manifestation of a high degree of alignment of the nanosheets parallel to the substrate.

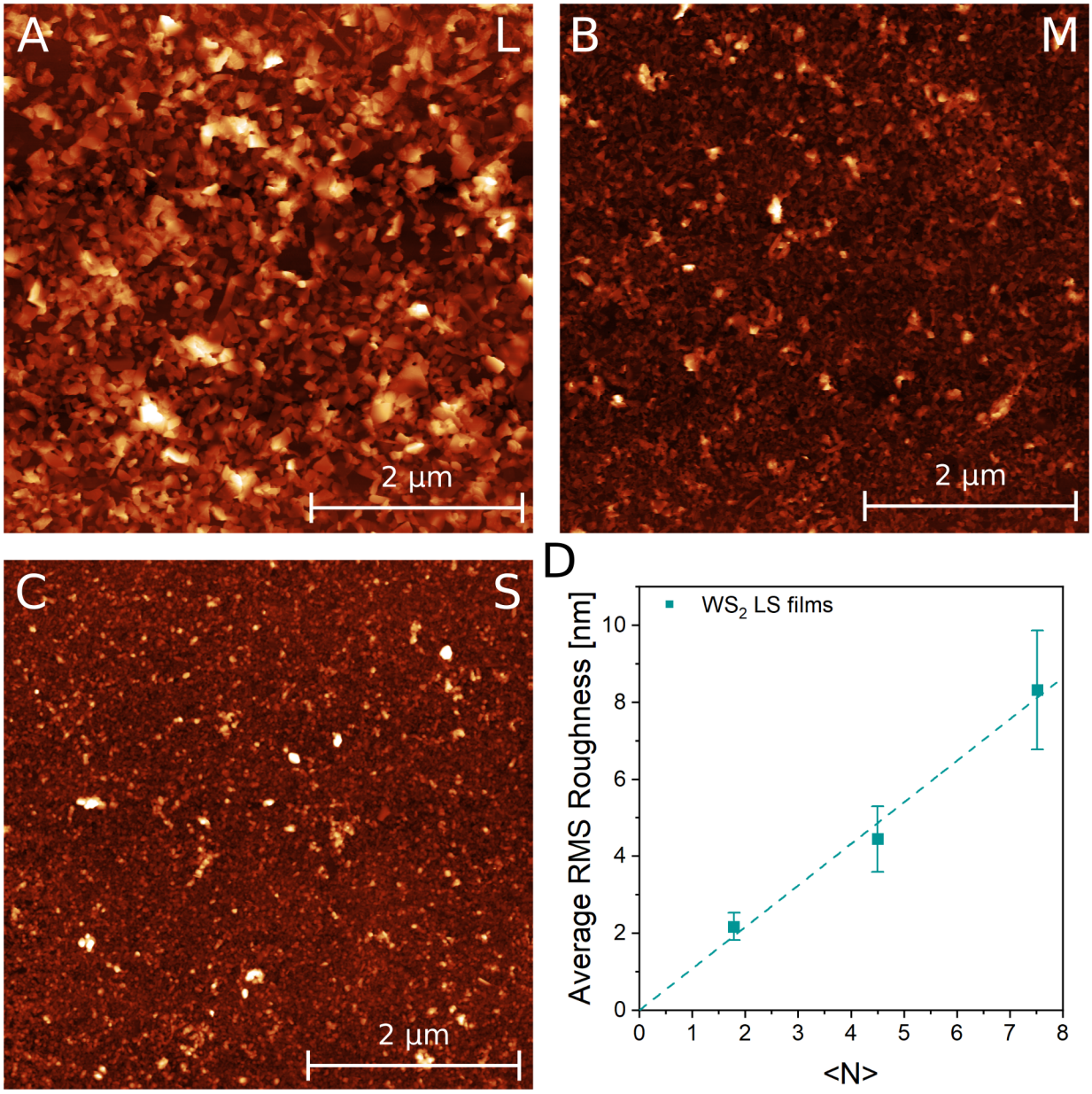

Figure 76: A-C) AFM images of nanosheet films on glass produced via the modified Langmuir-Schaefer technique for L (A), M (B) and S (C) nanosheets. D) Average root mean square roughness of films derived from AFM images for varying nanosheet sizes in A-C.

The standard deviation in surface roughness (error bars in figure 76, D) also decreases with decreasing size, most probably due to the reduced polydispersity in samples with smaller average dimensions. As the scatter in the local surface roughness for *S* nanosheets is very small, below 0.4 nm, an impact of the surface roughness is excluded as explanation for variations in film PL visible in figure 75, D. Since the PL/Raman mapping suffers from a significantly lower resolution, the origin of the variation in the

PL/Raman mapping are likely more macroscopic defects with dimensions in the range of 10s of µm.

Concluding, the modified Langmuir-Schaefer method was evaluated to be highly promising as a go-to method for film deposition in the academic lab, where size-dependent nanosheet properties are well translated to film properties. Film formation at a liquid-liquid interface and consecutive substrate transfer produces films of nanosheets aligned parallel to the substrate surface with minimal sheet overlap (tiled networks). A deposition setup was designed to facilitate and increase reliability of the film deposition and uniform coverage of relatively large substrates (3.24 cm^2) is feasible. The film thickness, roughness and minimum nanosheet mass necessary for closed film formation depend on the average layer number $<N>$ of nanosheets in the ink. Size-dependent trends in the optical properties are retained upon film deposition, even though peak shifts and PL quenching occurs to some extent across all sizes most probably due to substrate effects. The spatial resolution of the PL response reveals a normal distribution for PL in the films with high monolayer content rendering spot-to-spot variations minimal and film coverage uniform. However, film-to-film variations were evident and for future comparative studies, reference measurements of all films involved are recommended. Overall, the film roughness is minimal, i.e. approaching the nanosheet thickness itself.

The ability of producing such films with defined morphology enables a whole host of experimental designs previously reserved to 2D materials directly grown on the substrate, e.g. CVD grown nanosheets. These were up to now, widely inaccessible for porous networks of randomly restacked LPE nanosheets. For example, we showed in independent work that the formation of heterostacks of $MoSe_2$ and MoS_2 is feasible through multiple film layer deposition using this modified Langmuir-Schaefer method and indications for electronic coupling between the different materials were found.[241] Furthermore, deposition of a second layer on nanosheet films is not restricted to other layered materials. To explore this possibility in more detail, deposition of organic chromophores on top of the WS_2 films produced via this modified Langmuir-Schaefer method was attempted in this thesis as described in the following. This potentially allows for production of novel organic/inorganic hybrid materials which are often described as smart, functional materials in various application areas.[242]

Molecular dyes deposited were *N*,*N'*-Bis-(1-pentylhexyl)perylene-3,4,9,10-bis(dicarboximide) (PBI), 2,9-Bis-(heptafluoropropyl)-1,3,8,10-tetraazaperopyrene (TAPP-4H) and 2,9-Bis(heptafluoropropyl)-4,7,11,14-tetrabromo-1,3,8,10-tetraazaperopyrene (TAPP-4Br) in toluene respectively. Chemical structures of the chosen molecules are shown in figure 77. A common feature of the chosen dyes besides similarities in the

chemical structure is their pronounced fluorescence in solution: PBI shows intense fluorescence in chloroform with its maximum at 533 nm and quantitative fluorescence quantum yield, whereas for the non-halogenated tetraazaperopyrene TAPP-4H fluorescence maximum was observed at 448 nm in tetrahydrofuran solution with 51 % quantum yield.[243-244] For both compounds, a pronounced dependence of optical properties can be observed upon derivatization at the aromatic core. For tetraazaperopyrenes the HOMO-LUMO gap, and therefore emission, changes drastically upon introduction of electron withdrawing groups through halogenation: for a non-halogenated core (TAPP-4H) the calculated bandgap is 2.95 eV, while for the fourfold core brominated derivative TAPP-4Br the calculated bandgap decreases to 2.59 eV and emission is red-shifted to 486 nm while fluorescence quantum yield is significantly reduced to 12 %.[244] In contrast, little effect of core halogenation is visible for PBI derivatives but electron donating functionalities result in significant shifts in absorption and emission.[243] Side groups introduced in *N,N'*-position for PBI or 2,9-position for tetraazaperopyrenes on the other hand do not impact electronic properties significantly which can be exploited to promote solubility of the compounds in conventional organic solvents.[243, 245]

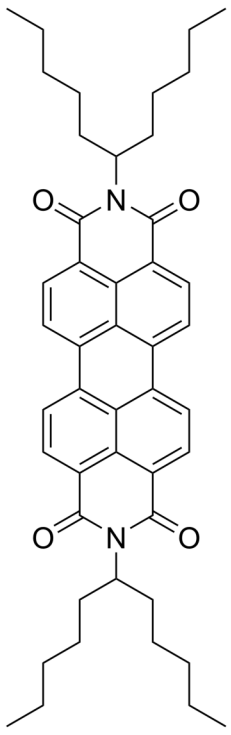

N,N'-Bis-(1-pentylhexyl)perylen-3,4,9,10-bis(dicarboximid)
PBI

698,95 g/mol

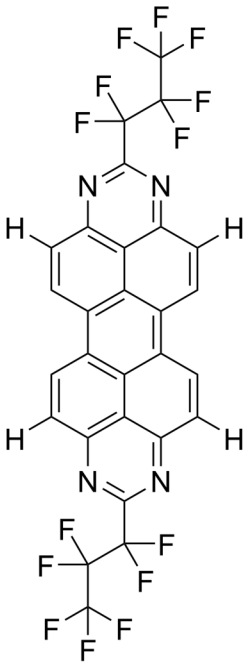

2,9-Bis-(heptafluoropropyl)-1,3,8,10-tetraazaperopyrene
TAPP-4H

666,38 g/mol

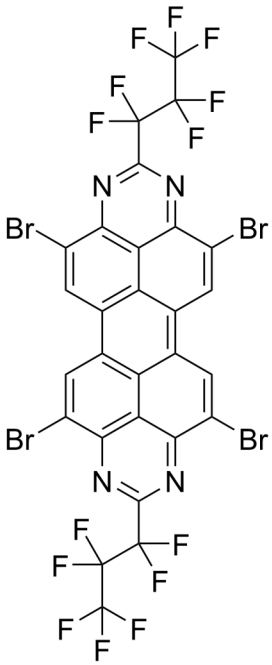

2,9-Bis-(heptafluoropropyl)-4,7,11,14-tetrabromo-1,3,8,10-tetraazaperopyrene
TAPP-4Br

981,96 g/mol

Figure 77: Chemical structures of organic molecules chosen for deposition.

Since these molecules show interesting optical properties, the effect of electronic interaction with other (nano)materials is of basic scientific interest. To date, an interaction with 2D TMDs is little explored. Similar studies for molecules of the perylen-3,4,9,19-bis(dicarboximid) family in combination with graphene,[143] black phosphorus,[141] and MoS_2[246] exist and conclude electronic interactions of the PBI molecules with the underlying two-dimensional material, resulting in quenching of PBI fluorescence and enabling Raman spectroscopy previously impossible on PBI due to its strong fluorescence. Furthermore, significant MoS_2 PL quenching was reported upon deposition of a perylene derivative,[246] although phenyl side groups are used instead of alkyl side groups. Additionally, a significant red-shift of dye absorption was shown upon adsorption on single-walled carbon nanotubes.[134] Therefore electronic interactions of dye molecules and WS_2 are expected but not yet explored. In particular, the mechanism of the electronic communication to the layered material is not understood and indeed difficult to rationalize. For a better understanding, it is important to develop a material platform that allows screening of both molecule and 2D material.

A spontaneous assembly approach of the molecules was attempted by dipping WS_2 films on glass substrates into a 10^{-4} mol/l[11] solution of PBI, TAPP-4H and TAPP-4Br in toluene for 10 minutes each for films of varying nanosheet sizes. The films were blow-dried and extinction spectra of films before and after deposition of the molecules are shown in figure 78, A-B. No significant changes in extinction can be discerned after dipping the film in the molecule solution. A minor increase in scattering contribution after deposition is visible for the M film in TAPP-4H (M B) however, the origin of increased scattering is due to TAPP-4H crystallites on the backside of the substrate likely attached due to saturation of the dye solution. The absence of any chromophore signals in extinction for such strong chromophores indicates very low amounts of dyes deposited on the film. For instance, the extinction coefficients in solution at the absorption maximum for PBI of 88 000 l/(mol·cm),[247] for TAPP-4H of 31 622 l/(mol·cm)[244] and TAPP-4Br of 81 283 l/(mol·cm),[244] are significantly higher compared to the WS_2 extinction coefficient at 235 nm in aqueous SC solution of 11 828 l/(mol·cm).[8] Furthermore, no significant shifts in A exciton position can be observed upon deposition of molecules (figure 78, C), which would be expected if a pronounced electronic interaction occured.

11 The chosen concentration was beyond the solubility product of TAPP-4H and TAPP-4Br in toluene and sedimentation occurred. Therefore effective concentration is likely lower.

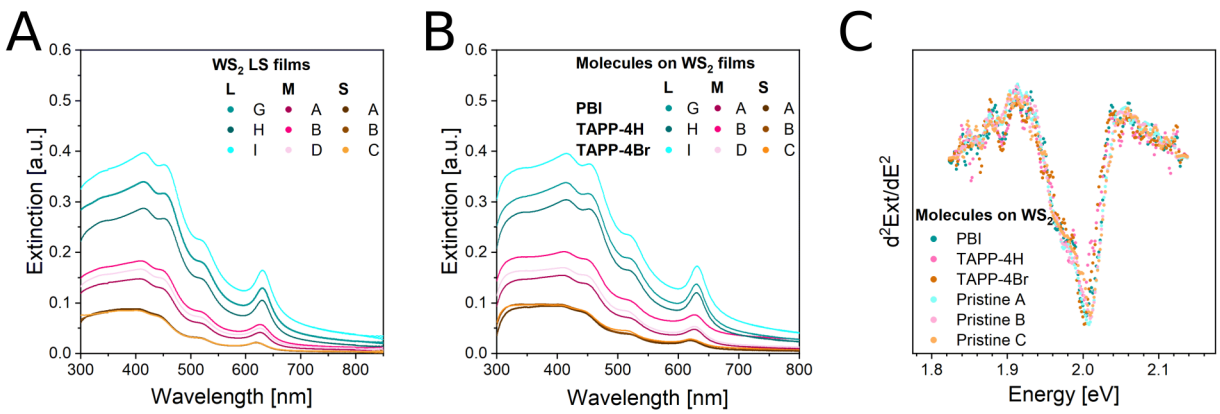

Figure 78: A) Extinction spectra of WS_2 films produced via the modified Langmuir-Schaefer technique for varying WS_2 nanosheet sizes prior to film deposition. B) Extinction spectra of the same WS_2 films after dipping the films in a solution of the different molecules. C) Second derivative of the spectral region around the A exciton signal with respect to the photon energy of the incident light for the S nanosheet films shown in A-B.

While extinction spectroscopy infers that only few molecules are deposited, a different scenario is anticipated from Raman/PL spectroscopy. When measuring the films in the Raman spectrometer with 532 nm excitation, the PL of PBI was too intense to properly resolve contributions of WS_2 while for TAPP-4H barely any molecule signal could be discerned. Therefore, the films were soaked in toluene over-night and remeasured in Raman spectroscopy. However, PBI appears to be completely removed upon washing whereas TAPP-4Br appears to stick to the WS_2 film (appendix 8.13).

The molecule deposition was then repeated using an altered protocol: WS_2 films were dipped for 10 seconds in PBI and TAPP-4Br and soaked for 10 minutes in TAPP-4H to compensate for apparent differences in the amount of molecules deposited. Raman mapping was then conducted to assess spot-to-spot variations and increase the signal-to-noise ratio upon averaging of individual spectra (figure 79). Averaged and normalized Raman spectra of WS_2 films with PBI deposited on the film surface are shown in figure 79, A. PL and vibrational modes of WS_2 as well as vibrational modes of the dye are superposed on the PL background even after the relatively short deposition times of 10 seconds. While PL quenching is incomplete, it is pronounced enough to resolve the characteristic vibrational modes of PBI, magnified in the inset in figure 79, A. Since PBI is excited resonantly at a laser wavelength of 532 nm, peak intensity of vibrational modes is high enough to be discernible against WS_2 signals also excited resonantly at this laser wavelength, especially if red-shifts of the dye absorption are assumed in accordance to literature.[134] In the case of PBI deposited on graphene, it was shown that no electronic excitation of PBI occurs at 633 nm excitation wavelength and the vibrational modes of the molecule can no longer be discerned in the Raman spectra, as the signal is not enhanced

resonantly.[248] For the *S* nanosheet film (orange trace) a peak at roughly 3000 1/cm is visible and most likely assigned to WS_2 PL however due to the intense background no credible baseline subtraction is possible and therefore an assessment of the PL/2LA intensity ratio is inaccessible. Thus, unfortunately, an impact of PBI adsorption on the PL of WS_2 cannot be evaluated based on the available data. Note that more complete PL quenching was observed in some combinations of PBIs with 2D materials,[141, 143, 246] and the reason for this difference remains purely speculative at this point and will require more systematic work. The data could point to a worse electronic coupling of LPE WS_2 compared to e.g. CVD MoS_2 or non-ideal adsorption geometry of the chromophore, as the electronic coupling efficiency should depend on the spatial proximity of the aromatic core to the material. On graphene, the adsorption geometry of PBI was shown to be either parallel to the surface or vertically tilted,[135] rendering the molecule core close to the surface, while for MoS_2 alkyl substitued PBI were suggested to adsorb mainly with the side chain while the aromatic core is longitudinally tilted by 62.3° away from the surface.[249] Furthermore, the impact of the side chains on the molecular packing on WS_2 surfaces is unknown, but a certain contribution is expected.[250] Since the side chains are different in the aforementioned literature, a direct comparison of results is complicated. Therefore, the exact origin of the apparently imperfect electronic coupling between PBI and WS_2 remains elusive.

For TAPP-4H no significant PL background is visible and reliable baseline subtraction is possible (figure 79, B). Due to the increased signal-to-noise ratio after spectra averaging, the vibrational modes of TAPP-4H are clearly resolved in addition to the WS_2 Raman modes, best seen magnified in the inset in figure 79, B. For TAPP-4Br similar observations are possible although vibrational modes of the molecule are more pronounced compared to TAPP-4H (figure 79, C).

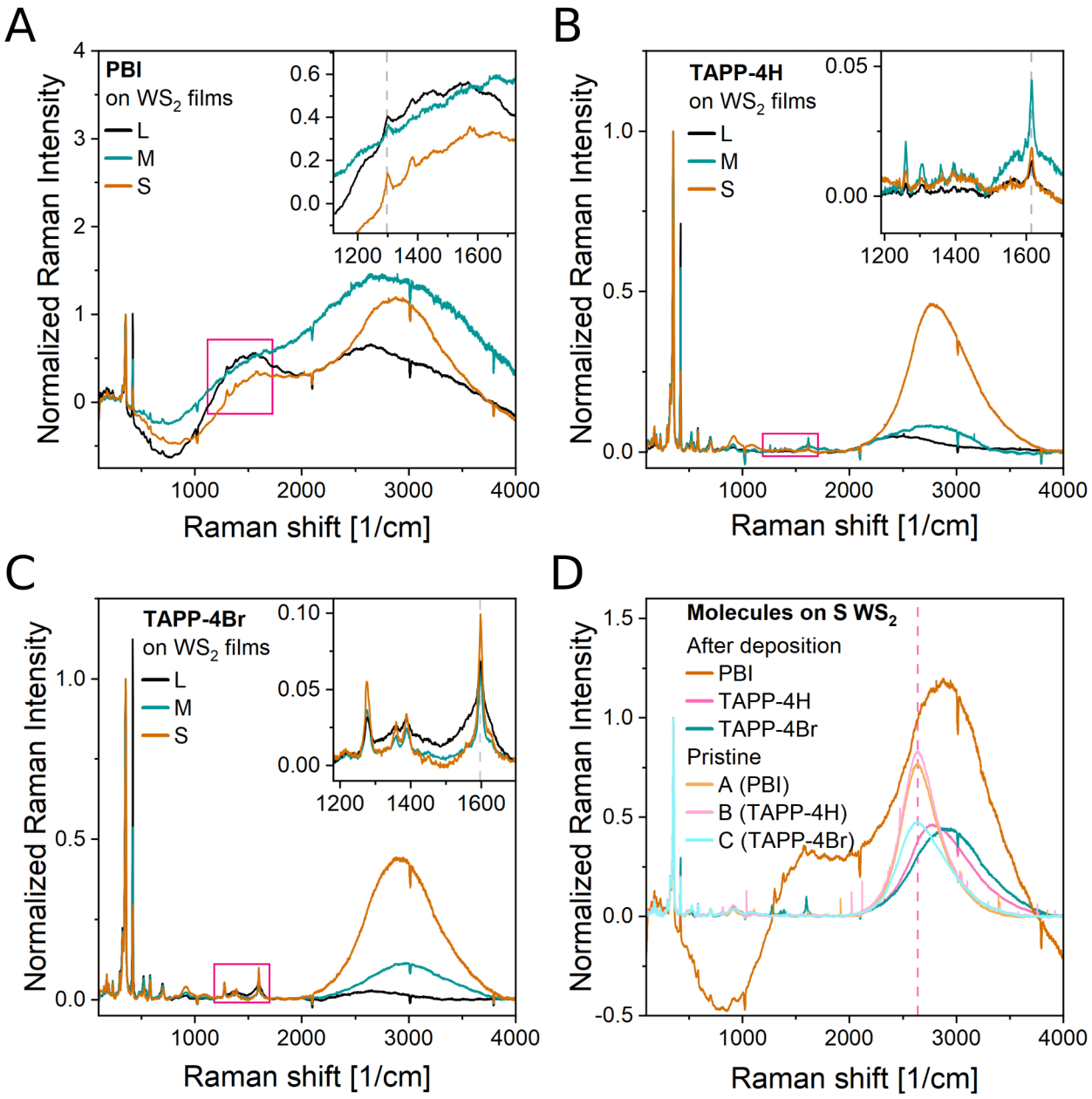

Figure 79: A-C) Averaged Raman spectra (λ_{exc} = 532 nm) of all measurements of nanosheet films produced via the modified Langmuir-Schaefer technique produced from dispersions of varying nanosheet sizes after deposition of PBI (A), TAPP-4H (B) and TAPP-4Br (C) normalized to the intensity of the WS_2 2LA vibrational mode. The inset shows an enlarged view of the spectral region around vibrational modes of the deposited molecules. Most intense vibrational modes are highlighted using grey dashed lines. Due to the high PL background in PBI samples, a constant baseline at the foot of the 2LA mode was subtracted. D) Comparison of average Raman spectra of S nanosheet films in A-C to representative film spectra prior to deposition. The PL position in the pristine film is highlighted using a dashed line.

The well-discerned signal of the molecular vibrations again indicates resonant excitation of the molecules. As no excitation is expected at 532 nm based on molecular absorption in solution, bathochromic shifts in the chromophore absorption upon deposition on WS_2 are suggested as origin in line with results for PBI on single-walled carbon

nanotubes.[134] The fact that TAPP-4Br shows a more pronounced relative contribution of the molecule vibrational modes compared to TAPP-4H can be explained following this argument. Since core bromination red-shifts the absorption of individual molecules in solution by 38 nm, this is intrinsically shifted closer to the excitation wavelength of the laser.[244] For TAPP-4Br, the molecule PL is again largely quenched indicating electronic communication of the WS_2 surface and the chromophores.

Before drawing a direct comparison of WS_2 in the hybrid films to pristine films, it must be noted that as-produced films were measured at 1 % laser power. However, after deposition of the molecules, the laser power was increased to 5 % in order to improve the signal-to-noise ratio of the individual spectra for mapping. Note that a certain dependency of relative peak intensities on the laser power is expected. In figure 79, D averaged Raman spectra of *S* nanosheet films are shown in comparison to reference spectra of films prior to deposition of the molecules. The WS_2 PL position changes significantly upon deposition of molecules way beyond any shifts that could be expected for an increase in laser power of the excitation of pristine WS_2.[251] This points further towards a possible electronic interaction of the organic dyes with WS_2. Another possible explanation for such intense peak shifts are changes in the dielectric environment of WS_2. However, such changes should also be reflected in the extinction where no significant shifts in the A exciton response were observed (compare figure 78, C). Furthermore, the PL broadens for all deposited molecules, although such broadening can be the result of averaging over different areas with a certain distribution of PL positions due to inhomogeneities in the inorganic-organic hybrid.

In order to assess the spatial distribution of changes in relation to the molecular coverage, Raman mapping was employed and the PL/2LA intensity ratios with spatial resolution are shown in figure 80. Again, a change in the PL/2LA ratio might be correlated to changes in laser power, however consistent behavior for all molecules would be expected if laser power is the sole origin of the observations. The WS_2 PL is reduced in the films after deposition of TAPP-4H (compare D and B in figure 80), strongly suggesting electronic interactions. Mild reduction in PL intensity was identified in literature for PBI derivatives on MoS_2 alongside significant peak broadening and related to increased trion formation due to the chromophore acting as an electron donor.[246] For TAPP-4Br quenching of WS_2 PL is less pronounced (figure 80, E). However, the PL of the pristine film is significantly lower (figure 80, C) in comparison to panel B. After deposition of the molecule, the PL itself appears less homogeneous in the probed area compared to the pristine film. The latter also applies to TAPP-4H indicating that the molecule coverage might be inhomogeneous.

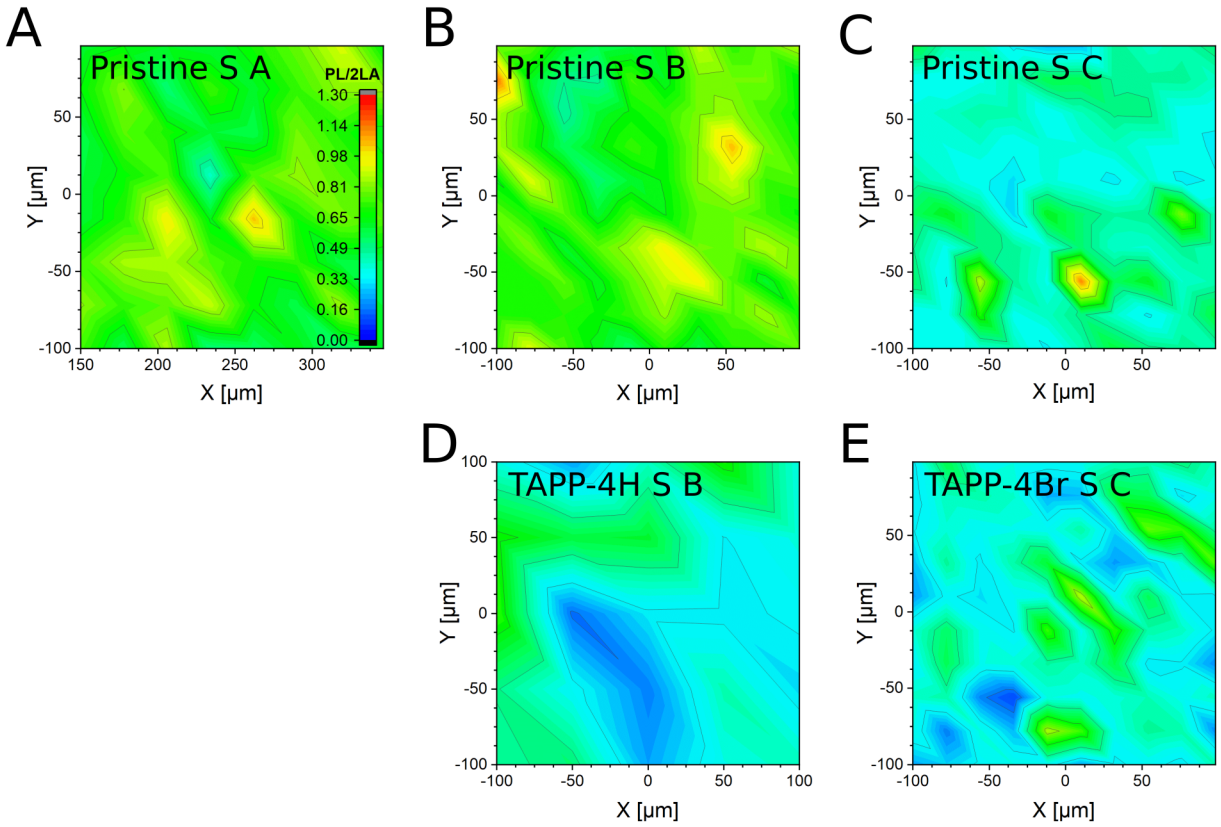

Figure 80: A-E) Raman PL/2LA intensity ratio maps of S nanosheet films prior to (A-C) and after deposition of molecules (D-E). For the construction of the maps, the WS_2 PL signals were fitted with Gaussians and the vibrational modes with Lorentzians. No fitting could be performed after deposition of PBI due to the intense PL background of the molecule. Legend in A applies to B-E as well.

Another noticeable change is a more pronounced size dependence of the A_{1g}/2LA ratio compared to pristine films (compare figure 79, A-C and figure 74, A). A dependence of the A_{1g}/2LA ratio on the layer number of WS_2 nanosheets is known[122] and likely affected by changes in the laser power, although the A_{1g} mode appears unusually enhanced here. In order to probe the homogeneity of the molecule coverage, the intensity ratio of the most intense vibrational mode of the respective molecules (see insets in figure 79, A-C) and the 2LA vibrational mode of WS_2 is mapped (figure 81). With the exception of film *PBI L* in figure 81, A, the molecule coverage on WS_2 films appears rather inhomogeneous with pronounced fluctuations in molecule/WS_2 intensity ratios. It appears that the spontaneous deposition approach produces incomplete coverage. In principle, such issues could be alleviated using more sophisticated deposition methods which is beyond the scope of this proof of principlework. It should be noted that incomplete coverage may partially mask electronic communication with molecules in averaged spectra and for future experiments, chromophore deposition should be improved to arrive at more reliable results.

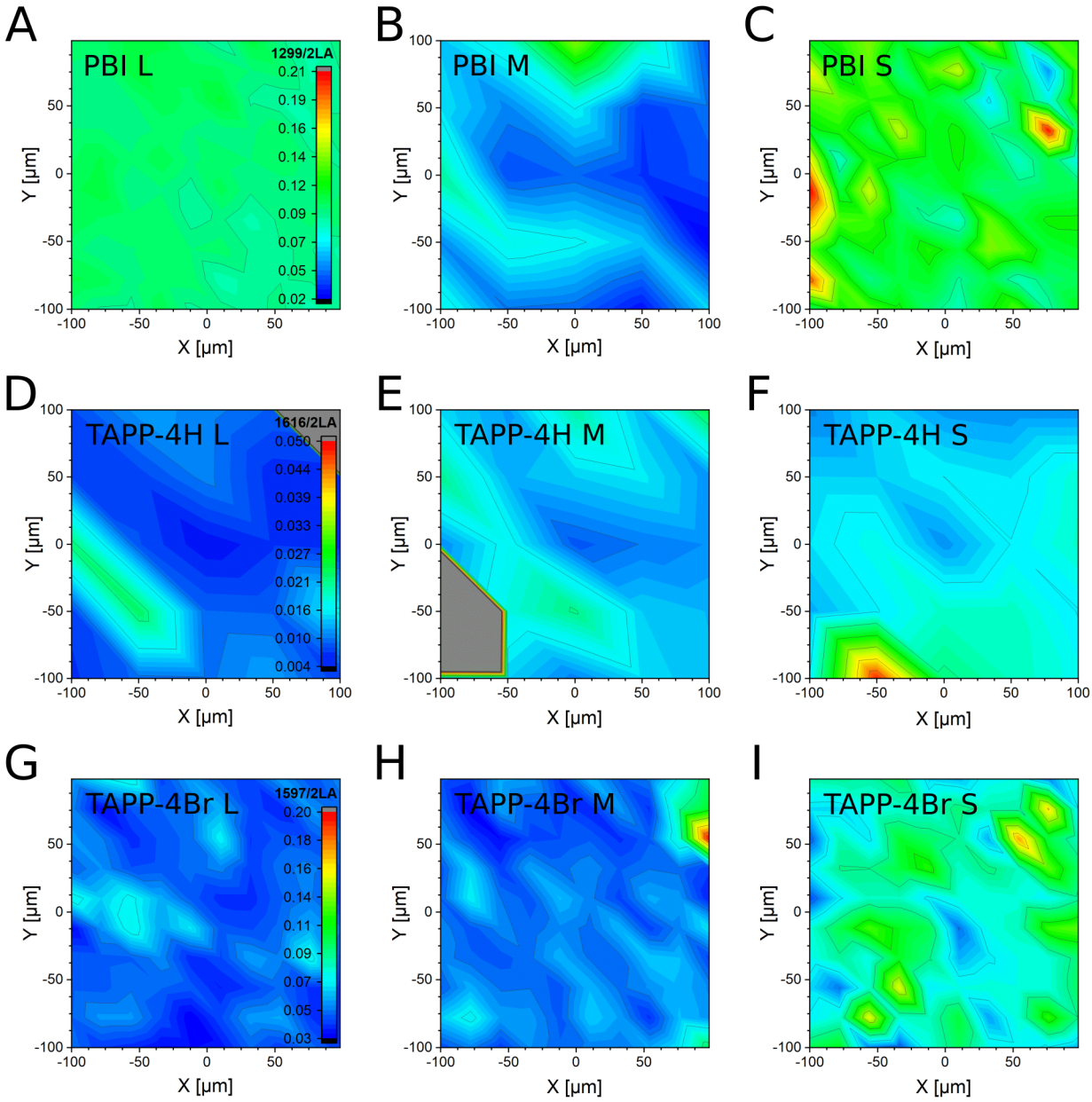

Figure 81: A-I) Raman maps of the intensity ratio of the most intense vibrational mode of the respective molecule and the 2LA vibrational mode of WS_2 for films treated with PBI (1299 1/cm, A-C), TAPP-4H (1616 1/cm, D-F) and TAPP-4Br (1597 1/cm, G-I) for L (A, D, G), M (B, E, H) and S (C, F, I) nanosheet films.

Concluding, it was shown that films produced via the modified Langmuir-Schaefer technique are well capable of serving as samples for solid state experiments with LPE nanosheets owing to their defined morphology and retention of size-dependent properties. This was demonstrated through deposition of organic chromophores on the surface of WS_2 films. As no signs of molecular absorption were evident from extinction spectroscopy, it is concluded that a thin dye layer was deposited. Nonetheless, the presence of molecules was evident from Raman spectroscopy. An impact of the chromophore on the PL of WS_2 is evident although effects of changes in laser power and effects of electronic interaction with molecules are convoluted. Furthermore, the molecule coverage was shown to be

inhomogeneous and needs to be improved in future experiments. This set of experiments serves as a good example of the inherent utility of this deposition method for research in the academic lab and encourages further studies into molecule/material interfaces.

5.3 Impact of film morphology on the hydrogen evolution reaction

Among its various promising properties, WS_2 is known for its catalytic activity towards the hydrogen evolution reaction in water splitting. In this application, the activity in *2H*-WS_2 features pronounced anisotropy, as edge regions are the main centers of activity while basal plane activity is significantly lower. Therefore, when fabricating working electrodes from *2H*-WS_2, control over film morphology is imperative to tailor activity. As such, a pronounced difference in activity is expected for random opposed to aligned nanosheet films and a comparison of electrodes made of WS_2 nanosheets on glassy carbon via either airbrush spray or modified Langmuir-Schaefer deposition will be discussed in the following chapter.

The total current generated for electrodes for the hydrogen evolution reaction (HER) is a function of electrode area. Since the porosity in airbrush spray deposited films is significantly higher compared to films derived from the modified Langmuir-Schaefer method, the effective area for airbrush spray films should be higher than its geometric area. In order to compensate this intrinsic difference, the development of means for surface area assessment of airbrush sprayed films is necessary. An electrochemical method to assess the electrochemical active surface area (ECSA) of an electrode is chronocoulometry.[252] This potential jump experiment entails measurement of transferred charges over time in the diffusion limit. If diffusion coefficients of redox couples involved are known, the ECSA can be calculated. The experimental setup used for the electrochemical analysis in the following chapter is shown in figure 82. In order to properly estimate the geometric electrode area, a home-built electrode enclosure was fabricated to control the contact area to the electrolyte (figure 82, A).

The substrate housing (1, beige in figure 82, A) is fabricated from PTFE with a hollow center for insertion of the substrate. A small circular opening with 4 mm diameter is cut into the front of the housing for a controlled electrode-electrolyte interface size. The glassy carbon substrate (3, grey in figure 82, A-B) is electrically contacted from the back through a brass contact plate (4, red in figure 82, A). A conductive contact thread (7, yellow in figure 82, A) is attached and fitted to a commercially available stainless steel threaded rod which allows for electrical connection to the glassy carbon. A PTFE screw (2, blue in figure 82, A) on the back of the housing is in place to compress the contact plate and the glassy carbon electrode. A rubber O-ring (5, black in figure 82, A) is attached to the circular

opening to seal the interior from the electrolyte as pressure is applied through the PTFE screw, which is also equipped with an O-ring (6, black in figure 82, A) for self-sealing.

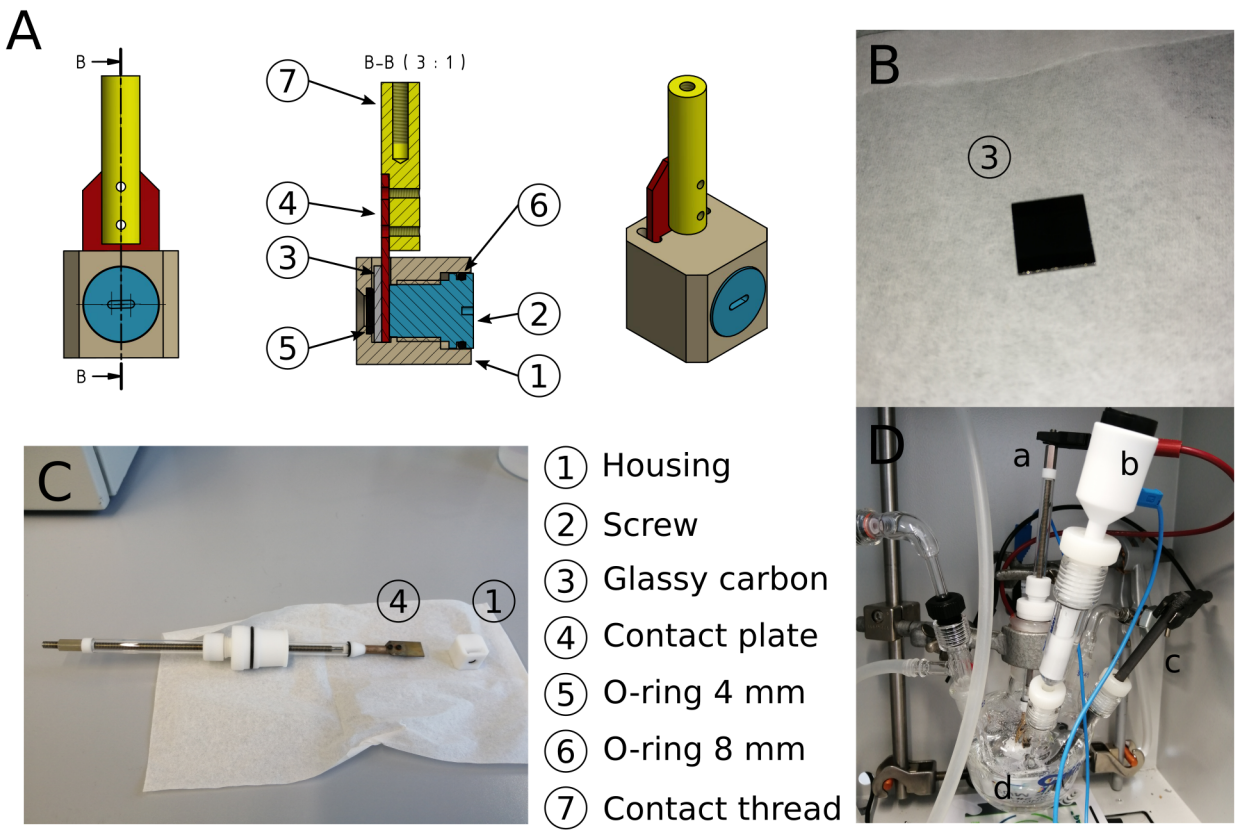

Figure 82: A) Sketch of the manufactured electrode enclosure viewed from the back and at an angle as well as an intersection. Individual parts are color coded and labeled. B) Image of the used 10×10×1 mm glassy carbon substrates. C) Photography of the manufactured electrode holder attached to a commercially available threaded rod and cell sealing. D) Assembled electrochemical cell consisting of the glassy carbon working electrode holder (a), reversible hydrogen reference electrode (b) and graphite rod counter electrode (c) in electrolyte solution (d).

The assembled working electrode setup is shown in figure 82, C with the home built electrode holder attached to the threaded rod. A standard cut fixture is attached to be able to seal the electrochemical cell (d in figure 82, D). For cell assembly, the working electrode (a in figure 82, D) is positioned in the cell center and a graphite rod counter electrode is positioned on the side (c in figure 82, D). The reversible hydrogen reference electrode (RHE, b in figure 82, D) is positioned in between working and counter electrode using an extended glass capillary filled with 0.5 mol/l sulfuric acid as close as possible to the working electrode surface without obstructing the latter.

For chronocoulometry, potassium ferricyanide $K_3[Fe(CN)_6]$ was chosen as analyte, as it shows well defined electrochemical redox chemistry and diffusion coefficients are literature known.[253] Furthermore, its redox chemistry happens at positive potentials versus RHE in 0.5 mol/l sulfuric acid and therefore no currents of the hydrogen evolution reaction

should overlap with the ferricyanide redox reaction. To establish the correct potential jumps, cyclic voltammetry of $K_3[Fe(CN)_6]$ (2 mmol/l) in aqueous KCl solution (1 mol/l) was conducted at airbrush sprayed WS_2 electrodes and shown in figure 83, A.

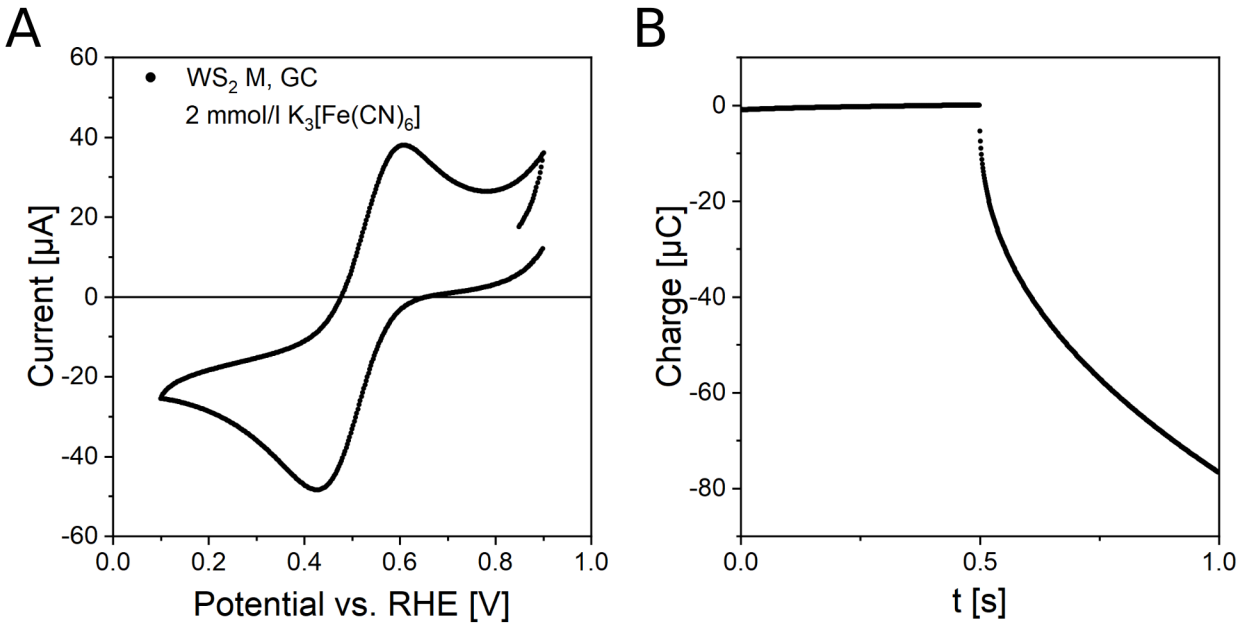

Figure 83: A) Example of a current potential diagram derived from cyclic voltammetry in 2 mmol/l potassium ferricyanide in aqueous 1 mol/l potassium chloride solution. B) Single step chronocoulometry of the ferricyanide reduction at a WS_2 electrode. The potential jump happens after 0.5 s in the same electrolyte as for panel A.

In the forward sweep cathodic currents transition through a maximum and show the characteristic shape of cyclic voltammograms with currents approaching the diffusion limit roughly between 0 and 0.1 V vs. RHE. In the backsweep however, increasing anodic currents after transition through the current maximum beyond 0.7 V vs. RHE are visible, indicating that oxidation reactions other than the ferrocyanide oxidation are taking place. This is attributed to oxidation of the working electrode WS_2 film.[254] As such no diffusion limited current is achieved for the backsweep and hence chronocoulometry is restricted to the ferricyanide reduction. The chronocoulometry potential jump was therefore chosen as going from 0.65 V vs. RHE, where no significant currents are expected, to 0 V vs. RHE, where diffusion limited currents are expected, after 0.5 seconds. The cumulative charge transferred over time is shown in figure 83, B. Transmitted charge is close to zero up until the potential jump occurs. After that reductive charge transfer occurs. According to the Anson equation, a square-root dependence of charge over time is expected and the electrochemical active surface area A_{ECSA} can be extracted from the slope of the plot $Q(t)$ versus $t^{1/2}$ (equation 27), as starting concentration c_0 and diffusion coefficient of the oxidized species D_O are known and z is 1 for the ferricyanide/ferrocyanide redox couple.[252]

$$\frac{dQ(t)}{d\sqrt{t}} = 2\,zFA_{ECSA}\,c_0\sqrt{\frac{D_O}{\pi}} \tag{27}$$

The roughness factor R_f of the electrode surface can then be calculated as the ratio of electrochemical active and geometric surface area (equation 28) with the latter calculated as a circle of 2 mm radius.

$$R_f = \frac{A_{ECSA}}{\pi r^2} \tag{28}$$

For further electrode characterization, cyclic voltammetry was conducted in sulfuric acid without the presence of an analyte for varying scan rates and nanosheet sizes. Current-voltage diagrams derived from cyclic voltammetry are shown in figure 84, A-C. The visible rectangular shape indicates non-faradaic currents dominating the current-voltage diagram increasing with increasing scan rates. Currents I should approach a threshold current after inversion points of cyclic voltammograms according to equation 29.

$$I = \nu\, C_{DL}\left(1 - e^{-\frac{t}{R_S C_{DL}}}\right) \tag{29}$$

Here, ν is the scan rate, C_{DL} the double layer capacitance, t the time and R_S the electrolyte resistance. This threshold current should scale linearly with the scan rate and the slope of this linear plot can be used to determine the double layer capacitance of the electrode in 0.5 mol/l sulfuric acid. Although no perfect threshold current parallel to the x-axis (figure 84, A-C) is achieved, most pronounced for small nanosheets, a well-behaved linear correlation of current and scan rate is observable. The double-layer capacitance derived from the slope of the linear fit as well as the roughness factors from chronocoulometry are shown in figure 84, D. As evident from the derived roughness factors, film roughness decreases for decreasing nanosheet sizes.

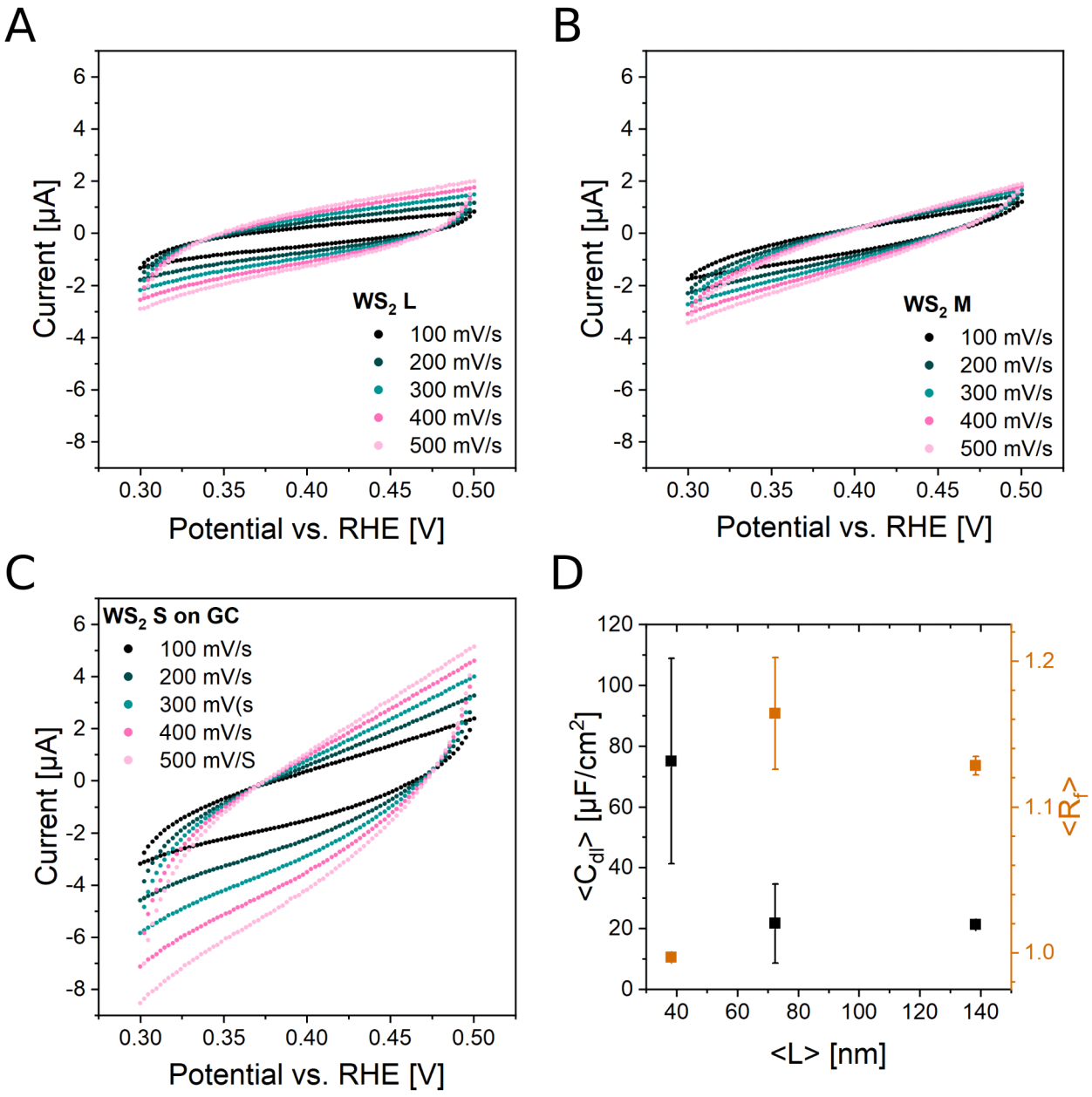

Figure 84: A-C) Current-potential diagrams derived from cyclic voltammetry in 0.5 mol/l sulfuric acid with varying scan rates for L (A), M (B) and S (C) nanosheet films. D) Double-layer capacitance derived from cyclic voltammetry in A-C and roughness factors derived from chronocoulometry plotted as function of the average length of the WS_2 nanosheets in the film.

This observation is in line with previous results from profilometry shown in table 6.[217]

Table 6: Root mean square roughness derived from profilometry for nanosheet films deposited via airbrush spray deposition of varying nanosheet sizes from previous works.[217]

Nanosheet size in films	RMS roughness [nm]
L (0.4 - 1k *g*, $\langle L \rangle$ = 150 nm)	13.4 ± 4.4
M (1 - 5k *g*, $\langle L \rangle$ = 75 nm)	12.4 ± 7.2
S (5 - 30k *g*, $\langle L \rangle$ = 42 nm)	7.6 ± 2.1

This can be seen as a result of random sheet deposition and can be explained in terms of a dependence of porosity and surface roughness on the average nanosheet length $<L>$. The double layer capcitance C_{DL} increases with decreasing nanosheet size in accordance to results from literature (figure 84, D).[255] Usually the double layer capacitance is a function of the electrode surface area and can be used to derive electrode area based on reference measurements under certain conditions. However, size-dependent changes in the double layer capacitance of WS_2 nanosheet films renders such an evaluation impossible. The roughness factors derived from chronocoulometry were then used to correct the electrode area and subsequently calculate the current density J of nanosheet films in further experiments.

For an evaluation of electrode performance in the hydrogen evolution reaction (HER), films were used as working electrodes in 0.5 mol/l sulfuric acid. As the reference electrode used was a reversible hydrogen electrode (RHE), the origin of the potential axis is set to the equilibrium potential of the $H_2/2H^+$ redox couple in the employed electrolyte and hence, all measured potentials in HER are overpotentials η. Linear sweep voltammetry was conducted from +0.2 to -0.5 V vs. RHE and the resulting polarization curves after roughness correction and compensation for Ohmic drop are shown in figure 85, A. The working electrodes can be roughly divided into four groups: modified Langmuir-Blodgett films with the manual method (purple traces) and modified Langmuir-Schaefer films with the optimized setup (pink traces) and airbrush sprayed films deposited from aqueous SC solution (teal traces) and from IPA (green traces). Generally, films produced from airbrush spray deposition outperform films produced via film formation at a liquid-liquid interface with higher current densities J for comparable overpotentials η. This is most likely due to nanosheet alignment parallel to the substrate for Langmuir-Blodgett and -Schaefer films, as this reduces the exposure of nanosheet edges to the environment through edge overlaps. On comparison of old (manual method) and new (deposition with PTFE setup) film deposition setups, the new deposition setup produces films with significantly lower activity compared to the old setup (compare purple and pink traces in figure 85, A) most probably owing to film defects occurring with the initial manual method, thus exposing more nanosheet edges to the electrolyte. It has to be noted that even with the new setup, significant film-to-film variations are visible and therefore complicate interpretation of subtle differences (best seen for duplicate films in pink traces in figure 85, A). For airbrush sprayed films, activity is higher due to more exposed nanosheet edges in the randomized film morphology. Remarkably, the activity upon deposition from IPA at 90 °C is generally higher for comparable sizes than for deposition from aqueous SC solution at 130 °C. It remains unclear if activity for deposition from SC suffers due to thermal degradation at elevated deposition temperatures or whether this is due to the presence of leftover surfactant molecules on the nanosheet films after washing.[256] Furthermore, for all

deposition techniques, smaller nanosheets increase HER activity in accordance with literature,[255] although progression with size is not always followed clearly. Again, film-to-film variations render interpretation of such small size-dependent changes difficult. Nonetheless, the smallest nanosheets are always the most active electrodes with highest current densities for comparable sizes and deposition methods. Furthermore, a change in slope is visible beyond certain potentials owing to the semiconducting nature of the electrode material.

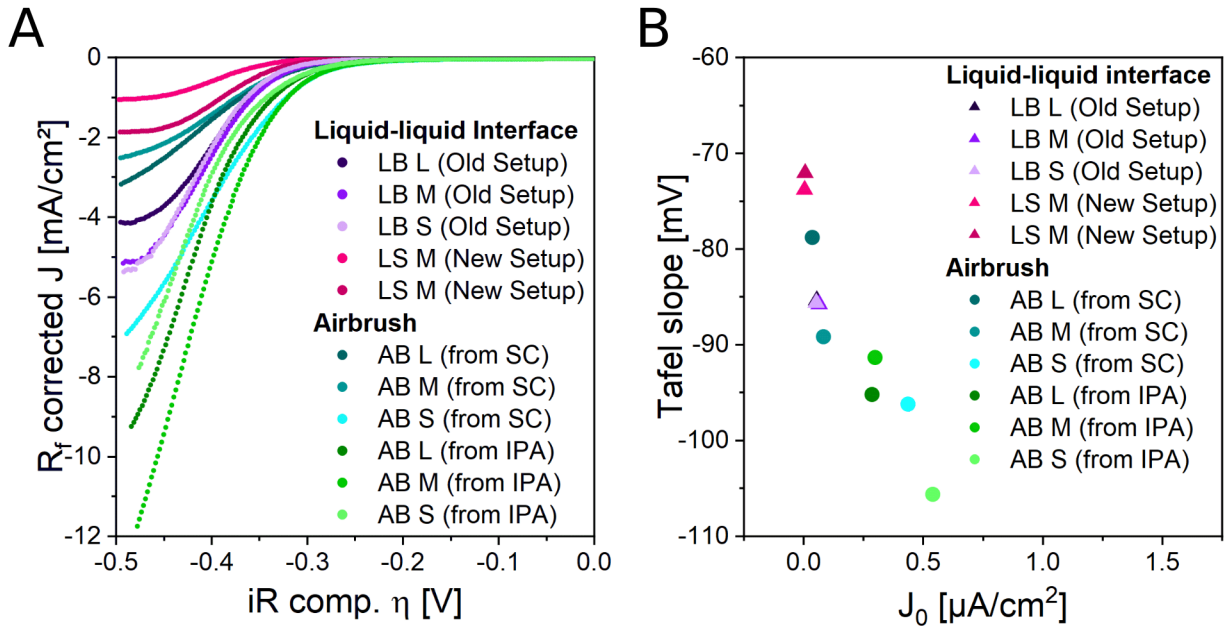

Figure 85: A) Linear sweep voltammograms of WS_2 nanosheet film electrodes produced via different deposition methods from dispersions containing nanosheets of different average size. Overpotentials were compensated for Ohmic drops, and current densities were corrected for film roughness. The roughness of films produced via the modified Langmuir-Schaefer method was assumed to be 1. B) Tafel slope and exchange current density extracted from polarization curves in A.

The current-voltage relationship of electrochemical redox reactions can be described using the Butler-Volmer equation (equation 30 for the case of non-limiting mass transfer).

$$J(\eta)=J_0\left(e^{\frac{\alpha\, zF}{RT}\eta}-e^{-\frac{(1-\alpha)zF}{RT}\eta}\right) \tag{30}$$

As only one branch of the redox reaction is usually explored (e.g. reductive currents for HER), the second branch can be neglected for sufficiently high overpotentials and the so-called Tafel equation (equation 31) can be derived after rearrangement of equation 30.

$$\eta=b\log(|J|)-b\log(J_0),\ \ with\ \ b=-\frac{RT\ln(10)}{(1-\alpha)zF}\ \ for\ \ |\eta|\gg\frac{RT}{zF} \tag{31}$$

Equation 31 is linearized and therefore advantageous for data analysis. The parameters of interest are then Tafel slope b and exchange current density J_0. Interpretation of these parameters is often less straightforward,[257-258] but for an efficient catalyst material, b is ideally low and J_0 ideally high. Low Tafel slopes enable a more pronounced increase in current density upon increasing overpotentials and its value is classically interpreted in HER as a function of the limiting reaction step in HER.[259] Exchange current densities on the other hand can be seen as a metric for the intrinsic activity of a catalyst. However, interpretation of J_0 is often complicated through crude estimations of the real surface area and non-linearity in Tafel plots, with the latter often occurring due to electrode porosity and complex reaction mechanisms.[259] J_0 is an extrapolated value and therefore depends on the Tafel slope b. This convolution of J_0 and b complicates discussion of parameters individually. Furthermore, interpretation of slope and exchange current densities is compromised due to the existence of a non-linear current evolution due to the semiconducting nature of the nanosheet electrodes.

Extracted Tafel slopes plotted versus exchange current densities are shown in figure 85, B. Example images of fitting and a brief discussion of Tafel plot shape can be found in appendix 8.14. A clear correlation of Tafel slope and exchange current density is evident from figure 85, B. Tafel slopes of Langmuir-Blodgett and -Schaefer films are generally lower compared to airbrush sprayed films although exchange current densities are higher for the latter. Therefore a clear dependence of the morphology on the HER performance is visible, likely due to the anisotropic electrocatalytic activity of WS_2 nanosheets. Furthermore, the impact of size appears more pronounced in airbrush sprayed films compared to Langmuir-Blodgett and -Schaefer type films, however film-to-film variations need to be considered, as the trend of increasing exchange current densities with decreasing nanosheet sizes is not always followed. The fact that all data points fall on the same curve irrespective of morphology and size indicates a behavior intrinsic to pure WS_2 nanosheet films. Unfortunately, the trend observed only allows for increases in exchange current densities if the Tafel slope increases significantly. As the Tafel slope is ideally low and exchange current densities ideally high, such a trend poses a significant obstacle for the optimization of electrode performance.

In order to test if this apparent performance limit can be overcome, another set of electrodes was fabricated. A possible caveat of using semiconductor materials for electrodes is always lower conductivity compared to metallic electrodes commonly used for HER (e.g. Ni or Pt). Therefore, attempts were made in literature to improve film conductivity by formation of composites with conductive fillers.[177] Furthermore, it was shown in the past that gold nanoparticle functionalization of WS_2 nanosheets in aqueous SC solution is capable of improving HER activity of electrodes fabricated from these

nanosheets.[160] This appears counter intuitive as gold functionalization occurs predominantly around nanosheet edges and the latter are regarded as the main reaction site for HER in 2*H*-WS_2. Based on this anisotropic functionalization, a dependence of film morphology on the HER performance of these nanosheets is expected and was not explored previously.

Therefore, electrodes of gold-functionalized WS_2 nanosheets were produced via the modified Langmuir-Schaefer deposition. Optical microscopy images of gold nanoparticle functionalized WS_2 nanosheet films produced via the modified Langmuir-Schaefer deposition are shown in figure 86, A-D. At low magnifications (panel A-B), wrinkled features can be seen. These features are likely situated in the nanosheet film however the glassy carbon substrates themselves feature scratches and inhomogeneities on the surface possibly visible through the thin nanosheet film. Therefore, the origin of these features cannot be assigned unambiguously. At higher magnifications (panel C-D), the appearance of WS_2 films on glass is reproduced with no major aggregates or holes visible. This is further corroborated by scanning electron microscopy images visible in figure 86, E-H. A dense nanosheet network is visible while individual nanosheets are hard to discern even at highest magnifications (panel H). They appear blurred-out due to intense charging effects during image acquisition. Small bright dots are distributed over the imaged area indicating the presence of gold nanoparticles on WS_2 nanosheets edges. The nanosheets are aligned parallel to the substrate in accordance with previous observations, with gold nanoparticle functionalized edges facing each other. Hence, nanosheet alignment can be exploited to produce defined channels of gold nanoparticles in a tiled network. Atomic force microscopy images of two individual films produced from gold-functionalized WS_2 nanosheets are shown in figure 86, I-J for film A and K-L for film B. While AFM images of film A appear very smooth with barely any significant features discernible, inhomogeneities are well visible for film B in accordance with wrinkles visible from optical microscopy (figure 86, A-B). Therefore, film B is expected to be slightly rougher and the active surface area for electrochemistry should be increased. This is also reflected in the root mean square roughness extracted from AFM imaging, with 6.11 nm for film A and 8.80 nm for film B as average of three individual images each. Raman spectra of gold-functionalized WS_2 nanosheet films produced via the modified Langmuir-Schaefer deposition on glassy carbon show the typical size-dependent evolution of WS_2 in the corresponding dispersion with the usual decrease in PL/2LA ratio (figure 86, M) with decreasing monolayer content. The exact degree of PL quenching is likely underestimated solely judging by bare eye due to the presence of the glassy carbon 2D mode at roughly 2679 1/cm overlapping with WS_2 PL. Interestingly, the PL position seems to be barely shifted in films compared to dispersion in contrast to film deposition on glass, where significant PL broadening and

peak shifts were visible (figure 74). This discrepancy highlights the effect of substrate choice on the optical properties in films.

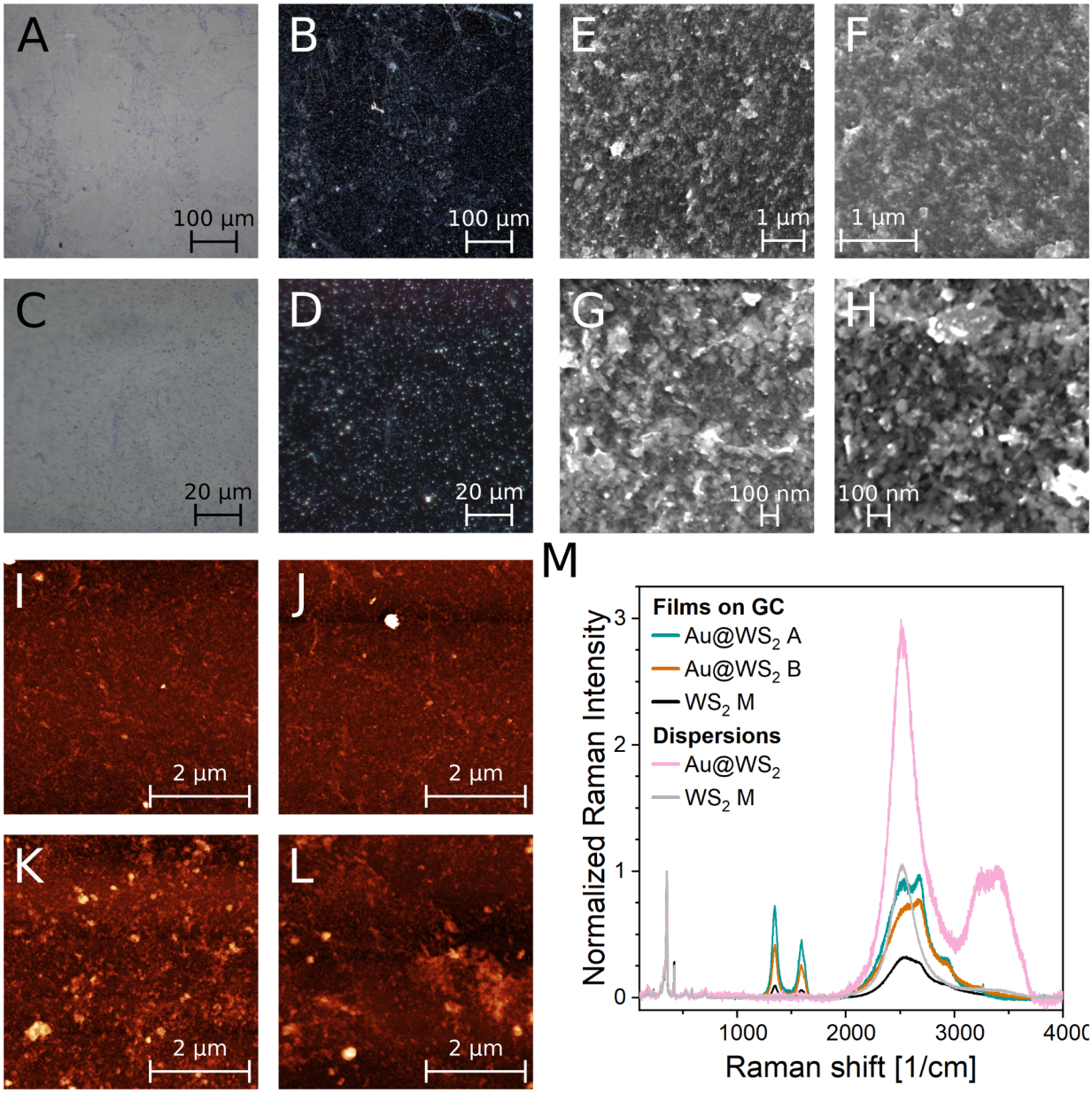

Figure 86: A-D) Optical microscopy images of gold-functionalized WS_2 nanosheet films produced via the Langmuir-Schaefer deposition (film B) on glassy carbon with x20 (A-B) and x100 (C-D) objective in bright (A, C) and dark field mode (B, D). E-F) SEM images of the same gold-functionalized WS_2 nanosheet films recorded at 1 kV acceleration voltage with x15 000 (E), x27 000 (F), x60 000 (G) and x80 000 (H) magnification. Images in panel G and H were recorded in gentle beam mode. I-L) AFM images of the same gold-functionalized WS_2 nanosheet films for film A (I-J) and B (K-L). M) Raman spectra (λ_{exc} = 532 nm) of gold-functionalized and pristine WS_2 nanosheet films produced via the modified Langmuir-Schaefer deposition on glassy carbon in addition to spectra of ink dispersions for reference normalized with respect to the intensity at the 2LA vibrational mode. The characteristic Raman features of sp^2/sp^3 carbon are detected at 1347, 1593 and 2679 1/cm in the films on glassy carbon.

Electrodes of gold-functionalized WS_2 nanosheets produced via the modified Langmuir-Schaefer deposition, as well as airbrush spray deposition from aqueous SC solution were then used as working electrodes for HER. Furthermore, reference films were deposited via the airbrush spray deposition for functionalized and non-functionalized WS_2 films with the addition of single-walled carbon nanotubes (SWNTs) as conductive[12] filler. Linear sweep voltammograms in 0.5 mol/l sulfuric acid are shown in figure 87, A.

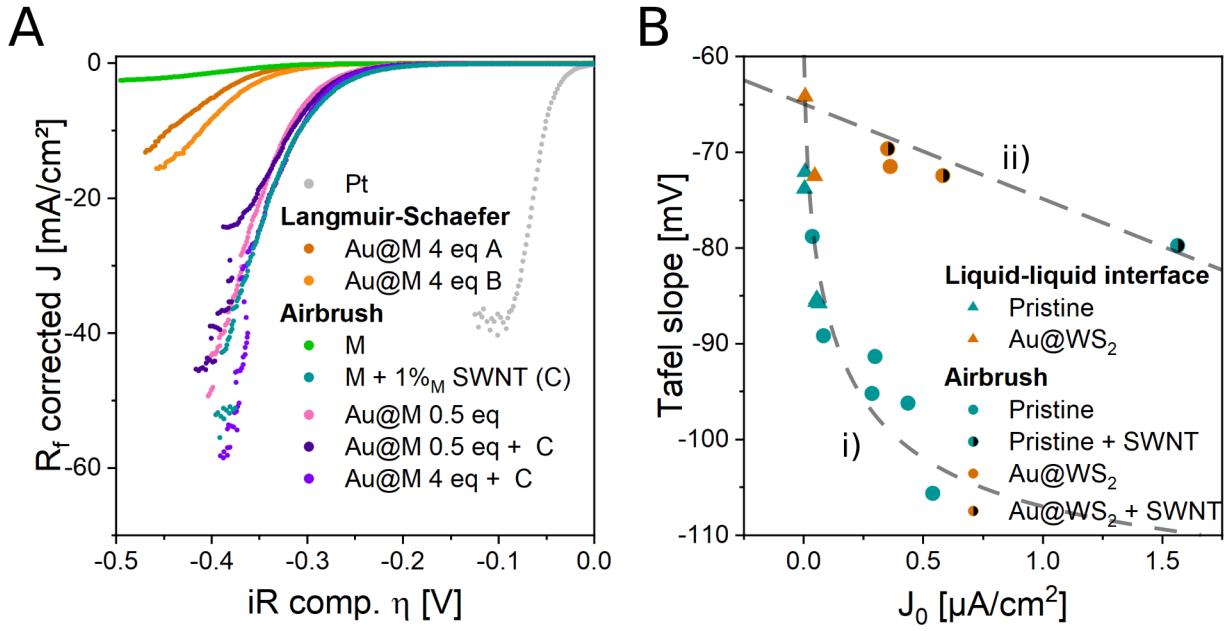

Figure 87: A) Linear sweep voltammograms of gold nanoparticle functionalized WS_2 nanosheet film electrodes produced via different deposition methods. Intermediate sized nanosheets (1 - 5k g) were used for all electrodes. Overpotentials were compensated for Ohmic drops and current densities were corrected for film roughness. Roughness of films produced via the modified Langmuir-Schaefer method was assumed to be 1 (roughness factors estimated from AFM were 1.05 - 1.07 and hence negligible, orange traces). B) Tafel slope and exchange current density extracted from polarization curves in A and figure 85. Guides for the eye are added using grey dashed lines.

According to expectation, gold nanoparticle functionalized WS_2 nanosheet films show significantly increased activity compared to non-functionalized WS_2 nanosheets, as current densities for a given overpotential are higher by at least an order of magnitude. For comparison, an airbrush film deposited from pristine *M* sized nanosheets in aqueous SC solution as well as a 3 mm Pt disc electrode are included (green and light grey trace respectively). While electrode activity is still far lower than for the noble metal electrode, enhancement due to gold nanoparticle functionalization is evident. Furthermore, electrode activity of airbrush sprayed films is higher than for Langmuir-Schaefer films presumably due to reasons already outlined for pristine WS_2 films as increased exposure of nanosheet edges for airbrush sprayed films. Interestingly, the curves apparently converge for airbrush sprayed films of gold nanoparticle functionalized nanosheets irrespective of the addition of

12 Note that semiconducting and metallic SWNTs were not separated prior to film deposition. As such, a mixture of both types of SWNTs is expected to be present in the film.

conducting SWNTs or the amount of chloroauric acid used for gold nanoparticle functionalization. In addition, the composite film of non-functionalized WS_2 films and SWNTs falls on the same curve. This behavior indicates that the origin of improvement in HER activity for both conductive composites and gold functionalization is of similar origin and due to improvements in film conductivity up to a certain upper limit after which intrafilm charge transport is not rate limiting anymore.

The combined Tafel slopes b and exchange current densities J_0 for all electrodes explored are shown in figure 87, B. A color code is used to highlight properties of certain groups of electrodes: Langmuir-Blodgett and -Schaefer type films are shown as triangles, while airbrush sprayed films are shown as circles. Gold nanoparticle functionalized WS_2 nanosheet films are colored in orange and pristine WS_2 in teal. In the cases where SWNTs are added to the film, a black semicircle is added. Films of gold nanoparticle functionalized WS_2 nanosheets show comparatively low Tafel slopes indicative of their improved HER activity. Furthermore, airbrush sprayed electrodes of improved conductivity due to conductive fillers or gold nanoparticle functionalization clearly deviate from the trend of b vs J_0 established for pure WS_2 electrodes (Figure 87, B, i) and fall on a rather linear trend of their own (ii). For electrode optimization, this trend is advantageous as the increase in Tafel slope is less pronounced for increases in exchange current density. Possibly this corroborates the assumption that the activity for trend i) is at least partially charge transport limited, while trend ii) is followed if no charge transport limitation is in place. Trends converge at low Tafel slopes, where b vs J_0 for Langmuir-Schaefer type films of gold-functionalized WS_2 nanosheets are positioned. This complicates unambiguous assignment of these films, but they appear closer to the trend of pure WS_2 films. This corroborates the hypothesis that the effect of increased film conductivity depends on the film morphology due to nanosheet anisotropy. In Langmuir-Schaefer type films, nanosheets face exclusively edge to edge contact and charges are therefore only transferred from substrate to nanosheets and from edges to edges between nanosheets (figure 88).

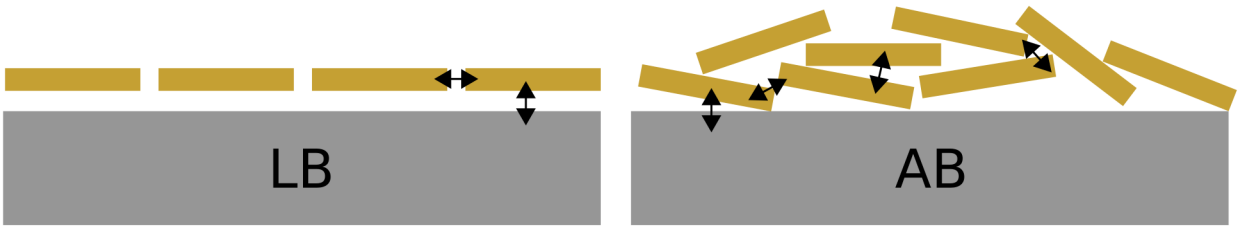

Figure 88: Sketch of possible current paths (black arrows) in Langmuir-Schaefer type films (left) and airbrush sprayed films (right) with nanosheets in yellow and glassy carbon substrate in grey.

Charge transfer between nanosheets is of minor importance for electrode performance in Langmuir-Schaefer type films as all nanosheets are equally exposed to the

electrolyte and therefore rendering charge transfer between the glassy carbon substrate and nanosheets the dominant parameter. A possible explanation for the beneficial effect of edge functionalization is a small improvement in charge transfer between the glassy carbon substrate and the nanosheets. Any intrinsic effect of gold functionalization should enhance activity in airbrush sprayed films as well and beyond improvements due to increased conductivity also observed after the addition of nanotubes. However, it appears that this is not the case: in airbrush sprayed films, improvement in film conductivity translates well to electrode activity, as nanosheet orientation is randomized. As such, edge to basal plane and basal plane to basal plane charge transfer are possible between the nanosheets. Due to different electrolyte exposure of nanosheets in porous networks, charge transfer across nanosheets is crucial. Conductive materials brought into the path of charge transfer therefore impact HER activity significantly and remove the bottleneck of intrafilm charge transport. As a result, all traces in figure 87, B fall on the same curve, as the new rate limiting step is intrinsic to the material. These results do not show any indications for additional effects occurring due to gold functionalization, such as an impact of layer number (as nanosheets after functionalization and purification are predominantly monolayered), new edge species due to oxidation[160] or hot electron generation due to high electric fields between nanosheets, where gold nanoparticles are located.[260] However, the implications of morphology are multifold in electrodes, as catalytic active sites and conductivity are anisotropic in WS_2 nanosheets and both change along with the morphology, complicating interpretation. No definite exclusion of possible sources of improvement can therefore be derived based on the available data, but the charge transport was confirmed as a key parameter.

Concluding, a protocol for the assessment of hydrogen evolution reaction activity for electrodes fabricated from LPE WS_2 via different deposition techniques was devised and the necessary experimental setup implemented. Chronocoulometry was evaluated as a potential tool for the estimation of the electrochemical surface area and therefore roughness of nanosheet electrodes based on redox chemistry of potassium ferricyanide. Linear sweep voltammetry of WS_2 electrodes in 0.5 mol/l sulfuric acid revealed a dependence of HER activity on the film morphology and was assigned to differences in electrolyte exposure of nanosheet edges as the main centers of catalytic activity. An increase of HER activity upon gold functionalization of WS_2 was evident for both deposition techniques explored and related to changes in film conductivity upon introduction of conductive fillers. This knowledge renders pure WS_2 electrodes rate-limited by charge transport. Unfortunately, a certain degree of ambiguity cannot be erased based on the available data due to the complexity of the systems investigated in chapter 5.3 and further investigations into this system are necessary to develop a sound understanding of HER activity.

6 Conclusion

In the first part of this thesis, the gold nanoparticle functionalization of layered materials was explored in detail. A workup and purification protocol based on literature for functionalization of tungsten(IV)sulfide nanosheets in aqueous SC solution was presented and the origins of reported monolayer enrichment demonstrated. Different reaction pathways were identified and their relative contribution to the overall reaction outcome was linked to the amounts of chloroauric acid employed for functionalization. On exchange of the surfactant employed for stabilization of the WS_2 nanosheets, significant differences in the reaction outcome were evident from extinction spectra and XPS revealed that severe material degradation took place. The reagent consumption was shown to be quantitative irrespective of surfactants employed indicating that the impact of surfactants resulted in a kinetic control of different reaction pathways. A model was developed to explain the observed surfactant influence and distinguishable reagent trajectories were devised. Kinetic control of the surfactant layer was then linked to preferential adsorption of surfactant molecules based on their molecular structure and size-dependent ζ potential measurements. Furthermore, additional experiments were designed and corroborated the hypothesis, e.g. interlayer growth of gold nanoparticles and temperature dependence.

The developed model was then employed to explain differences in gold functionalization between tungsten(IV)- and molybdenum(IV)sulfide nanosheets. Similar chemical behavior of these compounds is expected, however distinct differences in reactivity were revealed by the model reaction. In contrast to tungsten(IV)sulfide nanosheets, treatment with chloroauric acid does not lead to near complete structural degradation of molybdenum(IV)sulfide nanosheets in both surfactants employed. These differences were assigned to competing reaction channels for the oxidant with the relative share of each channel to the overall reaction determined not only by the kinetic barrier that arises along each individual pathway, but also to intrinsic material reactivity. The interpretation based on the devised model strongly suggests that the basal plane of molybdenum(IV)sulfide nanosheets is less reactive compared to tungsten(IV)sulfide. This underlines the advantage of gold functionalization as a probe for heterogeneous functionalization reactions, as reaction sites can be visualized through the produced nanoparticles. Such visualization is usually challenging for functionalization with e.g. organic molecules and can aid in disentangling reaction mechanisms for heterogeneous wet chemical reactions. Furthermore, the fact that surfactant molecules are capable of directing reactivity can be exploited to tune functionalization products without the need for adjustment in the choice of reagent and therefore might serve as a potent tool in functional material design.

Gold nanoparticle functionalization of tungsten(IV)sulfide nanotubes was employed to test the impact of the material structure on the gold functionalization. Therefore, a protocol for nanotube dispersion compatible with surfactant solutions was developed resulting in intact nanotubes in liquid dispersion. It was shown that the relatively large concentrations of chloroauric acid employed for nanosheets leads to excessive production of gold clusters. However, at lower relative reagent concentrations, well-behaved nanoparticle functionalization was demonstrated. Interestingly, gold nanoparticle functionalized nanosheets were found in dispersion due to oxidative stripping of the multi-walled tubular structures. Indications of gold nanoparticles produced in the interlayer space of nanotubes were found and linked to the production of nanosheets during functionalization. Isolation of nanosheets was attempted for functionalization in aqueous SC solution and, although the nanotube content in dispersion was significantly reduced, no pure nanosheet dispersions were achievable. The produced dispersions were polydisperse in nanosheet length, width and thickness. In contrast to nanosheets from LPE, the nanosheet area was not correlated with the nanosheet thickness and overall, larger thin nanosheets were produced. As such, oxidative nanotube stripping can be exploited for production of relatively large nanosheets with gold nanoparticles around nanosheet edges.

Preferential adsorption of surfactants to different sites on the nanosheets based on their chemical structure is in itself an interesting finding. Based on the presented data, additional research questions arise. For example, whether preferential adsorption can be observed for other surfactant types, such as linear cationic amphiphiles or even non-ionic surfactants. Furthermore, it is of interest if adsorption site preferences of a certain surfactant persist irrespective of the layered material. The experiments detailed in this thesis were limited to sulfur-based group VI TMDs, but interactions with other layered materials, such as graphene, might behave differently due to differences in surface chemistry. Large scale screening of surfactant adsorption on different layered materials, aided by the methods presented in this thesis, could help in establishing a systematic catalog of surfactant/material combinations in order to exploit preferential adsorption for experimental designs. For example, the regioselectivity of the reaction of WS_2 with chloroauric acid presented was linked to preferential adsorption of the surfactants used. If generalization of this mechanism would be possible, a toolbox of surfactant-material systems could be devised, enabling targeted functionalization without the necessity for modifications to the reagent. However, fundamental questions of the reagent-surfactant interactions need to be addressed prior to such endeavors. At this point, it is unclear if the directing influence of surfactants is related to electrostatic repulsion of reagent and surfactant and if this mechanism is therefore limited to ionic reagents of the same charge as the surfactant. Especially for introduction of organic functional groups in layered materials, reagents are often non-ionic and means of directing regioselectivity in these

functionalization reactions may prove valuable in the future and enable access to new, interesting material properties.

In the second part of this thesis, film deposition methods compatible with dispersions of layered nanomaterials derived from liquid phase exfoliation were explored and compared. The first method investigated was airbrush spray deposition in which ink dispersions are finely dispersed using a propellant gas and deposited on a heated substrate. Film morphology was investigated and random nanosheet orientation in films was observed producing porous films. Advantages of this method are the applicability of patterning, facile composite film production and readily adjustable film thickness. Disadvantages are elevated substrate temperatures beyond the solvent boiling point, ruptures in the deposited film and loss of some properties of the dispersion constituents in the film such as complete quenching of WS_2 PL in films due to random restacking.

The second method investigated was film formation at a liquid-liquid interface between *n*-hexane and water and subsequent substrate transfer, termed modified Langmuir-Blodgett or Langmuir-Schaefer technique. At first, manual transfer to the substrate was explored, and revealed a concentration dependence of film density with the optimum nanosheet mass necessary for a closed film being dependent on the average layer number of the nanosheets in dispersion. In contrast to spraying, nanosheets were aligned parallel to the substrate surface rendering the film morphology well-defined. Size-dependent trends in dispersion are well-transferred to film properties. For example, the monolayer PL is still discernible in these films rendering this method better suited for film production aimed towards optical applications and research into size-dependent properties. However, macroscopic film integrity was suboptimal as film tearing during transfer was evident and no homogeneous deposition on the majority of the substrate was possible.

To resolve these issues associated with manual film transfer, a deposition setup was built from PTFE and made to fit for commercially available 250 ml glass beakers. This setup allowed for more reliable and even film formation, as no penetration of the formed film occurs prior to substrate transfer. The produced films are micro- and macroscopically homogeneous over the whole substrate with size-dependent properties of nanosheets employed for deposition translated well to the films. A certain impact of substrate effects on optical properties was suggested and can serve as starting points for future experiments to investigate the properties of the nanosheets in the films on contact with varying surfaces. This could help in assessing the influence of substrates in certain measurement scenarios on e.g. trion formation or peak shifts.

The defined morphology in these films produced from the modified Langmuir-Schaefer deposition in conjunction with nanosheet alignment, smooth films with root mean square roughness approaching nanosheet thicknesses, retention of a portion of the PL, reproducibility, and reliability of the method are its key advantages. However, minor film-to-film variations were observed and the fact that film thickness can only be increased through laborious deposition of multiple layers is disadvantageous especially in the context of applications. For use in academic research however, the modified Langmuir-Schaefer deposition is superior to airbrush spraying, as the film morphology and absence of any thermal degradation are ensured, while size-dependent properties are retained.

At this point, the film production with the liquid-liquid interface method was investigated solely at the water/*n*-hexane interface with TMDs dispersed in IPA. However, some layered materials, such as graphene or *h*-BN, suffer from very poor colloidal stability in IPA and the possibility of using other solvents, such as NMP could help with film deposition of these materials. In turn, this would also require a change of the interface constituents, as the density of NMP is higher than that of water, leading to turbulence upon ink injection. A replacement of water in the system could also enable working in inert atmosphere, e.g. in a glovebox and therefore allow for deposition of materials sensitive to moisture or oxygen under ambient conditions. Therefore, investigations into other solvent systems for the modified Langmuir-Schaefer method are of interest, in order to expand the capabilities of this deposition approach.

For demonstration of the possibilities of films produced via the modified Langmuir-Schaefer deposition, organic molecules were deposited on the film surface. Molecule deposition was sparse, as no molecular features were evident from extinction spectroscopy. In Raman spectroscopy however, vibrational modes of organic molecules were clearly resolved indicating successful deposition. Differences in electronic interaction of molecules and WS_2 films based on the molecule used were observed even though molecule deposition was inhomogeneous based on Raman mapping. This serves as a proof-of-principle for the utility of the developed nanosheet film deposition method in academic research. A whole host of experimental designs with LPE nanosheets is enabled by this method, for example the film deposition on (pretreated) substrates to assess substrate effects, such as doping, on size-dependent optical properties, the covalent and non-covalent functionalization of nanosheets in the solid state, or the formation of van-der-Waals heterostructures from different layered materials as demonstrated in independent work.[241]

To underline the impact of film morphology in applied research, electrode activity towards the hydrogen evolution reaction was compared for film deposition via airbrush

spraying and the modified Langmuir-Blodgett and -Schaefer deposition. For this, a measurement setup including a home-built substrate enclosure for use of deposited films as working electrodes was implemented. Furthermore, chronocoulometry with potassium ferricyanide was explored as a tool for estimation of the electrochemical active surface area to compensate for differences in electrode roughness between the two deposition methods. For pure WS_2 films, airbrush spray deposited electrodes outperformed Langmuir-Blodgett and -Schaefer type films due to higher exposure of nanosheet edges to the electrolyte, as edges are catalytically more active than the basal plane. A limited activity in pure WS_2 electrodes was identified, irrespective of the deposition technique used, manifested as increases in exchange current density with increasing Tafel slopes. This poses a severe obstacle for electrode optimization. Upon introduction of conductive fillers in the form of either SWNTs or gold nanoparticle functionalization in airbrush sprayed films, a deviation from this trend was evident and a more advantageous relation of Tafel slope and exchange current density was visible. Unfortunately, the Tafel slope and exchange current density of films of gold-functionalized WS_2 nanosheets produced from the modified Langmuir-Schaefer deposition were positioned around the point of convergence of both trends and therefore it remains unknown whether these Langmuir-Schaefer films are charge transport limited or not. Overall, a significant dependence of the film morphology on the electrocatalytic activity of WS_2 nanosheet films was demonstrated. This underlines, that electrode activities are not only a material, but rather a film property for layered TMDs and as such, film morphologies should always be a point of consideration for the sensible evaluation of data from electrochemical experiments with TMD electrodes.

Concluding, insights into fundamental properties of the influence of the surface chemistry on heterogeneous functionalization reactions and the importance of controlling film morphology for layered nanomaterials have been presented in this thesis. These observations were lastly only possible due to the high structural anisotropy of layered nanomaterials and the impact of the latter on the properties of the material. Although the described observations were confined to a limited set of employed materials, generalization of findings to other two-dimensional systems is plausible and as such will hopefully aid current and future researchers in advancing scientific progress in the field in revealing exciting new properties and applications for the fascinating material class of two-dimensional nanomaterials.

7 Methods

This thesis was written using LibreOffice 5.4 and Endnote 20. Evaluation and plotting of experimental data was conducted using OriginPro 2021b. Furthermore, figures presented throughout this thesis were designed using Inkscape 1.1, ChemOffice Suite 2020, Discovery Studio Visualizer v21 and PovRay v3.7.

7.1 Index of Chemicals

In the following all chemicals used in the experiments detailed in this work are listed in table 7. These were used without further purification, if not detailed elsewhere.

Table 7: Index of Chemicals

Tungsten(IV)sulfide	99 %, powder, 2 µm	Sigma-Aldrich
Molybdenum(IV)sulfide	99 %, powder, < 2 µm	Sigma-Aldrich
Hexagonal boron nitride	98 %, powder, ~ 1 µm	Sigma-Aldrich
Tungsten(IV)sulfide nanotubes	Batch TWPO-00001-2014, powder	Tenne group, Weizmann Institute of Science
Single walled carbon nanotubes	75 %, > 2 nm diameter, > 1 µm length, powder	TUBALL™
Sodium cholate hydrate	≥ 99 %, from ox and/or sheep bile	Sigma-Aldrich
Sodium dodecyl sulfate	≥ 98.5 %, BioReagent	Sigma-Aldrich
Chloroauric acid trihydrate	≥ 99.9 %	Sigma-Aldrich
Potassium ferricyanide	≥ 99.0 %	Sigma-Aldrich
Potassium chloride	99.5 - 100.5 %	Sigma-Aldrich
(3-Aminopropyl)triethoxysilane	99 %	Sigma-Aldrich
Isopropanol	≥ 99.8 %	Honeywell
Acetone	≥ 99.8 %	Honeywell
n-Hexane	≥ 95 %	Sigma-Aldrich
Toluene	≥ 99.7 %	Honeywell
Hydrochloric acid	≥ 37 %, fuming	Honeywell
Sulfuric acid	95 - 98 %	Sigma-Aldrich
Activated carbon	Powder, puriss.	Sigma-Aldrich
N,*N'*-Bis-(1-pentylhexyl)perylene-3,4,9,10-bis(dicarboximide)	Crystalline powder	Hirsch group, University of Erlangen
2,9-Bis-(heptafluoropropyl)-1,3,8,10-tetraazaperopyrene	Crystalline powder	Gade group, University of Heidelberg
2,9-Bis-(heptafluoropropyl)-4,7,11,14-tetrabromo-1,3,8,10-tetraazaperopyrene	Crystalline powder	Gade group, University of Heidelberg

Deionized (DI) tap water was further purified using a *ThermoFisher Scientific Barnstead Easypure RoDi* water purification system. *n*-Hexane and IPA were distilled prior to usage, in the case of IPA only for use in dispersions (for e.g. substrate cleaning it was used without further purification).

All substrates employed in this thesis were cleaned prior to use by sequential sonication in acetone, IPA and DI water for 15 minutes each and were blow-dried using a N_2 gun. For recycling of glassy carbon substrates, wiping of the substrate and a sonication step in isopropanol mixed with activated carbon prior to the above-mentioned cleaning sequence were employed.

7.2 Liquid phase exfoliation of materials

For production of dispersions of layered nanomaterials, liquid phase exfoliation was employed. If not detailed elsewhere, exfoliation was carried out according to the standard protocol described in the following.

800.0 mg sodium cholate (1.86 mmol) or 536.4 mg of sodium dodecyl sulfate (1.86 mmol) and 2.4 g of tungsten(IV)sulfide or molybdenum(IV)sulfide (9.68 mmol for WS_2 and 14.99 mmol for MoS_2) were added to 80 ml deionized water (23.23 mmol/l surfactant and 121 mmol/l WS_2/ 187 mmol/l MoS_2) in an 80 ml stainless steel beaker and stirred for dissolution of the surfactant powder. The mixture is then initially sonicated using a *Sonics Vibra-Cell VCX500* sonic tip operating at 20 kHz frequency and equipped with a threaded probe and a replaceable flat horn tip with 3 cm diameter. Pulsed sonication is employed with intervals of 8 s sonication followed by 2 s pause for 1 h of effective sonication time. The dispersion beaker was cooled by an external water flow at 5 °C generated by a *Julabo F250* Chiller to avoid excessive heating of the dispersion. The amplitude of the sonic tip was attuned according to the energy input of the sonicator and usually ranged between 40 - 60 %. The sonic probe was positioned in the center of the beaker ~1.5 cm from the bottom. For removal of impurities, the surfactant solution was exchanged after this initial sonication step. To this end, the dispersion was distributed to four 50 ml vials and subjected to centrifugation in either a *Hettich Mikro 220R* benchtop centrifuge equipped with a 1016 fixed-angle rotor at 3 820 *g* or in a *Beckman Coulter Avanti J-26S XP* centrifuge equipped with a *25.50* fixed-angle rotor at 5 000 *g* for 1.5 h at 10 °C[13]. The supernatant was discarded after centrifugation and the sediment redispersed in 80 ml of aqueous sodium cholate (4.6 mmol/l) or sodium dodecyl sulfate (4.6 mmol/l) solution. The

13 The choice of centrifuge was solely based on availability and RCF values for the Hettich centrifuge were based on maximum RCF of the 1016 rotor. As exfoliation is incomplete at this stage, almost all material is sedimented during centrifugation and the exact RCF used is not relevant.

resultant dispersion was again sonicated for 5 h of effective sonication time with a 6 s sonication/2 s pause pulse sequence.

For exfoliation of *h*-BN in aqueous SC solution, the SC concentration in the initial sonication step was reduced (480 mg, 1.12 mmol) and the initial exfoliation pulse sequence was changed to 4 s sonication followed by 2 s pause.

Due to constraints in available material mass, some parts of the standard protocol were adjusted for the (unsuccessful) exfoliation of WS_2 nanotubes: 300 mg sodium cholate (0.70 mmol) and 50 mg WS_2 nanotube powder (0.20 mmol) were added to 30 ml deionized water and a tapered tip (20 % amplitude) was used.

For exfoliation of intact WS_2 nanotubes, 20 mg of WS_2 nanotube powder was added to 20 ml of either aqueous SC solution (4.6 mmol/l) or aqueous SDS solution (3.47 mmol/l) in a 50 ml round bottom flask and sonicated for 30 min in the hotspot of a *Branson 2800* sonication bath filled with cold water. The mixture was then stirred for 1 h before another 30 min sonication was applied. The sonication bath water was exchanged for fresh cold water and another 30 min sonication was employed for a total effective sonication time of 90 min. The mixture was diluted with 20 ml of the respective surfactant solution and sonicated for 10 min before liquid cascade centrifugation.

For preparation of a dispersion of single-walled carbon nanotubes (SWNTs), 83.3 mmol/l of *TUBALL SWNT* powder were added to 13.8 mmol/l aqueous sodium cholate solution and sonicated for 1 h in the sonic bath. The mixture was then sonicated for an effective sonication time of 7.5 min at the sonic tip (1 s of sonication followed by 1 s pauses, 20 %, 19 °C) before another bath sonication of 1 h was employed. The dispersion was then centrifuged for 1.5 h at 3 000 *g*. The supernatant was separated from the sediment and diluted with aqueous SC solution (4.6 mmol/l) by a factor of 225. A second centrifugation step for 1.5 h at 3 000 *g* was employed to finally achieve a clear dispersion in the supernatant. **SWNT dispersions in aqueous SC solution were provided by Daniel Heimfarth in the group of Jana Zaumseil at the Ruprecht-Karls-Universität Heidelberg.**

7.3 Liquid cascade centrifugation

As nanomaterial dispersions produced from liquid phase exfoliation are polydisperse in nature, size selection of the dispersed material is necessary to derive size-dependent trends. For this sequential centrifugation runs of iteratively increasing relative centrifugal forces were employed. The supernatant was separated after each run and subjected to the next step in the cascade with increasing relative centrifugal forces while the sediment was

redispersed in reduced volumes of fresh surfactant solution. Centrifugation was performed in either a *Hettich Mikro 220R* benchtop centrifuge equipped with a *1016* fixed-angle rotor up to 3 820 *g* or an *1195A* fixed-angle rotor up to 30 000 *g* or in a *Beckman Coulter Avanti J-26S XP* centrifuge equipped with a *25.50* fixed-angle rotor up to 10 000 g or a *25.15* fixed-angle rotor up to 30 000 *g* for 2 h at 10°C. The sediment produced during the first centrifugation step and the supernatant after the last step were discarded. Final samples were labeled according to the centrifugation boundaries used for their production. For example, if a sediment was produced in centrifugation at 1000 *g* and the previous step in the cascade was at 400 *g*, then the redispersed sediment was labeled 0.4 - 1k *g*. Details of the employed centrifugation steps are found in table 8.

Table 8: Liquid cascade centrifugation steps for different experimental designs.

	Samples produced
Standard WS_2/MoS_2	0.4 - 1k *g* (*L*), 1 - 5k *g* (*M*), 5 - 30k *g* (*S*)
h-BN	0.1 – 0.4k *g* (*XL*), 0.4 – 1k *g* (*L*), 1 - 5k *g* (*M*), 5 - 10k *g* (*S*), 10 - 22k *g* (*XS*)
'No size selection' WS_2	0.4 – 30k *g*
Extended size selection for ζ potential measurements of WS_2	0.1 - 0.8k *g* (*XL*), 0.8 - 2k *g* (*L*), 2 - 4k *g* (*M*), 4 - 6k *g* (*S*), 6 - 30k *g* (*XS*)
WS_2 nanotubes	0.1 – 3.8k *g*, note that centrifugation time was reduced to 1 h

For transfer of samples into IPA, a small amount of the dispersion as derived from liquid cascade centrifguation was diluted with the respective surfactant solution and completely sedimented through centrifugation at RCF values equal or above the upper boundary of the size selection (e.g. 30 000 *g* for 5 - 30k *g* samples). The supernatant was carefully removed and the sediment redispersed in IPA.

7.4 Gold nanoparticle functionalization

Gold nanoparticle functionalization of materials was achieved by treatment with chloroauric acid. Therefore dispersions as obtained from liquid cascade centrifugation were adjusted to 2 mmol/l WS_2 (or MoS_2) concentration and either 0.46 mmol/l aqueous SC solution or 3.47 mmol/l aqueous SDS solution[14]. For large volume functionalization, typically 40 ml WS_2 dispersion (0.08 mmol) were added to a 100 ml round bottom flask equipped with a thermometer, dropping funnel and stirring bar and stirred on an ice bath

14 Surfactant concentrations for SDS were adjusted to ensure stability of dispersion.

until the dispersion temperature was 2 °C. 40 ml of aqueous chloroauric acid (the concentration depends on the equivalents employed, e.g. 8 mmol/l for 0.32 mmol or 4 eq, however dispersion volume was always kept constant) were added dropwisely for 15 min in a way that the reaction temperature never exceeded 3 °C. After complete addition, the reaction mixture was stirred for another 30 min before the ice bath was removed and then stirred for another 30 min. The mixture was kept at 4 °C in the refrigerator over-night.

For **reaction workup**, unreacted chloroauric acid and soluble byproducts were removed through centrifugation. To this end, the dispersion was mildly sonicated for 5 - 10 minutes in a sonic bath to redisperse sedimented material and then typically centrifuged at 16 000 *g* (1 h, 10 °C) for complete sedimentation of dispersed materials. The supernatant was removed and the sediment redispersed in either fresh aqueous SC solution (0.23 mmol/l) or fresh aqueous SDS solution (3.47 mmol/l). For removal of aggregates, the redispersed sediment was centrifuged at 59 *g* (2 h, 10 °C) and the sediment removed. The supernatant was referred to as *Stock* dispersion.

For **purification**, the *Stock* dispersion was typically centrifuged at 4 000 *g* (2 h, 10 °C) to remove big gold nanoparticle decorated material in the sediment. The supernatant was again centrifuged at 16 000 *g* (2 h, 10 °C), the supernatant discarded, and the sediment redispersed in fresh surfactant solution to concentrate material in the purified dispersion. This method produces one fraction from gold nanoparticle functionalization with high monolayer enrichment for WS_2 in SC. However, an extended centrifugation cascade, e.g. 400 - 2 000 *g* and 2 000g - 16 000 *g* can be employed in purification to demonstrate increasing monolayer enrichment (see appendix 8.1).

For low volume functionalization for e.g. analytic concentration screening, 750 µl WS_2 (2 mmol/l) or MoS_2 dispersion (3.12 mmol/l) were mixed with 750 µl aqueous chloroauric acid solution of various molar equivalents in 1.5 ml eppendorf vials and stored for three days at 4 °C in the refrigerator to ensure complete conversion. Respective concentrations were kept constant. Workup was conducted as described previously, however no purification was conducted. For experiments at elevated temperatures, the reaction time was reduced to one day.

For functionalization of WS_2 nanotubes, some parameters of the large volume protocol were adjusted: nanotube dispersions were adjusted to an optical density at 235 nm $OD_{235\,nm} = 2\ 1/\mathrm{cm}$ and the aqueous chloroauric acid concentration was normalized to the optical density of the nanotube dispersion and expressed as extinction equivalents (e.g. $c = 0.08$ mmol/l, $eq_{ext} = 0.04$ mmol/(l·cm)). The reaction itself was performed as outlined above. For workup, centrifugation steps employed for removal of unreacted chloroauric

acid and aggregates were changed to 20 000 *g* (2 h, 10 °C, supernatant discarded) and 24 *g* (1.5 h, 10 °C, sediment discarded) respectively.

Enrichment of gold-functionalized nanosheets from nanotube functionalization was conducted by different centrifugation parameters as outlined in chapter 4.4, with best results for centrifugation at 200 *g* twice (2 h each, 10 °C, sediments discarded) and subsequent dispersion concentration at 20 000 *g* (2 h, 10 °C, supernatant discarded). The sediment was redispersed in fresh surfactant solution

7.5 Characterization of nanosheet dispersions and films

Extinction spectroscopy. Dispersions after exfoliation were characterized using optical extinction spectroscopy at ambient conditions to assess material concentration and estimate average lateral nanosheet size $<L>$ and average layer number $<N>$. Extinction spectra were recorded in an *Agilent* (formerly *Varian*) *Cary 6000i* UV-Vis-NIR spectrophotometer in fused quartz cuvettes with 4 mm path length. Dispersion spectra were acquired in the range from 200 to 1 000 nm with 0.5 nm resolution and 0.1 s integration time. Samples were diluted using the respective surfactant solution prior to the measurement and a baseline correction was performed with blank surfactant solution. For concentration determination, an extinction coefficient of $\varepsilon_{235\,\mathrm{nm}} = 47.71\ \mathrm{l/(g \cdot cm)}$ was used for WS_2 as the extinction coefficient is largely unaffected by changes in size at this wavelength.[8] For MoS_2, extinction coefficients at 250 nm are size-dependent. Therefore, the average lateral nanosheet size was first calculated using equation 32.[15]

$$<L>=\frac{1.97-\frac{Ext(270\,nm)}{Ext(345)}}{0.016\,\frac{1}{nm}\cdot\frac{Ext(270\,nm)}{Ext(345)}-0.0144\,\frac{1}{nm}} \tag{32}$$

Extinction coefficients at 250 nm were then estimated using a linear relationship given in equation 33 based on data available in literature.[15]

$$\varepsilon_{250\,nm}=-0.28449\,\frac{l}{g\cdot cm\cdot nm}\cdot<L>+119.7182\,\frac{l}{g\cdot cm} \tag{33}$$

For film measurements a substrate holder with 4 mm hole aperture was employed and measurements were conducted with reduced range from 300 to 800 nm due to absorption of glass substrates.

Raman spectroscopy. Raman spectra of dispersions after liquid cascade centrifugation were measured under ambient conditions using a *Renishaw inVia* confocal Raman microscope equipped with a CCD camera and an *Olympus LMPlanFL* x50 long working distance objective lens. The laser employed was either a *Renishaw RL633* HeNe laser dispersed by a 1200 l/mm grating or a *Renishaw RL532C100* laser dispersed by a 2400 l/mm grating. Measurements were conducted in streamline mode and Raman shifts were calibrated to the vibrational mode of Si at 520.6 1/cm prior to measurements. All measurements were conducted on Al foil covered glass slides.

For measurements of dispersions, a liquid droplet was placed on the Al foil and the focus was set 5 µm above the droplet surface. For both lasers, measurements were conducted in the range of 100 to 4 000 1/cm on three different spots of the droplet and averaged. For film spectra, the focus is set to the film surface and five different spots are used for averaging. For mapping, a 200×200 µm square region was chosen and the focus set to the film surface at the square center. Parameters of Raman measurements are found in table 9. If not detailed elsewhere, standard parameters were used.

Table 9: Parameters for Raman measurements for different sample types.

Sample types	Laser power [%]	Integration time	Accumulations
Standard	1	10	1
h-BN/WS_2 composite films	5	10	1
MoS_2, Au@MoS_2	5	10	2
TAPP-4H Maps	5	10	2
TAPP-4Br Maps	5	2	2
PBI Maps	5	1	5

Note that the lower three entries in table 9 were employed only for mapping after molecule deposition with individually adjusted deposition times. Film M of PBI was measured in high confocality mode instead of regular mode employed elsewhere to reduce PL background intensity due to PBI excitation. To compensate for excessive measurement times, 25 individual spectra were recorded for TAPP-4H and PBI maps instead of 100 used for TAPP-4Br and pristine films, however the scanned area was kept constant.

ζ potential measurements. WS_2 was exfoliated as described above in aqueous sodium cholate solution, but each sediment was redispersed in deionized water instead of surfactant solution. Prior to the measurement, the WS_2 dispersions were split into two aliquotes of 1 ml per size and the WS_2 concentration of each sample was adjusted to 1 mmol/l and then centrifuged at 30 000 *g* (2 h, 10 °C). The supernatant was removed, and

samples were redispersed in either 0.23 mmol/l aqueous sodium cholate solution or 0.23 mmol/l aqueous sodium dodecyl sulfate solution. This serves the purpose of excluding possible differences in exfoliation due to surfactant effects or batch-to-batch variations. For ζ potential measurements, a *Malvern Panalytical Zetasizer Nano ZSP*, equipped with a 633 nm HeNe laser was used and dispersions were measured in disposable *Malvern Panalytical DTS1070* folded capillary cells. Cells were equilibrated with the respective surfactant solution prior to each measurement. The sample viscosity was assumed to be the viscosity of water (1.0031 mPa·s at 20 °C) and the Smoluchowski approximation was used. Each sample was measured three times with a minimum of 10 runs per measurement, with no delay between measurements. The *ζ* analysis version used was v6.1. The distribution data of each measurement were fitted using a Gaussian and centers of the Gaussian fit $<\zeta>$ were extracted and averaged.

X-ray photoelectron spectroscopy. In order to assess the oxidation states of WS_2 after gold nanoparticle functionalization in aqueous SDS solution with 4 equivalents of chloroauric acid, X-ray photoelectron spectroscopy (XPS) was employed. Measurements were conducted in a *Physical Electronics XPS Versa Probe* with a monochromated Al Kα source (hv = 1486.7 eV) and a spot size of 100 µm. For sample preparation, 20 ml of the reaction mixture prior to workup were filtered on an AlO_x membrane with 20 nm pore size and extensively washed with 1 l of DI water. The filter cake was dried at 50 °C and then subjected to XPS measurements. The specimen was mounted electrically isolated to have a floating potential and electrical charging of the specimen surface was neutralized by using a combination of Ar^+ ion and electron flux. An overview scan of the whole energy region was performed and individual orbitals of interest (W 4f, S 2p, Au 4f, Cl 2p and C 1s) were investigated with high resolution scans. No features were discerned in the Cl 2p core level spectra which are therefore not shown. C 1s core level spectra position of adventitious hydrocarbon (248.8 eV) was used to compensate for static charge effects on peak position. Respective core level spectra were analyzed with use of *MultiPak* software. The respective peaks were fitted using doublets with a fixed peak area ratio 1:2 and 3:4 for p and d orbitals respectively. Separation of the doublet spin-orbit components for W 4f was ~2.17 eV and for S 2p ~1.16 eV. **XPS measurements were conducted by Beata M. Szydłowska in the group of Georg Düsberg at the Universität der Bundeswehr München.**

X-ray diffraction. For determination of possible crystal structure degradation upon production of gold nanoparticles in the interlayer space of WS_2, X-ray diffraction (XRD) was employed. A *Rigaku SmartLab* X-ray diffractometer equipped with a HyPix-3000 detector was used to collect X-ray powder diffraction data. Cu $K\alpha_1$ radiation with a wavelength of $\lambda = 1.54059$ Å was incident on a rotating sample (60 rpm) in Debye-Scherrer

geometry. The 1D diffraction pattern was recorded between 10° and 80° at a speed of 5°/min in 0.01° increments. For specimen preparation, multiple exfoliation and decoration runs were performed to collect sufficient material quantity. WS_2 was exfoliated in aqueous SC solution according to the standard protocol and liquid cascade centrifugation was performed according to the "no size selection" template (see chapters 7.2 and 7.3). For gold decoration, 150 ml WS_2 dispersion at 2 mmol/l was prepared using the large volume gold nanoparticle functionalization protocol with 0.5 eq of chloroauric acid. The workup step is altered, and no purification step was employed. For workup, the reaction mixture was centrifuged twice at 30 000 *g* (2 h, 10 °C), the supernatant discarded, and the sediment redispersed in DI water to remove surfactant present on the nanosheets. The redispersed sediment was then again centrifuged at 30 000 *g* (2 h, 10 °C), the supernatant removed, and the sediment redispersed in IPA. A final centrifugation at 30 000 *g* (2 h, 10 °C) was employed, the supernatant removed, and the sediment transferred into a small pear shaped glass flask using small amounts of IPA. After precipitation using a *Büchi Rotavapor R-100* rotary evaporator and subsequent drying in vacuo overnight, a dark powder with metallic shine was obtained and transferred into a special glass capillary (*WJM-Glas Mark-tubes*, 0.6 mm diameter, 80 mm length, 0.01 mm wall thickness) for measurement. An empty capillary was used to measure the background for baseline correction under identical measurement conditions. Since the baseline measurement was of higher intensity than the measurement of the specimen, multiplication of the baseline with a fixed factor of 0.411 was employed to compensate for significant X-ray absorption of the specimen. Extracted reflexes and assignments: 14.3° (WS_2, 002), 32.8° (WS_2, 100 or WO_3, 022), 33.6° (WS_2, 101 or WO_3, 202), 32.8° (WS_2, 100), 38.3° (Au, 111), 39.5° (WS_2, 103), 44.0° (WS_2, 006), 49.7° (WS_2, 105), 58.5° (WS_2, 110), 60.5° (WS_2, 112), 64.8° (Au, 220), 77.7° (Au, 311). **XRD measurements were performed by Vaishnavi J. Rao in the group of Jana Zaumseil at the Centre for Advanced Materials (CAM) at the Ruprecht-Karls-Universität Heidelberg.**

For reference measurements of bulk and exfoliated WS_2, a non-size-selected dispersion of WS_2 was produced through sonication of 1.4 g WS_2 powder in 70 ml of aqueous SC solution (13.8 mmol/l) for 6 h effective sonication time (60 % amplitude, pulses of 4 s sonication followed by 1 s pauses) using a *Heilsher UP200S* sonic probe (200 W, 24 kHz). For removal of unexfoliated material, the dispersion was subjected to centrifugation at 240 *g* for 90 minutes in a Hettich Mikro 22R centrifuge and the sediment discarded. Material for XRD measurement was then collected by filtering the supernatant onto AlO_x membranes to achieve a reasonably thick film, which was then mounted to a glass slide. Powder XRD measurements of the specimen was performed using a *Siemens D500* X-ray diffractometer equipped with a monochromated Cu Kα emission source (λ = 1.54056 Å). Data was collected in in 0.02° increments with 3 s integration time per

increment and analyzed using *Bruker EVA* software. **Reference XRD data was provided by Zahra Gholamvand in the group of Jonathan Coleman at the Trinity College Dublin.**

7.6 Imaging methods

Scanning electron microscopy. For imaging of nanosheet films and nanotubes, scanning electron microscopy (SEM) was employed. Imaging was performed using a *JEOL JSM-7610F* field emission scanning electron microscope equipped with a semi-in-lens objective lens. Standard imaging was conducted in secondary electron imaging mode with 5 kV acceleration voltage at 4.5 mm working distance. If excessive charging was present, gentle beam mode was employed with 3 kV acceleration voltage and 2 kV of negative voltage applied to the specimen to arrive at 1 kV of effective acceleration voltage and an upper electron converter was inserted. Samples were deposited on either polished p-doped Si (*Siegert Wafer*, single side polished, prime grade, cut to size using a diamond cutter) or glassy carbon substrates (10x10x1 mm, *ALS*, P-1 glassy carbon) and attached to a brass holder using adhesive carbon tape. For imaging of dispersions, a droplet was deposited on the substrate and the solvent evaporated. Substrates were washed with DI water and blow-dried at the N_2 gun.

Transmission electron microscopy. For resolution of individual nanosheets or gold nanoparticles, transmission electron microscopy (TEM) was employed using a *JEOL 2100Plus* transmission electron microscope with 120 kV acceleration voltage. For sample preparation, dispersions were diluted with DI water and dropcasted (20 droplets) onto holey carbon coated copper mesh grids of 3.05 mm diameter (*Agar scientific*, 400 mesh) and dried over-night at 50 °C at ambient pressure. **Transmission electron microscopy was performed at the Electron Microscopy Core Facility (EMCF) of the European Biology Laboratory (EMBL) in Heidelberg.**

Atomic force microscopy. For roughness determination of films produced via the modified Langmuir-Schaeffer method and for statistical analysis of nanosheet size distribution, atomic force microscopy (AFM) was performed using a *Bruker Dimension Icon* scanning probe microscope in *ScanAsyst* mode equipped with *OLTESPA-R3* visible apex tips (aluminum coated Si cantilever) under ambient conditions. Images were acquired in a 5×5 µm square area at scan rates of 0.5 Hz with 1024 line scans per image. For higher resolution images of gold nanoparticle functionalized MoS_2 nanosheets 2×2 µm areas were probed. For sample deposition, cleaned SiO_2-coated p-doped Si substrates (*Graphene Supermarket*, 90 nm oxide thickness, Si prime grade, cut to size using a diamond cutter) were treated with 2 ml (3-Aminopropyl)triethoxysilane (APTES) in 78 ml

DI water to form a self-assembled monolayer on the Si surface to improve material adhesion. 20 µl of a dispersion were added on the APTES coated surface and left to settle for 20 s, before the substrate was intensely washed with DI water and blow-dried. Prior to deposition of dispersions in SDS, a small amount of this dispersion was sedimented through centrifugation at 30k *g* (2 h, 10 °C) and redispersed in sodium cholate solution.

Digital microscopy. For imaging of films over the whole substrate area with low magnification, a *Leica DMS300* digital microscope was used and an external scale bar was imaged alongside the films.

Optical microscopy. For imaging of films, an *Olympus BX51* optical microscope equipped with x5, x10, x20, x50 and x100 *Olympus MplanFL* objective lenses and a *UC30* camera was used.

7.7 Thin-film deposition

Airbrush spray deposition. For film deposition with the home-built airbrush spray setup, glass (*Schott AF32 eco* glass slides, 25x20x0.3 mm or *Knittel Glas* cover slips, 18x18x0.15 mm) or glassy carbon substrates (*ALS*, P-1 glassy carbon, 10x10x1 mm) were inserted into a dent in the aluminum substrate holder and fixed in position using a stainless-steel shadow mask with a rectangular 4×12 mm opening with curved edges and four hexagon headed screws. The substrate holder was positioned on the heating stage and the temperature was set to 130 °C for deposition from aqueous solution or 90 °C for deposition from IPA. The spraying distance was adjusted to 7 cm measured from the ceiling of the enclosure using the lifting stage. The propellant gas pressure (N_2) was adjusted to 1 bar overpressure under open vent (typically 2 bar overpressure in the closed state) and enclosure ventilation was set to half-maximum power. Movement of the heating stage in one direction was controlled with a *Trinamic TMCM-1110 StepRocker* motor controller and the program *TMCL-IDE 3.0*. The script employed for autonomous motor movement is shown in appendix 8.11. The airbrush gun used was a *Harder & Steenbeck Infinity* airbrush gun equipped with a 0.15 mm vent needle, a 2 ml ink basin and a cut to size 10 ml pipette tip (*Eppendorf epT.I.P.S. Standard*) for ink supply. The needle retraction in the opened state was adjusted to 200 µm at the optical microscope and pure DI water (or IPA depending on the used ink) was added to the ink basin after installation of the gun. After calibration of the stage movement and the target stage temperature was reached, the airbrush gun was activated and kept running using a home-built *'auto-fire button'*. The actual nanomaterial ink (8 ml and 0.5 mg of nanomaterial) was then added to the ink basin during spraying when the pure solvent was almost emptied. All inks were sonicated for 30 min in the sonication bath prior to spraying with additives, such as *h*-BN (size *M*,

concentration unknown, expressed as volumina of equal concentrations) or SWNTs (1 $\%_W$) added prior to sonication if applicable. After complete deposition, films were washed by resting in DI water over-night, blow-drying at the N_2 gun and drying in vacuo at room temperature using a *PELCO 2245 Mini Hot Vac* vacuum hotplate the following day.

Modified Langmuir-Blodgett deposition (manual setup). For film deposition using the manual method, a commercially available 25 ml glass beaker was filled with 25 ml deionized water and 2 ml of *n*-hexane was layered on top. By using a 200 µl pipette tip (*Eppendorf epT.I.P.S. Standard*) 100 µl of diluted WS_2 dispersion (1.6 and 0.8 mmol/l) in IPA was injected to the beaker wall as close as possible to the liquid-liquid interface and left to settle for a few minutes. For sample transfer, the *n*-hexane layer was removed through careful pipetting and leftover *n*-hexane was left to evaporate at ambient conditions. Then either the glass (*Knittel Glas* cover slips, 18×18×0.15 mm) or the glassy carbon substrate (*ALS*, P-1 glassy carbon, 10×10×1 mm) was manually inserted into the solvent column as orthogonal to the interface as possible using metal tweezers and retracted at an angle. Films were then left to dry at ambient conditions.

Modified Langmuir-Schaefer deposition (home-built setup). In order to improve film deposition using the film formation at a liquid-liquid interface, a deposition setup was fabricated from PTFE. The substrates (either glass or glassy carbon) were placed on the substrate mounts and the latter was placed in the dent of the base. Holes were drilled into the base and the retrieving rods were attached to form the retriever part. The retriever was inserted into a commercially available 250 ml glass beaker and DI water was filled into the beaker until the substrate surface was entirely covered. The bucket part with 40 mm interior diameter was inserted and rests on top of the beaker. 500 to 750 µl *n*-hexane were layered on top of the liquid column in the bucket interior and left to settle until a biconcave liquid-liquid interface formed. A commercially available long glass Pasteur pipette was fixed with a clamp and a lifting stage was employed to lift the glass beaker until the liquid started to run up the pipette positioned close to the interior wall of the bucket. 250 µl of the WS_2 dispersion in IPA was added into the glass pipette. Note that the concentration was adjusted based on nanosheet size (3.2 mmol/l for *L*, 2.8 mmol/l for *M* and 2.4 mmol/l for *S* nanosheets). The film was left to settle until complete extraction of the dispersion from the pipette before the pipette was removed. The *n*-hexane layer was left to evaporate under ambient conditions (for 750 µl and the 40 mm bucket this took approximately 15 minutes) and the retriever was lifted through the interface for film transfer to the substrate. The film resting on a cushion of water was carefully removed from the substrate mount and left to dry under ambient conditions.

7.8 Molecule deposition

For deposition of molecules on films produced via the modified Langmuir-Schaefer deposition, films were dipped in solutions of molecules (*N*,*N'*-Bis-(1-pentylhexyl)perylene-3,4,9,10-bis(dicarboximide) (PBI), 2,9-Bis-(heptafluoropropyl)-1,3,8,10-tetraazaperopyrene (TAPP-4H) and 2,9-Bis-(heptafluoropropyl)-4,7,11,14-tetrabromo-1,3,8,10-tetraazaperopyrene (TAPP-4Br)) in toluene with concentrations of 10^{-4} mol/l. For the initial deposition approach, molecules were soaked for 10 min in the respective molecule solution, blow-dried, and washed by soaking in clean toluene over-night. As no traces of TAPP-4H and PBI remained after washing, alterations were made to the deposition protocol. For TAPP-4Br and PBI deposition times were reduced to 10 s and no washing was conducted after blow-drying.

7.9 Electrochemical methods

All electrochemical experiments were conducted in a *Gamry Instruments EuroCell* electrochemical cell with working volumes of 50 - 200 ml equipped with a high-density graphite rod counter electrode (6.3 mm diameter, 15 cm long), a *Gaskatel Hydroflex* reversible hydrogen electrode (RHE) in a reference electrode bridge tube filled with 0.5 mol/l sulfuric acid and capped with an unfired porous glass disk (3.5 mm diameter) as membrane and ace threaded ports for gas tight sealing of electrode entry points. The potential stability of the RHE was regularly checked using an *ALS RE-1B* Ag/AgCl reference electrode in 3 mol/l aqueous sodium chloride solution. A threaded stainless steel support rod encapsulated in glass tubing equipped with a 24/40 to 8 mm PTFE stopper for gas tight sealing and a home-built PTFE enclosure for electrodes deposited on glassy carbon as current collector were used as the working electrode. The geometric area of the circular electrode/electrolyte interface was $\pi(0.2\ \mathrm{cm})^2 = 1.2566\ \mathrm{cm}^2$. For reference measurements, a *Gamry* platinum disk electrode with 3 mm electrode area (7 mm outer diameter) was employed. Furthermore, a three way gas purge/blanket gas inlet (N_2) with gas bubbler tube and a gas outlet with anti-return air valve were attached to enable degassing of the electrolyte and working under inert atmosphere. The whole setup was enclosed in a Faradaic cage to negate environmental electric fields and equipped with a stirring bar. The cell setup was then connected as a three-electrode cell to a *Metrohm Autolab PGSTAT204* Potentiostat/Galvanostat equipped with a *FRA32M* module for frequency response analysis.

Cyclic voltammetry. To assess the electrode double layer capacitance, cyclic voltammetry of WS_2 electrodes was carried out in 0.5 mol/l sulfuric acid in a potential region of +300 - +500 mV vs. RHE, where only non-Faradaic currents were expected, at varying scan rates of 50, 100, 150, 200 and 250 mV/s with stirring in between measurements. Three equilibration runs were conducted before a fourth run was taken as

measured data. Cathodic and anodic currents were extracted at different potentials in forward and backward sweep where sufficient linearization occurred (see table 10) and plotted versus the scan rate to determine the double layer capacitance from the slope of a linear regression. The capacitance was normalized with respect to the geometric electrode area and averaged for cathodic and anodic currents as deviation was minor.

Table 10: Potentials at which currents were extracted for double layer capacitance estimation.

Nanosheet size	Forward sweep [mV vs. RHE]	Backward sweep [mV vs. RHE]
L	523	444
M	544	439
S	527	449

For assessment of potential windows for chronocoulometry, cyclic voltammetry of 2 mmol/l potassium ferricyanide in 1 mol/l aqueous potassium chloride solution was conducted in a potential region of 0 - +650 mV vs. RHE at 500 mV/s scan rate. Note that this did not entirely cover the anodic response of the ferricyanide/ferrocyanide redox couple, but irreversible oxidation of WS_2 electrodes occurred at potentials above +650 mV vs. RHE.

Chronocoulometry. In order to assess the electrochemical active surface area of WS_2 working electrodes, chronocoulometry in 2 mmol/l potassium ferricyanide in 1 mol/l aqueous potassium chloride solution was employed. A potential of zero current was applied to the electrode cell and maintained for 0.5 s before the applied potential was switched to a potential at which diffusion limited cathodic currents are expected from ferricyanide reduction and charge transferred was measured as a function of time for 0.5 s. The exact potentials were evaluated based on the current-voltage diagrams from cyclic voltammetry. While a variation was observed across different electrodes, they always fell in the potential window from 0 to +650 mV vs. RHE. The charged transferred after the potential jump was plotted versus $t^{1/2}$ and a linear regression was employed to calculate the electrochemical surface area, which was then normalized to the geometric electrode area yielding the roughness factor R_f.

Frequency response analysis. In order to correct for Ohmic drops occurring between working and reference electrode, frequency response analysis in 0.5 mol/l sulfuric acid was conducted. A potential of +200 mV vs. RHE was applied to the working electrode and sinusoidal modulated in the frequency range of 10^6 to 10^{-1} Hz at an amplitude of 10 mV. The imaginary part of impedance $Im(Z)$ was plotted versus the real part $\mathrm{Re(Z)}$ (Nyquist plot) and the uncompensated resistance R_Ω was then extracted at $Im(Z) = 0$. At +200 mV vs. RHE no electrochemical reaction is expected and hence, charge transfer

resistance was very large. Therefore, the semicircular shape of Nyquist plots was not observed. This should however not impact determination of the uncompensated resistance.

Linear sweep voltammetry. For assessment of the hydrogen evolution reaction activity of working electrodes in 0.5 mol/l sulfuric acid, linear sweep voltammetry ranging from +200 to -500 mV vs. RHE was employed and the resulting current was measured at scan rates of 5 mV/s. Measured overpotentials were corrected for Ohmic drop using equation 34.

$$\eta_{iRcomp} = \eta_{measured} - IR_{\Omega} \tag{34}$$

The measured currents were normalized with respect to the electrode area and corrected for electrode roughness derived from chronocoulometry using equation 35.

$$J = \frac{I}{A_{geo} \cdot R_f} \tag{35}$$

For extraction of the Tafel slope b and exchange current density J_0, linearization was conducted by plotting absolute overpotentials versus the logarithm of absolute current densities and a linear fit was employed to determine b from the slope and extrapolate J_0 according to equation 36.

$$\underbrace{|\eta| = b\log(J_0) - b\log(|J|)}$$
$$\frac{\partial|\eta|}{\partial\log(|J|)} = -b \quad \text{and} \quad J_0 = 10^{\frac{y_0}{b}} \tag{36}$$

8 Appendix

8.1 Extended purification cascade centrifugation

In chapter 4.1 purification is presented using only two centrifugation steps in purification in order to achieve dispersions highly enriched in monolayers for WS_2 in SC. However, as an alternative a centrifugation cascade can be employed in purification demonstrating successive monolayer enrichment in SC and the lack thereof in SDS. Respective extinction spectra are shown in figure 89.

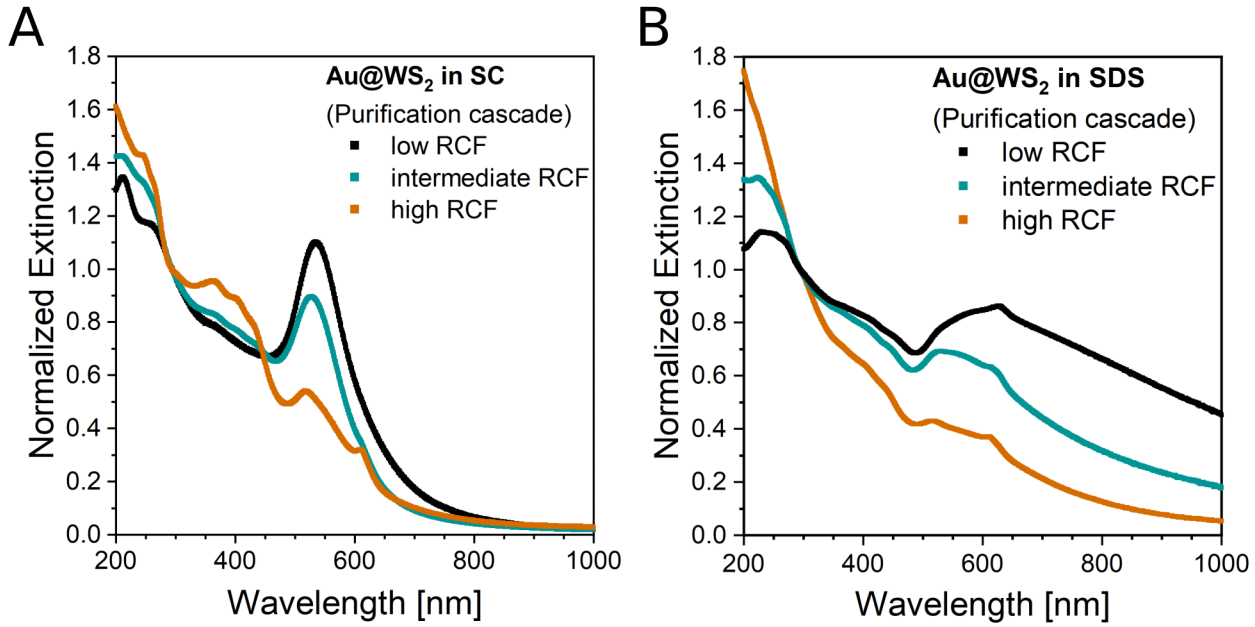

Figure 89: A-B) Extinction spectra of WS_2 dispersions after gold nanoparticle functionalization and subsequent workup for cascade centrifugation employed in purification normalized with respect to the extinction at 294 nm for functionalization in SC (A) and SDS (B).

After centrifugation, the supernatant is subjected to the next step in the cascade and the sediment is redispersed in fresh surfactant solution. Cascade parameters used are 400 *g* (low), 2 000 *g* (intermediate) and 16 000 *g* (high) for SC (A) and 400 *g* (low), 5 000 *g* (intermediate) and 16 000 *g* (high) for SDS (B). For increasing RCF employed, contribution of the gold nanoparticle surface plasmon resonance diminishes indicating succesive removal of bigger gold nanoparticles.

8.2 Determination of extinction coefficients

In order to properly assess the reactant consumption during functionalization, solvatochromic effects due to surfactant interactions must be identified. Since the reactant employed can act as a strong acid as well, pH should only vary between 2 and 4 in the screening experiment detailed in chapter 4.2. Due to the strong extinction coefficient of chloroauric acid, dilution is necessary prior to the measurement which will heavily impact

the solution pH in extinction measurements. Due to the nature of the reactant, a ligand exchange with hydroxide ligands in solution depending on pH (and therefore dilution) can occur which leads to peak maximum shifts and changes in extinction coefficients, visible in figure 90, A.[261]

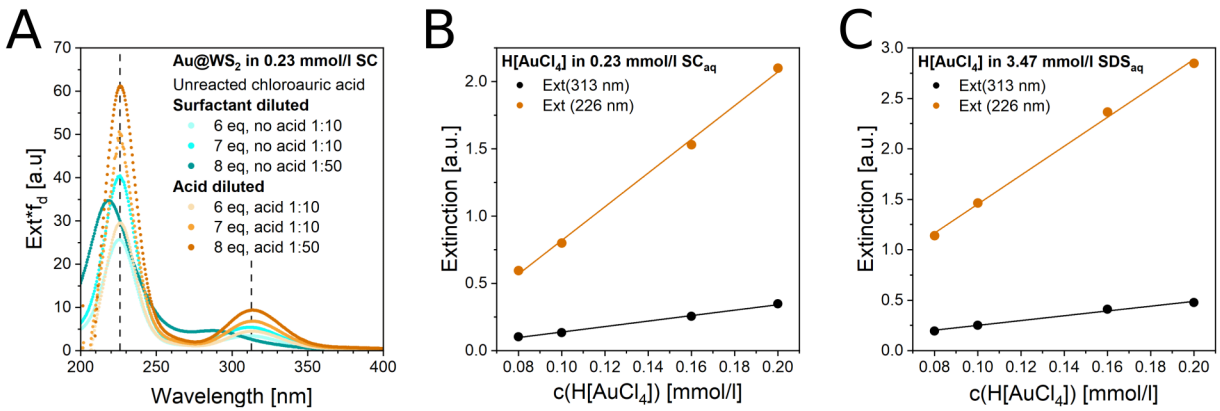

Figure 90: A) Extinction spectra of unreacted chloroauric acid separated after functionalization of WS_2 with high stoichiometric amounts of chloroauric acid with (orange traces) and without (teal traces) acidification prior to the measurement. Extinction maxima in the acidified case are indicated using dashed lines. B) Extinction of peak maxima labeled in A of chloroauric acid in acidified sodium cholate solution for different concentrations of chloroauric acid. The linear slope (solid lines) enables calculation of the extinction coefficient. C) Extinction of peak maxima labeled in A of chloroauric acid in acidified sodium dodecyl sulfate solution for different concentrations of chloroauric acid. The linear slope (solid lines) enables calculation of the extinction coefficient.

To circumvent this reaction from influencing the estimation of the reactant consumption, the reaction supernatant is diluted using concentrated hydrochloric acid in a way that the surfactant concentration does not change and the hydrochloric acid concentration in the measured sample is 1/8 of concentrated hydrochloric acid. To ensure that this treatment does not impact the extinction of chloroauric acid in surfactant solution, extinction coefficients are determined in acidified surfactant solution for SC and SDS (figure 90, B-C). Extinction coefficients were determined from the linear slope of peak maxima with the concentration of chloroauric acid $\varepsilon_{226\,nm} = 3.130 \cdot 10^4\,\mathrm{l\,mol^{-1}\,cm^{-1}}$ and $\varepsilon_{313\,nm} = 5.085 \cdot 10^3\,\mathrm{l\,mol^{-1}\,cm^{-1}}$ in SC solution and $\varepsilon_{226\,nm} = 3.586 \cdot 10^4\,\mathrm{l\,mol^{-1}\,cm^{-1}}$ and $\varepsilon_{313\,nm} = 5.955 \cdot 10^3\,\mathrm{l\,mol^{-1}\,cm^{-1}}$ in SDS solution.

8.3 Normalized extinction spectra of functionalized WS_2

In order to properly judge changes in extinction ratios, normalization of extinction spectra with respect to extinction at 294 nm is performed (figure 91). The surface plasmon resonance is more pronounced in SC than in SDS for comparable reactant amounts.

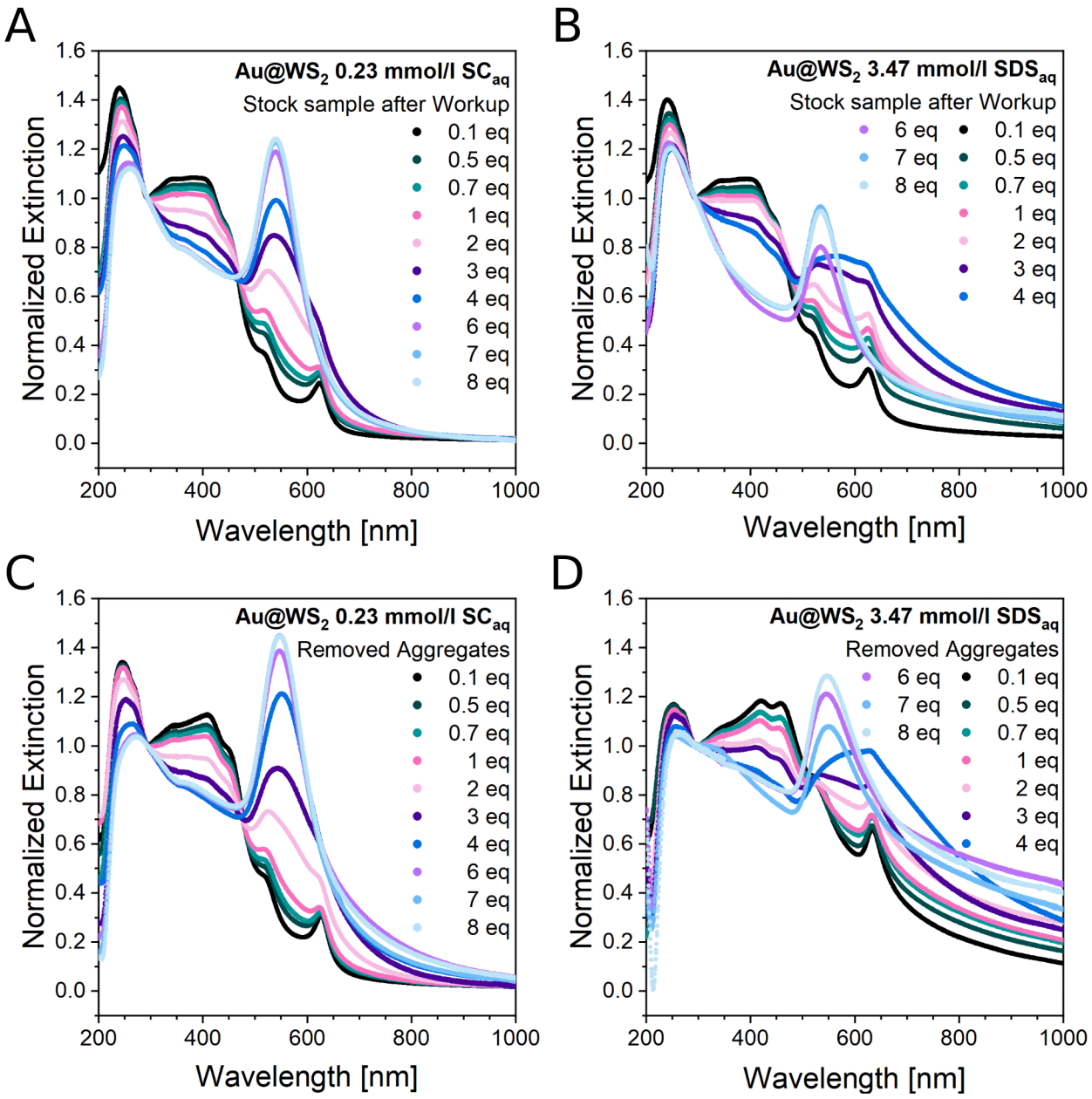

Figure 91: Extinction spectra normalized with to the extinction at 294 nm for Stock samples after workup in SC (A) and SDS (B) as well as removed aggregated material in SC (C) and SDS (D) for varying amounts of chloroauric acid employed.

8.4 Concentration screening for ζ potential measurements

In order to find concentrations in which ζ potentials are comparable for comparable concentrations, a surfactant concentration screening was conducted. Therefore, evaluation using the average ζ potential across the whole ζ range for each sample is used, averaged across 20 measurements (figure 92, A-B). This evaluation method may lack the precision of distribution fitting but should be sufficient for a crude screening experiment.

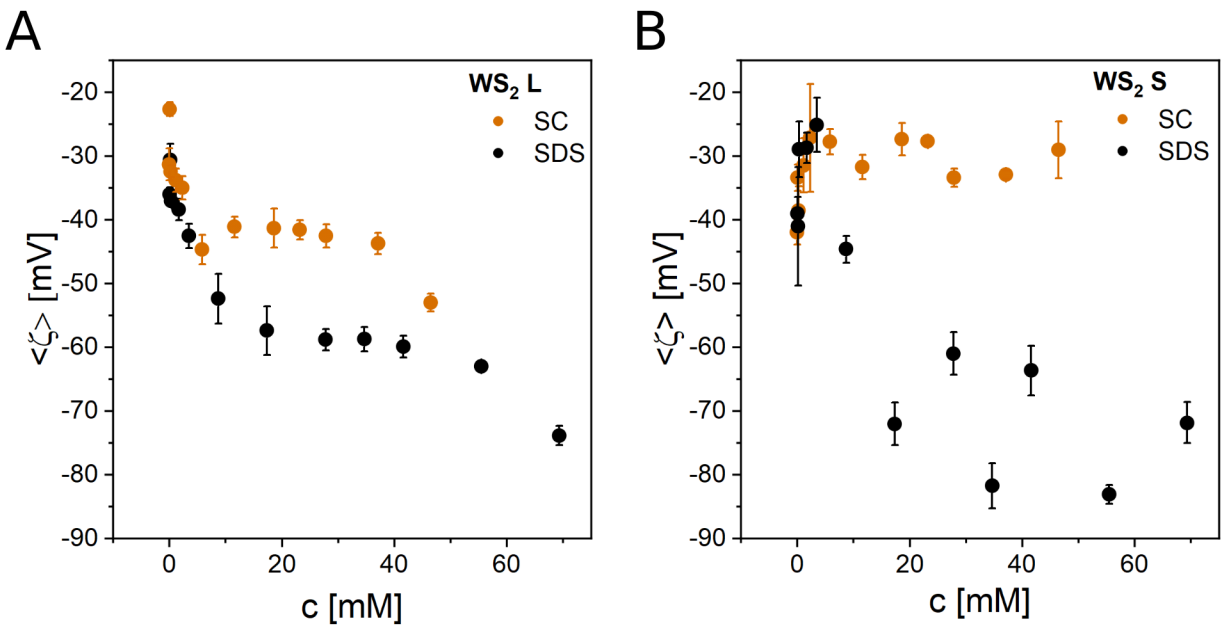

Figure 92: Mean ζ potentials of large (A, 0.4 - 1k g, <L> = 149 nm, <N> = 8) and small (B, 5 - 30k g, <L> = 41 nm, <N> = 2) WS_2 dispersions in SC and SDS for varying surfactant concentrations. Nanosheet dimensions were derived from samples in 5.75 mmol aqueous SC solution using previously published metrics.[8] *Mean ζ potentials reported in this graph are average values reported by the Zetasizer software. No peak fitting of distributions was performed for this particular experiment.*

In figure 92, A ζ potentials for different surfactant concentrations for large nanosheets are visible. For low surfactant concentrations ζ potentials are comparable across surfactants and get more negative for increasing surfactant concentrations. At intermediate surfactant concentrations ζ potentials stay relatively constant but at different levels for SC and SDS. This behavior may be interpreted as increasing adsorption of surfactant molecules to the nanosheet surface until saturated with different packing densities for different surfactants. At very high surfactant concentrations ζ potentials get more negative again. Reorganization of the adsorbed surfactant molecules at high concentrations may be possible but too few data points show this trend in order to reliably analyze it. In figure 92, B ζ potentials for different surfactant concentrations for small nanosheets are shown. At low surfactant concentrations, ζ potentials get less negative for increasing surfactant concentrations, which seems counterintuitive but error bars in the data points are large and mostly overlap in the low concentration regime which renders this trend questionable. Furthermore, ζ potentials for SC do not change much for increasing surfactant concentrations in contrast to SDS. While the scatter in the SDS data is significant, ζ potentials seem to decrease for increasing surfactant concentrations. From this data it can be concluded that adsorption of SC gets impeded for smaller nanosheets while SDS seems less affected. However, scattering in data is high and therefore interpretation of the data set is limited.

8.5 Normalized extinction spectra for temperature dependent screening

Extinction spectra of WS_2 dispersions retrieved after functionalization at varying temperatures (figure 93). Normalization more clearly resolves trends for spectral features associated with the probed nanomaterials.

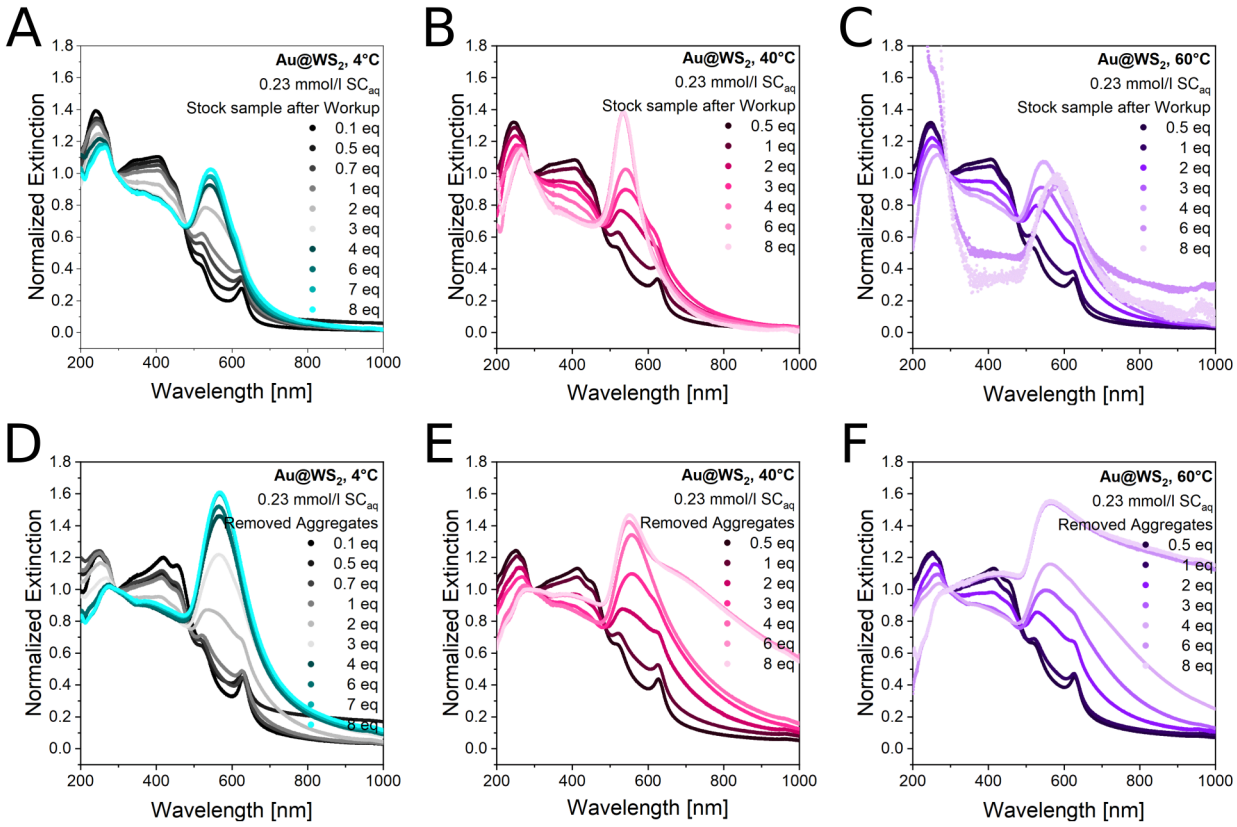

Figure 93: A-C) Extinction spectra of Stock samples after workup for reaction in aqueous SC solution at 4 °C (A), 40 °C (B) and 60 °C (C) normalized with respect to extinction at 294 nm for varying amounts of employed chloroauric acid. D-F) Extinction spectra of aggregated material removed during workup for reaction in aqueous SC solution at 4 °C (D), 40 °C (E) and 60 °C (F) normalized with respect to extinction at 294 nm for varying amounts of employed chloroauric acid.

8.6 Raman spectroscopy of pristine and functionalized MoS_2

Raman spectra of MoS_2 dispersions excited with a 633 nm laser with varying nanosheet sizes produced using liquid phase exfoliation and subsequent liquid cascade centrifugation are shown in figure 94. At this excitation wavelength, PL and vibrational modes of MoS_2 are superposed. In order to eliminate the contribution of the amount of material probed in Raman spectroscopy, spectra were normalized to the height of the E^1_{2g} vibrational mode at 385 1/cm on top of the PL background.

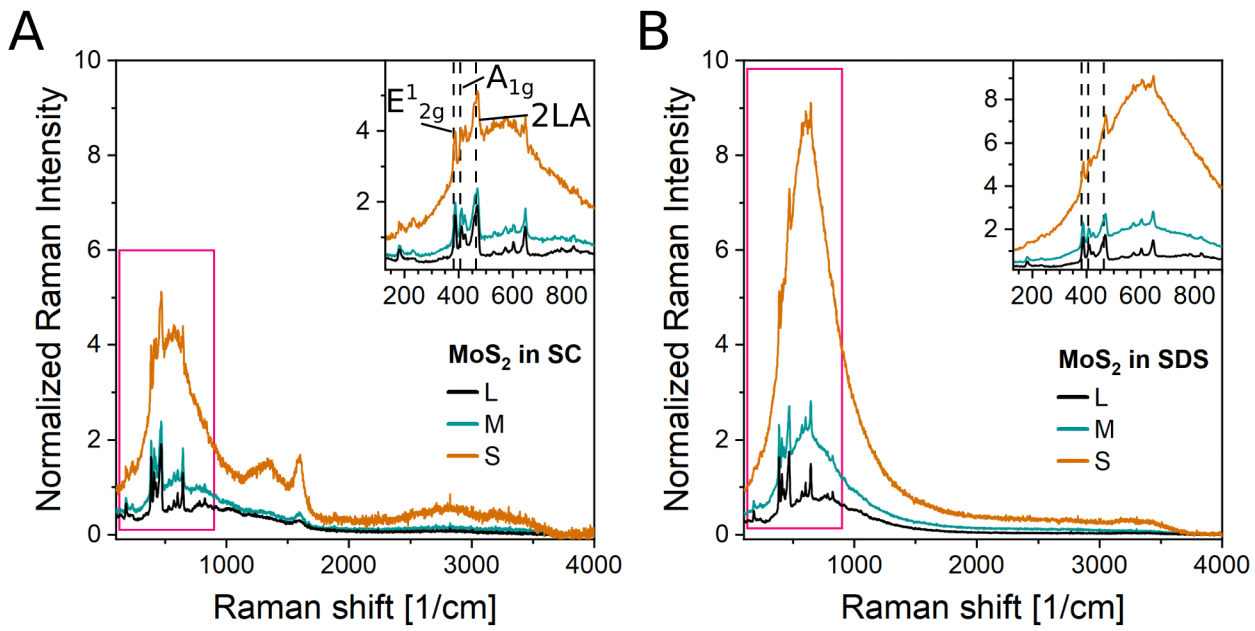

Figure 94: Raman spectra of MoS_2 dispersions measured on a droplet of the dispersion (λ_{exc} = 633 nm) for SC (A) and SDS (B). Three spectra are averaged each, a flat baseline was subtracted and the spectra were normalized with respect to the height of the E^1_{2g} vibrational mode. The inset shows an enlarged view on the spectral region around the 2LA, E^1_{2g} and A_{1g} mode as indicated. Samples are labeled with L for large (0.4 - 1k g, <L> = 185 nm), M for medium (1 - 5k g, <L> = 87 nm) and S for small (5 - 30k g, <L> = 60 nm) in order to illustrate changes in relation to the average lateral size <L> of the MoS_2 dispersion. <L> was determined from extinction spectra in 0.23 mmol/l aqueous SC solution using published metrics.[15] *Line assignment was taken from literature.*[262]

PL background increases significantly for decreasing nanosheet size $<L>$ due to a reduction of the average layer number $<N>$ and a transition from an indirect to direct bandgap in the monolayer limit. Comparison across surfactants reveals superior PL emission for all sizes of MoS_2 exfoliated in SDS (figure 94, B) with highest normalized PL and narrow lineshape for dispersion S in SDS. Due to the fact that different exfoliation batches are compared in figure 94, batch-to-batch variations cannot be excluded. However, this may be seen as an indication that exfoliation in SDS is beneficial to the material quality compared to SC.

8.7 AFM images of pristine and functionalized (4 eq) MoS_2 for statistics

For statistical evaluation of nanosheet dimensions AFM imaging was performed on nanosheets deposited on SiO_2. Example images are shown in figure 95.

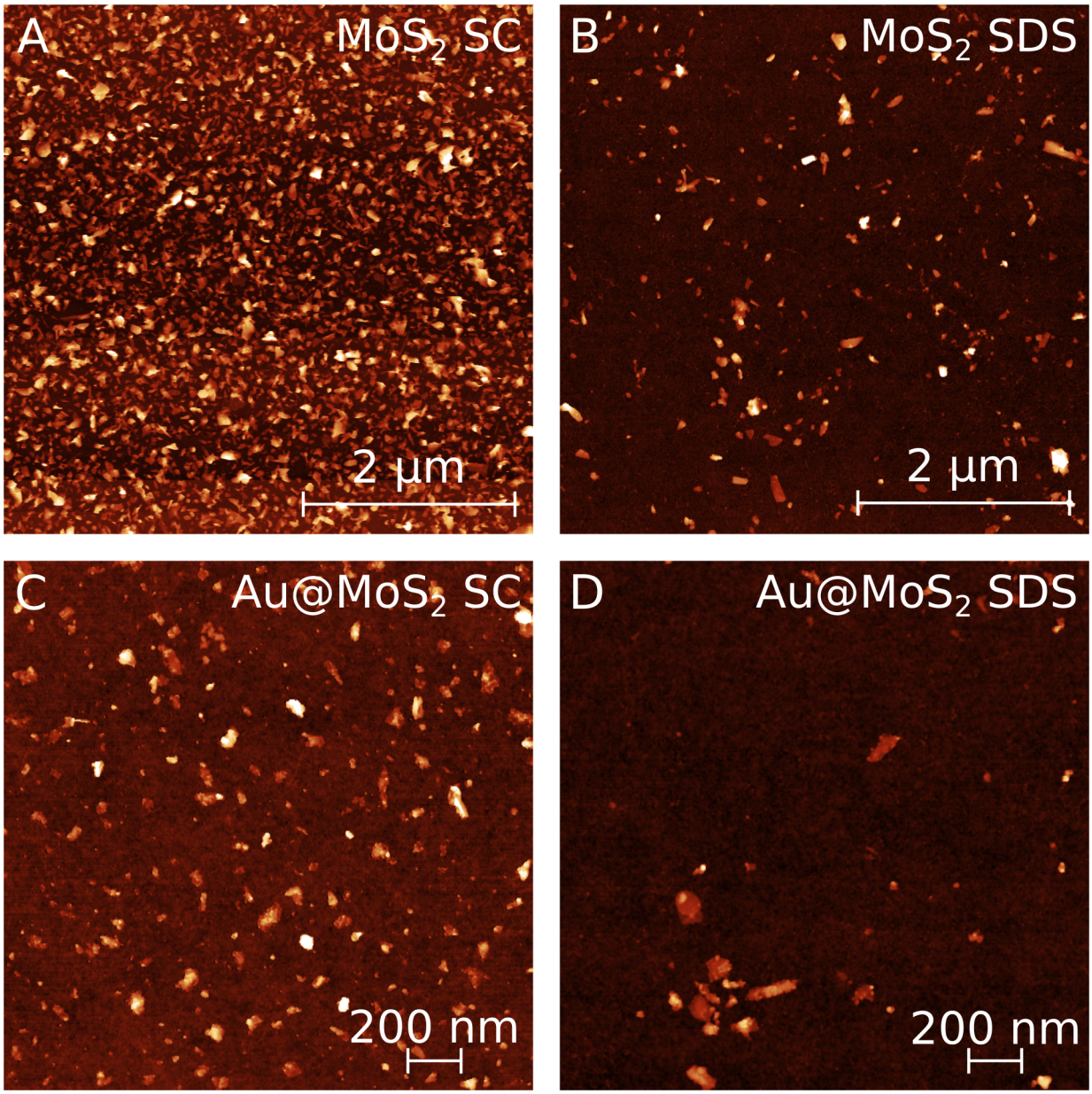

Figure 95: AFM images of pristine (A-B) and functionalized (C-D) MoS_2 nanosheets in SC (A, C) and SDS (B, D) on SiO_2. Functionalized nanosheets were imaged using increased magnification to help resolve features on the nanosheets.

Nanosheets are measured along the longest axis (L) and the axis orthogonal to it (W) and the height h is extracted from line scans across the nanosheets. The scatter plot of all evaluated data can be seen in figure 96. Upon functionalization in SC and SDS the average nanosheet area decreases while thickness decreases only in SC and stays constant in SDS.

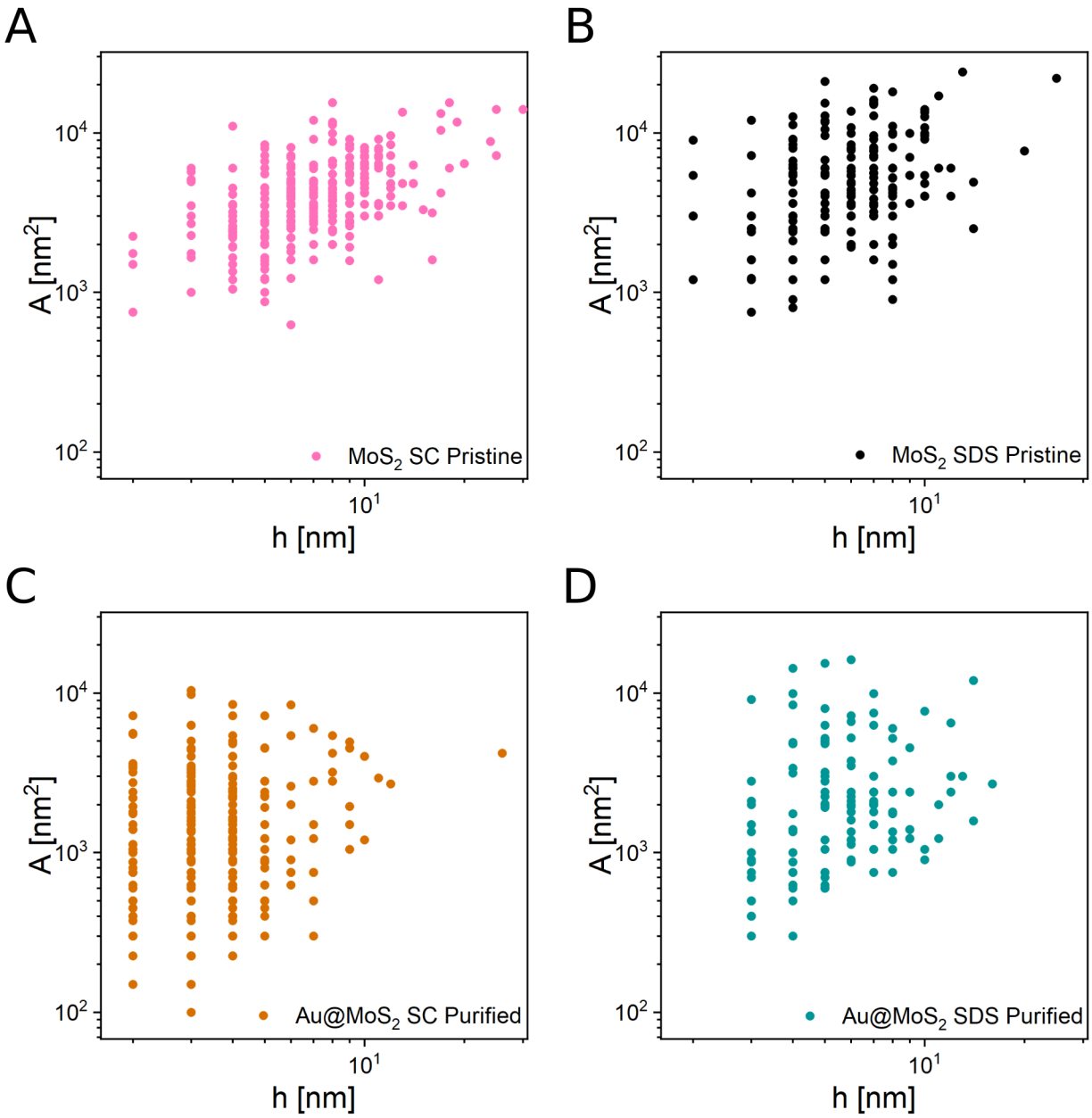

Figure 96: A-D) Scatter plots of nanosheet area A calculated as $L \cdot W$ versus thickness h on logarithmic scales for pristine MoS_2 exfoliated in SC (A) and SDS (B) as well as for MoS_2 after functionalization and purification in SC (C) and SDS (D).

8.8 Normalized extinction spectra of MoS_2 functionalization

In order to visualize trends in extinction ratios more clearly, extinction spectra of functionalized MoS_2 for *Stock* samples and for aggregated material removed during workup were normalized with respect to extinction at 345 nm and are shown in figure 97.

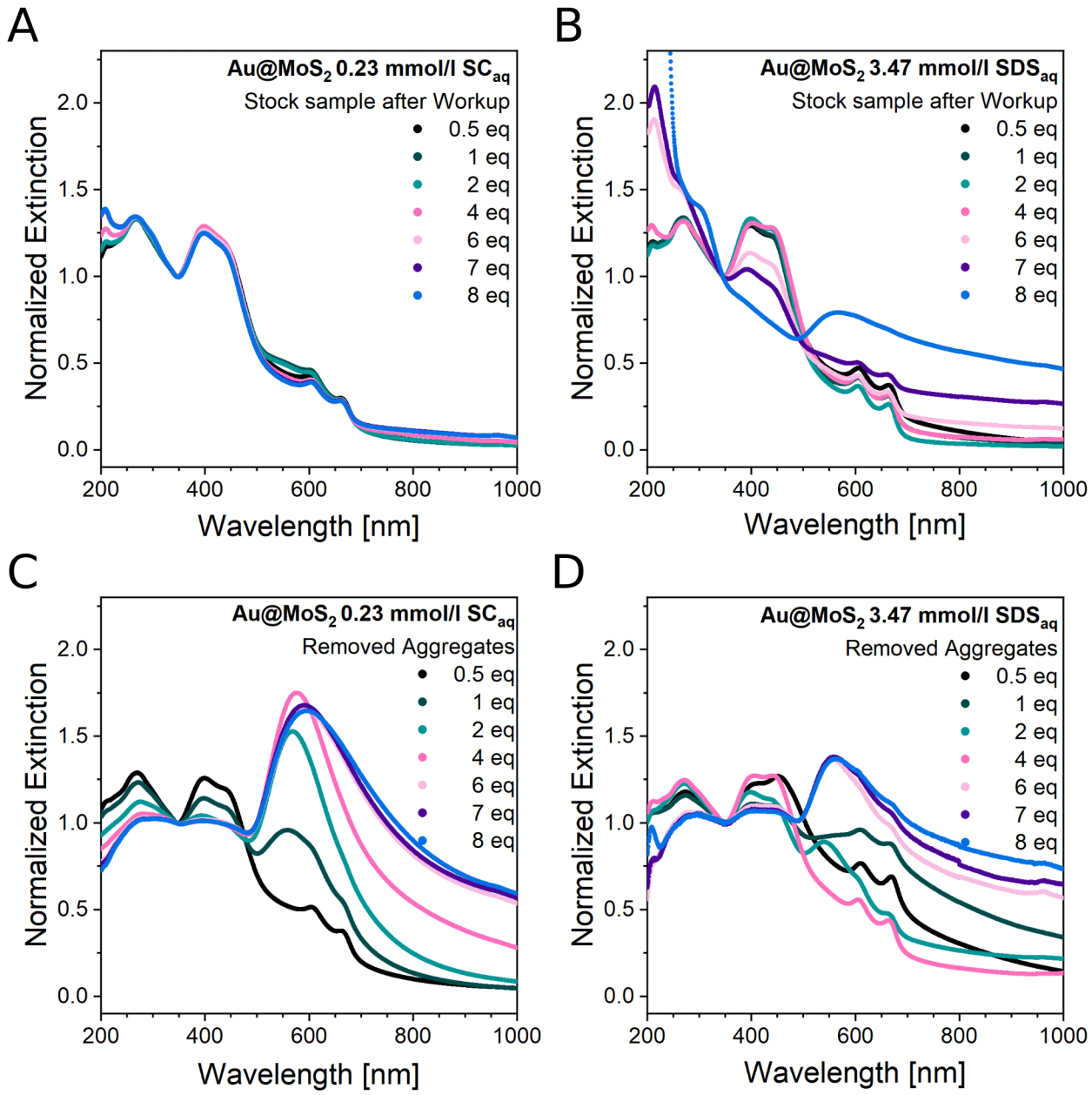

Figure 97: Extinction spectra normalized with respect to extinction at 345 nm for Stock samples after workup in SC (A) and SDS (B) as well as removed aggregated material in SC (C) and SDS (D) for varying amounts of chloroauric acid employed.

The spectral profile of MoS_2 is well replicated in SC *Stock* dispersions (A) for all equivalents employed with a slight decrease of the extinction ratio *Ext(270 nm)/Ext(345 nm)* based on a small reduction of nanosheet sizes during functionalization while degradation of the profile is visible in SDS (B). Surface plasmon resonance of gold nanoparticles in the removed aggregates is more pronounced in SC (C) than in SDS (D) and mostly absent in

the *Stock* dispersion after workup except for 8 equivalents in SDS. The spectral profile of MoS_2 is increasingly lost upon functionalization with increasing amounts of reactant.

8.9 Raman spectra of WS_2 nanotubes after exfoliation

Raman spectra of WS_2 nanotubes were recorded on droplets of dispersion produced from exfoliation with laser excitation at 532 and 633 nm and are shown in figure 98.

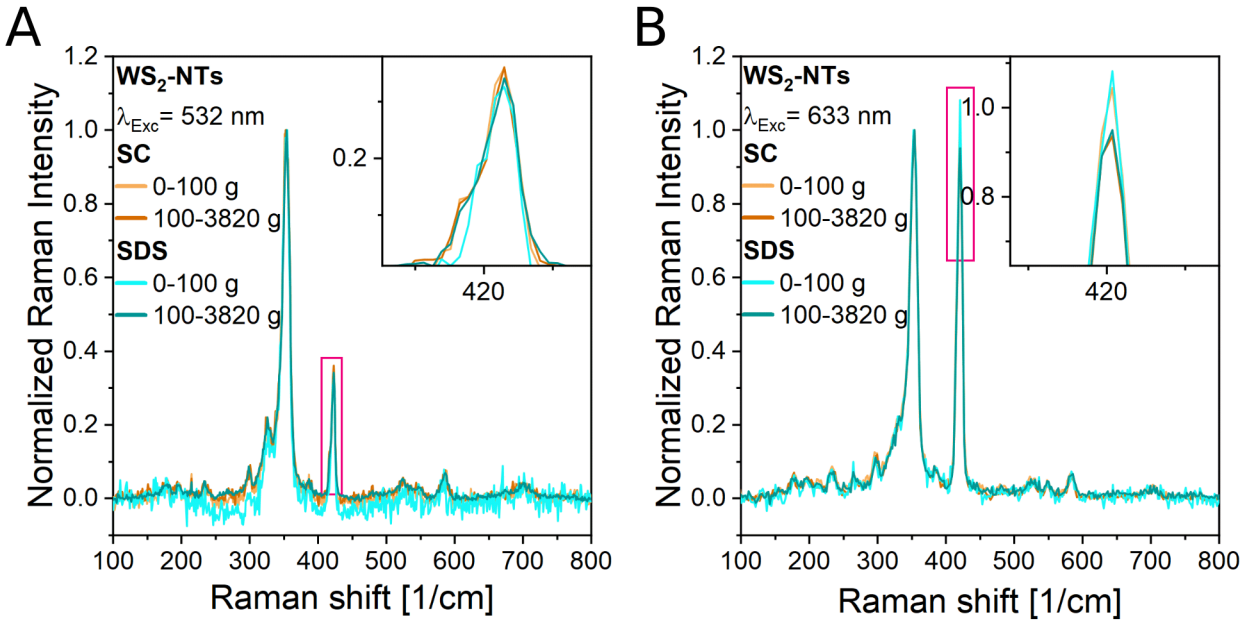

Figure 98: Raman spectra of WS_2 nanotube dispersions normalized with respect to intensity at the E^1_{2g} vibrational mode for exfoliation in SC and SDS and laser excitation at 532 (A) and 633 nm(B). Insets show an enlarged view of the vibrational mode at around 421 1/cm.

The characteristic vibrational modes (A_{1g} at 421 1/cm, E^1_{2g} at 352 1/cm and E_{1g} at 300 1/cm) for WS_2 nanotubes are well visible and differences to spectra of WS_2 nanosheets become apparent upon comparison of excitation with different laser wavelengths. Upon laser excitation at 532 nm (A) a shoulder at 416 1/cm in the left flank of the A_{1g} mode is revealed and assigned to the B_{1u} mode which should be Raman inactive according to group theory. It is activated by the nanotube curvature and therefore becomes visible in Raman spectroscopy.[237] This mode vanishes upon excitation with a laser wavelength of 633 nm (B) and only the A_{1g} mode at 421 1/cm remains visible in that region. This appears puzzling as literature predicts an increase in B_{1u} intensity upon decreasing excitation energy.[237] It may well be that B_{1u} contribution indeed increases but is not individually resolved anymore due to limitations in resolution. Interestingly a difference in the A_{1g}/E^1_{2g} ratio is visible for excitation with 633 nm upon removal of aggregated material (see inset in B) for both surfactants as is usually expected for WS_2 nanosheets and is there used as a metric to evaluate the layer number of individual nanosheets.[122] It remains questionable though if transfer of these findings to tubular WS_2 structures is adequate. Especially since such a behavior is not visible for measurement at 532 nm.

8.10 AFM images of gold-functionalized WS_2 nanotubes after purification

In order to assess average lateral dimensions and thickness of nanosheets derived from gold functionalization of WS_2 nanotubes in SC using 0.04 eq_{ext} chloroauric acid, AFM imaging was performed and selected images are shown in figure 99.

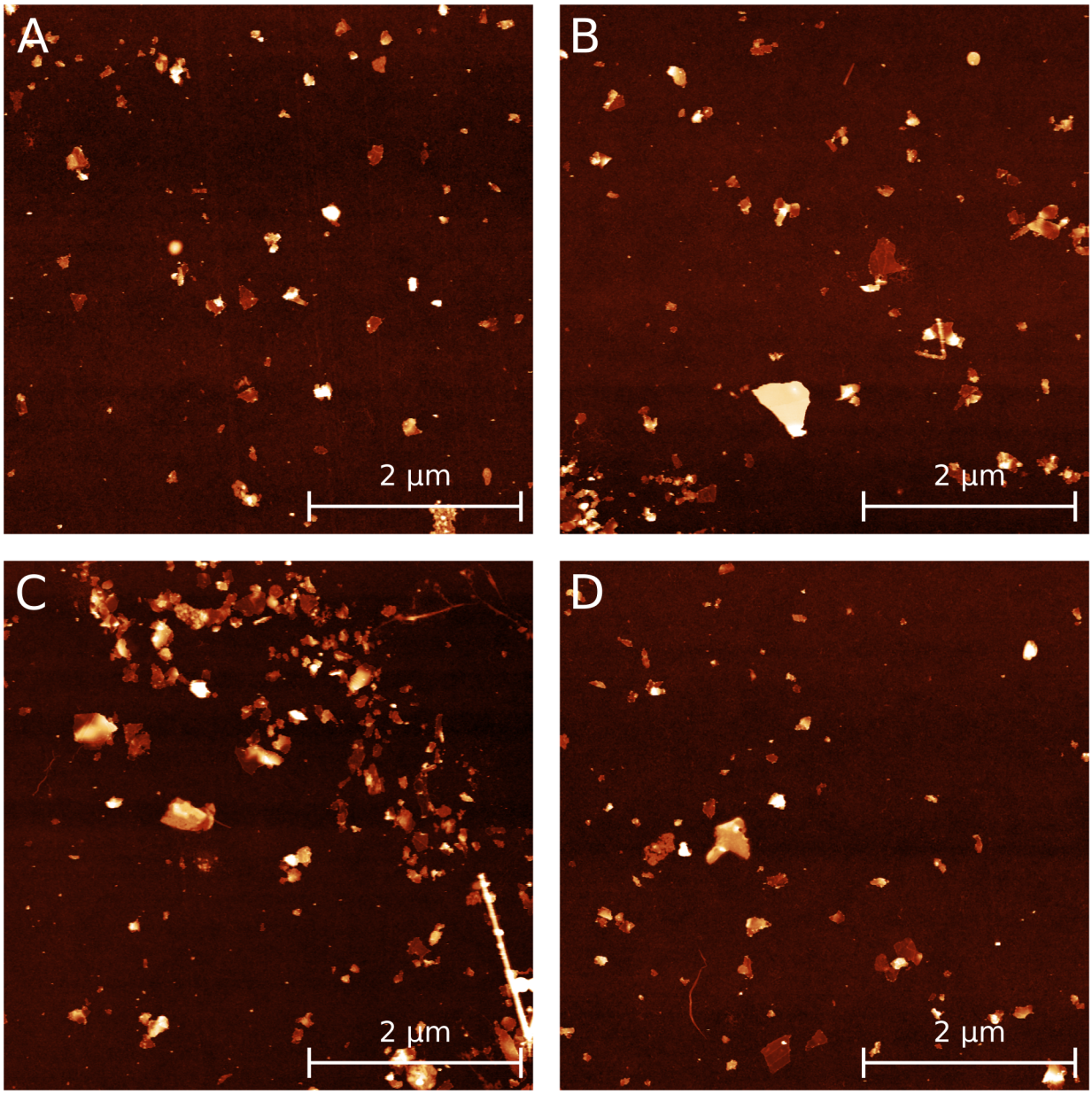

Figure 99: A-D) AFM images of gold-functionalized WS_2 nanotubes after purification employing double centrifugation at 200 g on SiO_2.

8.11 TMCL-IDE 3.0 script for airbrush spray control

In order to calibrate and control the substrate stage and enable a looping movement around the center position, a short TMCL-IDE 3.0 script was devised in earlier works and is shown for reference.[217]

```
WAIT TICKS, 0, 50          //initial pause after switch on (autorun must be activated)

Left:                      //initialization left limiter switch
ROL 0, 750                 //movement to the left with speed 750

L:                         //reference loop for left limiter switch
GAP 11, 0                  //stores left limiter switch status (0/1) into ACCU
COMP 1                     //compares ACCU with value 1
JC EQ, Right               //if ACCU matches value 1, initialization of right limiter switch starts
JA L                       //if not, reference loop for left limiter switch is repeated

Right:                     //initialization of right limiter switch
MST 0                      //motor stop
WAIT TICKS, 0, 50          //program pause to increase precision of stored position
SAP 1, 0, 0                //sets point of origin to motor position
ROR 0, 750                 //movement to the right with speed 750

R:                         //reference loop for right limiter switch
GAP 10, 0                  //stores right limiter switch status (0/1) into ACCU
COMP 1                     //compares ACCU with value 1
JC EQ, Calcu               //if ACCU matches value 1, jump to calculation step
JA R                       //if not, reference loop for right limiter switch is repeated

Calcu:                     //calculation step
MST 0                      //motor stop
WAIT TICKS, 0, 50          //program pause to increase precision of stored position
SAP 4 , 0 , 500            //sets maximum speed of future movements
SAP 5 , 0 , 500            //sets maximum acceleration of future movements
GAP 1, 0                   //saves motor position into ACCU
CALC DIV, 2                //divides value in ACCU by 2
AAP 0, 0                   //assigns value of ACCU as target position (enables tracking in program)
ACO 10, 0                  //stores ACCU values as coordinate 10 = center position
MVP COORD, 0, 10           //moves to center position
WAIT POS, 0, 0             //program pause until movement is finished
MST 0                      //motor stop
SAP 4 , 0 , 750            //sets maximum speed of future movements (overrides earlier configuration)
SAP 5 , 0 , 500            //sets maximum acceleration of future movements (overrides earlier configuration)

Mainloop:                  //spraying loop

MVP REL, 0, 60000          //sets loop distance right (1 cm ~ 43 500 units)
WAIT POS, 0, 0             //program pause until movement is finished
MVP COORD, 0, 10           //return to center position
WAIT POS, 0, 0             //program pause until movement is finished
MVP REL, 0, -60000         //sets loop distance left (1 cm ~ 43 500 units)
WAIT POS, 0, 0             //program pause until movement is finished
MVP COORD, 0, 10           //return to center position
WAIT POS, 0, 0             //program pause until movement is finished
JA Mainloop                //loop is repeated indefinitely
```

8.12 Composite films via airbrush spray deposition

A certain advantage of using airbrush spray deposition is facile production of composite films through mixing of dispersions for ink production. A concise demonstration of this is presented herein. WS_2 and *h*-BN nanosheet composite films were produced through ink mixing of dispersions in aqueous SC solution derived from liquid phase exfoliation and liquid cascade centrifugation for the respective materials. Both dispersions employed contained LPE nanosheets removed between 1 - 5k *g*.

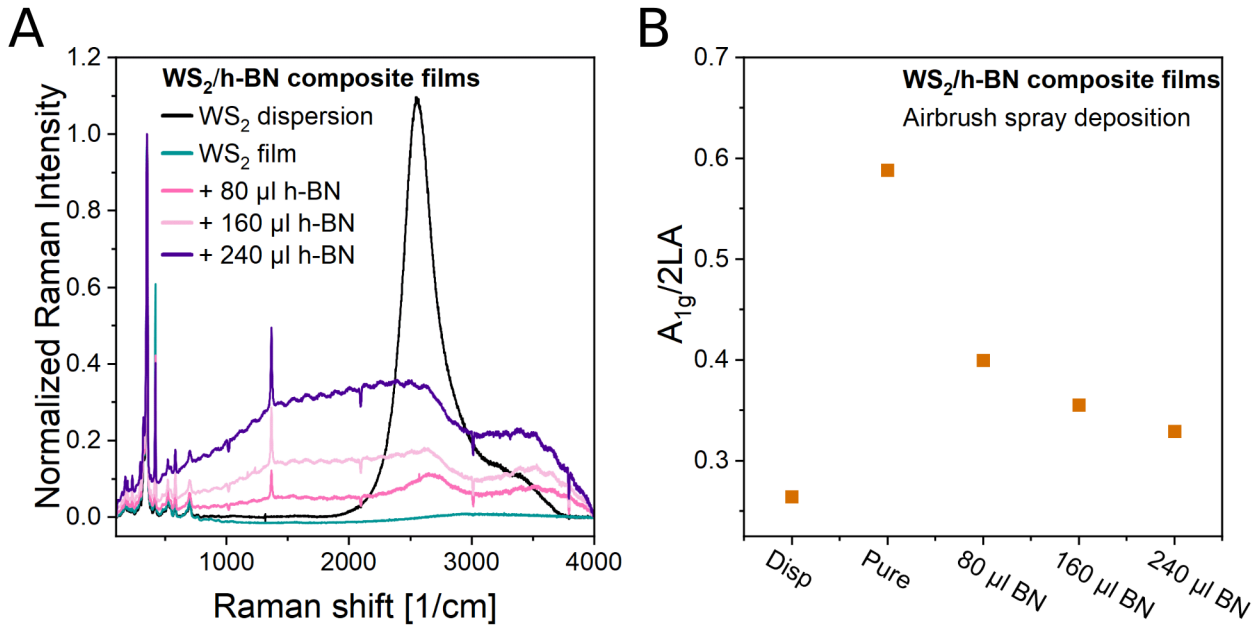

Figure 100: A) Normalized Raman spectra (λ_{Exc} = 532 nm) of pure WS_2 dispersions in aqueous SC, a pure WS_2 film and WS_2/h-BN composite films with varying amounts of h-BN added to the ink. Three spectra are averaged each, a constant baseline was subtracted and the spectra were normalized with respect to the 2LA mode of WS_2. B) A_{1g}/2LA intensity ratio for films in A. For extraction of peak ratios, respective vibrational modes were fitted with Lorentzians and intensity at the maximum of fit were extracted to compensate the increasing background in spectra for increasing amounts of h-BN added.

Raman spectra of WS_2/*h*-BN composite films as well as reference spectra are shown in figure 100, A. A vibrational mode at 1366 1/cm absent in pure WS_2 emerges in composite films and is assigned to the G band of *h*-BN.[17] The G band of *h*-BN increases in intensity compared to the 2LA mode of WS_2 with increasing addition of *h*-BN to the ink. Generally, the G band of *h*-BN appears rather low in intensity compared to WS_2 signals however in contrast to WS_2, *h*-BN is not excited resonantly and therefore WS_2 signals are strongly enhanced compared to WS_2. As initial dispersion concentration of *h*-BN is hard to estimate reliably,[17] the WS_2/*h*-BN mass ratio is unknown and *h*-BN content might be very high. The increasing background and oscillation with higher amounts of *h*-BN added can be assigned to an increase in sample temperature during measurement. Apparently heat dissipation in the film suffers with increasing addition of *h*-BN. As expected for airbrush spray deposition, PL is completely quenched in pure WS_2 films (compare black and teal

trace in figure 100, A). However, for low amounts of h-BN (pink trace) a small PL signal in is retained in the film and vanishes again for higher amounts of *h*-BN added. It is therefore unclear based on the presented data whether *a* filler material can impede random restacking in airbrush deposited films and if this effect is just masked in WS_2/*h*-BN composites due to sample heating. An interesting feature of Raman spectra is a significant decrease in A_{1g}/2LA intensity ratio for increasing amounts of *h*-BN added. This is visualized via Lorentzian fitting of A_{1g} and 2LA modes and maximum of fit position is extracted and shown in figure 100, B. In films A_{1g}/2LA intensity ratio is generally increased compared to dispersion and a clear correlation of the intensity ratio and the amount of filler material is evident. This is remarkable as both A_{1g} and 2LA modes are WS_2 vibrational modes and therefore an impact of *h*-BN being present is unexpected. It appears that the A_{1g}/2LA intensity ratio is sensitive to the nanosheet environment and possibly film morphology and a more systematic study into this phenomenon might be worthwhile.

8.13 Raman spectra of molecules on WS_2 films after soaking and washing

In order to assess adhesion of molecules to the WS_2 film surface, Raman spectra of films after soaking in molecule solution prior to and after washing in toluene were measured (figure 101).

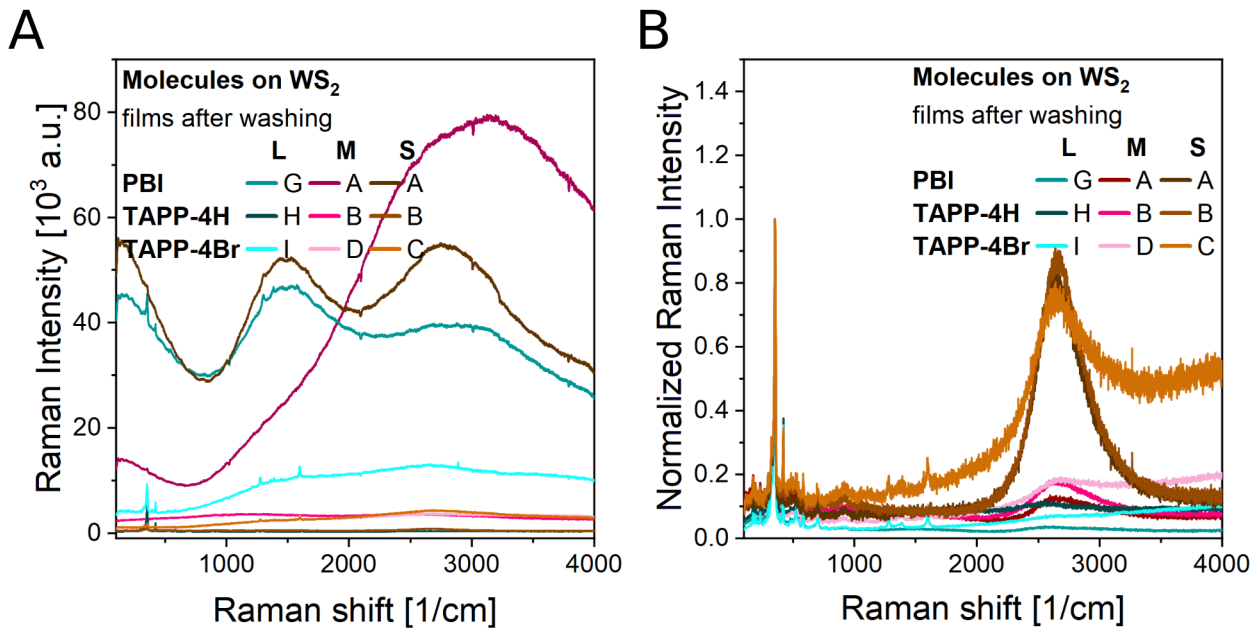

Figure 101: A) Raman spectra of WS_2 films produced via the modified Langmuir-Schaeffer method after molecule deposition before washing. B) Raman spectra of WS_2 films produced via the modified Langmuir-Schaefer method after molecule deposition and washing in toluene normalized to the intensity at the 2LA vibrational mode. No baselines were substracted in A and B.

Before washing (figure 101, A), PBI spectra are dominated by intense background signals owing to the molecules PL, as PBI is well excited upon laser irradiation at 532 nm, which renders any kind of baseline substraction unreliable.[243] Superposed on this

background, molecule peaks can be discerned with the most intense peak positioned at 1299 1/cm. For TAPP-4H no PL background is visible[244] Furthermore, no molecule peaks can be discerned indicating insufficient adhesion of the molecule to the film surface. For TAPP-4Br surprisingly a minor PL background is visible although its absorption maximum is positioned at 475 nm in solution.[244] Possibly molecule absorption is shifted upon film deposition however as no traces of such absorption are visible in extinction spectra verification of this hypothesis is not possible. For TAPP-4Br, vibrational modes of the molecule are well visible with the strongest mode positioned at 1597 1/cm. Films were then washed by soaking them in toluene over-night and Raman spectra were remeasured (figure 101, B). For PBI PL background as well as vibrational modes of the molecule are completely removed after washing and WS_2 PL is again clearly resolved indicating that deposition is reversable. For TAPP-4Br, the molecule PL background is significantly reduced and the WS_2 PL is again clearly resolved, however molecule vibrational modes are still present. This shows that TAPP-4Br shows best adhesion among the molecules deposited, in contrast to insufficient adhesion of TAPP-4H. PBI is easily deposited from and removed with toluene however high amounts of deposited PBI impair acquisition of Raman spectra due to its intense PL. Therefore, molecule deposition was repeated after washing with altered deposition times: For PBI and TAPP-4Br, films are dipped for 10 s in the molecule solution whereas TAPP-4H was soaked for 10 minutes. No washing was carried out afterwards for all three molecules.

8.14 Examples of Tafel plot fitting

For extraction of Tafel slopes and exchange current densities, linear sweep voltammograms are linearized and shown in figure 102. The classic Tafel plot (panel A) plots the logarithm of the current density versus overpotential. For semiconductor electrodes, two linear regimes are expected, assigned to the depletion and the accumulation region. The accumulation region is not accessible in its entirety as increasing H_2 production during HER results in bubble formation adversely affecting effective electrode area. Therefore, linear fits are only employed to the depletion region to extract the Tafel slope and exchange current density. McAteer at al. employed an alternative Tafel plot (figure 102, B) which is also used in this thesis.[177] The type of plotting did not affect the resultant parameters b and J_0. The fact that two linear regimes are hinted at in panel A is most probably related to the fact that the flat band potential, at which the space charge region developed from potential differences of electrode and electrolyte is erased due to the electrode bias, is reached. This might indicate *n*-doping of the WS_2 films employed although, for such claims more sophisticated experiments are necessary. However, for semiconductor electrodes, a Tafel slope of RF/T (25.7 mV at 25 °C) is expected for the depletion region far from the Tafel slopes extracted in the experiments.[258] Similar observations for WSe_2 electrodes and comparable Tafel slopes for WS_2 nanosheet films

were made in literature with the former being assigned to averaging of macroscopic kinetics over a certain distribution of reaction sites on the electrode with different individual activities.[255, 258] This explains the observed Tafel slopes as HER activity of WS_2 nanosheet edges is known to be superior compared to its basal plane activity, as demonstrated using MoS_2 nanosheets[15].[255, 263-264] This implies a certain size-dependence of the Tafel slope due to variations in the edge-to-basal plane area ratio. Furthermore, any kind of assignment of individual reaction steps as rate limiting based on the Tafel slope value is not credible, as it is impacted by contributions of different reaction sites with possibly different rate limiting steps.

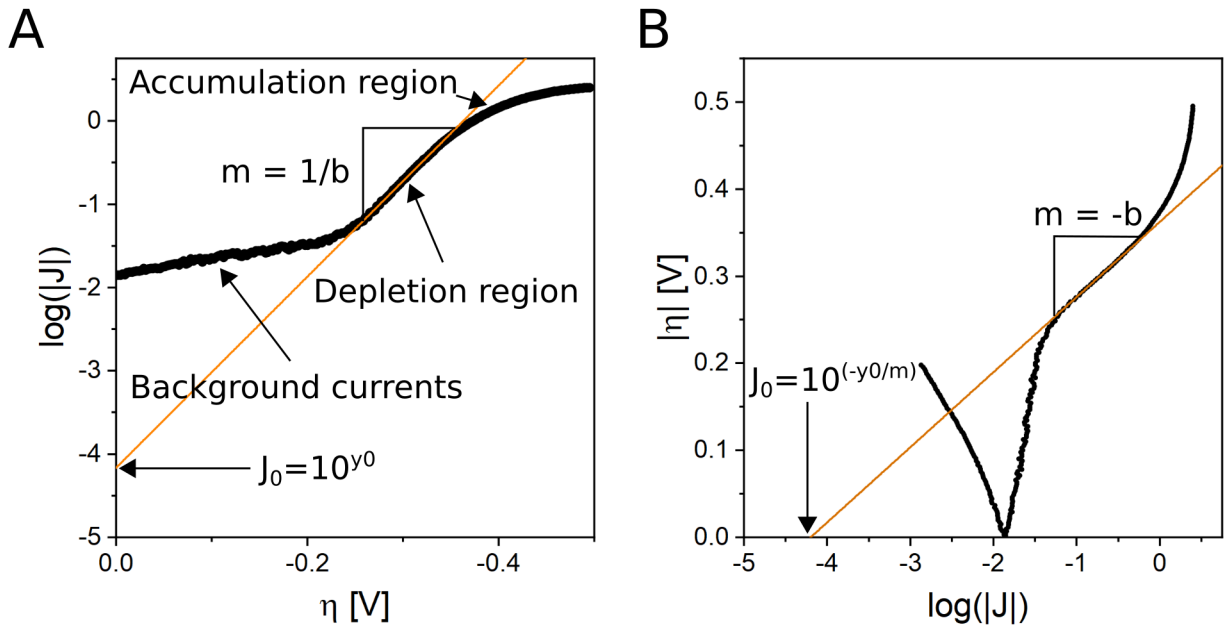

Figure 102: A) Classic Tafel plot for linear sweep voltammetry of HER at semiconducting WS_2 electrodes and linear regression. Different current regimes are labeled.[258] *B) Modified Tafel plot employed by McAteer et al. for ease of identification of the depletion region.*[177]

15 Electrochemical response is largely comparable for WS_2 and MoS_2.

9 Bibliography

[1] G. Fiori, F. Bonaccorso, G. Iannaccone, T. Palacios, D. Neumaier, A. Seabaugh, S. K. Banerjee, L. Colombo, *Nature Nanotechnology* **2014**, *9*, 768-779.

[2] J. Shim, H.-Y. Park, D.-H. Kang, J.-O. Kim, S.-H. Jo, Y. Park, J.-H. Park, *Advanced Electronic Materials* **2017**, *3*, 1600364.

[3] L. Peng, Y. Zhu, D. Chen, R. S. Ruoff, G. Yu, *Advanced Energy Materials* **2016**, *6*, 1600025.

[4] X. Chia, M. Pumera, *Nature Catalysis* **2018**, *1*, 909-921.

[5] T. Low, A. Chaves, J. D. Caldwell, A. Kumar, N. X. Fang, P. Avouris, T. F. Heinz, F. Guinea, L. Martin-Moreno, F. Koppens, *Nature Materials* **2017**, *16*, 182-194.

[6] N. Wiberg, *Lehrbuch der Anorganischen Chemie*, 102 ed., De Gruyter, **2008**.

[7] C. Backes, R. J. Smith, N. McEvoy, N. C. Berner, D. McCloskey, H. C. Nerl, A. O'Neill, P. J. King, T. Higgins, D. Hanlon, N. Scheuschner, J. Maultzsch, L. Houben, G. S. Duesberg, J. F. Donegan, V. Nicolosi, J. N. Coleman, *Nature Communications* **2014**, *5*, 4576.

[8] C. Backes, B. M. Szydłowska, A. Harvey, S. Yuan, V. Vega-Mayoral, B. R. Davies, P.-l. Zhao, D. Hanlon, E. J. G. Santos, M. I. Katsnelson, W. J. Blau, C. Gadermaier, J. N. Coleman, *ACS Nano* **2016**, *10*, 1589-1601.

[9] M. Šiškins, M. Lee, F. Alijani, M. R. van Blankenstein, D. Davidovikj, H. S. J. van der Zant, P. G. Steeneken, *ACS Nano* **2019**, *13*, 10845-10851.

[10] Y. Zhang, G. Li, J. Zhang, L. Zhang, *Nanotechnology* **2004**, *15*, 762-765.

[11] A. Harvey, J. B. Boland, I. Godwin, A. G. Kelly, B. M. Szydłowska, G. Murtaza, A. Thomas, D. J. Lewis, P. O'Brien, J. N. Coleman, *2D Materials* **2017**, *4*, 025054.

[12] B. Yang, X. Li, Y. Cheng, S. Duan, B. Zhao, W. Yi, C. Wang, H. Sun, Z. Wang, D. Gu, S. Chen, X. Liu, *Journal of Materials Chemistry C* **2020**, *8*, 12314-12322.

[13] J. Gu, Z. Du, C. Zhang, J. Ma, B. Li, S. Yang, *Advanced Energy Materials* **2017**, *7*, 1700447.

[14] R. Frisenda, Y. Niu, P. Gant, M. Muñoz, A. Castellanos-Gomez, *npj 2D Materials and Applications* **2020**, *4*, 38.

[15] K. Synnatschke, P. A. Cieslik, A. Harvey, A. Castellanos-Gomez, T. Tian, C.-J. Shih, A. Chernikov, E. J. G. Santos, J. N. Coleman, C. Backes, *Chemistry of Materials* **2019**, *31*, 10049-10062.

[16] C. P. Cullen, C. Ó Coileáin, J. B. McManus, O. Hartwig, D. McCloskey, G. S. Duesberg, N. McEvoy, *Nanoscale* **2021**, *13*, 7403-7411.

[17] A. Griffin, A. Harvey, B. Cunningham, D. Scullion, T. Tian, C.-J. Shih, M. Gruening, J. F. Donegan, E. J. G. Santos, C. Backes, J. N. Coleman, *Chemistry of Materials* **2018**, *30*, 1998-2005.

[18] A. Harvey, C. Backes, Z. Gholamvand, D. Hanlon, D. McAteer, H. C. Nerl, E. McGuire, A. Seral-Ascaso, Q. M. Ramasse, N. McEvoy, S. Winters, N. C. Berner, D. McCloskey, J. F. Donegan, G. S. Duesberg, V. Nicolosi, J. N. Coleman, *Chemistry of Materials* **2015**, *27*, 3483-3493.

[19] D. Lam, K.-S. Chen, J. Kang, X. Liu, M. C. Hersam, *Chemistry of Materials* **2018**, *30*, 2245-2250.

[20] A. Harvey, X. He, I. J. Godwin, C. Backes, D. McAteer, N. C. Berner, N. McEvoy, A. Ferguson, A. Shmeliov, M. E. G. Lyons, V. Nicolosi, G. S. Duesberg, J. F. Donegan, J. N. Coleman, *Journal of Materials Chemistry A* **2016**, *4*, 11046-11059.

[21] K. Synnatschke, S. Shao, J. van Dinter, Y. J. Hofstetter, D. J. Kelly, S. Grieger, S. J. Haigh, Y. Vaynzof, W. Bensch, C. Backes, *Chemistry of Materials* **2019**, *31*, 9127-9139.

[22] M. Naguib, O. Mashtalir, J. Carle, V. Presser, J. Lu, L. Hultman, Y. Gogotsi, M. W. Barsoum, *ACS Nano* **2012**, *6*, 1322-1331.

[23] D. Hanlon, C. Backes, E. Doherty, C. S. Cucinotta, N. C. Berner, C. Boland, K. Lee, A. Harvey, P. Lynch, Z. Gholamvand, S. Zhang, K. Wang, G. Moynihan, A. Pokle, Q. M. Ramasse, N. McEvoy, W. J. Blau, J. Wang, G. Abellan, F. Hauke, A. Hirsch, S. Sanvito, D. D. O'Regan, G. S. Duesberg, V. Nicolosi, J. N. Coleman, *Nature Communications* **2015**, *6*, 8563.

[24] R. Z. Lange, K. Synnatschke, H. Qi, N. Huber, G. Hofer, B. Liang, C. Huck, A. Pucci, U. Kaiser, C. Backes, A. D. Schlüter, *Angewandte Chemie International Edition* **2020**, *59*, 5683-5695.

[25] S. Leubner, V. E. G. Bengtsson, K. Synnatschke, J. Gosch, A. Koch, H. Reinsch, H. Xu, C. Backes, X. Zou, N. Stock, *Journal of the American Chemical Society* **2020**, *142*, 15995-16000.

[26] C. Xing, Z. Xie, Z. Liang, W. Liang, T. Fan, J. S. Ponraj, S. C. Dhanabalan, D. Fan, H. Zhang, *Advanced Optical Materials* **2017**, *5*, 1700884.

[27] Z. Xie, C. Xing, W. Huang, T. Fan, Z. Li, J. Zhao, Y. Xiang, Z. Guo, J. Li, Z. Yang, B. Dong, J. Qu, D. Fan, H. Zhang, *Advanced Functional Materials* **2018**, *28*, 1705833.

[28] H. Kaur, R. Tian, A. Roy, M. McCrystall, D. V. Horvath, G. Lozano Onrubia, R. Smith, M. Ruether, A. Griffin, C. Backes, V. Nicolosi, J. N. Coleman, *ACS Nano* **2020**, *14*, 13418-13432.

[29] G. Guan, J. Xia, S. Liu, Y. Cheng, S. Bai, S. Y. Tee, Y.-W. Zhang, M.-Y. Han, *Advanced Materials* **2017**, *29*, 1700326.

[30] V. J. Rao, H. Qi, F. J. Berger, S. Grieger, U. Kaiser, C. Backes, J. Zaumseil, *ACS Nano* **2021**.

[31] The Royal Swedish Academy of Sciences, Nobel Prize Outreach AB 2021, Accessed at 06.12.2021, https://www.nobelprize.org/prizes/physics/2010/press-release/.

[32] A. H. Castro Neto, F. Guinea, N. M. R. Peres, K. S. Novoselov, A. K. Geim, *Reviews of Modern Physics* **2009**, *81*, 109-162.

[33] A. K. Geim, K. S. Novoselov, in *Nanoscience and Technology*, Co-Published with Macmillan Publishers Ltd, UK, **2009**, pp. 11-19.

[34] M. Chhowalla, H. S. Shin, G. Eda, L.-J. Li, K. P. Loh, H. Zhang, *Nature Chemistry* **2013**, *5*, 263-275.

[35] S. Das, J. A. Robinson, M. Dubey, H. Terrones, M. Terrones, *Annual Review of Materials Research* **2015**, *45*, 1-27.

[36] X. Xu, C. Liu, Z. Sun, T. Cao, Z. Zhang, E. Wang, Z. Liu, K. Liu, *Chemical Society Reviews* **2018**, *47*, 3059-3099.

[37] R. Balog, B. Jørgensen, L. Nilsson, M. Andersen, E. Rienks, M. Bianchi, M. Fanetti, E. Lægsgaard, A. Baraldi, S. Lizzit, Z. Sljivancanin, F. Besenbacher, B. Hammer, T. G. Pedersen, P. Hofmann, L. Hornekær, *Nature Materials* **2010**, *9*, 315-319.

[38] D. Usachov, O. Vilkov, A. Grüneis, D. Haberer, A. Fedorov, V. K. Adamchuk, A. B. Preobrajenski, P. Dudin, A. Barinov, M. Oehzelt, C. Laubschat, D. V. Vyalikh, *Nano Letters* **2011**, *11*, 5401-5407.

[39] G. Bottari, M. Á. Herranz, L. Wibmer, M. Volland, L. Rodríguez-Pérez, D. M. Guldi, A. Hirsch, N. Martín, F. D'Souza, T. Torres, *Chemical Society Reviews* **2017**, *46*, 4464-4500.

[40] S. Eigler, A. Hirsch, *Angewandte Chemie International Edition* **2014**, *53*, 7720-7738.

[41] S. Z. Butler, S. M. Hollen, L. Cao, Y. Cui, J. A. Gupta, H. R. Gutiérrez, T. F. Heinz, S. S. Hong, J. Huang, A. F. Ismach, E. Johnston-Halperin, M. Kuno, V. V. Plashnitsa, R. D. Robinson, R. S. Ruoff, S. Salahuddin, J. Shan, L. Shi, M. G. Spencer, M. Terrones, W. Windl, J. E. Goldberger, *ACS Nano* **2013**, *7*, 2898-2926.

[42] A. Hirsch, F. Hauke, *Angewandte Chemie International Edition* **2018**, *57*, 4338-4354.

[43] Á. Coogan, Y. K. Gun'ko, *Materials Advances* **2021**, *2*, 146-164.

[44] J. A. Wilson, A. D. Yoffe, *Advances in Physics* **1969**, *18*, 193-335.

[45] D. Voiry, A. Goswami, R. Kappera, C. d. C. C. e. Silva, D. Kaplan, T. Fujita, M. Chen, T. Asefa, M. Chhowalla, *Nature Chemistry* **2015**, *7*, 45-49.

[46] A. Splendiani, L. Sun, Y. Zhang, T. Li, J. Kim, C.-Y. Chim, G. Galli, F. Wang, *Nano Letters* **2010**, *10*, 1271-1275.

[47] G. Wang, A. Chernikov, M. M. Glazov, T. F. Heinz, X. Marie, T. Amand, B. Urbaszek, *Reviews of Modern Physics* **2018**, *90*, 021001.

[48] K. F. Mak, C. Lee, J. Hone, J. Shan, T. F. Heinz, *Physical Review Letters* **2010**, *105*, 136805.

[49] M. A. Green, *AIP Advances* **2013**, *3*, 112104.

[50] J. R. Schaibley, H. Yu, G. Clark, P. Rivera, J. S. Ross, K. L. Seyler, W. Yao, X. Xu, *Nature Reviews Materials* **2016**, *1*, 16055.

[51] R. Cheng, D. Li, H. Zhou, C. Wang, A. Yin, S. Jiang, Y. Liu, Y. Chen, Y. Huang, X. Duan, *Nano Letters* **2014**, *14*, 5590-5597.

[52] O. Lopez-Sanchez, D. Lembke, M. Kayci, A. Radenovic, A. Kis, *Nature Nanotechnology* **2013**, *8*, 497-501.

[53] Y. Zhan, Z. Liu, S. Najmaei, P. M. Ajayan, J. Lou, *Small* **2012**, *8*, 966-971.

[54] X. Ling, Y.-H. Lee, Y. Lin, W. Fang, L. Yu, M. S. Dresselhaus, J. Kong, *Nano Letters* **2014**, *14*, 464-472.

[55] Q. Ji, Y. Zhang, T. Gao, Y. Zhang, D. Ma, M. Liu, Y. Chen, X. Qiao, P.-H. Tan, M. Kan, J. Feng, Q. Sun, Z. Liu, *Nano Letters* **2013**, *13*, 3870-3877.

[56] D. Dumcenco, D. Ovchinnikov, K. Marinov, P. Lazić, M. Gibertini, N. Marzari, O. L. Sanchez, Y.-C. Kung, D. Krasnozhon, M.-W. Chen, S. Bertolazzi, P. Gillet, A. Fontcuberta i Morral, A. Radenovic, A. Kis, *ACS Nano* **2015**, *9*, 4611-4620.

[57] H. Kim, W. Kim, M. O'Brien, N. McEvoy, C. Yim, M. Marcia, F. Hauke, A. Hirsch, G.-T. Kim, G. S. Duesberg, *Nanoscale* **2018**, *10*, 17557-17566.

[58] K. Kang, S. Xie, L. Huang, Y. Han, P. Y. Huang, K. F. Mak, C.-J. Kim, D. Muller, J. Park, *Nature* **2015**, *520*, 656-660.

[59] L. Tang, J. Tan, H. Nong, B. Liu, H.-M. Cheng, *Accounts of Materials Research* **2021**, *2*, 36-47.

[60] J. H. Zhan, Z. D. Zhang, X. F. Qian, C. Wang, Y. Xie, Y. T. Qian, *Journal of Solid State Chemistry* **1998**, *141*, 270-273.

[61] R. Fan, X. Chen, Z. Chen, *Chemistry Letters* **2000**, *29*, 920-921.

[62] N. Savjani, E. A. Lewis, M. A. Bissett, J. R. Brent, R. A. W. Dryfe, S. J. Haigh, P. O'Brien, *Chemistry of Materials* **2016**, *28*, 657-664.

[63] W. Jung, S. Lee, D. Yoo, S. Jeong, P. Miró, A. Kuc, T. Heine, J. Cheon, *Journal of the American Chemical Society* **2015**, *137*, 7266-7269.

[64] C. Backes, in *Graphene (Second Edition)* (Eds.: V. Skakalova, A. B. Kaiser), Woodhead Publishing, **2021**, pp. 251-314.

[65] K. S. Novoselov, A. K. Geim, S. V. Morozov, D. Jiang, Y. Zhang, S. V. Dubonos, I. V. Grigorieva, A. A. Firsov, *Science* **2004**, *306*, 666.

[66] K. S. Novoselov, D. Jiang, F. Schedin, T. J. Booth, V. V. Khotkevich, S. V. Morozov, A. K. Geim, *Proceedings of the National Academy of Sciences of the United States of America* **2005**, *102*, 10451.

[67] A. E. D. Mahmoud, A. Stolle, M. Stelter, *ACS Sustainable Chemistry & Engineering* **2018**, *6*, 6358-6369.

[68] J. Djamil, A.-L. Hansen, C. Backes, W. Bensch, U. Schürmann, L. Kienle, A. Düvel, P. Heitjans, *Nanoscale* **2018**, *10*, 21142-21150.

[69] Y. Hernandez, V. Nicolosi, M. Lotya, F. M. Blighe, Z. Sun, S. De, I. T. McGovern, B. Holland, M. Byrne, Y. K. Gun'Ko, J. J. Boland, P. Niraj, G. Duesberg, S. Krishnamurthy, R. Goodhue, J. Hutchison, V. Scardaci, A. C. Ferrari, J. N. Coleman, *Nature Nanotechnology* **2008**, *3*, 563-568.

[70] M. Gutiérrez, A. Henglein, *Ultrasonics* **1989**, *27*, 259-261.

[71] T. G. Leighton, *Progress in Biophysics and Molecular Biology* **2007**, *93*, 3-83.
[72] Z. Izadifar, P. Babyn, D. Chapman, *Journal of Medical and Biological Engineering* **2019**, *39*, 259-276.
[73] W. Lauterborn, H. Bolle, *Journal of Fluid Mechanics* **1975**, *72*, 391-399.
[74] R. Pecha, B. Gompf, *Physical Review Letters* **2000**, *84*, 1328-1330.
[75] P. Turner, M. Hodnett, R. Dorey, J. D. Carey, *Scientific Reports* **2019**, *9*, 8710.
[76] R. E. Apfel, C. K. Holland, *Ultrasound in Medicine & Biology* **1991**, *17*, 179-185.
[77] Z. Li, R. J. Young, C. Backes, W. Zhao, X. Zhang, A. A. Zhukov, E. Tillotson, A. P. Conlan, F. Ding, S. J. Haigh, K. S. Novoselov, J. N. Coleman, *ACS Nano* **2020**, *14*, 10976-10985.
[78] C. Backes, D. Campi, B. M. Szydlowska, K. Synnatschke, E. Ojala, F. Rashvand, A. Harvey, A. Griffin, Z. Sofer, N. Marzari, J. N. Coleman, D. D. O'Regan, *ACS Nano* **2019**, *13*, 7050-7061.
[79] S. Ott, N. Wolff, F. Rashvand, V. J. Rao, J. Zaumseil, C. Backes, *Chemistry of Materials* **2019**, *31*, 8424-8431.
[80] K. R. Paton, E. Varrla, C. Backes, R. J. Smith, U. Khan, A. O'Neill, C. Boland, M. Lotya, O. M. Istrate, P. King, T. Higgins, S. Barwich, P. May, P. Puczkarski, I. Ahmed, M. Moebius, H. Pettersson, E. Long, J. Coelho, S. E. O'Brien, E. K. McGuire, B. M. Sanchez, G. S. Duesberg, N. McEvoy, T. J. Pennycook, C. Downing, A. Crossley, V. Nicolosi, J. N. Coleman, *Nature Materials* **2014**, *13*, 624-630.
[81] S. Liang, Z. Shen, M. Yi, L. Liu, X. Zhang, C. Cai, S. Ma, *Journal of Nanoscience and Nanotechnology* **2015**, *15*, 2686-2694.
[82] R. Rizvi, E. P. Nguyen, M. D. Kowal, W. H. Mak, S. Rasel, M. A. Islam, A. Abdelaal, A. S. Joshi, S. Zekriardehani, M. R. Coleman, R. B. Kaner, *Advanced Materials* **2018**, *30*, 1800200.
[83] G. Eda, H. Yamaguchi, D. Voiry, T. Fujita, M. Chen, M. Chhowalla, *Nano Letters* **2011**, *11*, 5111-5116.
[84] T. C. Achee, W. Sun, J. T. Hope, S. G. Quitzau, C. B. Sweeney, S. A. Shah, T. Habib, M. J. Green, *Scientific Reports* **2018**, *8*, 14525.
[85] G. Cunningham, M. Lotya, C. S. Cucinotta, S. Sanvito, S. D. Bergin, R. Menzel, M. S. P. Shaffer, J. N. Coleman, *ACS Nano* **2012**, *6*, 3468-3480.
[86] S. D. Bergin, Z. Sun, D. Rickard, P. V. Streich, J. P. Hamilton, J. N. Coleman, *ACS Nano* **2009**, *3*, 2340-2350.
[87] Y. Hernandez, M. Lotya, D. Rickard, S. D. Bergin, J. N. Coleman, *Langmuir* **2010**, *26*, 3208-3213.
[88] A. Griffin, K. Nisi, J. Pepper, A. Harvey, B. M. Szydłowska, J. N. Coleman, C. Backes, *Chemistry of Materials* **2020**, *32*, 2852-2862.
[89] A. J. Hilmer, T. P. McNicholas, S. Lin, J. Zhang, Q. H. Wang, J. D. Mendenhall, C. Song, D. A. Heller, P. W. Barone, D. Blankschtein, M. S. Strano, *Langmuir* **2012**, *28*, 1309-1321.
[90] R. J. Smith, M. Lotya, J. N. Coleman, *New Journal of Physics* **2010**, *12*, 125008.
[91] N. R. Tummala, A. Striolo, *The Journal of Physical Chemistry B* **2008**, *112*, 1987-2000.
[92] A. Gupta, V. Arunachalam, S. Vasudevan, *The Journal of Physical Chemistry Letters* **2015**, *6*, 739-744.
[93] A. Gupta, S. Vasudevan, *The Journal of Physical Chemistry C* **2018**, *122*, 19243-19250.
[94] S. Grieger, B. M. Szydłowska, V. J. Rao, E. Steinmann, M. Dodds, Z. Gholamvand, G. S. Duesberg, J. Zaumseil, C. Backes, *Angewandte Chemie International Edition* **2020**, *59*, 13785-13792.
[95] M. S. Arnold, J. Suntivich, S. I. Stupp, M. C. Hersam, *ACS Nano* **2008**, *2*, 2291-2300.
[96] S. Lin, C.-J. Shih, M. S. Strano, D. Blankschtein, *Journal of the American Chemical Society* **2011**, *133*, 12810-12823.
[97] *Colloid Science: Principles, Methods and Applications*, 2nd ed., John Wiley and Sons, **2010**.
[98] J. O. m. Bockris, M. A. V. Devanathan, K. Müller, J. A. V. Butler, *Proceedings of the Royal Society of London. Series A. Mathematical and Physical Sciences* **1963**, *274*, 55-79.
[99] G. Wedler, *Lehrbuch der Physikalischen Chemie*, 5th ed., Wiley-VCH, **2004**.

[100] B. Derjaguin, L. Landau, *Progress in Surface Science* **1993**, *43*, 30-59.
[101] J. N. Coleman, *Advanced Functional Materials* **2009**, *19*, 3680-3695.
[102] D. Chapot, L. Bocquet, E. Trizac, *Journal of Colloid and Interface Science* **2005**, *285*, 609-618.
[103] J. D. Sherwood, H. A. Stone, *Physics of Fluids* **1995**, *7*, 697-705.
[104] R. J. Hunter, *Zeta Potential in Colloid Science: Principles and Applications*, 1st ed., Academic Press, **1988**.
[105] S. Bhattacharjee, *Journal of Controlled Release* **2016**, *235*, 337-351.
[106] P. May, U. Khan, J. M. Hughes, J. N. Coleman, *The Journal of Physical Chemistry C* **2012**, *116*, 11393-11400.
[107] R. J. Smith, P. J. King, M. Lotya, C. Wirtz, U. Khan, S. De, A. O'Neill, G. S. Duesberg, J. C. Grunlan, G. Moriarty, J. Chen, J. Wang, A. I. Minett, V. Nicolosi, J. N. Coleman, *Advanced Materials* **2011**, *23*, 3944-3948.
[108] J. L. Cole, J. W. Lary, T. P. Moody, T. M. Laue, in *Methods in Cell Biology, Vol. 84*, Academic Press, **2008**, pp. 143-179.
[109] L. R. Murphy, N. Matubayasi, V. A. Payne, R. M. Levy, *Folding and Design* **1998**, *3*, 105-118.
[110] P. H. Brown, A. Balbo, H. Zhao, C. Ebel, P. Schuck, *PLOS ONE* **2011**, *6*, e26221.
[111] K. Synnatschke, PhD thesis, University of Heidelberg **2021**.
[112] A. A. Green, M. C. Hersam, *Nano Letters* **2009**, *9*, 4031-4036.
[113] J. Kang, J.-W. T. Seo, D. Alducin, A. Ponce, M. J. Yacaman, M. C. Hersam, *Nature Communications* **2014**, *5*, 5478.
[114] T. Ford, J. Graham, D. Rickwood, *Analytical Biochemistry* **1994**, *220*, 360-366.
[115] E. C. Pollard, L. J. Grady, *Biophysical Journal* **1967**, *7*, 205-213.
[116] M. L. Mastronardi, F. Hennrich, E. J. Henderson, F. Maier-Flaig, C. Blum, J. Reichenbach, U. Lemmer, C. Kübel, D. Wang, M. M. Kappes, G. A. Ozin, *Journal of the American Chemical Society* **2011**, *133*, 11928-11931.
[117] A. Harvey, C. Backes, J. B. Boland, X. He, A. Griffin, B. Szydlowska, C. Gabbett, J. F. Donegan, J. N. Coleman, *Nature Communications* **2018**, *9*, 4553.
[118] M. Selig, G. Berghäuser, A. Raja, P. Nagler, C. Schüller, T. F. Heinz, T. Korn, A. Chernikov, E. Malic, A. Knorr, *Nature Communications* **2016**, *7*, 13279.
[119] Y. Li, A. Chernikov, X. Zhang, A. Rigosi, H. M. Hill, A. M. van der Zande, D. A. Chenet, E.-M. Shih, J. Hone, T. F. Heinz, *Physical Review B* **2014**, *90*, 205422.
[120] W. Zheng, Y. Zhu, F. Li, F. Huang, *Photon. Res.* **2018**, *6*, 991-995.
[121] P. Tonndorf, R. Schmidt, P. Böttger, X. Zhang, J. Börner, A. Liebig, M. Albrecht, C. Kloc, O. Gordan, D. R. T. Zahn, S. Michaelis de Vasconcellos, R. Bratschitsch, *Opt. Express* **2013**, *21*, 4908-4916.
[122] A. Berkdemir, H. R. Gutiérrez, A. R. Botello-Méndez, N. Perea-López, A. L. Elías, C.-I. Chia, B. Wang, V. H. Crespi, F. López-Urías, J.-C. Charlier, H. Terrones, M. Terrones, *Scientific Reports* **2013**, *3*, 1755.
[123] M. R. Rosenberger, H.-J. Chuang, K. M. McCreary, C. H. Li, B. T. Jonker, *ACS Nano* **2018**, *12*, 1793-1800.
[124] N. Kang, H. P. Paudel, M. N. Leuenberger, L. Tetard, S. I. Khondaker, *The Journal of Physical Chemistry C* **2014**, *118*, 21258-21263.
[125] H. Wang, C. Zhang, F. Rana, *Nano Letters* **2015**, *15*, 339-345.
[126] Y. Li, C.-Y. Xu, P. Hu, L. Zhen, *ACS Nano* **2013**, *7*, 7795-7804.
[127] D.-H. Kang, J. Shim, S. K. Jang, J. Jeon, M. H. Jeon, G. Y. Yeom, W.-S. Jung, Y. H. Jang, S. Lee, J.-H. Park, *ACS Nano* **2015**, *9*, 1099-1107.

[128] S. Najmaei, X. Zou, D. Er, J. Li, Z. Jin, W. Gao, Q. Zhang, S. Park, L. Ge, S. Lei, J. Kono, V. B. Shenoy, B. I. Yakobson, A. George, P. M. Ajayan, J. Lou, *Nano Letters* **2014**, *14*, 1354-1361.

[129] S. Mouri, Y. Miyauchi, K. Matsuda, *Nano Letters* **2013**, *13*, 5944-5948.

[130] N. Peimyoo, W. Yang, J. Shang, X. Shen, Y. Wang, T. Yu, *ACS Nano* **2014**, *8*, 11320-11329.

[131] J. Choi, H. Zhang, J. H. Choi, *ACS Nano* **2016**, *10*, 1671-1680.

[132] S. H. Amsterdam, T. K. Stanev, Q. Zhou, A. J. T. Lou, H. Bergeron, P. Darancet, M. C. Hersam, N. P. Stern, T. J. Marks, *ACS Nano* **2019**, *13*, 4183-4190.

[133] R. Canton-Vitoria, H. B. Gobeze, V. M. Blas-Ferrando, J. Ortiz, Y. Jang, F. Fernández-Lázaro, Á. Sastre-Santos, Y. Nakanishi, H. Shinohara, F. D'Souza, N. Tagmatarchis, *Angewandte Chemie International Edition* **2019**, *58*, 5712-5717.

[134] C. Backes, F. Hauke, A. Hirsch, *Advanced Materials* **2011**, *23*, 2588-2601.

[135] N. C. Berner, S. Winters, C. Backes, C. Yim, K. C. Dümbgen, I. Kaminska, S. Mackowski, A. A. Cafolla, A. Hirsch, G. S. Duesberg, *Nanoscale* **2015**, *7*, 16337-16342.

[136] M. Marcia, A. Hirsch, F. Hauke, *FlatChem* **2017**, *1*, 89-103.

[137] J. M. Englert, J. Röhrl, C. D. Schmidt, R. Graupner, M. Hundhausen, F. Hauke, A. Hirsch, *Advanced Materials* **2009**, *21*, 4265-4269.

[138] A. Schlierf, H. Yang, E. Gebremedhn, E. Treossi, L. Ortolani, L. Chen, A. Minoia, V. Morandi, P. Samorì, C. Casiraghi, D. Beljonne, V. Palermo, *Nanoscale* **2013**, *5*, 4205-4216.

[139] D. McManus, S. Vranic, F. Withers, V. Sanchez-Romaguera, M. Macucci, H. Yang, R. Sorrentino, K. Parvez, S.-K. Son, G. Iannaccone, K. Kostarelos, G. Fiori, C. Casiraghi, *Nature Nanotechnology* **2017**, *12*, 343-350.

[140] H. Yang, F. Withers, E. Gebremedhn, E. Lewis, L. Britnell, A. Felten, V. Palermo, S. Haigh, D. Beljonne, C. Casiraghi, *2D Materials* **2014**, *1*, 011012.

[141] G. Abellán, V. Lloret, U. Mundloch, M. Marcia, C. Neiss, A. Görling, M. Varela, F. Hauke, A. Hirsch, *Angewandte Chemie International Edition* **2016**, *55*, 14557-14562.

[142] R. S. Swathi, K. L. Sebastian, *The Journal of Chemical Physics* **2008**, *129*, 054703.

[143] N. V. Kozhemyakina, J. M. Englert, G. Yang, E. Spiecker, C. D. Schmidt, F. Hauke, A. Hirsch, *Advanced Materials* **2010**, *22*, 5483-5487.

[144] A. J. Molina-Mendoza, L. Vaquero-Garzon, S. Leret, L. de Juan-Fernández, E. M. Pérez, A. Castellanos-Gomez, *Chemical Communications* **2016**, *52*, 14365-14368.

[145] F. J. Berger, J. Lüttgens, T. Nowack, T. Kutsch, S. Lindenthal, L. Kistner, C. C. Müller, L. M. Bongartz, V. A. Lumsargis, Y. Zakharko, J. Zaumseil, *ACS Nano* **2019**, *13*, 9259-9269.

[146] R. Canton-Vitoria, E. Istif, J. Hernández-Ferrer, E. Urriolabeitía, A. M. Benito, W. K. Maser, N. Tagmatarchis, *ACS Applied Materials & Interfaces* **2019**, *11*, 5947-5956.

[147] M. Vázquez Sulleiro, R. Quirós-Ovies, M. Vera-Hidalgo, I. J. Gómez, V. Sebastián, J. Santamaría, E. M. Pérez, *Chemistry – A European Journal* **2021**, *27*, 2993-2996.

[148] S. Bertolazzi, M. Gobbi, Y. Zhao, C. Backes, P. Samorì, *Chemical Society Reviews* **2018**, *47*, 6845-6888.

[149] H. C. Feng, J. M. Chen, *Journal of Physics C: Solid State Physics* **1974**, *7*, L75-L78.

[150] M. Makarova, Y. Okawa, M. Aono, *The Journal of Physical Chemistry C* **2012**, *116*, 22411-22416.

[151] R. Canton-Vitoria, Y. Sayed-Ahmad-Baraza, M. Pelaez-Fernandez, R. Arenal, C. Bittencourt, C. P. Ewels, N. Tagmatarchis, *npj 2D Materials and Applications* **2017**, *1*, 13.

[152] A. Förster, S. Gemming, G. Seifert, D. Tománek, *ACS Nano* **2017**, *11*, 9989-9996.

[153] D. Voiry, H. Yamaguchi, J. Li, R. Silva, D. C. B. Alves, T. Fujita, M. Chen, T. Asefa, V. B. Shenoy, G. Eda, M. Chhowalla, *Nature Materials* **2013**, *12*, 850-855.

[154] P. Vishnoi, A. Sampath, U. V. Waghmare, C. N. R. Rao, *Chemistry – A European Journal* **2017**, *23*, 886-895.

[155] K. C. Knirsch, N. C. Berner, H. C. Nerl, C. S. Cucinotta, Z. Gholamvand, N. McEvoy, Z. Wang, I. Abramovic, P. Vecera, M. Halik, S. Sanvito, G. S. Duesberg, V. Nicolosi, F. Hauke, A. Hirsch, J. N. Coleman, C. Backes, *ACS Nano* **2015**, *9*, 6018-6030.

[156] M. Cai, F. Zhang, C. Zhang, C. Lu, Y. He, Y. Qu, H. Tian, X. Feng, X. Zhuang, *Journal of Materials Chemistry A* **2018**, *6*, 138-144.

[157] X. Chen, D. McAteer, C. McGuinness, I. Godwin, J. N. Coleman, A. R. McDonald, *Chemistry – A European Journal* **2018**, *24*, 351-355.

[158] C. Backes, N. C. Berner, X. Chen, P. Lafargue, P. LaPlace, M. Freeley, G. S. Duesberg, J. N. Coleman, A. R. McDonald, *Angewandte Chemie International Edition* **2015**, *54*, 2638-2642.

[159] M. Vera-Hidalgo, E. Giovanelli, C. Navío, E. M. Pérez, *Journal of the American Chemical Society* **2019**, *141*, 3767-3771.

[160] J. R. Dunklin, P. Lafargue, T. M. Higgins, G. T. Forcherio, M. Benamara, N. McEvoy, D. K. Roper, J. N. Coleman, Y. Vaynzof, C. Backes, *npj 2D Materials and Applications* **2018**, *1*, 43.

[161] M.-K. Chuang, S.-S. Yang, F.-C. Chen, *Materials* **2015**, *8*.

[162] L. Zhou, B. He, Y. Yang, Y. He, *RSC Advances* **2014**, *4*, 32570-32578.

[163] Z. Cheng, B. He, L. Zhou, *Journal of Materials Chemistry A* **2015**, *3*, 1042-1048.

[164] J. I. Paredes, J. M. Munuera, S. Villar-Rodil, L. Guardia, M. Ayán-Varela, A. Pagán, S. D. Aznar-Cervantes, J. L. Cenis, A. Martínez-Alonso, J. M. D. Tascón, *ACS Applied Materials & Interfaces* **2016**, *8*, 27974-27986.

[165] M. A. Hussain, M. Yang, T. J. Lee, J. W. Kim, B. G. Choi, *Journal of Colloid and Interface Science* **2015**, *451*, 216-220.

[166] X. Huang, Z. Zeng, S. Bao, M. Wang, X. Qi, Z. Fan, H. Zhang, *Nature Communications* **2013**, *4*, 1444.

[167] T. S. Sreeprasad, P. Nguyen, N. Kim, V. Berry, *Nano Letters* **2013**, *13*, 4434-4441.

[168] Y.-M. Liu, M. Zhou, Y.-Y. Liu, G.-F. Shi, J.-J. Zhang, J.-T. Cao, K.-J. Huang, Y.-H. Chen, *RSC Advances* **2014**, *4*, 22888-22893.

[169] X. Xia, Z. Zheng, Y. Zhang, X. Zhao, C. Wang, *Sensors and Actuators B: Chemical* **2014**, *192*, 42-50.

[170] Z. Yin, B. Chen, M. Bosman, X. Cao, J. Chen, B. Zheng, H. Zhang, *Small* **2014**, *10*, 3537-3543.

[171] L. Yuwen, F. Xu, B. Xue, Z. Luo, Q. Zhang, B. Bao, S. Su, L. Weng, W. Huang, L. Wang, *Nanoscale* **2014**, *6*, 5762-5769.

[172] F. Raza, D. Yim, J. H. Park, H.-I. Kim, S.-J. Jeon, J.-H. Kim, *Journal of the American Chemical Society* **2017**, *139*, 14767-14774.

[173] J. Kim, S. Byun, A. J. Smith, J. Yu, J. Huang, *The Journal of Physical Chemistry Letters* **2013**, *4*, 1227-1232.

[174] P. Topolovsek, L. Cmok, C. Gadermaier, M. Borovsak, J. Kovac, A. Mrzel, *Nanoscale* **2016**, *8*, 10016-10020.

[175] M. D. Sharma, C. Mahala, M. Basu, *ChemistrySelect* **2019**, *4*, 378-386.

[176] H. Liu, D. Grasseschi, A. Dodda, K. Fujisawa, D. Olson, E. Kahn, F. Zhang, T. Zhang, Y. Lei, N. Branco Ricardo Braga, L. Elías Ana, C. Silva Rodolfo, Y.-T. Yeh, M. Maroneze Camila, L. Seixas, P. Hopkins, S. Das, J. S. de Matos Christiano, M. Terrones, *Science Advances* **2020**, *6*, eabc9308.

[177] D. McAteer, Z. Gholamvand, N. McEvoy, A. Harvey, E. O'Malley, G. S. Duesberg, J. N. Coleman, *ACS Nano* **2016**, *10*, 672-683.

[178] T. M. Higgins, S. Finn, M. Matthiesen, S. Grieger, K. Synnatschke, M. Brohmann, M. Rother, C. Backes, J. Zaumseil, *Advanced Functional Materials* **2019**, *29*, 1804387.

[179] G. Kelly Adam, T. Hallam, C. Backes, A. Harvey, S. Esmaeily Amir, I. Godwin, J. Coelho, V. Nicolosi, J. Lauth, A. Kulkarni, S. Kinge, D. A. Siebbeles Laurens, S. Duesberg Georg, N. Coleman Jonathan, *Science* **2017**, *356*, 69-73.

[180] D. J. Finn, M. Lotya, G. Cunningham, R. J. Smith, D. McCloskey, J. F. Donegan, J. N. Coleman, *Journal of Materials Chemistry C* **2014**, *2*, 925-932.

[181] S. Ghosh, A. Winchester, B. Muchharla, M. Wasala, S. Feng, A. L. Elias, M. B. M. Krishna, T. Harada, C. Chin, K. Dani, S. Kar, M. Terrones, S. Talapatra, *Scientific Reports* **2015**, *5*, 11272.

[182] A. G. Kelly, D. Finn, A. Harvey, T. Hallam, J. N. Coleman, *Applied Physics Letters* **2016**, *109*, 023107.

[183] R. Worsley, L. Pimpolari, D. McManus, N. Ge, R. Ionescu, J. A. Wittkopf, A. Alieva, G. Basso, M. Macucci, G. Iannaccone, K. S. Novoselov, H. Holder, G. Fiori, C. Casiraghi, *ACS Nano* **2019**, *13*, 54-60.

[184] K. Parvez, Z.-S. Wu, R. Li, X. Liu, R. Graf, X. Feng, K. Müllen, *Journal of the American Chemical Society* **2014**, *136*, 6083-6091.

[185] J. Hassoun, F. Bonaccorso, M. Agostini, M. Angelucci, M. G. Betti, R. Cingolani, M. Gemmi, C. Mariani, S. Panero, V. Pellegrini, B. Scrosati, *Nano Letters* **2014**, *14*, 4901-4906.

[186] X. Yang, W. Fu, W. Liu, J. Hong, Y. Cai, C. Jin, M. Xu, H. Wang, D. Yang, H. Chen, *Journal of Materials Chemistry A* **2014**, *2*, 7727-7733.

[187] E. Kymakis, E. Stratakis, M. M. Stylianakis, E. Koudoumas, C. Fotakis, *Thin Solid Films* **2011**, *520*, 1238-1241.

[188] S. Lu, J. A. Cardenas, R. Worsley, N. X. Williams, J. B. Andrews, C. Casiraghi, A. D. Franklin, *ACS Nano* **2019**, *13*, 11263-11272.

[189] A. G. Kelly, V. Vega-Mayoral, J. B. Boland, J. N. Coleman, *2D Materials* **2019**, *6*, 045036.

[190] J. Neilson, M. P. Avery, B. Derby, *ACS Applied Materials & Interfaces* **2020**, *12*, 25125-25134.

[191] S. P. Ogilvie, M. J. Large, H. J. Wood, A. Amorim Graf, F. Lee, J. P. Salvage, A. A. K. King, A. B. Dalton, *Nanoscale* **2022**, *14*, 320-324.

[192] R. M. Clark, K. J. Berean, B. J. Carey, N. Pillai, T. Daeneke, I. S. Cole, K. Latham, K. Kalantar-zadeh, *Journal of Materials Chemistry C* **2017**, *5*, 6937-6944.

[193] A. G. Kelly, D. O'Suilleabhain, C. Gabbett, J. N. Coleman, *Nature Reviews Materials* **2021**.

[194] W. J. Hyun, E. B. Secor, M. C. Hersam, C. D. Frisbie, L. F. Francis, *Advanced Materials* **2015**, *27*, 109-115.

[195] P. G. Karagiannidis, S. A. Hodge, L. Lombardi, F. Tomarchio, N. Decorde, S. Milana, I. Goykhman, Y. Su, S. V. Mesite, D. N. Johnstone, R. K. Leary, P. A. Midgley, N. M. Pugno, F. Torrisi, A. C. Ferrari, *ACS Nano* **2017**, *11*, 2742-2755.

[196] E. B. Secor, S. Lim, H. Zhang, C. D. Frisbie, L. F. Francis, M. C. Hersam, *Advanced Materials* **2014**, *26*, 4533-4538.

[197] J. Baker, D. Deganello, D. T. Gethin, T. M. Watson, *Materials Research Innovations* **2014**, *18*, 86-90.

[198] F. Bonaccorso, A. Bartolotta, J. N. Coleman, C. Backes, *Advanced Materials* **2016**, *28*, 6136-6166.

[199] R. D. Deegan, O. Bakajin, T. F. Dupont, G. Huber, S. R. Nagel, T. A. Witten, *Nature* **1997**, *389*, 827-829.

[200] K. X. Steirer, M. O. Reese, B. L. Rupert, N. Kopidakis, D. C. Olson, R. T. Collins, D. S. Ginley, *Solar Energy Materials and Solar Cells* **2009**, *93*, 447-453.

[201] G. I. Taylor, *Proceedings of the Royal Society of London. Series A. Mathematical and Physical Sciences* **1964**, *280*, 383-397.

[202] O. V. Salata, *Current Nanoscience* **2005**, *1*, 25-33.

[203] G. Perfetti, T. Alphazan, P. van Hee, W. J. Wildeboer, G. M. H. Meesters, *European Journal of Pharmaceutical Sciences* **2011**, *42*, 262-272.

[204] S. Bose, S. S. Keller, T. S. Alstrøm, A. Boisen, K. Almdal, *Langmuir* **2013**, *29*, 6911-6919.
[205] B. Yu, D. Vak, J. Jo, S. Na, S. Kim, M. Kim, D. Kim, *IEEE Journal of Selected Topics in Quantum Electronics* **2010**, *16*, 1838-1846.
[206] J. W. Owen, N. A. Azarova, M. A. Loth, M. Paradinas, M. Coll, C. Ocal, J. E. Anthony, O. D. Jurchescu, *Journal of Nanotechnology* **2011**, *2011*, 914510.
[207] K. Ariga, Y. Yamauchi, T. Mori, J. P. Hill, *Advanced Materials* **2013**, *25*, 6477-6512.
[208] S. Srivastava, D. Leiske, J. K. Basu, G. G. Fuller, *Soft Matter* **2011**, *7*, 1994-2000.
[209] M. Pohjakallio, T. Aho, K. Kontturi, E. Kontturi, *Soft Matter* **2011**, *7*, 743-748.
[210] T. Bauer, Z. Zheng, A. Renn, R. Enning, A. Stemmer, J. Sakamoto, A. D. Schlüter, *Angewandte Chemie International Edition* **2011**, *50*, 7879-7884.
[211] W. Pisula, Ž. Tomović, U. Kolb, K. Müllen, *Langmuir* **2011**, *27*, 1524-1529.
[212] R. Y. N. Gengler, D. Gournis, A. H. Aimon, L. M. Toma, P. Rudolf, *Chemistry – A European Journal* **2012**, *18*, 7594-7600.
[213] X. Li, G. Zhang, X. Bai, X. Sun, X. Wang, E. Wang, H. Dai, *Nature Nanotechnology* **2008**, *3*, 538-542.
[214] G. Cunningham, U. Khan, C. Backes, D. Hanlon, D. McCloskey, J. F. Donegan, J. N. Coleman, *Journal of Materials Chemistry C* **2013**, *1*, 6899-6904.
[215] G. Cunningham, D. Hanlon, N. McEvoy, G. S. Duesberg, J. N. Coleman, *Nanoscale* **2015**, *7*, 198-208.
[216] X. Yu, M. S. Prévot, N. Guijarro, K. Sivula, *Nature Communications* **2015**, *6*, 7596.
[217] S. Grieger, Master thesis, University of Heidelberg (Heidelberg), **2018**.
[218] W. Haiss, N. T. K. Thanh, J. Aveyard, D. G. Fernig, *Analytical Chemistry* **2007**, *79*, 4215-4221.
[219] K. M. McCreary, A. T. Hanbicki, G. G. Jernigan, J. C. Culbertson, B. T. Jonker, *Scientific Reports* **2016**, *6*, 19159.
[220] M. Amani, D.-H. Lien, D. Kiriya, J. Xiao, A. Azcatl, J. Noh, R. Madhvapathy Surabhi, R. Addou, K. C. Santosh, M. Dubey, K. Cho, M. Wallace Robert, S.-C. Lee, J.-H. He, W. Ager Joel, X. Zhang, E. Yablonovitch, A. Javey, *Science* **2015**, *350*, 1065-1068.
[221] H. Bretscher, Z. Li, J. Xiao, D. Y. Qiu, S. Refaely-Abramson, J. A. Alexander-Webber, A. Tanoh, Y. Fan, G. Delport, C. A. Williams, S. D. Stranks, S. Hofmann, J. B. Neaton, S. G. Louie, A. Rao, *ACS Nano* **2021**, *15*, 8780-8789.
[222] S. Pyrpassopoulos, D. Niarchos, G. Nounesis, N. Boukos, I. Zafiropoulou, V. Tzitzios, *Nanotechnology* **2007**, *18*, 485604.
[223] P. A. G. O'Hare, W. N. Hubbard, G. K. Johnson, H. E. Flotow, *The Journal of Chemical Thermodynamics* **1984**, *16*, 45-59.
[224] P. A. G. O'Hare, B. M. Lewis, B. A. parkinson, *The Journal of Chemical Thermodynamics* **1988**, *20*, 681-691.
[225] J. A. Woollam, R. B. Somoano, *Materials Science and Engineering* **1977**, *31*, 289-295.
[226] W. J. Schutte, J. L. De Boer, F. Jellinek, *Journal of Solid State Chemistry* **1987**, *70*, 207-209.
[227] L. F. Mattheiss, *Physical Review B* **1973**, *8*, 3719-3740.
[228] J. R. Lince, M. R. Hilton, A. S. Bommannavar, *Thin Solid Films* **1995**, *264*, 120-134.
[229] S. Ott, M. Lakmann, C. Backes, *Nanomaterials* **2021**, *11*, 1072.
[230] O. Read, Y. Shin, C.-x. Hu, M. Zarattini, M. Boyes, X. Just-Baringo, A. Panigrahi, I. Larrosa, C. Casiraghi, *Carbon* **2022**, *186*, 550-559.
[231] A. Rothschild, J. Sloan, R. Tenne, *Journal of the American Chemical Society* **2000**, *122*, 5169-5179.
[232] H. Yang, S. Liu, J. Li, M. Li, G. Peng, G. Zou, *Nanotechnology* **2006**, *17*, 1512-1519.
[233] A. Y. Polyakov, L. Yadgarov, R. Popovitz-Biro, V. A. Lebedev, I. Pinkas, R. Rosentsveig, Y. Feldman, A. E. Goldt, E. A. Goodilin, R. Tenne, *The Journal of Physical Chemistry C* **2014**, *118*, 2161-2169.

[234] A. Y. Polyakov, A. V. Nesterov, A. E. Goldt, V. Zubyuk, T. Dolgova, L. Yadgarov, B. Visic, A. A. Fedyanin, R. Tenne, E. A. Goodilin, *Journal of Physics: Conference Series* **2015**, *643*, 012046.

[235] A. Y. Polyakov, D. A. Kozlov, V. A. Lebedev, R. G. Chumakov, A. S. Frolov, L. V. Yashina, M. N. Rumyantseva, E. A. Goodilin, *Chemistry – A European Journal* **2018**, *24*, 18952-18962.

[236] Y. Yomogida, Z. Liu, Y. Ichinose, K. Yanagi, *ACS Omega* **2018**, *3*, 8932-8936.

[237] M. Staiger, P. Rafailov, K. Gartsman, H. Telg, M. Krause, G. Radovsky, A. Zak, C. Thomsen, *Physical Review B* **2012**, *86*, 165423.

[238] O. Grinberg, S. Deng, E. Zussman, T. Livneh, A. Zak, *Physical Chemistry Chemical Physics* **2017**, *19*, 18443-18451.

[239] L. Karger, K. Synnatschke, S. Settele, Y. J. Hofstetter, T. Nowack, J. Zaumseil, Y. Vaynzof, C. Backes, *Advanced Materials* **2021**, *33*, 2102883.

[240] A. Matković, I. Milošević, M. Milićević, T. Tomašević-Ilić, J. Pešić, M. Musić, M. Spasenović, D. Jovanović, B. Vasić, C. Deeks, R. Panajotović, M. R. Belić, R. Gajić, *2D Materials* **2016**, *3*, 015002.

[241] S. Terres, Master thesis, University of Heidelberg (Heidelberg), **2021**.

[242] S. H. Mir, L. A. Nagahara, T. Thundat, P. Mokarian-Tabari, H. Furukawa, A. Khosla, *Journal of The Electrochemical Society* **2018**, *165*, B3137-B3156.

[243] F. Würthner, *Chemical Communications* **2004**, 1564-1579.

[244] L. Hahn, F. Maaß, T. Bleith, U. Zschieschang, H. Wadepohl, H. Klauk, P. Tegeder, L. H. Gade, *Chemistry – A European Journal* **2015**, *21*, 17691-17700.

[245] S. C. Martens, U. Zschieschang, H. Wadepohl, H. Klauk, L. H. Gade, *Chemistry – A European Journal* **2012**, *18*, 3498-3509.

[246] S. M. Obaidulla, M. R. Habib, Y. Khan, Y. Kong, T. Liang, M. Xu, *Advanced Materials Interfaces* **2020**, *7*, 1901197.

[247] H. Langhals, J. Karolin, L. B-Å. Johansson, *Journal of the Chemical Society, Faraday Transactions* **1998**, *94*, 2919-2922.

[248] A. Hirsch, J. M. Englert, F. Hauke, *Accounts of Chemical Research* **2013**, *46*, 87-96.

[249] Arramel, X. Yin, Q. Wang, Y. J. Zheng, Z. Song, M. H. bin Hassan, D. Qi, J. Wu, A. Rusydi, A. T. S. Wee, *ACS Applied Materials & Interfaces* **2017**, *9*, 5566-5573.

[250] K. Balakrishnan, A. Datar, T. Naddo, J. Huang, R. Oitker, M. Yen, J. Zhao, L. Zang, *Journal of the American Chemical Society* **2006**, *128*, 7390-7398.

[251] K. M. McCreary, A. T. Hanbicki, S. Singh, R. K. Kawakami, G. G. Jernigan, M. Ishigami, A. Ng, T. H. Brintlinger, R. M. Stroud, B. T. Jonker, *Scientific Reports* **2016**, *6*, 35154.

[252] F. C. Anson, *Analytical Chemistry* **1966**, *38*, 54-57.

[253] S. J. Konopka, B. McDuffie, *Analytical Chemistry* **1970**, *42*, 1741-1746.

[254] A. Y. S. Eng, A. Ambrosi, Z. Sofer, P. Šimek, M. Pumera, *ACS Nano* **2014**, *8*, 12185-12198.

[255] Z. Gholamvand, D. McAteer, A. Harvey, C. Backes, J. N. Coleman, *Chemistry of Materials* **2016**, *28*, 2641-2651.

[256] G. B. de-Mello, L. Smith, S. J. Rowley-Neale, J. Gruber, S. J. Hutton, C. E. Banks, *RSC Advances* **2017**, *7*, 36208-36213.

[257] T. Shinagawa, A. T. Garcia-Esparza, K. Takanabe, *Scientific Reports* **2015**, *5*, 13801.

[258] B. R. Horrocks, M. V. Mirkin, A. J. Bard, *The Journal of Physical Chemistry* **1994**, *98*, 9106-9114.

[259] A. Lasia, *Hydrogen evolution reaction, in Handbook of Fuel Cells – Fundamentals, Technology and Applications, Vol. 106*, John Wiley & Sons, **2003**.

[260] Y. Shi, J. Wang, C. Wang, T.-T. Zhai, W.-J. Bao, J.-J. Xu, X.-H. Xia, H.-Y. Chen, *Journal of the American Chemical Society* **2015**, *137*, 7365-7370.

[261] J. A. Peck, C. D. Tait, B. I. Swanson, G. E. Brown, *Geochimica et Cosmochimica Acta* **1991**, *55*, 671-676.

[262] B. C. Windom, W. G. Sawyer, D. W. Hahn, *Tribology Letters* **2011**, *42*, 301-310.

[263] T. Sun, H. Zhang, X. Wang, J. Liu, C. Xiao, S. U. Nanayakkara, J. L. Blackburn, M. V. Mirkin, E. M. Miller, *Nanoscale Horizons* **2019**, *4*, 619-624.

[264] F. Jaramillo Thomas, P. Jørgensen Kristina, J. Bonde, H. Nielsen Jane, S. Horch, I. Chorkendorff, *Science* **2007**, *317*, 100-102.

GESAMTFAKULTÄT FÜR MATHEMATIK, INGENIEUR- UND NATURWISSENSCHAFTEN

COMBINED FACULTY OF MATHEMATICS, ENGINEERING AND NATURAL SCIENCES

RUPRECHT-KARLS-
UNIVERSITÄT
HEIDELBERG

Eidesstattliche Versicherung gemäß § 8 der Promotionsordnung für die Gesamtfakultät für Mathematik, Ingenieur- und Naturwissenschaften der Universität Heidelberg /
Sworn Affidavit according to § 8 of the doctoral degree regulations of the Combined Faculty of Mathematics, Engineering and Natural Sciences at Heidelberg University

1. Bei der eingereichten Dissertation zu dem Thema / The thesis I have submitted entitled

   Gold nanoparticle functionalization and thin-film deposition of layered group VI transition metal dichalcogenides

   handelt es sich um meine eigenständig erbrachte Leistung / is my own work.

2. Ich habe nur die angegebenen Quellen und Hilfsmittel benutzt und mich keiner unzulässigen Hilfe Dritter bedient. Insbesondere habe ich wörtlich oder sinngemäß aus anderen Werken übernommene Inhalte als solche kenntlich gemacht. / I have only used the sources indicated and have not made unauthorised use of services of a third party. Where the work of others has been quoted or reproduced, the source is always given.

3. Die Arbeit oder Teile davon habe ich ~~wie folgt~~/bislang nicht[1)] an einer Hochschule des In- oder Auslands als Bestandteil einer Prüfungs- oder Qualifikationsleistung vorgelegt. / I have not yet/have already[1)] presented this thesis or parts thereof to a university as part of an examination or degree.

   Titel der Arbeit / Title of the thesis: -

   Hochschule und Jahr / University and year: -

   Art der Prüfungs- oder Qualifikationsleistung / Type of examination or degree: -

4. Die Richtigkeit der vorstehenden Erklärungen bestätige ich. / I confirm that the declarations made above are correct.

5. Die Bedeutung der eidesstattlichen Versicherung und die strafrechtlichen Folgen einer unrichtigen oder unvollständigen eidesstattlichen Versicherung sind mir bekannt. / I am aware of the importance of a sworn affidavit and the criminal prosecution in case of a false or incomplete affidavit.

Ich versichere an Eides statt, dass ich nach bestem Wissen die reine Wahrheit erklärt und nichts verschwiegen habe. / I affirm that the above is the absolute truth to the best of my knowledge and that I have not concealed anything.

…….. ……..
Ort und Datum / Place and date Unterschrift / Signature

[1)] Nicht Zutreffendes streichen. Bei Bejahung sind anzugeben: der Titel der andernorts vorgelegten Arbeit, die Hochschule, das Jahr der Vorlage und die Art der Prüfungs- oder Qualifikationsleistung. / Please cross out what is not applicable. If applicable, please provide: the title of the thesis that was presented elsewhere, the name of the university, the year of presentation and the type of examination or degree.

The German text is legally binding.